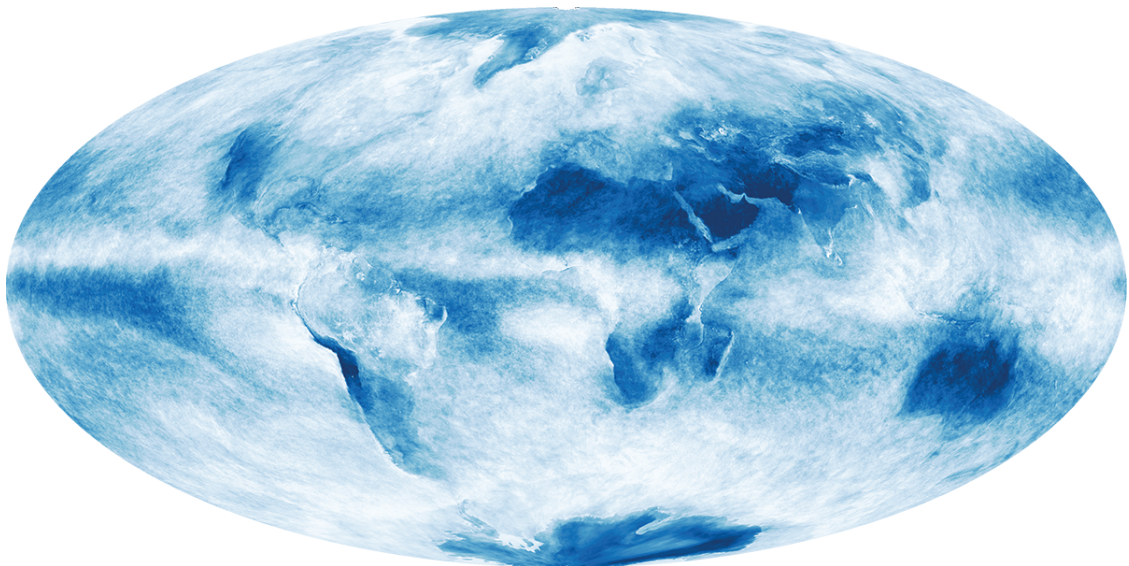# Large-eddy simulations of land-atmosphere interactions and mid-latitude storms: from conceptual models to realistic cases

Guido Cioni

Hamburg 2018

Hinweis

Die Berichte zur Erdsystemforschung werden vom Max-Planck-Institut für Meteorologie in Hamburg in unregelmäßiger Abfolge herausgegeben.

Sie enthalten wissenschaftliche und technische Beiträge, inklusive Dissertationen.

Die Beiträge geben nicht notwendigerweise die Auffassung des Instituts wieder.

Die "Berichte zur Erdsystemforschung" führen die vorherigen Reihen "Reports" und "Examensarbeiten" weiter.

Anschrift / Address

Max-Planck-Institut für Meteorologie
Bundesstrasse 53
20146 Hamburg
Deutschland

Tel./Phone: +49   (0)40 4 11 73 - 0
Fax: +49   (0)40 4 11 73 - 298

name.surname@mpimet.mpg.de
www.mpimet.mpg.de

Notice

The Reports on Earth System Science are published by the Max Planck Institute for Meteorology in Hamburg. They appear in irregular intervals.

They contain scientific and technical contributions, including Ph. D. theses.

The Reports do not necessarily reflect the opinion of the Institute.

The "Reports on Earth System Science" continue the former "Reports" and "Examensarbeiten" of the Max Planck Institute.

Layout
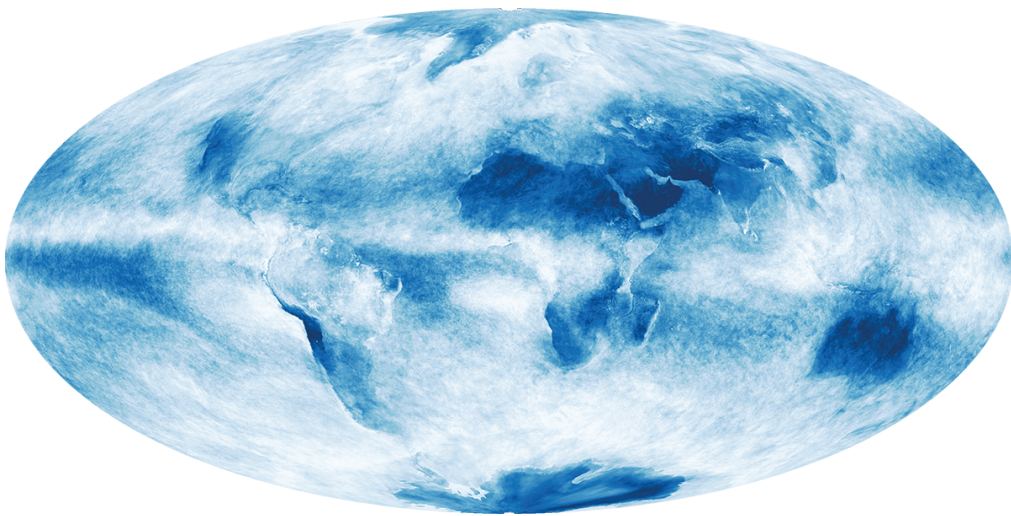
Bettina Diallo and Norbert P. Noreiks
Communication

Copyright

Large-eddy simulations of land-atmosphere interactions and mid-latitude storms: from conceptual models to realistic cases

Dissertation with the aim of achieving a doctoral degree
at the Faculty of Mathematics, Informatics and Natural Sciences
Department of Earth Sciences of Universität Hamburg

submitted by

Guido Cioni

Hamburg 2018

Guido Cioni

Max-Planck-Institut für Meteorologie
Bundesstrasse 53
20146 Hamburg

Tag der Disputation: 26.06.2018

Folgende Gutachter empfehlen die Annahme der Dissertation:

Dr. Cathy Hohenegger
Prof. Dr. Martin Claussen

ABSTRACT

An ability to predict the weather depends on an ability to explicitly represent atmospheric processes in Numerical Weather Prediction (NWP) models. Limited computational resources still force many weather operational centers to perform simulations with a grid spacing of $\mathcal{O}(10 \text{ km})$, thus requiring to parametrize many subgrid-scale processes, and in particular moist convection. On the other hand, Large Eddy Simulation (LES) models, characterized by a grid spacing of $\mathcal{O}(100 \text{ m})$, are usually employed for research purposes in highly idealized setups. This dissertation aims at bridging together these two approaches by using the newly developed Icosahedral Non-hydrostatic Large-Eddy Model (ICON-LEM), which finally allows running LES models over large scales, thereby capturing individual convective clouds, their associated mesoscale circulation and the large-scale environment in which they are embedded. The main idea is to exploit this new ability to represent convection in order to reconsider old unsolved questions and to focus on new problems which were not affordable with older approaches.

In the first part of the dissertation the main objective is to develop conceptual models to explain different aspects of the coupling between soil moisture and convective precipitation. I firstly focus on initial homogeneous conditions and on the precipitation response to increase/decrease of the initial soil moisture. Although convection can be triggered earlier over dry soils than over wet soils under certain atmospheric conditions, total precipitation is found to always decrease over dry soils. A simple conceptual model shows that this can be explained by the fact that precipitation intensity strongly correlates with surface latent heat flux, hence implying more rain over wet soils.

Secondly, the focus is on heterogeneous conditions as resulting from heterogeneous surface soil moisture. Such heterogeneous conditions are known to trigger thermally-indirect circulations that advect moisture from wet to dry patches. Given that also local evaporation contributes to precipitation, my aim is to disentangle the effect of both sources over the course of a diurnal cycle. A simple conceptual model is derived using the results of LES simulations performed over a surface with varying degrees of soil moisture heterogeneity. The precipitation is expressed as a sum of advection and evaporation, each weighted by its own efficiency. By expressing advection and evaporation as functions of soil moisture I isolate the main parameters that control the variations of precipitation over a spatially drier patch. It is found that these changes surprisingly do not depend on soil mois-

ture itself but instead solely on the initial atmospheric state. This is so because the propagation of the front associated with the mesoscale circulation is mostly driven by cold pools which effectively remove the dependency on the surface state.

In the second part of the dissertation ICON-LEM is employed to simulate more realistic atmospheric cases including a convective diurnal cycle over Germany and a Tropical-Like Cyclone (TLC) over the Mediterranean Sea. The first scenario is used to test the conceptual model capacity to link precipitation to advection and evaporation weighted by different efficiencies. Two days from the exceptional period of severe weather that interested Germany in June 2016 are chosen due to their distinct diurnal cycle. It is found that, depending on the day and on the area analyzed, the model predicts different values for the efficiencies and that the one related to advection is not usually larger than the one associated with evaporation. Moreover, the model using two different efficiencies exhibits a greater skill than the one using a single efficiency in explaining precipitation variability over different regions of the domain.

A different conceptual model, which attempts to reproduce the dependency of latent heat release by deep convection on the model resolution, is tested against simulations performed with ICON-LEM in the last chapter of the dissertation. The rare case of a TLC that affected the central Mediterranean between 7 and 9 November 2014 is simulated. The goal is to determine whether ICON-LEM can reproduce the internal dynamic and evolution of this cyclone, which was poorly predicted by most General Circulation Models (GCMs). It is found that simulations performed with grid spacing larger than 2.5 km completely miss the intensification phase of the cyclone due to poorly resolved convective processes. The simulations characterized by a smaller grid spacing, instead, show the ability of the model to reproduce the internal structure of the cyclone, characterized by a warm core, and its evolution over time. An interpretation of this abrupt change in the model skill is given based on a thermodynamic argument and on Potential Vorticity (PV)-thinking.

Overall this dissertation shows how the interaction between convection and the land surface or the large-scale circulation can now be well captured with convection-explicit models like ICON-LEM which allow us to resolve the full spectrum of scales on which convection acts.

ZUSAMMENFASSUNG

Die Fähigkeit das Wetter vorherzusagen hängt von der Fähigkeit ab, atmosphärische Prozesse in numerischen Wettermodellen explizit darzustellen. Beschränkungen der Rechenleistung zwingen Wetterdienste dazu, ihre Modelle mit Gitterweiten von $\mathcal{O}(10 \text{ km})$ zu betreiben, weshalb Parametrisierungen vieler sub-skaliger Prozesse, insbesondere von feuchter Konvektion, notwendig sind. Auf der anderen Seite werden für Forschungszwecke LES mit charakterischen Gitterweiten von $\mathcal{O}(100 \text{ m})$ verwendet, typischerweise in idealisierten Bedingungen. Diese Dissertation strebt eine Verknüpfung der beiden Ansätze an, indem das neu entwickelte ICON-LEM verwendet wird. Das Modell erlaubt LES auf größeren Skalen und löst dabei konvektive Skalen, deren meso-skalige Zirkulation sowie die groß-skalige Umgebung auf. Die Grundidee beruht dabei auf der Fähigkeit Konvektion explizit darzustellen, um alten Fragen mit neuen Mitteln zu begegnen und schließlich neue Fragen aufzugreifen, die mit alten Ansätzen nicht zu lösen waren.

Das Hauptziel des ersten Teils der Dissertation ist die Entwicklung eines konzeptionellen Modells, das unterschiedliche Aspekte der Kopplung von Bodenfeuchte und konvektivem Niederschlag erklärt. Zuerst konzentriere ich mich dabei auf anfänglich homogene Bedingungen und auf die Reaktion des Niederschlags auf Zu- und Abnahmen der anfänglichen Bodenfeuchte. Obwohl unter bestimmten atmosphärischen Bedingungen Konvektion über trockenem Boden früher als über feuchtem Boden ausgelöst werden kann, ist der Gesamtniederschlag über trockenem Boden immer geringer. Ein einfaches konzeptionelles Modell zeigt, dass dieser Zusammenhang durch die starke Korrelation der Niederschlagsintensität mit dem latenten Wärmefluss erklärt werden kann, was schließlich mehr Regen über feuchteren Böden bedeutet.

Im Weiteren setze ich den Fokus auf heterogene Bedingungen, die sich aus einer heterogenen Verteilung der Bodenfeuchte ergeben. Von solchen heterogenen Bedingungen ist bekannt, dass sie thermische Zirkulationen erzeugen, die Feuchtigkeit von feuchten in trockene Bereiche transportieren und zu einer Intensivierung der Konvektion über den trockeneren Bereichen führen. Unter der Annahme, dass auch die lokale Verdunstung zum Niederschlag beiträgt, ist es mein Ziel, die beiden Quellen über den Tagesverlauf voneinander getrennt zu betrachten. Daraus entwickele ich ein einfaches konzeptionelles Modell, inspiriert von Ergebnissen der LES Simulationen, die über Oberflächen unterschiedlich heterogener Bodenfeuchte durchgeführt wurden. Der Niederschlag wird als Summe von Advektion und Ver-

dunstung, mit jeweiliger Gewichtung durch eine spezifische Effizienz, betrachet. Durch die Formulierung von Advektion und Verdunstung als Funktionen der Bodenfeuchte, isoliere ich die grundlegenden Parameter, die Niederschlag über einem räumlich trockeneren Bereich kontrollieren. Es zeigt sich, dass diese Veränderungen überraschenderweise nicht von der Bodenfeuchte selbst, sondern allein vom Anfangszustand der Atmosphäre abhängen. Dies ist eine Folge der Ausbreitung der meso-skaligen Zirkulation, die hauptsächlich von Kaltluftausflüssen bestimmt wird, die die Kopplung zum Boden unterdrücken.

Im zweiten Teil meiner Dissertation verwende ich ICON-LEM, um realistische atmosphärische Szenarien zu simulieren. Als Beispiele dienen der Tagesverlauf von Konvektion über Deutschland und ein tropensturmähnliches Sturmtief (TLC) über dem Mittelmeer. Das erste Szenario wird verwendet, um das konzeptionelle Modell des ersten Teils, das Niederschlag mit Advektion und Verdunstung von jeweils spezifischer Effizienz koppelt, zu testen. Zwei Tage eines Zeitraums von aussergewöhnlich starker Gewitteraktivität über Deutschland im Juni 2016 wurden aufgrund ihres ausgeprägten Tagesgangs herausgesucht. Es wird gezeigt, dass das Modell, abhängig von der betrachteten Zeit und vom betrachteten Ort, unterschiedliche Werte für die Effizienzen prognostiziert und dass die Effizienz der Advektion üblicherweise nicht größer ist, als die der Verdunstung. Zudem erzielt das Modell bei der Vorhersage von Niederschlagsvariabilität über unterschiedlichen Bereichen des Modells bessere Ergebnisse, wenn zwei und nicht nur eine Effizienz angewendet werden.

Ein anderes konzeptionelles Modell, das versucht die Abhängigkeit des latenten Wärmeflusses durch tiefe Konvektion von der Modellauflösung zu erklären, wird im letzten Teil der Dissertation durch eine ICON-LEM Simulation getestet. Der seltene Fall eines Medicanes, der den zentralen Mittelmeerraum zwischen dem 7. und 9. November 2014 beherrschte, wird simuliert. Das Ziel ist zu bestimmen, ob das angewandte Modell die Dynamik und Entwicklung des Wirbelsturms, der von Globalen Zirkulationsmodellen (GCMs) unzureichend vorhergesagt wurde, darstellen kann. Es wird gezeigt, dass Modelle mit Gitterweiten größer als 2.5 km die Intensivierung des Wirbelsturms gar nicht erkennen können, da konvektive Prozesse zu schwach aufgelöst sind. Simulationen mit höherer Aufösung zeigen hingegen, dass im Modell die innere Struktur des Wirbelsturms, charakterisiert durch einen warmen Kern und seine zeitliche Entwicklung, dargestellt werden können. Die vorgestellte Interpretation dieses abrupten Unterschieds im Modellverhalten beruht auf der thermodynamischen Argumentation und auf dem "Potential Vorticity (PV)-thinking".

Im Gesamten zeigt diese Dissertation, wie die Interaktion von Konvektion mit der Landoberfläche oder der groß-skaligen Zirkulation

in Modellen mit explizierter Darstellung von Konvektion (wie ICON-LEM) erfasst werden kann und wie das volle Spektrum an Skalen, die von Konvektion beeinflusst sind, aufgelöst wird.

PRE-PUBLISHED WORK RELATED TO THIS DISSERTATION

Cioni, G. and C. Hohenegger, 2017. *Effect of Soil Moisture on Diurnal Convection and Precipitation in Large-Eddy Simulations.* J. Hydrometeor. **18**, 1885–1903. https://doi.org/10.1175/JHM-D-16-0241.1

Cioni, G. and C. Hohenegger, 2018. *A simplified model of precipitation enhancement over a heterogeneous surface.* Hydrol. Earth Syst. Sci. Discuss. https://doi.org/10.5194/hess-2017-547, in review.

Cioni, G., Cerrai, D. and Klocke, D. 2018. *Investigating the predictability of a Mediterranean Tropical-like Cyclone using a non-hydrostatic high-resolution model.* Quarterly Journal of the Royal Meteorological Society, in press.

Un dì all'azzurro spazio guardai profondo,
e ai prati colmi di viole, pioveva loro il sole,
e folgorava d'oro il mondo: parea la terra un immane tesor,
e a lei serviva di scrigno il firmamento.

— *Andrea Chenier*

ACKNOWLEDGEMENTS

CONTENTS

LIST OF FIGURES

LIST OF TABLES

ACRONYMS

CAPE	Convective Available Potential Energy
CIN	Convective INhibition
CMIP	Coupled Model Intercomparison Project
COSMO	COnsortium for Small-scale MOdeling
CRE	Cloud Radiative Effect
CTBL	Cloud-Topped Boundary Layer
CTP	Convective Trigger Potential
DALES	Dutch Atmospheric Large-Eddy Simulation
DCBL	Dry Convective Boundary Layer
DNS	Direct Numerical Simulation
DPV	Dry Potential Vorticity
DWD	Deutscher WetterDienst
ECMWF	European Center for Medium range Weather Forecast
EMIC	Earth System Models of Intermediate Complexity
GCM	General Circulation Model
GFS	Global Forecasting System
GKDE	Gaussian Kernel Density Estimate
HD(CP)^2	High Definition Clouds and Precipitation for advancing Climate Prediction
ICON-LEM	Icosahedral Non-hydrostatic Large-Eddy Model
ICON	ICOsahedral Non-hydrostatic
IFS	Integrated Forecast System
IR	Infra-Red
LAM	Limited Area Model
LCL	Lifted Condensation Level
LEM	Large Eddy Model
LES	Large Eddy Simulation

LFC	Level of Free Convection
LSM	Land-Surface Model
LST	Local Standard Time
MCS	Mesoscale Convective System
MSE	Moist Static Energy
MSLP	Mean Sea-Level Pressure
MTLC	Mediterranean Tropical-Like Cyclone
NCEP	National Centers for Environmental Prediction
NHC	National Hurricane Center
NICAM	Nonhydrostatic ICosahedral Atmospheric Model
NOAA	National Oceanic and Atmospheric Administration
NWP	Numerical Weather Prediction
PALM	PArallelized Large-eddy simulation Model
PBL	Planetary Boundary Layer
PDF	Probability Density Function
PV	Potential Vorticity
PWAT	Precipitable WATer
RCM	Regional Climate Model
RICO	Rain In Cumulus over the Ocean
RRTM	Rapid Radiative Transfer Model
SST	Sea Surface Temperature
TC	Tropical Cyclone
TKE	Turbulent Kinetic Energy
TLC	Tropical-Like Cyclone
UCLA-LES	University of California Los Angeles Large-Eddy Simulation
UTC	Coordinated Universal Time
VIIRS	Visible Infrared Imaging Radiometer Suite
WPV	Wet Potential Vorticity

1

INTRODUCTION

In the early morning of October, 16th 2017 *Ophelia*, a former major hurricane, was making landfall over southern Ireland as an extratropical depression. Wind gusts up to 191 km h^{-1} were recorded at Fastnet Rock off the coast of County Cork: this was the highest wind speed ever measured in Ireland. Three deaths were reported in Ireland while total losses from the storm reached USD 70.1 million (Stewart, 2018).

Ophelia was the easternmost Atlantic major hurricane ($\geq$ Category 3) that has been recorded since the beginning of the satellite era. The genesis of this cyclone on October, 6th was fairly unique in its kind as Ophelia formed over the north-eastern Atlantic (between the Canary Islands and the Azores, an area usually not prone to tropical cyclogenesis) from the remnants of an occluded front. Located over an area with warm Sea Surface Temperatures (SSTs) (see also Fig. 1.2), the storm steadily intensified over the next two days and became a hurricane on October,11th and a major hurricane on October, 14th south of the Azores. Fig. 1.1 shows a satellite picture of Ophelia dangerously close to the Azores and the Iberian peninsula. In the following

Ophelia's story
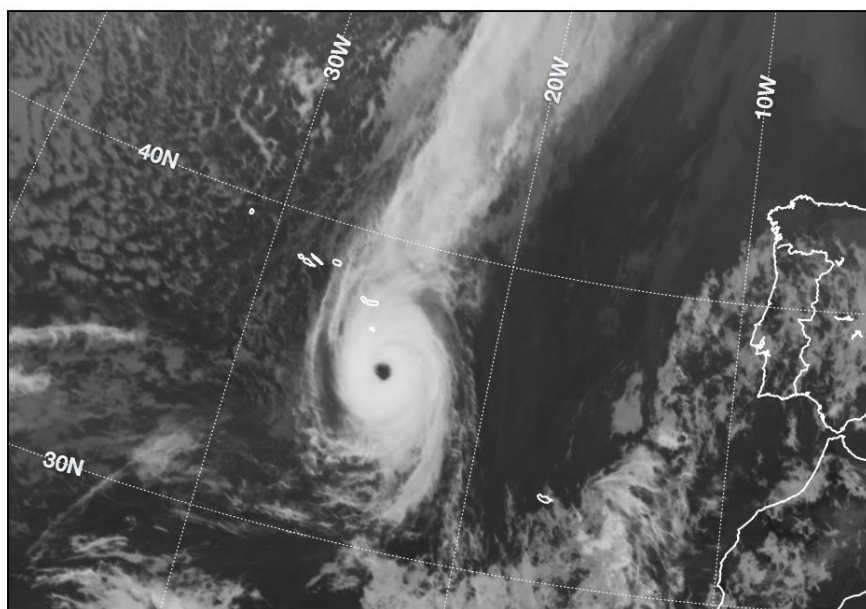
Figure 1.1: MSG-SEVIRI infrared satellite image acquired on 14 October 2017 at 2010 UTC. Copyright by EUMETSAT.

days, Ophelia began weakening as it moved over progressively colder waters towards Ireland and Great Britain. Between 15 and 16 Octo-

1

ber Ophelia underwent an extra-tropical transition which caused a re-intensification of the system before its final approach on the Irish coast.

Although substantial, the losses suffered in Ireland and in neighboring countries were far less than initially feared, given the exceptional case of an ex-hurricane passing so close to the old continent. This was certainly related to the emission of several alerts already 4-5 days in advance. For example, Met Éireann, Ireland's national meteorological service, already reported on 12 October that the storm would have reached Ireland. This was followed by a 'Status Red', the highest storm category warning, on 14 October. Issuing such a warning more than 48 hours in advance was "unprecedented", as 'Status Red' warnings are normally issued within 24 hours of the event.

These warnings were issued following the indications of Numerical Weather Prediction (NWP) models, which foresaw the possibility of an interaction between Ophelia and Europe up to 6 days in advance, that is when the system was just a tropical storm in the middle of the Atlantic. Figure 1.2 shows the trajectory of Ophelia predicted, as an example, by the operational version of the ICOsahedral Non-hydrostatic (ICON) model over the European domain, usually referred to as ICON-EU ($\sim$ 7 km grid spacing[1]). It shows how the landfall over Ireland was already predicted 5 days in advance by this model, although with a delay of approximately 6 hours. The deepening of the cyclone, with a minimum MSLP of 964 hPa, and its intensity, characterized by maximum wind speeds of 140 km h^{-1}, are also not far from what it was observed.

Being able to predict with fairly good accuracy the extra-tropical transition of a major hurricane 5 days in advance clearly shows how the science of NWPs has evolved since the "Richardson's dream" (Lynch, 2006). Improvements in technology have allowed most national weather centers in the world to run NWP models globally every 6 hours, with forecasts extending up to the following 300 hours (almost 2 weeks). However, due to the still limited computational power, we are far away from running NWP global models at a grid spacing fine enough to resolve deep convection, which is a driving force behind extreme events like Ophelia.

At the time of writing, for example, the European Center for Medium range Weather Forecast (ECMWF)-Integrated Forecast System (IFS) model, one of the best-skilled global forecast systems, computes the future evolution of the atmosphere employing a grid spacing of approximately 9 km. This means that most of the processes exhibiting a spatio-temporal structure below the scale of the model grid resolution (e.g. convection, land surface, thermodynamic phase changes) need to be *parametrized*. Physics *parametrizations* make use of empir-

---

1 See https://www.dwd.de/EN/ourservices/nwp_forecast_data/nwp_forecast_data.html for further details on the operational model configuration.
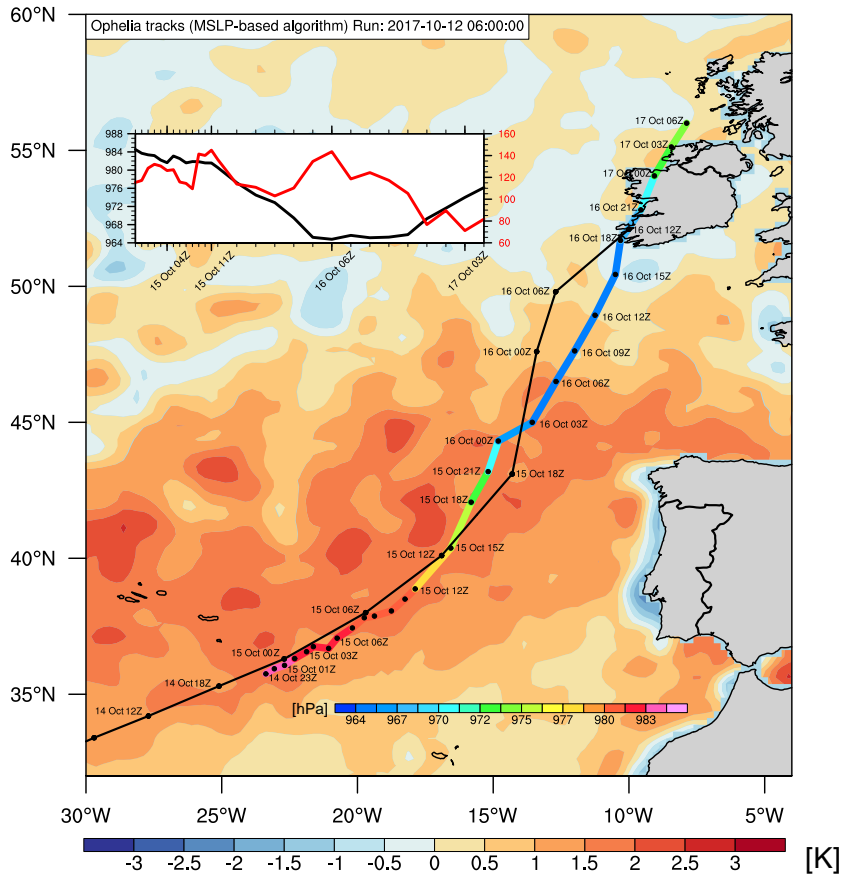
Figure 1.2: Track of hurricane Ophelia predicted by ICON-EU and observed. The black line shows the observed trajectory according to the NHC archive. Color filled contours show the SST anomaly averaged between 6 and 15 October 2017 according to NOAA. The colored line shows the track of hurricane Ophelia predicted by the ICON-EU run initialized on October, 12th at 0600 UTC and is colored according to the predicted value of MSLP. The inset shows the time evolution of MSLP (black line, hPa) and wind speed (red line, km h^{-1}) for the tracked cyclone. The algorithm for the tracking follows Cioni et al. (2016).

ical laws, based either on higher resolution models or observations, which allow describing sub-grid scale processes as complex functions of the grid box mean values of the prognostic variables of the forecast model (see e.g. EMCWF, 2001). Parametrizations, unfortunately, introduce errors given that they are not based on the full set of Navier-Stokes equations (see e.g. Maher et al., 2018) but rather on empirical formulations.

Although some of the parametrized processes take place on scales that NWP models will likely never be able to resolve (e.g. microphysical processes, molecular diffusion), some processes, like deep moist convection, won't need to be parametrized in the future if employed grid spacing will converge to $\mathcal{O}$ (1 km) (Weisman et al., 1997). A commonly used strategy to reduce the number of parametrizations

Parametrization of sub-grid scale processes and convection-resolving models

used in a model, while keeping the computational costs limited, is to perform simulations in a limited domain, like the one of ICON-EU, while employing a finer grid spacing: these are usually referred to as Limited Area Models (LAMs). Models characterized by a grid spacing fine enough to resolve deep convection are usually called *convection-permitting*. However, even convection-permitting simulations are not exempt of biases due to a grid spacing that is still too coarse to properly resolve all the scales of convective processes which usually results in many biases (e.g. a delayed triggering of convection Hohenegger, Walser, et al., 2008).

In fact, using energy spectra, it has been shown that the *effective resolution* of NWP models is usually within a range of 6-8 times the grid spacing (Skamarock, 2004; Wedi, 2014), which makes a further increase of the grid spacing necessary. Further grid refinements can be repeated multiple times in order to have a domain with a kilometer or even a sub-kilometer grid spacing, which is usually referred to as *convection-explicit* grid spacing. Convection-explicit models use the full set of Navier-Stokes equations without the need to employ empirical formulations to describe sub-grid scale energy transports, which make them ideal to study atmospheric processes like convection. Only processes driving the turbulent transport in the Planetary Boundary Layer (PBL) need to be described by a subgrid-scale model. When adopting a grid spacing below 1 kilometer the parametrizations usually employed for turbulence are no longer valid. Among these scale of motions, Large Eddy Simulation (LES) models (Sagaut,

LES models   2006) have been largely employed. LES models represent, essentially, a trade-off between the more expensive Direct Numerical Simulation (DNS) models, which resolve all scales of turbulent motions, and the convection-permitting NWP models. Hence, LES can be seen as a *poor-man* DNS where only turbulent motions up to a certain scale are resolved while other scales are computed through a sub-grid scale model.

Given their range of optimal resolutions, LES models have been extensively used in the literature to study both shallow and deep atmospheric moist convection (see e.g. Siebesma et al., 2003). Up to today, they are still the best available option that one has to resolve most of the turbulent motions driving shallow cumuli formation and their transition into congestus or even more organized structure like thunderstorms. Unfortunately, their research nature has often prevented their employment in a setup driven by realistic boundary conditions or even their application in NWP models. Instead, setups consisting of idealized boundary and initial conditions have usually been adopted in the literature.

ICON-LEM   The Icosahedral Non-hydrostatic Large-Eddy Model (ICON-LEM) is one of the first models that extends the LES approach to larger scales and realistic setups. The model has been applied to simulate many

atmospheric configurations with a resolution of 600, 300 and 150 m over Germany in the context of the High Definition Clouds and Precipitation for advancing Climate Prediction (HD(CP)^2) project (Heinze et al., 2016). These simulations have just started to scratch the surface with the goal of understanding whether running models with higher resolution effectively improves our ability to predict the weather, and potentially the climate. More importantly, they show that we are finally able to perform LES simulation on large scales, thereby capturing not only the scale of individual convective clouds but also their mesoscale associated circulation and the interaction with the large-scale environment.

In this dissertation I want to move this analysis one step further. The main goal is to use convection-explicit simulations as a tool for process understanding of different atmospheric processes involving moist deep convection. In particular, results from simulations from either idealized or realistic setups are used to develop conceptual models and test ideas of how convection interacts with different atmospheric configurations. To do so I will focus on two main topics:

1. the interaction between the land surface and the atmosphere mediated through deep moist convection and

2. the role of deep moist convection embedded in larger scale atmospheric systems

In the following sections I will provide a brief description of these processes and highlight some of the aspects that have been neglected or poorly described in the literature. This will eventually lead to the research questions motivating this dissertation, which will be presented in the last section of this chapter. These research questions essentially constitute different ways of formulating the previous more generally stated goal of the research.

1.1 LAND-ATMOSPHERE INTERACTIONS ACROSS SCALES

An observer floating in space looking in the middle of the Pacific would be convinced to say that Earth is nothing but a blue marble given that the entire surface area from his point of view would be covered by oceans. The latter makes up indeed 71 % of the total surface area. However, the remaining 29 % of the Earth's surface area is where humans have been living for the past million years: the land. According to the GRUMP dataset (CIESIN, 2004), a mere 3 % of this area is covered by urban areas, while 40 % is dedicated to agriculture. This shows that land, although being a small fraction of the Earth's surface, is of vital importance for humans.

The atmosphere, on the other hand, covers the entire Earth's surface by floating above both land and oceans. Therefore, it is not hard to

The importance of the land surface

imagine why many past studies have been focusing on the interaction between the land surface and the overlying atmospheric layer. In many areas of the world, the land is not only means of support for agriculture but also the only forcing to the atmosphere. In particular, clouds and their distribution are strongly modulated by the presence and alteration of the land surface.

This can be seen in Fig. 1.3 where a high-resolution satellite pic-
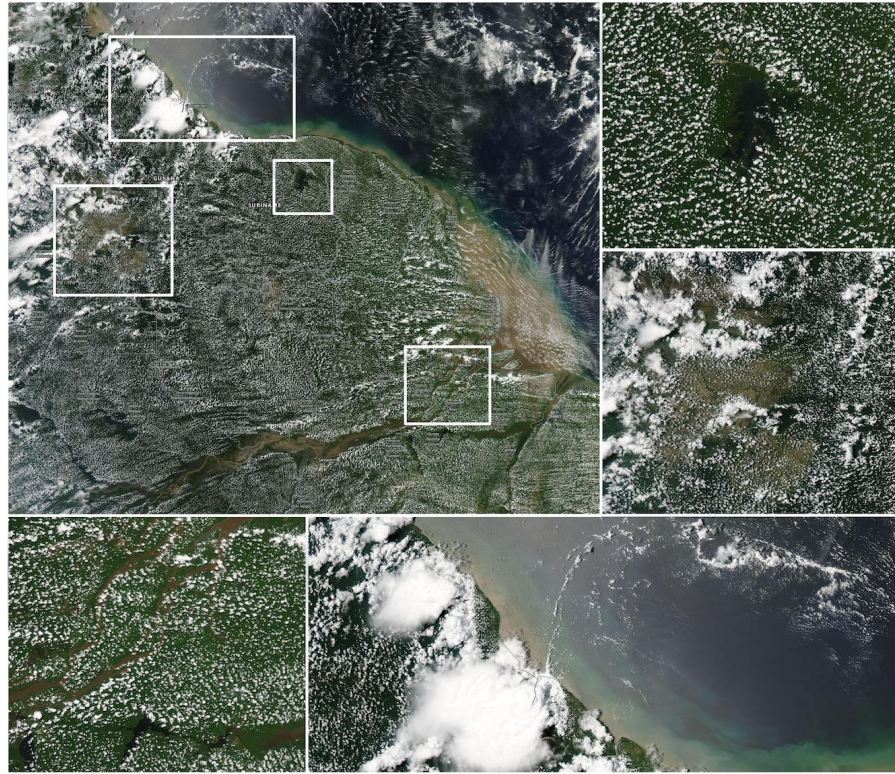
Figure 1.3: MODIS satellite imagery acquired on 19 August 2009 over South America. White rectangles in the uppermost left panel represent the regions where the image has been zoomed-in, which are visible in the panels on the bottom and right part of the figure.

Coupling of the land surface and convection

ture of a wide area covering parts of Brasil, Suriname and Guyana is shown. Several cloud spatial patterns emerge in the picture. First of all, there is an abundance of clouds over land with respect to the ocean which locally appears to be cloud-free (lowermost right inset in Fig. 1.3). This is reflected also in the spatial distribution of clouds over the *Brokopondo* lake (Suriname, uppermost right inset) and over the estuary of the Amazonian River (bottom leftmost inset). It is evident that clouds seem to avoid water bodies while developing over land.

However, not only the spatial distribution of clouds appears to be affected by the land surface. In fact, clouds density and size also respond to the land surface forcing. This is evident at the border between Guyana and Brasil (middle right inset in Fig. 1.3) where shallow clouds covering a deforested area are surrounded by a denser

population of deep clouds developing over the equatorial forest. Finally, the thunderstorms in the vicinity of Georgetown (Guyana), probably created by an afternoon land-sea breeze, stick out just from their larger size and white color (lower rightmost inset in Fig. 1.3).

From Fig. 1.3 one could be fooled to think that the interaction between the land surface and the atmosphere is only limited to the diurnal cycle. Instead, given the slow response of deep soil layers to atmospheric perturbations, the land often exerts an influence on monthly and seasonal timescales. This interaction is so pronounced that clouds can, in fact, reveal the shape of continents, as highlighted by Fig. 1.4 where the cloud cover averaged during the month of September 2017 is shown. Spatial features showing up in Fig. 1.4

Land-atmosphere interactions reveal continents
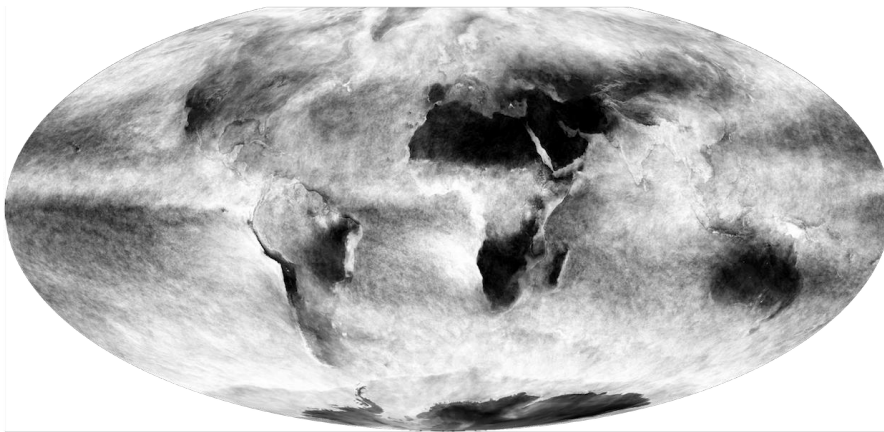
Figure 1.4: MODIS derived cloud fraction monthly-averaged during September 2017.

allow one to distinguish almost entirely Australia, Africa, the Middle East, Antarctica and South America. Here the characteristic negative cloud signature of the Amazonian River, which was highlighted previously in Fig. 1.3, appears strikingly well. The Atacama desert also stands out due to its almost non-existent cloud cover.

Although observations, like the satellite picture above, give us strong indications and good examples of the coupling between the land surface and the atmosphere, their interpretation is sometimes ambiguous as causality can often not be determined (Tuttle and Salvucci, 2017). For example, a previously flooded area may be affected in the following days by a series of thunderstorms. Are the recurring thunderstorms just a coincidence or are they related to the initial flooding, i.e. an abundance of water that percolated into the soil which then evaporated back to the atmosphere? This causality is hard to be determined using only observations. Models, even with all their limitations, can instead give us insights into the complex interactions that drive the coupled land-atmosphere system.

Causality in land-atmosphere interactions

Determining the causality is also important from a NWP perspective given that the state of the land surface may affect the evolution of the

atmosphere over daily, monthly or even seasonal timescales, as antic-ipated before. In particular, Fukutome et al. (2001) has shown that, under certain atmospheric conditions, prescribing the *perfect* soil con-ditions has a strong impact over forecast periods from 10 to 15 days. MacLeod et al. (2016) used the exceptional summer of 2003 over Eu-rope, as a case of strong coupling between the land surface and the atmosphere, to show that seasonal predictions can be improved by including stochastic perturbations in the soil state. Finally, Hurk et al. (2012) showed that, by using realistic soil moisture initialization, the forecast skill of summertime temperature and precipitation over Eu-rope up to 8 weeks ahead can be improved.

Surface Fluxes   But why do these complex interactions between the land surface and the atmosphere arise in the first place? The land surface and the at-mosphere are coupled through fluxes of heat, surface and moisture that develop at the interface due to the partitioning of the incoming solar radiation (Budyko, 1961). In many areas of the world where the atmospheric forcing does not vary appreciably during the year (e.g. semi-arid or desertic regions) the land strongly influences the parti-tioning of these fluxes through different characteristics. Avissar (1995) indicated that five land surface characteristics in particular, stomatal conductance, soil moisture, surface roughness, leaf area index and albedo, affect the coupling of the land surface with the overlying at-mosphere through the control on surface fluxes. In the following section I will primarily focus on the influence of the soil moisture on the development of convection and ensuing precipitation.

1.1.1 *The coupling of soil moisture and precipitation*

Over some regions of the globe by changing the soil moisture it is possible to modify the future atmospheric state on timescales rang-ing from the diurnal cycle to the seasonal scale. For instance, Fischer et al. (2007) used model simulations of the anomalously hot summer of 2003 to show that, by simply decreasing soil moisture by 25% in spring, summer temperature anomalies can increase by more than 2°C. In this particular case, reduced soil moisture availability limits the surface latent heat flux which, as a compensation, requires the land to heat more so that the energy balance can be maintained by an associated increase in sensible heat flux and outgoing long-wave radiation, both of which are strongly dependent on the surface tem-perature. Although the coupling between near-surface air tempera-ture and soil moisture is straightforward (Miralles, Berg, et al., 2012; Miralles, Teuling, et al., 2014), the coupling between precipitation and soil moisture has been debated many times.
The main question underlying such a debate is the following:

> *Will an initially wetter soil lead to more or less precipitation?*

A wetter soil promotes larger surface latent heat fluxes in a soil moisture-limited regime (Budyko, 1974), thus increasing the moisture contribution to the atmosphere. From an atmospheric moisture balance perspective, this increase in the amount of water vapor increases the potential amount of precipitation. The precipitation eventually falls on the ground and replenishes the soil moisture reservoir therefore closing the feedback loop. This is the main idea behind the mechanism of *precipitation recycling* (Trenberth, 1999) which implies a positive *soil moisture-precipitation feedback*. Precipitation recycling is nevertheless thought to not play a big role on the regional scale. Van der Ent et al. (2010), for instance, reported a recycling ratio of less than 10% for horizontal scales of 500 km, which agrees with the estimate obtained by Schär et al. (1999) based on a 1-month model simulation over Europe. The major source of water vapor for precipitation is indeed constituted by the advection of moisture into a region rather than direct local evapotranspiration.

Precipitation recycling

Instead of locally increasing water vapor, soil moisture can modify the efficiency at which water vapor is converted into precipitation. For example, Findell and Eltahir (2003b) showed that, over a homogeneous surface, the resulting coupling over a diurnal cycle, being an increase or decrease of precipitation with initial soil moisture, strongly depends on the early morning atmospheric state. Some atmospheric states may benefit from an increase in soil moisture to produce more precipitation (wet soil advantage) while others need the surface to dry out (dry soil advantage).

Efficiency and different soil advantages

A third mechanism by which soil moisture can impact precipitation is through the generation of thermally induced mesoscale circulations triggered by surface heterogeneity created by the land-sea gradient or simply by wet and dry soil patches (Segal and Arritt, 1992). Such thermally-driven mesoscale circulations transport moist air from spatially wetter patches to spatially drier patches, acting against the initial perturbation of soil moisture.

Given the importance of the soil moisture-precipitation feedback in regulating the global and continental hydrological cycle, many studies have tried to estimate its likely sign and magnitude using either observations (e.g. Miralles, Teuling, et al., 2014; Ford et al., 2015), coarse resolution models with parametrized convection (e.g. Schär et al., 1999; Wang et al., 2007), convection-permitting models with explicit convection (e.g. Hohenegger, Brockhaus, et al., 2009; Schlemmer, Hohenegger, et al., 2012) or conceptual models (e.g. Findell and Eltahir, 2003b; Tawfik et al., 2015; Gentine, Holtslag, et al., 2013). The main problem regarding observational studies is that the effect of synoptic variability is difficult to filter out. In contrast, model studies rely on their parametrizations.

Previous studies

Hohenegger, Brockhaus, et al. (2009) showed, using model simulations of an entire summer season over the Alps, that the sign of the

soil moisture-precipitation feedback strongly depends on the design of the model. In particular, the parametrization of convection is the model feature that greatly affects the sign of the feedback. The latter can even reverse its sign depending on the use or not as well as on the design of such a parametrization. Even convection-permitting simulations are not exempt of biases which might alter the resulting soil moisture-precipitation feedback.

Finally, it should be noted that studies often use metrics to diagnose the soil moisture-precipitation feedback that were designed to assess the potential for triggering of convection over a certain surface state, without actually considering the amount of precipitation. These gaps in the literature allow me to reconsider the characterization of the coupling between soil moisture and precipitation using LES models. The advantage of such models is that they can explicitly resolve convection and its interaction with the land surface.

1.2 A PARTICULAR EXAMPLE OF MID-LATITUDE STORMS: MEDITER-RANEAN TROPICAL-LIKE CYCLONES

Reports of small but exceptionally severe storms, developing over the Mediterranean sea and feared by sailors for the harm produced to ships, date back to ancient times. Boschovich (1749) writes about "storms very similar to the feared hurricanes of America" which "lasted a whole day deranging a large part of the sea and advancing for many leagues into the land". It is not hard to believe what Boscovich says given that the Mediterranean basin is one of the most cyclogenetic areas of the world (e.g. Campins et al., 2011).

Along with extra-tropical disturbances, Tropical-Like Cyclones (TLCs), characterized by a symmetric structure formed by a central warm-core cloud-free region surrounded by deep convective clouds and spiraling distributed cloud bands, are known to form over the Mediterranean and have been documented since the satellite era began (Ernst and Matson, 1983; Billing et al., 1983). In the latest 15-20 years they have received much attention because of the damages caused in coastal areas and gained the epithet of Mediterranean Tropical-Like Cyclones (MTLCs) or, in short, *Medicanes* for Mediterranean Hurricanes (Emanuel, 2005). Figure 1.5 shows an example of the MTLC *Numa* which occurred at the end of 2017. Note the central cloud-free region and the deep convective clouds in the eastern sector of the cyclone.

Main features of MTLCs   Although MTLCs share many features of Tropical Cyclones (TCs), they appear to be much smaller in radius (50 to 300 km, Miglietta, Laviola, et al., 2013; Tous and Romero, 2013) but are still able to produce hurricane-force winds (Moscatello et al., 2008). They are originally of baroclinic nature and, under specific environmental conditions, undergo a phase of development that causes a transition to a tropical-
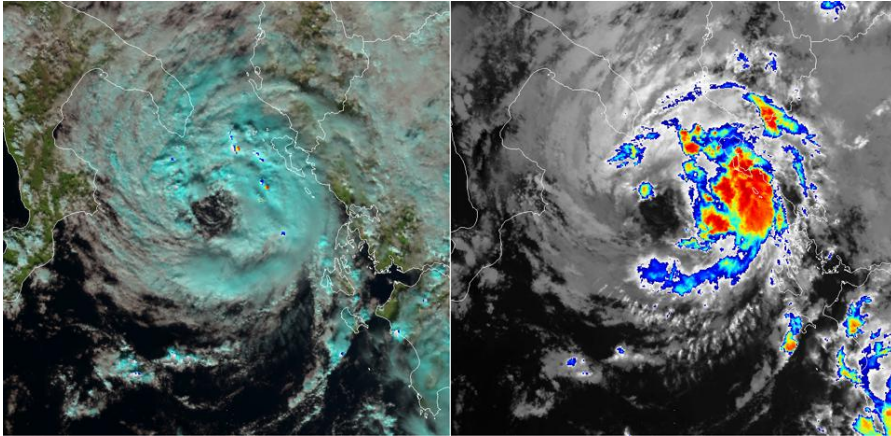
Figure 1.5: Satellite pictures of MTLC *Numa* acquired on 18 November 2017 at 1214 UTC by the VIIRS instrument. The left panel shows a Natural Color RGB picture while right panel contains a brightness temperature map obtained using data from the infra-red band.

like structure which often presents co-existing hybrid extra-tropical features. Conditions favorable to MTLCs genesis include, but are not limited to, the presence of an initial low-level disturbance, usually in the form of a MSLP minimum, and of an upper-level cold through (Reale and Atlas, 2001; Fita et al., 2007; Tous and Romero, 2013) that contributes to increasing the air-sea gradient of saturation Moist Static Energy (MSE) (Emanuel, 2005).

The genesis and intensification processes of MTLCs have also been explained using the Potential Vorticity (PV)-thinking (Hoskins et al., 1985). A so-called PV *streamer* (Massacand et al., 1998) usually contributes to the deepening of the initial MSLP disturbance following the same mechanism of the extra-tropical systems intensification (Hoskins et al., 1985). Subsequently, low-level PV maxima created by deep convection close to the cyclone center interact with the high-level PV maxima induced by the presence of the streamer. This mechanism has been described in Homar et al. (2003), Cioni et al. (2016) and Miglietta, Cerrai, et al. (2017).

The forecasting challenge

The reduced spatial scale of MTLCs poses a challenge to global NWP models, which usually employ grid spacing too coarse to explicitly resolve convection. MTLCs can be correctly predicted only by convection-permitting or convection-explicit models, given a certain spin-up time needed to create the consistent dynamical structure of the cyclone starting from initial and boundary conditions taken from coarser resolution models. For this reason, an extensive body of literature has focused on the challenges regarding the modeling of MTLC, including their sensitivity to the sea surface state (Homar et al., 2003; Fita et al., 2007; Tous, Romero, and Ramis, 2013) and to different modeling strategies (Davolio et al., 2009; Miglietta, Moscatello, et al., 2011; Miglietta, Mastrangelo, et al., 2015; Cioni et al., 2016; Ricchi et al., 2017). It was found that the SSTs exert different influences on the

intensification and evolution of MTLCs depending on the particular case. Instead, the importance of the large-scale environment, which enters the model through initial and boundary conditions, has been recognized by many authors as the main driver of their evolution (e.g. Homar et al., 2003). Equivalently, a misrepresentation of the upper-level, as well as the lower-level, PV anomalies can compromise to some extent the forecast cyclone evolution (Homar et al., 2003).

Notwithstanding the importance of the model resolution in simulating the evolution of these particular cyclones, most of past modeling studies have primarily focused, as mentioned before, on sensitivity studies to surface fluxes, SSTs or boundary conditions, without actually considering the dependency on the model grid spacing. This caused many published studies, even recent ones as Pytharoulis et al. (2017), to completely neglect the role of model resolution by performing simulations of a MTLC with a grid spacing of $\mathcal{O}(10\ \mathrm{km})$. Not surprisingly, Pytharoulis et al. (2017) concluded that "no single setup was able to provide the best reproduction of all the cyclones' features" given that the simulated trajectory of the cyclone significantly diverged from the observed one.

This issue can be addressed specifically by exploiting the versatility of the ICON model, which can be applied in a variety of different configurations where resolution is varied. Moreover, given that a sub-km grid spacing and a LES model have never been used to simulated a MTLC, the employment of ICON-LEM could potentially shed some light on the processes driving the formation and intensification of MTLCs, which are still poorly understood.

1.3   RESEARCH OBJECTIVES AND THESIS OUTLINE

Main motivation of part i

This dissertation is divided into two main parts. In part i idealized simulations performed with ICON-LEM will be used to develop conceptual models of land-atmosphere interactions and, in particular, of the coupling between soil moisture and precipitation. The idealized setups adopted in this part will be the ideal tool to retain only the main physical processes that make up the coupling, i.e. only surface evaporation over a homogeneous surface and both surface evaporation and advection of moisture over a heterogeneous surface.

Main motivation of part ii

In part ii the focus will be, instead, on realistic representations of the atmosphere, that is simulations in a NWP configuration which attempt to forecast the evolution of the atmosphere using as a starting point an observed state. In particular, ICON-LEM will be used to investigate the characteristics of mesoscale convective processes in two different examples of atmospheric circulations. First, a case of weakly forced circulation over central Europe in which the evolution of the atmosphere is predominantly related to the surface forcing. These simulations will be used to test some of the ideas developed in part

i. Second, a case of strongly forced cyclonic circulation where the evolution of the atmosphere is driven mainly by the large-scale flow. The parts and chapter of the thesis are described in the following.

Part I: Conceptual models of the interaction between soil moisture, convection and precipitation

Implementation of the coupling between TERRA-ML and ICON-LEM in an idealized configuration

The ICON model has been successfully used in a NWP-like setup to perform convection explicit simulations with a grid spacing as small as 125 m over Germany (Heinze et al., 2016). In such a configuration the land surface was coupled to the atmosphere in every grid point and boundary conditions were prescribed by using data from the COnsortium for Small-scale MOdeling (COSMO)-DE (Doms et al., 2011) model. In order to develop my conceptual model, ICON-LEM needs to be run in an idealized configuration where the domain is doubly-periodic, i.e. in a pseudo-Torus geometry (Dipankar et al., 2015). Until now such a configuration didn't include a land surface scheme. For this reason, Chapter 2 describes my implementation of the coupling between the Land-Surface Model (LSM) TERRA-ML and the atmospheric model ICON-LEM along with a validation of the model setup using test cases from previous studies.

May drier soils receive more precipitation than wetter ones in homogeneous conditions?

There is still uncertainty regarding whether the initial atmospheric state can affect the efficiency in converting the surface moisture flux into precipitation. Since the surface moisture flux strongly depends on the soil state, the main issue is to determine whether precipitation increases or decreases depending on soil moisture and whether this regime may change depending on the atmospheric state. Findell and Eltahir (2003b) showed that, over a homogeneous surface, the coupling of soil moisture and precipitation over a diurnal cycle strongly depends on the early morning atmospheric state. Different combinations of low-level instability and moisture content may result either in a dry soil advantage (more precipitation over dry soils) or in a wet soil advantage (more precipitation over wet soils). However, the analysis of Findell and Eltahir (2003b) did not consider the production of precipitation, which is necessary to assess the sign and magnitude of the coupling between soil moisture and precipitation.
To fill this gap, the modeling framework introduced in Chapter 2 is used to perform several idealized experiments mimicking the full diurnal cycle of convection starting from different spatially homogeneous soil moisture conditions. The first goal consists in quantifying

the likelihood of precipitation on soils that are either wetter or drier than normal. The second goal consists in evaluating whether large-scale effects, cloud-surface interactions or the presence of winds or plants can modify the sign and magnitude of the coupling. Within this set-up the methodology proposed by Findell and Eltahir (2003b) is revisited. Instead of focusing only on the dependence of the triggering of convection on soil moisture, attention is set on the entire diurnal cycle of convection and its precipitation. This research question is addressed in Chapter 3.

Can a simple conceptual model explain how precipitation responds to soil moisture changes over a heterogeneous surface?

Homogeneous conditions, like the ones assumed in Chapter 3, are difficult to observe in the real world, especially over mid-latitude regions. In fact, the land surface is often covered by different types of soil, plants or can even present heterogeneities in surface soil moisture. Such heterogeneities influence the onset of convection and subsequent evolution of precipitating systems through the triggering of mesoscale circulations (Segal and Arritt, 1992). However, local evaporation also plays a role in determining precipitation amounts (Wei et al., 2016). Although previous studies (e.g. Taylor et al., 2012) have qualitatively shown how precipitation is influenced by soil moisture, soil moisture gradients and by the atmospheric environment, in this chapter I aim at developing a simplified conceptual model to formally isolate the control of advection and evaporation on precipitation. In particular, I aim at finding a mathematical expression for the derivative of precipitation with respect to soil moisture in the case of a heterogeneous surface.

The derivation of the conceptual model is inspired by the results of simulations performed with the modeling framework described in Chapter 2 over a surface with varying degrees of heterogeneity. A key element of the conceptual model is the representation of precipitation as a weighted sum of advection and evaporation, each weighted by its own efficiency. The model is then used to isolate the main parameters that control the variations of precipitation over a spatially drier patch. The results of simulations, as well as the derivation of the conceptual model, are presented in Chapter 4.

Part II: The coupling of convection with the land surface and the large-scale flow in realistic simulations

Can the effects of advection and evaporation on precipitation be recognized in a diurnal cycle over Germany?

In Chapter 4 a conceptual model was derived to quantify the individual contribution of advection and evaporation to precipitation. The

derivation of such a conceptual model, however, was based on idealized simulations which considered no synoptic forcing and the superposition of only two different dry and wet patches. For this reason, in Chapter 5 I attempt to apply the theory derived in Chapter 4 to more realistic simulations of a diurnal cycle over Germany. The goal is to verify whether such a conceptual model can still be considered valid in a more realistic configuration.

Two days characterized by a weak synoptic forcing and a distinct diurnal cycle are chosen from a 15 days period (May-June 2016) which was characterized by the persistence of severe weather over Germany (Piper et al., 2016). By deriving advection, evaporation and precipitation from these simulations the parameters describing the conceptual model can be obtained and compared to the one obtained in Chapter 4.

Does poorly resolved convection influence the forecast of a Mediterranean tropical-like cyclone?

Chapter 5 has shown that a conceptual model expressing advection and evaporation contributions to precipitation can be applied to interpret the results of a realistic simulation performed over Germany with ICON-LEM. In this section of the dissertation I want to develop a different conceptual model explaining how the latent heat release, caused by the presence of deep convection embedded in a more organized structure, changes with model resolution. This will be eventually used to assess whether increasing the resolution is really necessary to increase the forecast skill of such structure.

I make use of a MTLC occurred between 7 and 8 November 2014. The choice of this particular event is justified by the fact that it was poorly predicted by operational General Circulation Models (GCMs) which failed in reproducing the trajectory of the cyclone, probably due to the coarse resolution adopted in the model. Using ICON-LEM I conduct a retrospective analysis of the event by performing several simulations in a configuration similar to the one adopted in the previous chapters. This will eventually lead to identifying the minimum resolution needed to correctly forecast the MTLC's evolution.

Part I

CONCEPTUAL MODELS OF THE
INTERACTION BETWEEN SOIL MOISTURE,
CONVECTION AND PRECIPITATION

DESCRIPTION OF THE MODELING FRAMEWORK

<div style="text-align: right; font-size: 3em;">2</div>

In this chapter the modeling framework used throughout the first part of the thesis will be briefly described. The ICON model, and especially its large-eddy version ICON-LEM, will be described in section 2.1. This atmospheric model will then be coupled to a land-surface model (TERRA-ML) in sections 2.2. Given that this setup has never been used before in a idealized configuration, section 2.3 provides a validation using other equivalent modeling frameworks.

2.1 THE ICON-LEM MODEL: BASIC DESCRIPTION AND EQUATIONS

The ICON model is a new-generation unified modeling system for NWP and climate studies which allows for an explicit representation of non-hydrostatic processes and can be applied across a wide range of scales. It has been developed as a collaboration between the Max Planck Institute for Meteorology and the Deutscher WetterDienst (DWD) (German National Weather Service) where it is currently used to produce global operational forecasts since 2015. In order to maximize the model performance and to remove the singularity at the poles, ICON employs an unstructured icosahedral grid where all the common mathematical operators are expressed in terms of components either normal or perpendicular to the triangle edges (Wan et al., 2013). The non-hydrostatic dynamical core has been validated by means of several idealized cases including a flow over orography and a baroclinic development, as well as through NWP skill scores (see Zängl et al., 2015, for details).

In the context of the HD(CP)[2] project, a large-eddy version of the ICON model, hereinafter referred to as ICON-LEM, has been developed. ICON-LEM uses the same dynamical core as ICON and shares many of its parametrizations, except for the representation of turbulence, cloud cover, convection and gravity waves. A comprehensive description of the model can be found in Dipankar et al. (2015); in the following I will only describe some of the main features relevant for my study.

ICON-LEM solves the Favre-filtered (following Hinze, 1975) equations of motion for the prognostic variables v_1 (horizontal velocity component normal to the triangle edges), v_2 (horizontal velocity component tangential to the triangle edges), v_3 (vertical wind component perpendicular to the triangle edges), ρ (density), θ_v (virtual potential temperature) and the specific masses of tracers (q_i with $i \in$[water va-

por, cloud, rain, snow, graupel, hail, ice] depending on the employed microphysics):

$$\frac{\partial v_1}{\partial t} + \frac{\partial\left(\frac{\mathbf{v_h}\cdot\mathbf{v_h}}{2}\right)}{\partial x_1} - (\zeta + f)v_2 + v_3\frac{\partial v_1}{\partial x_3} = -c_{\mathrm{pd}}\theta_v\frac{\partial\pi}{\partial x_1} + Q_{v_1} \qquad (2.1)$$

$$\frac{\partial v_3}{\partial t} + \mathbf{v_h}\cdot\nabla_{\mathbf{h}}v_3 + v_3\frac{\partial v_3}{\partial x_3} = -c_{\mathrm{pd}}\theta_v\frac{\partial\pi}{\partial x_3} + Q_{v_3} \qquad (2.2)$$

$$\frac{\partial(\rho\theta_v)}{\partial t} + \nabla(\mathbf{v}\rho\theta_v) = Q_{\theta_v} \qquad (2.3)$$

$$\frac{\partial(\rho q_i)}{\partial t} + \nabla(\mathbf{v}\rho q_i) = Q_{q_i} \qquad (2.4)$$

$$\frac{\partial\rho}{\partial t} + \nabla(\mathbf{v}\rho) = 0 \qquad (2.5)$$

A list of symbols used can be found in Tab. 2.1. The model solves

π	Exner function
$\mathbf{v_h}$	2-D velocity component
$\mathbf{v}$	full 3-D velocity vector
ζ	vertical vorticity component
f	Coriolis parameter
c_{pd}	heat capacity for dry air

Table 2.1: Symbols used in the governing equations.

only for the velocities v_1, v_3 while the tangential velocity component v_2 is diagnosed using the radial basis function reconstruction (Narcowich and Ward, 1994).

Forcing terms in the governing equations The Q terms in Eqs. 2.1, 2.2, 2.3, 2.4 and 2.5 contain the contribution due to subgrid turbulent diffusion and forcings (microphysics, radiation, condensation). They are computed as the divergence of the subgrid-scale stress tensor following the approach of Lilly (1962) who revisited the classical Smagorinsky scheme. The contributions of sub-grid slow-physics (e.g. radiation) and fast-physics (e.g. cloud microphysics) are expressed through a flux-gradient relationship in Eqs. 2.3 and 2.4.

The governing equations 2.1, 2.2, 2.3, 2.4 and 2.5 are integrated in time using the two-time level predictor-corrector scheme (Zängl et al., 2015) except for the terms corresponding to the vertical soundwave propagation, which are integrated implicitly. The tracers are integrated using a flux-form-semi-Lagrangian scheme for its better conservation properties.

Horizontal and vertical grids While the vertical grid is discretized in the same way as the ICON-NWP configuration, in the horizontal a pseudo-Torus grid is adopted in order to have doubly periodic boundary conditions. The domain is thus assumed to be flat so that Cartesian coordinates are used instead of the default spherical coordinates. This is suitable only for simulation over small domains, where the Earth curvature is negligible.

Parametrizations At the typical scale of ICON-LEM model simulations, clouds are sup-

posed to be explicitly resolved, so that there is no need for a convective parametrization. Cloud microphysical properties are parametrized using the 2-moment mixed-phase microphysics scheme of Seifert and Beheng (2006) including prognostic equations for cloud water, rain, ice, graupel, hail and snow. Radiation is parametrized with the aid of the Rapid Radiative Transfer Model (RRTM) scheme (see Clough et al., 2005, for a general review). The ICON-LEM modeling framework has been validated using a Dry Convective Boundary Layer (DCBL) and a Cloud-Topped Boundary Layer (CTBL) setup in Dipankar et al. (2015) and showed consistent results when compared to University of California Los Angeles Large-Eddy Simulation (UCLA-LES) and PArallelized Large-eddy simulation Model (PALM) (Maronga et al., 2015) models.

In part i the ICON-LEM model is always initialized using an input sounding (vertical atmospheric profile) which is then interpolated on the model vertical grid. Thus, at the initial time, every grid point resembles the same vertical structure. A random perturbation is then added in the 3 lowermost atmospheric levels on the prognostic variables θ_v and v_3 with an amplitude of 0.2 K and 0.05 m/s, respectively, to break the perfectly homogeneous initial state.

2.2 THE LAND SURFACE MODEL

The coupling between the atmosphere and the land surface is realized through surface fluxes of momentum, heat and moisture. They enter the atmospheric part of ICON-LEM model as the lower boundary conditions for the subgrid-scale stress tensor in the Q_{v_1}, Q_{v_3} terms of the momentum equations 2.1, 2.2 and as the fluxes of θ_v, q_i in the Q_{θ_v}, Q_{q_i} terms found Eqs. 2.3 and 2.4, respectively. In the following I will only focus on surface fluxes of moisture (latent heat flux) and heat (sensible heat flux) as these are the components affected by the soil model TERRA-ML.

2.2.1 *Surface fluxes formulation*

The sensible and latent heat fluxes at the surface [W m^{-2}] are parametrized using a drag-law formulation:

$$F_{\text{sens}} = -\rho c_{\text{pd}} C |\mathbf{v_h}(\Delta x_3)| \left[\theta(\Delta x_3) - \theta_{\text{surf}}\right] \qquad (2.6)$$

$$F_{\text{lat}} = -\rho L_v C |\mathbf{v_h}(\Delta x_3)| \left[q_v(\Delta x_3) - q_{v_{\text{surf}}}\right] \qquad (2.7)$$

where $\mathbf{v_h}(\Delta x_3), \theta(\Delta x_3), q_v(\Delta x_3)$ indicate the values at the first atmospheric level and $\Delta x_3, q_{v_{\text{surf}}}, \theta_{\text{surf}}$ indicate the values of humidity and potential temperature at the surface, respectively, and are computed by the soil model and L_v is the specific latent heat of vaporization. The bulk aerodynamic transfer coefficient C is assumed equal for both sensible and latent heat flux and is calculated diagnostically as

described in (Doms et al., 2011).

It should be noted that the minus sign is implicitly included in the formulation of the turbulent fluxes and reflects the convention in which fluxes are considered negative when there is a net transport of heat from the land surface to the atmosphere. The calculation of the fluxes in Eqs. 2.6 and 2.7 requires the knowledge of temperature and specific humidity at the ground surface ($\theta_{surf}, q_{v_{surf}}$), which are predicted by the soil model through a simultaneous solution of a separate set of equations described in the following section.

2.2.2   *The TERRA-ML soil model*

In this section a brief overview of the soil model TERRA-ML is presented: further details can be found in Doms et al. (2011). The main goal of TERRA-ML is to compute the evolution in time of the water reservoir and temperature of every soil layer. In the operational version of ICON the discretized structure of the soil includes 8 different layers, with 7 active soil layers for temperature and 6 active soil layers for moisture. This is so because the temperature is assumed to be constant in the lowermost layer while soil moisture cannot change in the lowermost 2 layers. The soil layers have the following depths: 0.01 m, 0.02 m, 0.06 m, 0.18 m, 0.54 m, 1.62 m, 4.86 m and 14.58 m. Note that the soil layer depths have to be specified beforehand as they are hard-coded into ICON. While for the validation (section 2.3) I will change those values to be comparable with the ones used in the other models, in the rest of the dissertation the default operational configuration will be used instead.

2.2.2.1   *Soil temperature budget*

The temperature T_k [K] of every soil layer k with thickness Δz_k evolves in time, as a result of different forcing, following a simple diffusion equation:

$$\frac{\partial T_k}{\partial t} = \frac{1}{\rho c}\frac{\partial}{\partial z}\left(\lambda \frac{\partial T_k}{\partial z}\right) \tag{2.8}$$

where T_k is the soil layer temperature, ρc is the heat capacity and λ is the heat conductivity. The volumetric heat capacity ρc is determined by taking into account the respective values for a dry soil ($\rho_0 c_0$, Table A.1) and for water ($\rho_w c_w = 4.18 \cdot 10^6$ J m^{-3} K^{-1}). The determination of heat conductivity λ takes into account the liquid water content of the soil and uses an approximate formula which can be found in Doms et al. (2011).

Equation 2.8 requires boundary conditions to be solved in the uppermost and lowermost layer. At the bottom, a climatological temperature, T_{clim}, constant in time is prescribed. Instead, at the upper

boundary, the heat flux in Eq. 2.8 is replaced by the atmospheric forcing due to the sum of net incoming radiation Q_{net}, sensible heat flux F_{sens} and latent heat flux F_{lat} as defined in Eqs. 2.6 and 2.7.
The evolution of surface temperature can thus be expressed (note the sign convention) as:

$$\rho c \frac{\partial T_{\text{surf}}}{\partial t} = \frac{1}{\Delta z_1}\left[\lambda \frac{T_2 - T_1}{\Delta z_2 - \Delta z_1} + F_{\text{sens}} + F_{\text{lat}} + Q_{\text{net}}\right] \qquad (2.9)$$

The sensible heat flux is known from the surface layer parametrization (Eq. 2.6) once the surface temperature has been determined by the LSM. The latent heat flux is determined by TERRA-ML once all the terms of the soil water budget have been determined, as shown in the following section.
Equation 2.9 constitutes the surface energy balance (Budyko, 1961). It shows that the main source of energy in the land-atmosphere coupled system is incoming radiation. This source is then redistributed in sensible and latent heat fluxes, as well as a soil heat flux term. This redistribution of energy strongly depends on the parametrization employed in the soil model: for this reason it will be the main goal of the validation study presented in section 2.3.

2.2.2.2 *Soil water budget*

Exchange of water between the soil and the atmosphere takes place through evaporation and precipitation in the uppermost soil layer. Exchange and transport of water between the soil water reservoirs occur instead via infiltration, percolation and capillary movements. A runoff term is considered both at the surface and in every soil layer (including the interception reservoir). Figure 2.1 depicts the various processes parametrized in the model and described by the governing equations for the mass budgets of the various reservoir.

Governing equations for soil moisture reservoirs

INTERCEPTION RESERVOIR

$$\rho_w \frac{\partial W_i}{\partial t} = \alpha \cdot P_r + E_i - I_{\text{perc}} - R_{\text{inter}} \qquad (2.10)$$

FIRST SOIL LAYER $k = 1$

$$\rho_w \frac{\partial W_1}{\partial t} = \left[E_b + I_{\text{perc}} + (1 - \alpha)P_r - R_{\text{infil}}\right] \qquad (2.11)$$

SOIL LAYERS $k > 1$

$$\rho_w \frac{\partial W_k}{\partial t} = F_{k,k+1} - F_{k-1,k} + Tr_k - R_k \qquad (2.12)$$

where ρ_w [kg m^{-3}] is the density of water. The other symbols have the following meanings:

W_i, W_k water content of interception store and soil layers [m H$_2$O]
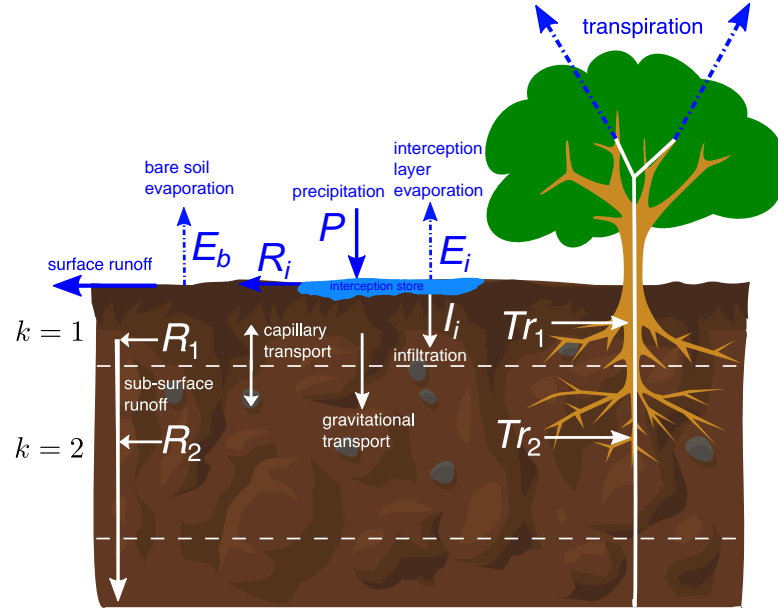
Figure 2.1: Hydrologic processes considered in the soil model.

E_i evaporation from interception reservoir [kg m^{-2} s^{-1}]

E_b evaporation from bare soil [kg m^{-2} s^{-1}]

Tr_k water extraction by roots [kg m^{-2} s^{-1}]

P_r precipitation rate of rain [kg m^{-2} s^{-1}]

α factor for distributing rain between interception reservoir and infiltration

I_{perc} infiltration contributions from percolation [kg m^{-2}s^{-1}]

$R_{\text{inter}}, R_{\text{infil}}, R_k$ runoff from interception reservoir, from limited infiltration rate and from soil layers, respectively [kg m^{-2}s^{-1}]

$F_{k,k+1}$ gravitational and capillary flux of water between layers $k+1$ and k [kg m^{-2}s^{-1}]

The parametrizations adopted for these terms will now briefly explained.

The vertical soil water transport between the soil layers is parametrized using the Richards equation (see Hillel (2012)):

$$F_{k,k+1} = -\rho_w \left[-D_w(w_k)\frac{\partial w_k}{\partial z}\bigg|_{k,k+1} + K_w(w_k) \right] \tag{2.13}$$

where $w_k = W_k/\Delta z_k$ is the fractional water content of the soil layer k. Hydraulic diffusivity D_w and hydraulic conductivity K_w depend on water content, pore volume w_{pv}, air dryness point w_{adp} and the soil type as in Rijtema (1969). At the lower boundary $D_w = 0$ is

assumed in order to consider only the downward gravitational transport. Equation 2.13 shows that the transport of moisture acts to reduce any vertical gradient in soil moisture; horizontal transport of moisture between adjacent cells is not considered in this model.

Evaporation from interception store and bare soil are parametrized as:

E_i and E_b

$$
\begin{aligned}
E_i &= \max\left[-\frac{\rho_w}{\Delta t}W_i\,,\, f_i \cdot E_{\text{pot}}(\theta_{\text{surf}})\right] & (2.14)\\
E_b &= (1-f_i)(1-f_{\text{plnt}})\cdot\min\left[-E_{\text{pot}}(\theta_{\text{surf}})\,,\, F_m\right] & (2.15)
\end{aligned}
$$

where f_i is the fractional area of surface soil covered by water, f_{plnt} is the one covered by plants and F_m is the maximum moisture flux through the surface that the soil can sustain (Dickinson, 1984), which depends on the soil type.

The potential evaporation E_{pot} in Eqs. 2.14 and 2.15 is parametrized through a simple drag-law formula:

$$
E_{\text{pot}}(\theta_{\text{surf}}) = \rho C|\mathbf{v_h}|(q_v - q_v^{\text{sat}}(\theta_{\text{surf}})) \qquad (2.16)
$$

where q_v^{sat} denotes the saturation specific humidity. Since $E_{\text{pot}}(\theta_{\text{surf}})$ is a measure of the amount of evaporation that would occur at temperature θ_{surf} over a fully saturated surface, it is clear that water in the interception layer and in the bare soil cannot evaporate more than the potential evaporation. Equations 2.14 and 2.15 are considered only if $E_{\text{pot}}(\theta_{\text{surf}}) < 0$, which indicates upward directed potential evaporation.

The plant transpiration is considered only if $E_{\text{pot}}(\theta_{\text{surf}}) < 0$ by taking into account both the resistance for water vapor transport from the foliage to the canopy air (foliage resistance r_f) and the resistance for water vapor transport from the canopy air to the air above the canopy (atmospheric resistance r_a):

Tr_k and Tr

$$
Tr = f_{\text{plnt}}(1-f_i) \cdot E_{\text{pot}}(\theta_{\text{surf}})\frac{r_a}{r_a + r_f} \qquad (2.17)
$$

The atmospheric resistance is given by $r_a = (C|\mathbf{v_h}|)^{-1}$. The formulation of the foliage resistance can be found in Doms et al. (2011). The total transpiration Tr is distributed in every layer as Tr_k by weighting Tr with the part of the soil layer filled by root and the fractional water content of the layer.

A fraction of precipitation falling on the ground is collected by the interception reservoir at a rate αP_r. This liquid part of the precipitation can either evaporate at the potential rate E_{pot} or percolate to the uppermost soil layer according to the value of $I_{\text{perc}} = I_i$. If the percolated amount of water causes the uppermost soil layer to exceed its pore volume, this water is removed as runoff R_{inter}. The fraction of water that is not used for percolation or evaporation is available for infiltration. This process is also limited by the available pore volume of the

Evolution of the interception reservoir

uppermost soil layer, so that a runoff R_{infil} is produced when the capacity is exceeded and contributes to a total runoff $R_i = R_{\text{infil}} + R_{\text{inter}}$.

Runoff   The runoff term R_k is considered if the total water content w_k of the layer exceeds the field capacity w_{fc} (see Tab. A.1) and if the divergence of the fluxes described by Eq. 2.13 in this layer is negative. It is parametrized through

$$R_k = -\frac{w_k - w_{\text{fc}}}{w_{\text{pv}} - w_{\text{fc}}} \left(\frac{\partial F_k}{\partial z}\right) \Delta z_k \tag{2.18}$$

Thus every layer loses soil moisture already when the value of w_{fc} is reached, even though the maximum value that soil moisture can attain is w_{pv} which is represented by a fully saturated soil.

Once all the terms shown in this section have been computed they are summed up to obtain the latent heat flux which is then used in Eq. 2.7 to obtain $q_{v_{\text{surf}}}$.

$$E_b + Tr + E_i = -F_{\text{lat}} \tag{2.19}$$

This closes the system as all the fluxes, as well as surface variables, are determined and can be used as forcing for the atmospheric component of the model.

2.3   MODEL VALIDATION

To the author knowledge a coupled configuration of ICON-LEM and TERRA-ML has never been tested in idealized simulations, that is in the pseudo-Torus geometry. This configuration has instead been used in a realistic case with a domain enclosing Germany (Heinze et al., 2016). To be able to use the TERRA-ML model in idealized conditions some modifications to the ICON code had to be performed by including a new test case in the non-hydrostatic branch of the model. This new implementation includes the initialization of the soil variables by using an external soil profile and the creation of an `extpar` file which contains all the soil spatial features like soil type, topography, root depth etc... The `extpar` file is first created using the target grid employed in the simulation and then modified to prescribe either homogeneous constant values over the whole grid (e.g. in Chapter 3) or patches with different values of soil moisture (e.g. in Chapter 4). In Appendix A an extensive list of the parameters used in the `extpar` file and of their values is presented. Surface temperature and specific humidity, which are usually computed from prescribed initial and boundary conditions, are initialized using the lowermost atmospheric level temperature and the saturation specific humidity at the same temperature, respectively. Given that snow is not considered all the surface variable related to it are set to 0. Finally, the radiation code is modified in order to allow for a solar zenith angle which depends only on the time of the day and not on the position over the

Modification of the test case in ICON

domain.

To validate the implementation of the new case into ICON a comparison study is set up using results from the UCLA-LES and Dutch Atmospheric Large-Eddy Simulation (DALES) models (see Stevens, Moeng, et al., 2005; Savic-Jovcic and Stevens, 2008; Heus et al., 2010, for details) for an idealized case of DCBL. Two main types of experiments, with constant and interactive radiation, are conducted to test the performance of ICON-LEM.

Some differences between the employed models should be pointed out before highlighting the differences in the LSM and before discussing the results of the simulations. First of all, the ICON-LEM model uses the fully compressible set of equations, UCLA-LES uses the anelastic approximation and DALES uses the Boussinesq approximation. Therefore ICON-LEM is forced to use a smaller time step as it allows for the propagation of sound-waves. ICON-LEM uses θ_v as the prognostic variable for the thermodynamic equation, whereas UCLA-LES and DALES models use θ_l (liquid potential temperature).

Regarding moist processes, ICON-LEM uses q_v, q_c (water vapor and cloud water mixing ratios) as the prognostic variables, whereas UCLA-LES and DALES use $q_t = \sum_i q_i$ which is conserved in absence of precipitation. In order to parametrize sub-grid scale turbulence ICON-LEM and UCLA-LES use the classical Smagorinsky turbulence scheme, whereas DALES uses a prognostic Turbulent Kinetic Energy (TKE)-based turbulence scheme. Finally, the parametrization of radiation differs in all the models: while in UCLA-LES the radiation is described by means of a Monte-Carlo scheme (Pincus and Stevens, 2009), DALES uses a simpler parametrization, as described in Stull (2000) and ICON-LEM uses the RRTM radiation, as mentioned earlier.

The LSM employed in ICON-LEM differs from the one used in DALES and UCLA-LES models (Rieck, 2015), mainly because the former is tuned for operational forecasts. In the following I list only some of the main similarities and differences between the employed LSMs. The equations for heat conduction 2.8 and water movement in the soil 2.13 are the same for both models, as well as the formulations of the surface fluxes. Conversely, the vegetation formulation adopted in TERRA-ML is more complex since it allows for different plant types and uses a different formulation for the foliage resistance r_f.

TERRA-ML also considers a classification for different soil types and land use classes which affects the plant transpiration and the bare soil evaporation. Since results were strongly affected by the type of plants and land cover I decided not to consider land use classes and plants which were removed from the domain during the validation process. The presence of plants will only be considered in section 3.4.5.

Furthermore, the skin layer in TERRA-ML is implemented as the first thin layer in the soil discretization and has a heat capacity which is about half the one used in the LSM coupled to UCLA-LES and DALES

	z_1	z_2	z_3	z_4	z_5	z_6
half level height [m]	0.005	0.04	0.205	0.905	2.165	3.93
soil layer depth [m]	0.01	0.07	0.34	1.47	2.86	5.00
soil layer thickness [m]	0.01	0.06	0.27	1.13	1.39	2.14
θ [K]	296	290	287	285	283	283
ϕ [m^3·m^{-3}]	0.273	0.273	0.274	0.276	0.335	0.335

Table 2.2: Values of the depth, thickness, temperature and soil moisture for each soil level used in the validation of the LSM.

models. In the latter models the skin layer is not hydrologically active. Finally, as already shown in Eqs. 2.15 and 2.14, the evaporation is flux-limited, while UCLA-LES and DALES always evaporate at a rate equal to E_{pot} in absence of plants.

The soil layers are initialized with the temperature and moisture profiles shown in Table 2.2, resembling a soil below the field capacity. The entire domain is covered with a uniform soil type (loam, see Table A.1) which has the same features in every grid point (root depth, stomatal resistance, roughness length, etc.). Note that in TERRA-ML I used a total of 6 layers, instead than the 4 used by Rieck (2015), given the difference between the models highlighted before.

Setup used for the validation The atmospheric initial conditions are taken from the Cabauw measurement site in the Netherlands and are representative of a cloudless day without the influence of synoptic-scale forcing (C. C. Van Heerwaarden et al., 2010). The temperature is constant (292.5 K) in the first 800 meters, while an inversion takes place in the subsequent 100 meters and a constant lapse rate ($\sim$ 6 K km^{-1}) is prescribed at altitudes above. The specific humidity is vertically homogeneous in the whole atmosphere column with a prescribed value of $q_v = 5$ g kg^{-1}. Both profiles are shown as black lines in Figs. 2.4, 2.6.

The horizontal domain comprises 64×64 points with a grid size of 50 m, while the vertical grid is discretized by means of 96 points and a vertical spacing which increases with height through a scaling factor of approximately 0.3. The minimum grid spacing is set to 25 meters, in order to mimic the constant spacing used by Rieck (2015) while the model top lies at 20 km in ICON-LEM, as opposed to the 3 km used in UCLA-LES and DALES models, because of an intrinsic limitation with RRTM. All models are integrated for 5 hours of simulation time.

2.3.1 *Experiment with fixed radiation*

First of all, the performance of TERRA-ML is tested with constant incoming radiation at the surface. In UCLA-LES and DALES models this is achieved by imposing a constant value for $Q_{net} = F_{SW} + F_{LW} = 450$W m^{-2}, where F_{SW}, F_{LW} are the net short-wave and long-wave radiation fluxes at the surface, respectively. In ICON-LEM the only way to get the

same effect is to modify the solar constant in order to properly scale the incoming shortwave flux at the surface so as to obtain an effective $Q_{net} \sim 450W\,m^{-2}$. However, since the surface temperature is always changing, the emitted long-wave flux at the surface will change, thus affecting Q_{net}, as one can recognize in Fig. 2.3.

A quick inspection of Fig. 2.2 confirms that the soil model is correctly simulating the evolution of temperature and moisture. The temperature in the first soil layer, which is 1 cm thick, increases from the initial temperature of 296 K up to approximately 300 K. It may also be noted that the second layer (7 cm depth) is heating at a similar rate, but starting from a colder temperature (291 K, recall Table 2.2) and thus reaching a final temperature of about 297 K. The other layers experience a slower and delayed warming, as expected, while the temperature of the lowermost two layers is almost constant in time, since the depth doesn't allow for efficient thermal exchange during the 5 hours of model simulation.

The bare soil evaporation, which is entirely contributing to the sur-

Evolution of soil moisture and temperature
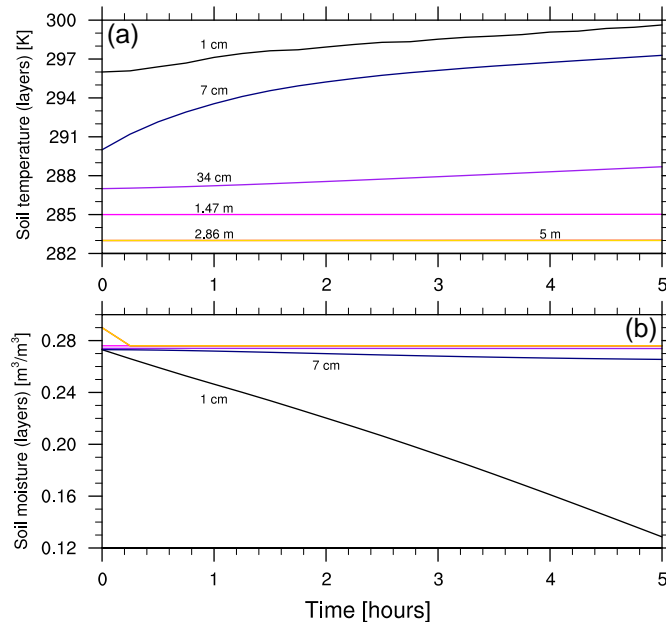
Figure 2.2: Time series of (a) soil layer temperatures and (b) soil layer moisture during the 5 hours of the simulation in the ICON model. The different soil layers are indicated by different colors while the depth is indicated only when necessary by explicit labels. Note that some of the lines are not visible due to overlapping.

face latent heat flux, acts to reduce the soil moisture in the uppermost layer. The latter is evaporating at a rate between the potential evaporation and the maximum sustainable moisture flux (Eq. 2.15), thus reducing the soil moisture content. The jump observed in the first 15 minutes (yellow line in Fig. 2.2) is due to the fact that the lowermost 2 layers are not hydrologically active and thus the moisture value is

set to the one of the overlying layer at the second model time step. The time evolution of sensible and latent heat fluxes depicted in Figs. 2.3 (a,b) shows a similar behavior for all models. The values obtained with ICON-LEM are nevertheless smaller and thus worth discussing. The difference between the fluxes computed by the various models in
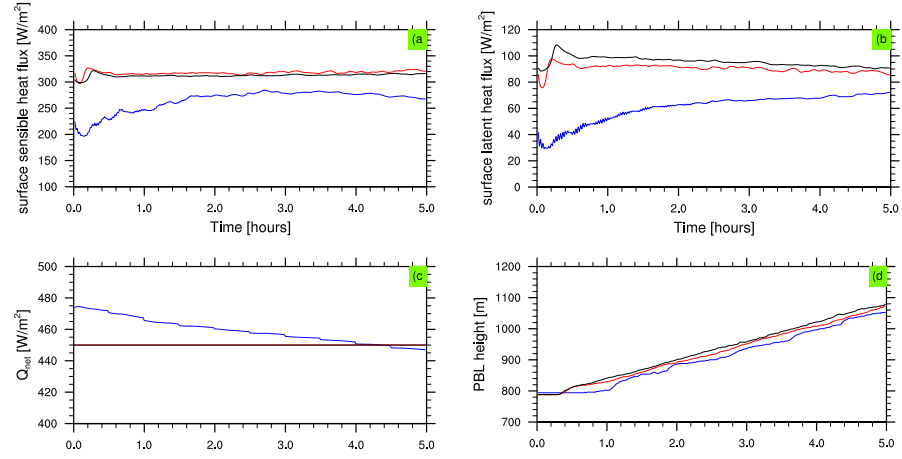
Figure 2.3: Time series of domain-mean (a) surface sensible heat flux, (b) surface latent heat flux, (c) net radiation flux at the surface and (d) boundary layer height for ICON-LEM (blue), UCLA-LES (red) and DALES (black). Note that Q_{net} is constant (flat line) in both UCLA-LES and DALES. The height of the boundary layer is defined here as the height of the maximum vertical θ gradient.

Explaining discrepancies between models

the first hour is mainly due to two different reasons. First of all, the spin-up phase of the ICON-LEM model, which has proven to be longer when compared to other models (order of 1.5 hour, see Dipankar et al., 2015). Second, the different definition of the surface temperature. In DALES and UCLA-LES models T_{surf} assumes the value of the skin layer temperature, which is initially set to 296 K. In TERRA-ML this temperature is computed by using Eq. 2.9, which in turn exploit the latent heat flux defined by Eq. 2.19. Since the evaporation from bare soil is limited (recall Eq. 2.15) the surface temperature in ICON-LEM is always colder than the one computed in the other models. This affects the time evolution of the surface fluxes. Regarding the differences observed in the subsequent hours, it can be inferred that ICON-LEM differs from the other models mostly by a constant offset, which is due to the different parameters defining the soil type in TERRA-ML. The evolution of the vertical profiles of the temperature and specific humidity is shown in Fig. 2.4. All models show a warming and moistening of the boundary layer with time, although these processes are slower in ICON-LEM model, in agreement with the smaller surface fluxes. However, the time evolution resembles the same structure in all three models and progressively adjust to the initial profile over approximately 1.2 km.
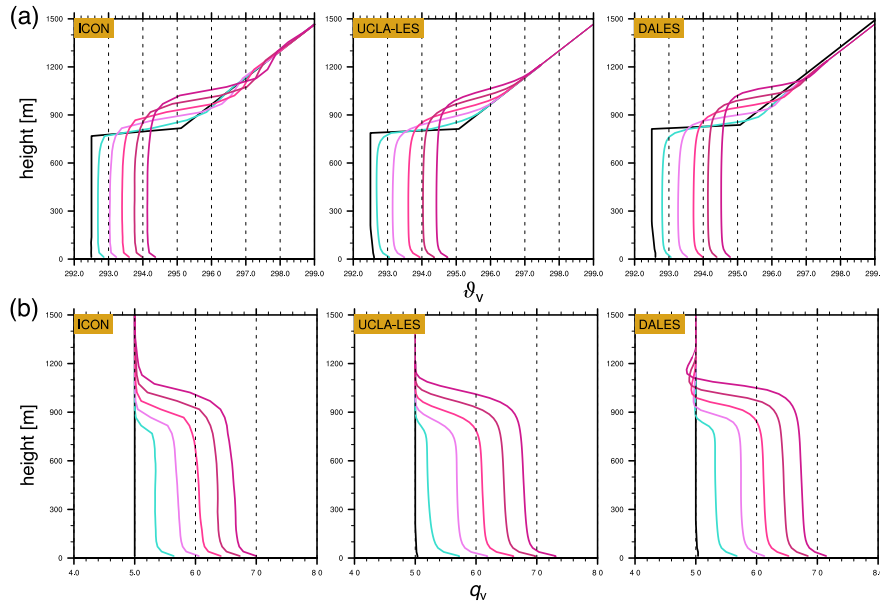
Figure 2.4: Vertical profiles of domain-mean (a) potential temperature [K] and (b) specific humidity [g kg^{-1}] for the models ICON-LEM, UCLA-LES and DALES. Black lines indicate the initial conditions while colored lines show values every consecutive hour (from light blue to dark pink). Case with fixed radiation balance at the surface.

2.3.2 *Experiment with interactive radiation*

In this case the available net radiation at the surface is computed interactively by the radiation scheme. For this reason Q_{net} is not constant, but varies over time. Following Rieck (2015) the radiation scheme is initialized at day 287 of the year (14 October) at a latitude of 48N, while the model is run once again for 5 hours between 8 Local Standard Time (LST) and 13 LST. The maximum insolation is reached before the model is stopped. Although the radiative balance has the same temporal evolution in all the models, the value of Q_{net}, which is highly dependent on the parametrization adopted, is different in all models. In order to account for this effect, the values of surface fluxes shown in Fig. 2.5 are normalized over the correspondent value of Q_{net}.

Aside from the spin-up phase, there is a clear convergence among the different models. The biggest difference can be seen in the latent heat flux value, especially in the first hour, and is easily explained by considering that this value is the most influenced by soil properties through bare soil evaporation. In absolute terms, the latent heat flux computed in ICON-LEM differs from the one obtained by DALES model by 30-40 % in the spin-up phase and less than 10% in the subsequent hours. The sensible heat flux of the aforementioned models shows a similar time evolution and a maximum discrepancy of about 20%. The UCLA-LES shows very different absolute values of the fluxes

Comparison of variables evolution over time
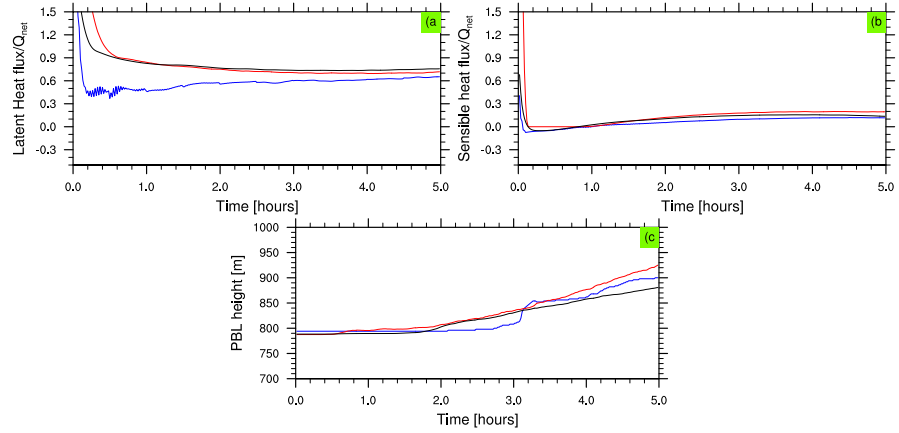
Figure 2.5: Time series of domain-mean (a) surface latent heat flux, (b) surface sensible heat flux, both normalized over Q_{net} and (c) boundary layer height for ICON-LEM (blue), UCLA-LES (red) and DALES (black). The height of the boundary layer is defined here as the height of the maximum vertical θ_v gradient.

if compared to ICON-LEM and DALES, most likely because of the different formulation of the incoming radiation distribution. The fluxes computed in ICON-LEM are almost always below the ones computed in the other models. The growth rate of the PBL is also similar in all models. The one simulated by ICON-LEM is less smooth, most certainly because of the coarser vertical resolution adopted in ICON-LEM. The vertical profiles obtained with ICON-LEM model (Fig. 2.6) are
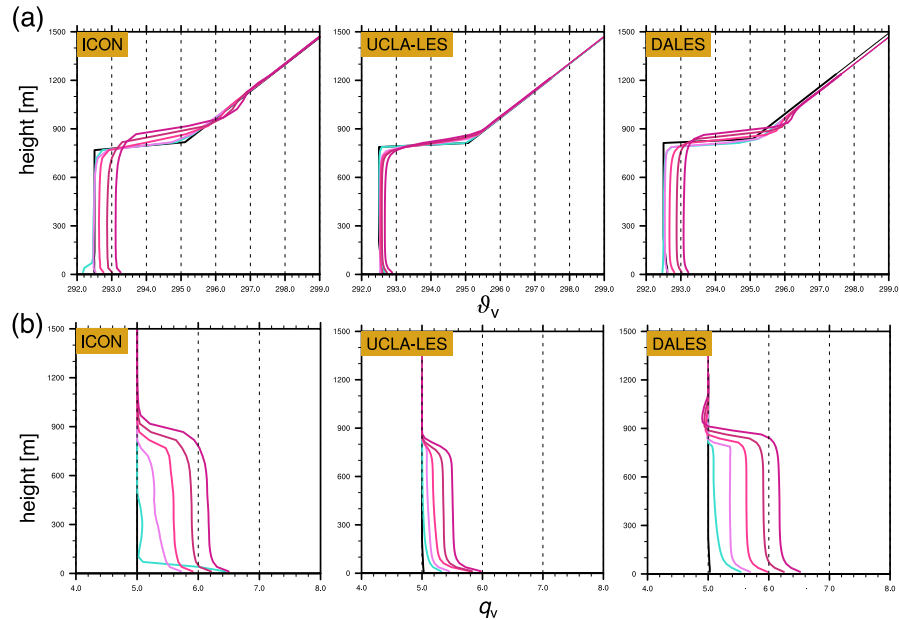
Figure 2.6: Vertical profiles of domain-mean (a) potential temperature [K] and (b) specific humidity [g kg^{-1}] for the models ICON-LEM, UCLA-LES and DALES. Black lines indicate the initial conditions while colored lines show values every consecutive hour (from light blue to dark pink). Case with interactive radiation.

very similar to those obtained with the DALES model. Hence it can be deduced that a larger Q_{net} compensates for smaller fluxes. During the first hour the atmosphere simulated by ICON-LEM model is still undergoing the initial spin-up phase. While the temperature inversion located in the lower 100 meters of ICON-LEM simulation is also observed, with slightly less intensity, in the DALES simulation, the strong gradient of q_v obtained with ICON-LEM doesn't have a matching feature in the other models.

However, an accurate inspection of the time evolution related to the vertical profile of q_v computed with ICON-LEM model, with a resolution of 60 seconds, confirmed that this feature is only related to the initial spin-up of the simulation. This is due to the fact that in the first hour the incoming radiation, which is lower than in the fixed-radiation case, does not compensate the large evaporation computed by the model. This causes the surface temperature to decrease from the prescribed value (296 K) to about 292 K in the first 30 minutes. The cooling of the surface induces the formation of a small inversion layer which constantly moistens over time because of the surface evaporation. This explains the high value of q_v observed in the lower layers of the ICON-LEM model. As soon as the incoming radiation increases, more vigorous thermals are able to break the inversion layer and to support boundary layer mixing, which redistributes the humidity all over the vertical profile.

Comparison of vertical profiles over time

THE INFLUENCE OF SOIL MOISTURE ON DIURNAL CONVECTION AND PRECIPITATION OVER A HOMOGENEOUS SURFACE

3.1 INTRODUCTION

Soil moisture strongly modulates the partition of the surface net incoming radiation into fluxes of heat and moisture. These fluxes modify the atmospheric state and can either increase the total water vapor content, i.e. the amount of precipitable water, or modify the efficiency at which water vapor is converted into precipitation. By exploring this scenario Findell and Eltahir (2003b) showed that, over a homogeneous surface, the resulting coupling of soil moisture and precipitation over a diurnal cycle strongly depends on the early morning atmospheric state. Larger values of sensible heat flux, as the ones found over dry soils, produce a deeper PBL that can more easily reach the Level of Free Convection (LFC) thus triggering convection. On the other hand, larger values of latent heat flux, as the ones found over wet soils, lead to a moistening of the PBL and thus to a lowering of the Lifted Condensation Level (LCL), making it easier to trigger convection.

Different combinations of low-level instability and moisture amount favor one or the other mechanism resulting either in a dry soil advantage (more precipitation over dry soils) or in a wet soil advantage (more precipitation over wet soils). In Findell and Eltahir (2003b) these two scenarios are differentiated using the Convective Trigger Potential (CTP) index, which considers convective instability between 900 and 700 hPa, and the HI_{low} humidity index, which corresponds to the sum of the dew point depressions at 950 and 850 hPa. However, the 2-D model used in Findell and Eltahir (2003b) did not allow for an estimation of the precipitation obtained with either dry soil or wet soil advantage profiles given that the integration was automatically interrupted when convection was triggered. Thus, the different advantages were mostly related to the triggering of convection instead that to the actual amount of precipitation. In this chapter I want to assess whether these two advantages can be found also when analyzing precipitation.

Dry and wet soil advantages

The first goal consists in quantifying the likelihood of precipitation on soils that are either wetter or drier than normal. I here neglect any effect that would arise due to the presence of heterogeneous soil moisture conditions, which will be reviewed in Chapter 4. The second goal consists in evaluating whether large-scale effects, cloud-surface

Main goals

interactions or the presence of winds or plants can modify the sign
and magnitude of the coupling.

In order to address these main goals, idealized experiments are per-
formed with the coupled configuration of ICON-LEM and TERRA-ML
described in Chapter 2. This set-up allows for an explicit representa-
tion of convection and of land-surface interactions on scales of $\mathcal{O}(100$
m). Within this set-up, the methodology proposed by Findell and
Eltahir (2003b) is revisited. Instead of focusing only on the depen-
dence of the triggering of convection on soil moisture, attention is set
on the entire diurnal cycle of convection and its precipitation.

Outline of the
chapter
The chapter is organized as follows. Section 3.2 describes the model-
ing framework and the experimental setup. In section 3.3 the results
of the experiments using the same initial atmospheric conditions as in
Findell and Eltahir (2003b) are discussed and a simple expression is
derived to assess the likelihood of observing more precipitation over
drier soils. In section 3.4 the role of clouds, large-scale forcing, winds
and plants on the soil moisture-precipitation coupling is investigated.
A short summary is given in section 3.5.

3.2   METHODS

3.2.1   *Basic configuration*

In order to study the response of the diurnal cycle of convection and
precipitation to soil moisture, different experiments are setup using
the idealized coupled configuration of ICON-LEM and TERRA-ML de-
scribed in Chapter 2. The only difference pertains the employment of
the single-moment 3-cat ice microphysics (Doms et al., 2011), instead
than the dual-moment microphysics used in Chapter 2. The two early
morning (12 Coordinated Universal Time (UTC)/6 LST) soundings pro-
posed by Findell and Eltahir (2003b), taken on 3 July and 23 July 1999
in Lincoln, Illinois (USA), are used to initialize the atmosphere as I
specifically want to repeat their analysis but including precipitation.
The profiles are illustrated in Fig. 3.1. Since the effect of winds is not
considered in the basic configuration, the (v_1, v_2, v_3) velocity compo-
nents are set to 0 over the whole atmospheric column at the beginning
Basic model setup
of the simulation .

The July, 3rd sounding should represent a wet soil advantage and
thus favor convection over wetter soils, whereas the sounding taken
on July, 23rd should favor convection over drier soils. The two cases
are referred to in the chapter as WA for wet soil advantage and DA
for dry soil advantage. For each atmospheric profile, the simulations
start at 6 LST and end at 24 LST. To avoid that differences in the in-
solation between the two cases may affect the coupling, the radiation
code is always initialized with the date of the WA sounding and coor-
dinates of Lincoln, Illinois (40.15 N, 89.37 W).
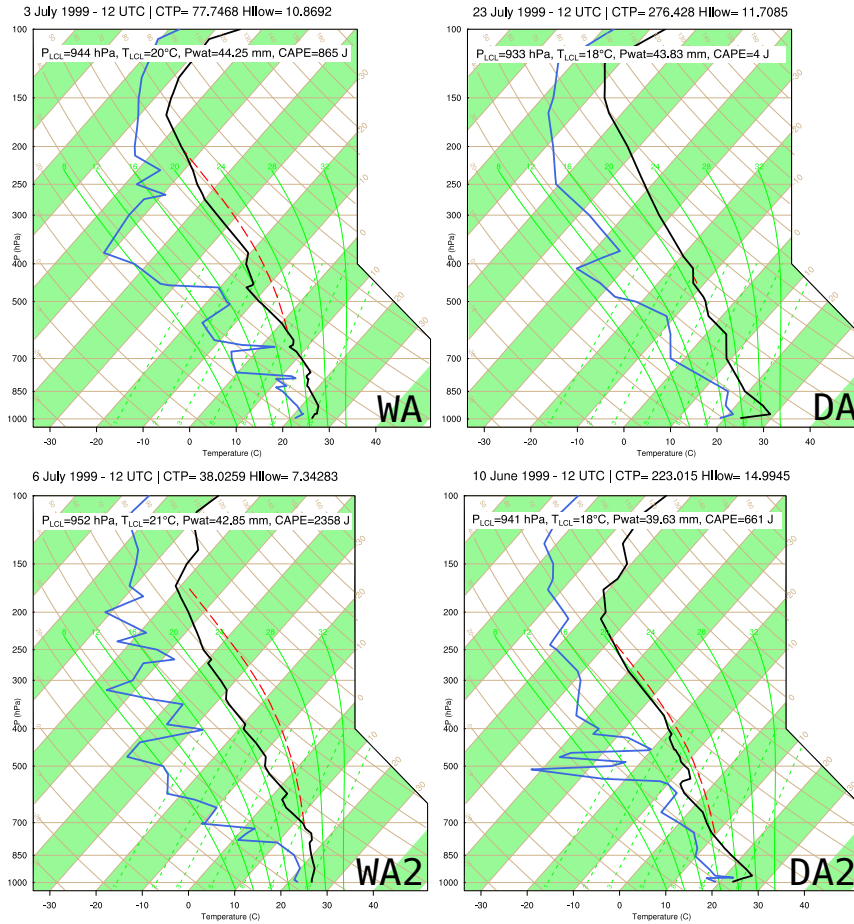
Figure 3.1: Atmospheric profiles measured at Lincoln, Illinois (USA). Temperature [° C] is represented by the black line, dew point temperature [° C] by the blue line. The red dashed line highlights the area where the surface parcel is positively buoyant with respect to the environment. The plot title contains the value of CTP and HI_{low} computed following Findell and Eltahir (2003b). Text insets indicate values of pressure and temperature at the LCL, vertically integrated water vapor content (Pwat) and CAPE.

The horizontal domain comprises 400×400 points on a doubly periodic domain with a resolution of 250 m, which should explicitly resolve deep moist convection (Bryan et al., 2003; Petch et al., 2002), giving a total size of approximately 100×100 km^2. This should be large enough to allow organization of convection (Tompkins, 2001). It should be recalled that, on an icosahedral grid, the resolution can be formulated with different metrics: throughout this chapter I will always refer to the distance between triangle edges. Rotation is not considered in the model since the Coriolis term f is set to 0. In the vertical 150 levels are adopted: the spacing varies from 10 meters in the lowermost layer to approximately 400 meters at the model top situated by 21 km. In the uppermost 20 atmospheric levels a sponge layer (Klemp et al., 2008) prevents upward-propagating gravity waves to be reflected.

Soil model specific
configuration

As in the operational set-up of ICON, the soil column is discretized in 8 soil layers (see section 2.2.2). The soil temperature of the climatological layer amounts to 281 K, whereas the soil type is set to loam. This corresponds to the most common soil type used in ICON over mid-latitude areas (e.g. Germany). Table A.1 summarizes the parameters used by TERRA-ML for the chosen soil type.

To obtain a spread of surface fluxes large enough to see a significant atmospheric response, soil moisture is varied starting from the saturation value (this corresponds to the pore volume w_{pv} in Tab. A.1) all the way down to a condition of a dry soil but still over the wilting point. The soil moisture values considered are 100%, 80%, 70%, 60%, 50% and 40% of the saturation value, respectively. For the sake of simplicity they are set homogeneous over the whole soil column.

The soil temperature profile is prescribed by linearly interpolating the near-surface temperature from the lowermost atmospheric level to the climatological value of 281 K. Given the consideration of a single diurnal cycle, the values of soil moisture and temperature in deeper soil layers shouldn't affect appreciably the surface latent heat fluxes. As a comparison Findell and Eltahir (2003b) also used a vertically constant soil moisture but their values were 100% and 20% with respect to saturation.

Name	Date	# simulations	Soil moisture	Description
			Basic configuration	
WA	3/07/1999	6	100%,80%,70%,...	Wet soil advantage
DA	23/07/1999	6	...60%,50%,40% saturation	Dry soil advantage
			Perturbed experiments	
DA_transp	23/07/1999	3		Transparent clouds
DA_subs	23/07/1999	3		Induced subsidence
DA_asce	23/07/1999	3		Induced ascent
DA_wind	23/07/1999	3		Non-zero winds
DA_plants	23/07/1999	3	100, 70, 40% saturation	With plants
WA_plants	23/07/1999	3		With plants
WA2	6/07/1999	3		Additional Wet soil adv.
WA2_plants	6/07/1999	3		With plants
DA2	10/06/1999	3		Additional Dry soil adv.
DA2_plants	10/06/1999	3		With plants

Table 3.1: Experiments description. In the text the following notation is adopted to refer to a specific experiment: SOUNDING_CASE_MOISTURE, e.g. WA_100 represents the simulation run with the wet soil advantage sounding (3 July 1999) and a fully saturated soil, while DA_wind_40 refers to the simulation run with the dry soil advantage sounding (23 July 1999) considering the presence of winds with a soil moisture of 40% of the saturation value.

3.2.2 *Perturbed experiments*

A series of additional experiments (see Table 3.1) are performed to test specific controls on the soil moisture-precipitation coupling. To save computing time and given the observed quasi-monotonic response of precipitation to soil moisture in DA and WA, only soil moisture values of 100%, 70% and 40% of the saturation value are considered. For most of these experiments the DA sounding was used exclusively in order to see whether drier soils could produce more precipitation than wetter soils.

First, it should be noted that, given the HI_{low} threshold of 10°C proposed by Findell and Eltahir (2003b) to distinguish between the wet and dry soil advantage, the WA sounding, with a computed HI_{low} of 10.9°C, may not be viewed as the best case study. For this reason, and in order to have a larger data sample, two additional early morning soundings are selected from the same period. The two retained dates are 6 July and 10 June 1999 and the respective profiles are shown in Figure 3.1. For these atmospheric states the following values of CTP-HI_{low} are obtained: (38 J kg^{-1}, 7° C) and (223 J kg^{-1}, 15° C), respectively. Considering the thresholds proposed by Findell and Eltahir (2003b) these cases better fall into the different hypothesized regions of the coupling behavior, with 6 July falling into the wet soil advantage and 10 June in the dry soil advantage. The two simulations are called WA2 and DA2, respectively.

Additional soundings

Second, the impact of Cloud Radiative Effects (CREs) on the coupling is explored. By inspecting the surface radiative balance in model simulations over Europe, Schär et al. (1999) found that the reduction of incoming short-wave radiation due to cloud shading is overcompensated by an increase in long-wave radiation. This consequently supports higher surface fluxes over wet soils in cloudier conditions than over dry soils in sunnier conditions. The latter response further emphasizes a positive soil moisture-precipitation feedback. However, from observations, a decrease of the net radiation by cloud radiative effect is generally expected. To quantify the potential amplification or dampening of the response of precipitation to an initial change in soil moisture by CREs, simulations are performed starting from the DA sounding and using a modified version of ICON-LEM, where liquid and ice clouds are set transparent to the radiation both in the short- and long-wave. These simulations are called DA_transp. Making clouds transparent to radiation has been successfully used in several studies (see e.g. Stevens, Bony, et al., 2012; Fermepin and Bony, 2014) to isolate the impacts of CREs on the dynamic of convection.

Cloud Radiative Effects

Third, the impact of large-scale forcing is considered. The presence of subsidence favors the development of an inversion layer at the top of the PBL which could eventually suppress deep convection formation. In this regime, only a strong enough sensible heat flux that can break

Large-scale forcing

through the inversion may promote the development of deep convection, thus possibly leading to more precipitation over drier soils. The effect of large-scale forcing is mimicked by prescribing a large-scale subsidence velocity w_{LS} that acts on the tendency equations of momentum, temperature and moisture (Randall and Cripe, 1999). The subsidence velocity in the perturbed experiments `DA_subs` is specified following the Rain In Cumulus over the Ocean (RICO) setup (VanZanten et al., 2011):

$$
w_{LS} = \begin{cases}
w_s^0 \cdot z & \text{for } z < 1 \text{ km} \\
w_s^0 & \text{for } 1 \text{ km} < z < 3 \text{ km} \\
w_s^0 \cdot (4 - z) & \text{for } 3 \text{ km} < z < 4 \text{ km} \\
0 & \text{for } z > 4 \text{ km}
\end{cases}
\tag{3.1}
$$

with $w_s^0 = -0.005$ m s^{-1}. This choice produces a constant subsidence velocity $w_{LS} = w_s^0$ between 1 and 3 km, that linearly decreases to 0 outside of this layer. Moreover, an additional set of simulations with a forced ascent, called `DA_asce`, is carried out where w_{LS} is simply set equal to a constant value of 0.005 m s^{-1} over the whole atmospheric column. Forced ascent can be thought as representing an additional buoyancy source for the parcel, associated e.g. to frontal induced lift. The reason behind not using a vertically constant subsidence velocity in `DA_subs` is due to the fact that early test simulations showed that convection was strongly suppressed in such simulations, making a reliable estimation of the coupling practically impossible.

Impact of winds   Fourth, the impact of winds on the soil moisture-precipitation coupling is investigated in a set of simulations called `DA_wind`. A follow-up study by Findell and Eltahir (2003a) on their original work already indicated that winds strongly influence the coupling. Strong low-level wind shear can suppress the convective potential, making it harder to rain regardless of the surface state, while vertically veering winds with small low-level shears may provide more buoyancy and enhance convection. Moreover, wind shear can promote the organization of convection through interaction with cold pools (Rotunno et al., 1988; Schlemmer and Hohenegger, 2014). Organized convection may be less dependent on surface fluxes as the convective evolution becomes dictated by the cold pools evolution. In the case `DA_wind` the simulations are initialized with the wind field measured by the balloon sounding. Note that winds are only prescribed in the initial condition and freely evolve during the day in every atmospheric level.

Plants   Finally, the dependency of the results on the specification of the land surface is investigated by fully covering the soil with plants in cases `WA_plants`, `DA_plants`, `WA2_plants` and `DA2_plants`. The land cover class is set to a mosaic of cropland (50-70%) and vegetation (20-50%) with a maximum leaf area index of 3, a minimum stomatal resistance

of 160 s m^{-1} and a root depth of 0.5 m (these parameters are taken from the COSMO model). Surface roughness length is increased from 0.1 m to 0.25 m. Within this setup, the only contribution to surface latent heat flux comes from the transpiration term, given that bare soil is fully covered by plant leaves. For the exact formulations of the different parametrizations adopted with plants (e.g. canopy resistance) the reader is referred to Doms et al. (2011).

3.3 RESULTS OF THE BASIC CONFIGURATION

3.3.1 *Surface energy balance*

Changes in soil moisture directly affect the partitioning of the incoming solar radiation into latent and sensible surface heat fluxes, as expected. Figure 3.2 highlights the decrease of surface latent heat fluxes from a maximum of about 0.8 mm h^{-1} in the wettest soil case (DA_100) to a nearly constant null value in the case with the driest soil (DA_40). Conversely, the surface sensible heat flux is inversely related to soil moisture and its diurnal maximum increases from an initial value of about 0.2 mm h^{-1} (DA_100) to a final value of almost 0.6 mm h^{-1} (DA_40). As a consequence, most of the incoming solar radiation in the DA_40 case is used to heat up the surface, which reaches a maximum temperature of 52° C, and to heat up the air above the surface, which reaches a maximum temperature of 37° C. Instead, in DA_100 the surface reaches a maximum temperature of about 37° and the lowermost atmospheric layer heats up to 31° C in the early afternoon. Comparison of Fig. 3.2 (a) and (b) also clearly highlights the effect of a soil moisture that begins to limit the evaporation when starting from drier initial soil moisture conditions. Up to 11 LST, DA_100 and DA_70 exhibit similar fluxes, but afterward the latent heat flux levels out in DA_70 and slightly decreases until the end of the day. The different temporal evolutions of net surface radiation visible in Fig. 3.2 during the afternoon hours reflect the different evolution of convection among the cases. In particular, the reduction of net surface radiation is due to cloud shading which changes accordingly to the different evolution of convective clouds.

Bowen ratio values averaged between 12 and 15 LST vary from 0.23 in the saturated case, 0.63 in the DA_70 case, 3.08 in the DA_60 case to 118.36 in the driest case. Therefore the employed bare soil evaporation scheme produces near null values when soil moisture approaches the wilting point. The almost complete shut-down of the latent heat flux in the DA_40 case may appear exaggerated but is observed over semi-arid regions (e.g. Couvreux et al., 2012), which should be comparable to my bare-soil setup. The reason for this behavior is that the bare soil evaporation scheme adopted in TERRA-ML was adapted from the former generation of two-layers soil mod-

Underestimation of evaporation over dry soils
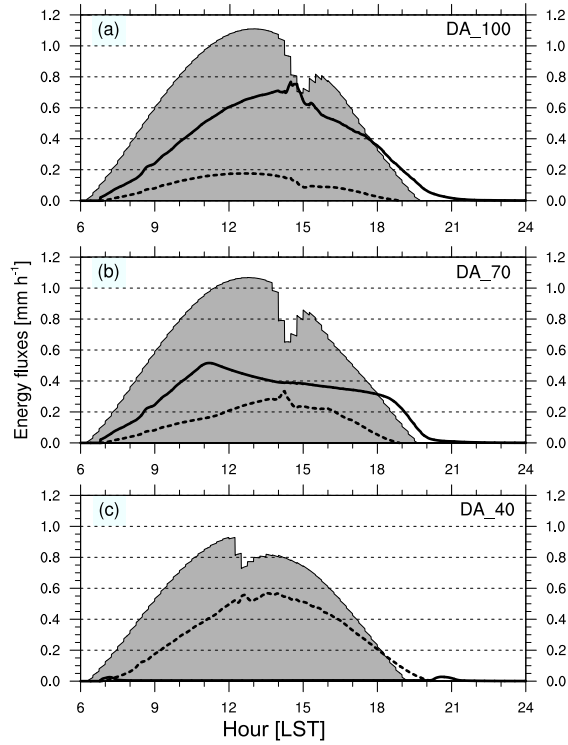
Figure 3.2: Time series [LST] of domain averaged surface latent heat flux (thick black line), sensible heat flux (thick black dashed line) and net radiation at the surface (grey shading) for the DA case and different soil moisture states: (a) `DA_100`, (b) `DA_70` and (c) `DA_40`. Latent and sensible heat fluxes are taken as positive away from the surface.

els and is not tuned for setups characterized by many soil layers. As stated by Schulz et al. (2016), this scheme systematically over-estimates (underestimates) evaporation under wet (dry) conditions, giving a wider variation of surface fluxes compared to observed ones. This is not of a concern for this study as the important quantity determining the precipitation response is the latent heat flux, not the soil moisture, as it will be shown in section 3.3.3. Moreover, a larger variation in surface fluxes allows for a larger and hence more robust precipitation response.

3.3.2 *Convection and precipitation*

Figure 3.3 shows the evolution of the diurnal cycle of convection in both WA and DA cases, for two different values of the soil moisture as an example. All the simulations show a reasonable evolution of convection over time: clouds first appear in the late morning/early afternoon and dissipate in the late afternoon or even during the evening. After the growth of the first clouds in the late morning, rain is produced in less than one hour, followed by a further vertical extension of the cloud tops which reach their maximum extent a few hours
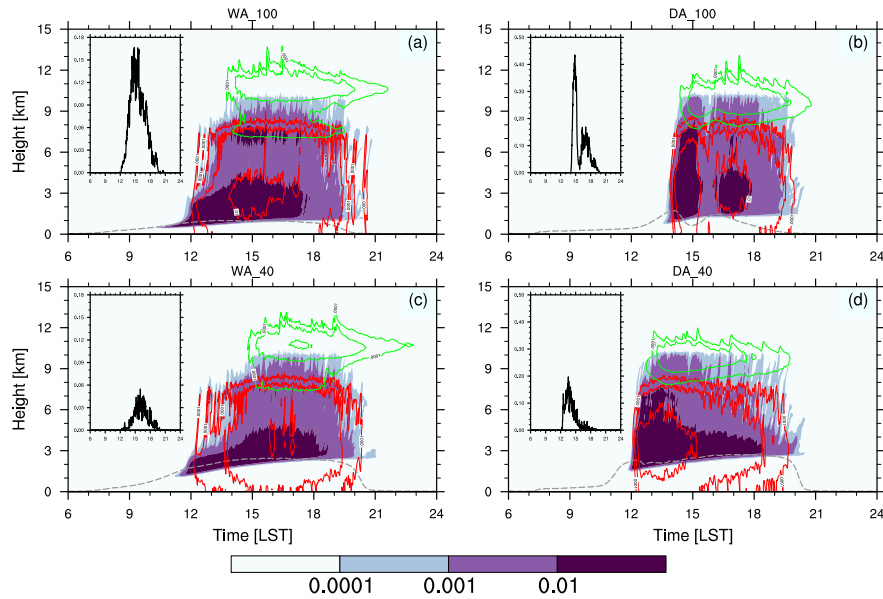
Figure 3.3: Profiles of domain averaged quantities as functions of time for (a,c) the `WA` and (b,d) `DA` cases and two soil moisture states. Color shading represents the cloud water mixing ratio [g kg^{-1}], while cloud ice and rain mixing ratios are plotted by the green and red contour, respectively (same units and contour levels as cloud water): note the logarithmic scale. The height of the PBL is shown by the gray dashed line [km]. It is computed using the bulk Richardson number approach (Seibert et al., 2000, and references therein). The vertical axis represents the height from the surface [km], while the horizontal axis indicates the time of the simulation [LST]. In the insets surface precipitation rate [mm h^{-1}] is plotted as a function of time [LST]. Note that the same extents for the *y*-axis are used in (a,c) and (b,d), respectively.

later: at this time ice is produced at the top and lasts until the late evening. The mean cloud thickness reaches lower values over drier soils, as found in Schlemmer, Hohenegger, et al. (2012), because of the higher LCL due to the decreased latent heat flux, while the cloud top remains unchanged. It can also be noticed that strong precipitation, as in `DA_100`, leads to a collapse of the PBL around 15 LST. The simulated small magnitude of the precipitation rate (upper left inset in Fig. 3.3) reflects the limited spatial extension of the precipitating area, which covers at best 10-15% of the domain. The values are in the order of magnitude of other LES studies that have investigated processes leading to the development of convection over mid-latitude regions (e.g. Schlemmer, Hohenegger, et al., 2012).

More importantly, Fig. 3.3 reveals variations of convective precipitation as a function of soil moisture. Both the precipitation rates and the timing of convection respond to the changes in soil moisture, and hence surface fluxes. In order to better organize the results obtained for the cases presented in Table 3.1, domain-averaged accumulated precipitation and time of convection triggering are computed and shown in Fig. 3.4. The triggering of convection [LST] is defined by

Convection triggering and precipitation

the first time instant when domain-averaged cloud cover exceeds 0.1. Convection is triggered 2 hours earlier over the driest soil in the DA
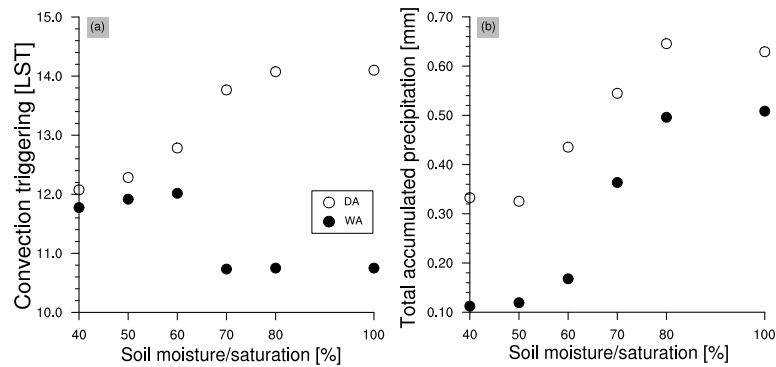
Figure 3.4: (a) Time of convection triggering [LST], computed as the simulation time step when domain-averaged cloud cover exceeds a user-defined threshold of 0.1 and (b) total domain-averaged accumulated precipitation as a function of soil moisture scaled by the saturation value [%] for the DA and WA cases.

case, whereas being lagged in the WA case (Fig. 3.4, a). The earlier triggering over dry soils in DA in contrast to WA can also be recognized in the precipitation rate time series of Fig. 3.3. These findings are in agreement with the results obtained by Findell and Eltahir (2003b) with their 1-D model.

The earlier triggering over dry soils in DA is due to the fact that the growth of the PBL through induced surface sensible heat fluxes is more efficient than moistening to trigger convection. In the WA case, in contrast, the lowering of LFC, due to surface moistening through latent heat fluxes, is the energetically most efficient mechanism, giving an earlier triggering over wet soils. However, in terms of precipitation (Fig. 3.4, b), both cases show a decrease over dry soils. From Fig. 3.4 (b) it can also be noted that above a degree of saturation of 80% and below a degree of saturation of 50%, the accumulated precipitation does not exhibit any dependency on soil moisture, most likely because of similar latent heat flux and triggering. This hypothesis will be explored in section 3.3.3.

Wetter soils become drier, drier soils stay dry

It should be noted that the relatively small amounts of precipitation do not allow the soil to recover from the losses caused by evaporation. In the DA_100 case, at the end of the simulated diurnal cycle, the uppermost layer soil moisture reaches about 65% of its initial value, while in the DA_70 case it reaches almost 90%. This results from the fact that in DA_100 the saturated soil instantaneously produces runoff that brings the soil moisture to the field capacity (see Tab. A.1), a model constraint, while in the other case soil moisture is lost only because of evaporation (see Chapter 2). Interestingly enough, in the DA_40 case, the absence of evaporation allows a slight increase of soil moisture of about 1% of its initial value due to the recorded precipitation. Thus, in the simulations, wetter soils generally become drier

while drier soils maintain their moisture reservoir and the change in soil moisture over one day does not reflect the precipitation changes across the simulations. To avoid confusion between the soil moisture and the precipitation response, I will not refer to a negative soil moisture-precipitation coupling in the following but rather to a dry soil advantage when more precipitation is observed to fall over initially drier soils.

The properties of the convective diurnal cycle are further analyzed through the computation of CAPE and of cloud water and rain distribution. Figure 3.5 shows the time series of domain-averaged CAPE for both the WA and DA cases. It can be inferred that, regardless of the

Evolution of CAPE
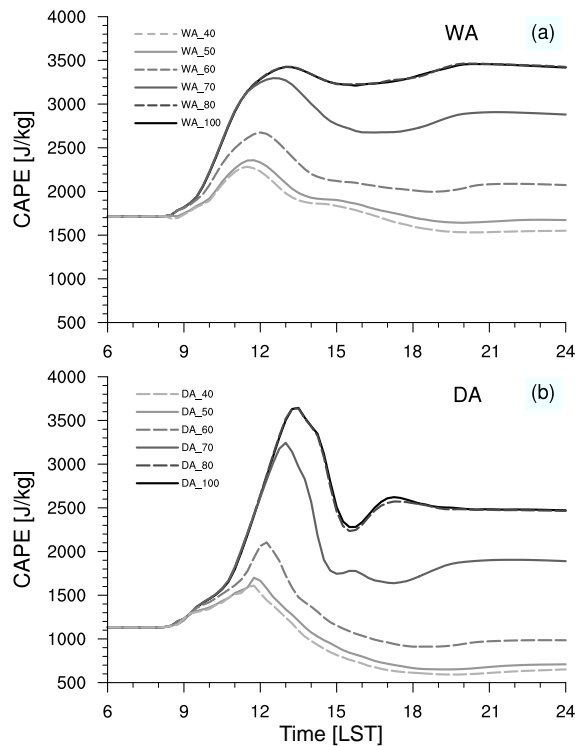
Figure 3.5: Time series [LST] of domain-averaged CAPE [J/kg] for the (a) WA and (b) DA cases and different soil moisture states.

initial sounding, the energy available to feed convection decreases with soil moisture. This large, more than 1000 J kg^{-1} difference at 13 LST between 100% and 40% soil moisture saturation is linked to different profiles of temperature and relative humidity in the first 1.5 km of the atmosphere due to the different Bowen ratios of the two simulations. In particular, both warming and drying of the PBL, as found over dry soils, lead to a lower CAPE. This is consistent with the obtained decrease of precipitation rate (insets of Fig. 3.3) over drier soils, regardless of the initial sounding used. None of the simulations nevertheless fully deplete their CAPE reservoir, which makes this simple explanation questionable. Note that the decrease of CAPE over drier soils is consistent with what already found by Barthlott

and Kalthoff (2011) in more realistic simulations over south-western Germany.

Figure 3.5 further reveals that in the DA case CAPE exhibits a very strong peak in the early afternoon and is rapidly depleted. Over soils with a soil moisture above 60% of the saturation value, however, large latent heat fluxes provide enough energy to rebuild a second peak of CAPE in the late afternoon. This allows for a second development of convection. The presence of two convective events over wet soils that merge to one over dry soils is also clearly visible in Fig. 3.3 (b) and (d).

Redistribution of cloud water and rain   As an alternative to CAPE, Fig. 3.6 shows the full time and spatial average of cloud water mixing ratio $\langle q_c \rangle$ and rain mixing ratio $\langle q_r \rangle$ as functions of soil moisture. Note that snow and cloud ice are not considered, given that they appear to be only minor components. The
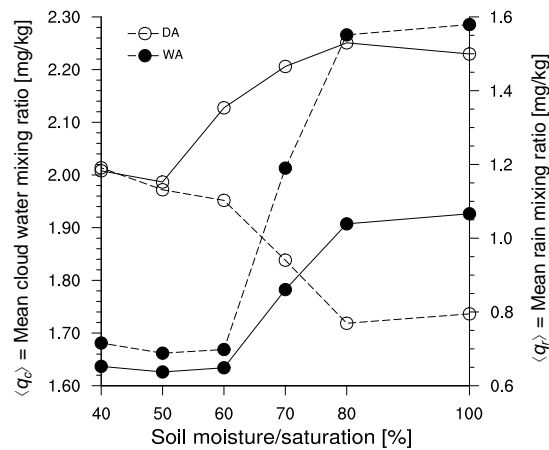
Figure 3.6: Space-averaged time-averaged cloud water mixing ratio $\langle q_c \rangle$ (dashed lines) and rain mixing ratio $\langle q_r \rangle$ (solid lines) for the DA (open circles) and WA (filled circles) case as a function of the degree of soil moisture saturation.

behavior of $\langle q_r \rangle$ is consistent with the behavior of the precipitation rate and shows a decrease towards drier soils irrespective of the initial atmospheric state. In contrast, the response of $\langle q_c \rangle$ depends on the initial sounding and does show an unexpected increase over dry soils in the DA case, which could point to different efficiencies in converting clouds to precipitation among the two soundings considered. An increase in $\langle q_c \rangle$ over dry soils may be caused either by a larger value of produced cloud water q_c or by the presence of longer-lived clouds. Larger values of produced q_c over drier soils seem unlikely, given the presence of a drier and warmer PBL regardless of the initial sounding. Longer-lived clouds may be created due to less evaporation of q_c or due to less conversion of q_c into q_r. Less evaporation of q_c over dry soils seems again unlikely, given the presence of a drier PBL. Hence, the only mechanism responsible for an increase of $\langle q_c \rangle$

over dry soils in the DA case must be linked to the efficiency in converting q_c into q_r. This appears as a reasonable hypothesis given what follows.

The diurnal evolution simulated in the DA case over wet soil consists of two distinct convective events which progressively merge into a single event over drier soils. The first event among the two shows larger precipitation rates and thicker clouds (see Fig. 3.3, b). The lagged triggering of convection over wet soils in DA, due to reduced sensible heat flux, causes an accumulation of energy that is released abruptly when clouds are formed (Fig. 3.5) and leads to a fast production of cloud water q_c. These local positive anomalies of cloud water are quickly converted into q_r, thus depleting the reservoir. This is mainly related to the fact that autoconversion processes and collection mechanisms in the microphysics depend nonlinearly on the amount of cloud water mixing ratio q_c (see Eqs. 5.107-5.112 in section 5.6 of Doms et al., 2011). Over dry soils the convection is less explosive so that the critical threshold is unlikely to be reached and thus q_c is only partially depleted. When examining the values attained by q_c in DA_40, it appears that this variable has a larger mean but a lower spatial absolute maximum. On the other hand, DA_100 contains the highest value of q_c, although having a lower mean. In this regard, the WA case is equivalent to DA over dry soils: the slow growth of clouds doesn't produce high peaks of cloud water mixing ratio for any of the initial soil moisture, and q_c follows the moisture input from the surface.

3.3.3 *Under which conditions may drier soils receive more precipitation?*

The results outlined in the previous section seem to suggest that, in terms of total accumulated precipitation, there is no dry soil advantage. If the soil moisture is reduced, the surface latent heat flux decreases and thus the moisture flux from the surface to the atmosphere is limited. The atmosphere is not able to compensate for this lack of moisture contribution by becoming more efficient at converting water vapor into precipitation, the prerequisite to obtaining more precipitation over drier soils. However, the previous section also showed that convection can indeed be triggered earlier over dry soils, which, under certain circumstances, may be able to overcompensate for the lack of moisture input.

To explore the feasibility of this scenario, the surface rain accumulated in time and spatially averaged, R, needs to be estimated a priori. Note that the terms rain and precipitation are used interchangeably as surface precipitation is always in liquid form. Moreover, the specifi-

Estimation of surface precipitation

cation *domain-averaged* is dropped given that every quantity is always averaged over the full domain area. R [mm] is computed as:

$$R = \sum_{i=1}^{N} \mathrm{RR}_i \cdot \Delta t = \sum_{i=1}^{N_1} \mathrm{RR}_i \cdot \Delta t + \sum_{i=1}^{N_0} 0 \cdot \Delta t = \sum_{i=1}^{N_1} \mathrm{RR}_i \cdot \Delta t \qquad (3.2)$$

that is, by summing the product of the instantaneous rain rate predicted by the model at the time step i, RR_i [mm h^{-1}], and the output time step, Δt [h], over the entire simulation. The output time step Δt is chosen small enough (30 seconds with a model time step of 2 seconds) to consider RR_i an instantaneous value. The total number of time steps N can be split into the number of rainy ($\mathrm{RR}_i > 0$ mm h^{-1}) events, N_1, and the number of time steps with no rain, N_0. By introducing a mean over rainy events $\widetilde{\mathrm{RR}} \equiv \frac{1}{N_1} \sum_{i=1}^{N_1} \mathrm{RR}_i$ Eq. (3.2) can be rewritten as

$$R = \sum_{i=1}^{N_1} \mathrm{RR}_i \cdot \Delta t = \widetilde{\mathrm{RR}} \cdot N_1 \cdot \Delta t \simeq \widetilde{\mathrm{RR}}(t_1 - t_0) \qquad (3.3)$$

where now t_0, t_1 indicate the time (hour, LST) when precipitation begins and ends, respectively. It should be noted that the only used approximation, i.e. $N_1 \cdot \Delta t \simeq (t_1 - t_0)$, holds for a typical precipitation intensity-time distribution over one diurnal cycle with no long temporal gap between precipitation events, which is indeed the case in the examples displayed in Fig. 3.3.

Finally, by assuming that $(t_1 - t_0)$ is approximately equal to the period when deep convective clouds are present on the domain, one can infer that R is related to three main parameters: the time when convection is triggered (t_0), which strongly depends on the atmospheric profile and exhibits either a wet or dry soil advantage in agreement with Findell and Eltahir (2003b), the time when convection dissipates (t_1) and finally the mean rainfall rate ($\widetilde{\mathrm{RR}}$).

Duration of precipitation

In Fig. 3.7 (a) the duration of precipitation ($t_1 - t_0$) is computed for all the WA and DA simulations directly using the value of N_1 from the simulation output. The duration shows an interesting V-shaped distribution in the DA case, with a central minimum by a soil saturation of 70 %, whereas such central minimum is absent in the WA case. While convection is triggered earlier over drier soils than over wetter ones in DA, clouds dissipate later on wetter soils (see Fig. 3.3). This gives a total response with a central minimum.

Precipitation and surface latent heat flux

Concerning the variation of $\widetilde{\mathrm{RR}}$ with soil moisture, it can be claimed that, based on the results of the previous section, $\widetilde{\mathrm{RR}}$ scales with $\widetilde{\mathrm{LH}}$, i.e. the latent heat flux averaged over the precipitation duration . This is confirmed by Fig. 3.7 (b), which shows the values of $\widetilde{\mathrm{RR}}$ and $\widetilde{\mathrm{LH}}$ computed using data from both WA and DA simulations. The two cases even exhibit a similar slope, but different offsets. The slope of this line may be interpreted as a precipitation efficiency which, given the absence of large-scale moisture advection, is equivalent to the recycling

Figure 3.7: (a) precipitation duration $t_1 - t_0$ as a function of the degree of soil moisture saturation; (b) scatter plot of $\widetilde{RR}$ vs. $\widetilde{LH}$: the equations represent the regression lines (slope and offset) together with the square of the Pearson correlation coefficient χ^2; (c) accumulated precipitation R estimated by exploiting the linear fit and the duration term (see text for details).

ratio. It again suggests that, at least to a first order, the two soundings are not associated with fundamentally different convective dynamics once convection is triggered. There is nevertheless a larger scatter among the points in the DA case than in the WA case as also revealed by smaller χ^2 values.

As a sanity check, Fig. 3.7 (c) uses the linear fit of Fig. 3.7 (b) to estimate $\widetilde{RR}$ and, combined with the diagnosed value of $t_1 - t_0$, to compute R. The resulting accumulated precipitation should be compared to the one diagnosed from the simulations in Fig. 3.4 (b). The relative errors of the different simulations range from about 2 to 20 % for the WA case and from 1 to 15 % for the DA case. The relative error averaged over all the simulation is about 10%. Although not perfect, the values predicted by this simple approximation resemble the simulated ones, and in particular the decrease of precipitation over dry soils is captured fairly well. I stress that the aim of this chapter is not to predict the accumulated precipitation with the smallest possible error but rather to reproduce the overall observed behavior.

A priori estimation of precipitation

The advantage of Eq. (3.3) is indeed that it splits the contribution of the total accumulated precipitation into two distinct terms, one favoring a wet soil advantage, and one favoring either a dry or a wet soil advantage. Thus, it is possible to infer which precipitation duration would be needed to offset the decrease in $\widetilde{RR}$ due to changes in latent heat flux. For instance, Fig. 3.7 (b) predicts that a decrease in latent heat flux from approximately 0.3 mm h^{-1} over wet soils to almost 0 mm h^{-1} over dry soils is accompanied by a halve of the rain rate. This means that, in order to have more rain over dry soils, the duration term in Eq. (3.2) needs to balance a factor of at least 2. In other words, more than 16 hours of continuous precipitation are needed to offset the lack of surface latent heat fluxes. This is unlikely to occur over one diurnal cycle.

Can drier soils receive more precipitation?

These considerations are generalized in Fig. 3.8. There, the values of the slope and of the offset obtained in the linear regressions in Fig. 3.7 (b) for the WA case are used to compute an estimated value of $\widetilde{RR}$ which is then used to obtain R. In order to do so we consider a wide variation of surface latent heat flux values (the x-axis of Fig. 3.8) and precipitation durations less than 24 hours (the y-axis of Fig. 3.8). The result is a discrete function $R(\widetilde{LH}, t_1 - t_0)$ which is shown by the color filled contour lines. The results of the WA case are represented by dots
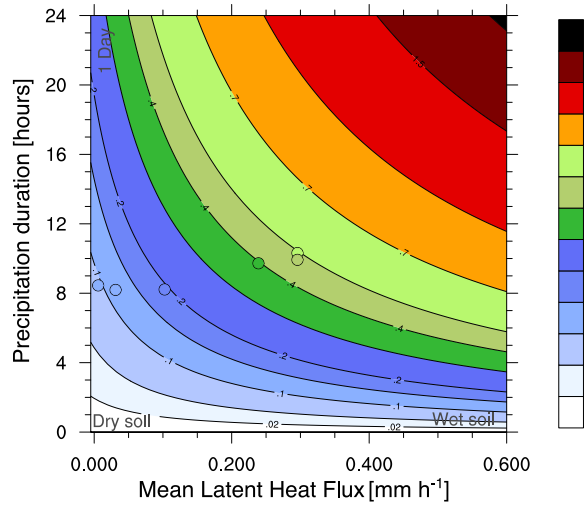
Figure 3.8: Contour plot showing the estimated accumulated precipitation R [shading, mm] as a function of $\widetilde{LH}$ [mm h^{-1}] and $t_1 - t_0$ [h] for the WA case. $\widetilde{RR}$ is computed by using the values of the slope and offset obtained in Fig. 3.7 (b) for the WA case: see the text for more details. Dots are placed on the plot using the values of $\widetilde{LH}$, $t_1 - t_0$ and R directly diagnosed from the WA experiment.

using the values of $(\widetilde{LH}, t_1 - t_0, R)$ obtained in every simulation. They reveal a good agreement with the theoretical estimates.

To compensate a change in latent heat flux one has to move along the isoline of accumulated precipitation in Fig. 3.8. Given the curvature of the isolines, only small changes in latent heat flux may be accommodated by changes in the duration, making the occurrence of more precipitation over drier soils unlikely. Moreover, the potential earlier triggering of convection over dry soils under certain atmospheric conditions, as in the DA case, is usually compensated by an equal shift of t_1, annihilating the triggering advantage. Hence it may be concluded that the only possibility to obtain more precipitation over drier soils consists in not triggering convection at all over wet soils, which, for the tested situations, never happened.

Although this scenario is unlikely to occur, according to the values used to construct Fig. 3.8 some environmental conditions could lead to a weakening of the coupling. In fact, the curvature of the isolines

in Fig. 3.8 depends on the slope and on the offset derived from the $\widetilde{\text{RR}}$-$\widetilde{\text{LH}}$ relationship. This is evident if rewriting Eq. 3.3 as:

$$R = m \ \widetilde{\text{LH}} \ (t_1 - t_0) + q \ (t_1 - t_0) \tag{3.4}$$

where m and q are the slope and offset of the linear fit associated with the $\widetilde{\text{RR}}$-$\widetilde{\text{LH}}$ relationship, respectively. While the slope may be interpreted as the atmospheric efficiency in converting water vapor to rain, the offset may be interpreted as the overall availability of precipitable water, which depends both on the atmospheric state and on external forcing. Given that changes in m are weighted by the values of $\widetilde{\text{LH}} \ll 1$, one can imagine that changes of the same magnitude in q are more likely to affect R. Increasing m while keeping q constant causes a steepening of the contour lines for small values of $\widetilde{\text{LH}}$ making it even more unlikely to get more rain over drier soils. On the other hand, if q becomes large enough the isolines become flatter even for small values of $\widetilde{\text{LH}}$ and the sensitivity of precipitation to latent heat flux is dampened. In order to get more rain over drier soil q should be large enough so that the m term becomes negligible, and $t_1 - t_0$ should be zero only over wet soils. This is shown using an additional figure in Appendix B. Another possibility would be to have a negative value of m. Since this does not seem to happen in the simulations presented up to now we further investigate how environmental conditions and external forcing could concur to a dry soil advantage in the next section.

3.4 SENSITIVITY EXPERIMENTS

3.4.1 *Additional cases*

An inspection of the temporal evolution of cloud water and precipitation (not shown), similar to the one presented in Fig. 3.3, reveals a noticeable resemblance between the WA-WA2 and DA-DA2 cases, respectively. In particular, the simulations initialized with the DA2 atmospheric profile exhibit again two distinctive convective events over wet soils, merging into one single long-lived convective event over dry soils below a soil moisture saturation of 60 %. The computation of $\langle q_c \rangle$ and $\langle q_r \rangle$ for the DA2 case (not shown) also confirms the presence of an increase of $\langle q_c \rangle$ and of a decrease of $\langle q_r \rangle$ over dry soils, as observed in DA. In DA2 convection is triggered earlier over dry soils, as in DA, whereas in WA2 convective clouds appear first over wet soils, as in WA. As a consequence, the duration of precipitation for the DA2 case shows again a central minimum, whereas in WA2 a monotonic decrease is observed (not shown). The total accumulated precipitation nevertheless again decreases over dry soils irrespective of the initial sounding and the $\widetilde{\text{RR}}$-$\widetilde{\text{LH}}$ linear relationship exhibits a comparable slope as in the DA and WA cases (Fig. 3.9). Due to the large spread ob-

served in the DA_2 case, the χ^2 value is smaller, while in the WA_2 case it reflects the one obtained in WA. The only difference worth noting
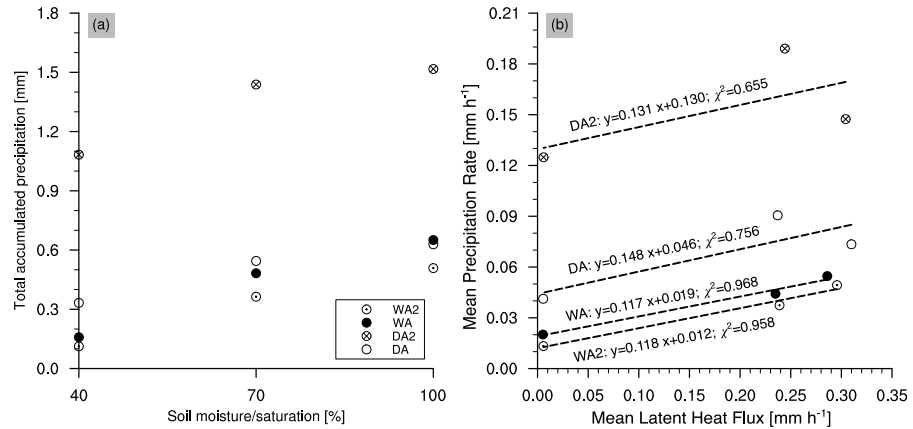
Figure 3.9: (a) Total domain-averaged accumulated precipitation and (b) Scatter plot of $\widetilde{RR}$ vs. $\widetilde{LH}$ for simulations with different soil moisture and the DA, DA2, WA and WA2 cases. The equations give the regression lines (slope and offset) together with the square of the Pearson correlation coefficient χ^2.

consists of the larger amount of accumulated precipitation observed in the DA2 case, which reflects the larger offset of the line in Fig. 3.9 (b), due to enhanced instability. The latter case is an example of a weaker coupling of soil moisture and precipitation due to a larger offset in the $\widetilde{LH}$-$\widetilde{RR}$ relationship (see the additional figure in Appendix B and the final part of section 3.3.3). Nevertheless, the larger offset cannot reverse the relationship and lead to more precipitation over drier soils.

3.4.2 *Transparent clouds*

Making clouds transparent do not change the overall wet soil advantage (Fig. 3.10, a) but the increase in the total accumulated precipitation with soil moisture is larger than in the DA case where CREs are included. This difference is linked to a larger sensitivity of the mean rain rate $\widetilde{RR}$ to the mean latent heat flux $\widetilde{LH}$ (see Fig. 3.10, b). In order to explain this larger sensitivity one can note that the surface energy balance is modified in DA_transp by the lack of CREs. The reduction of the net surface radiation seen in Fig. 3.2 between 13 LST and 16 LST in the DA_100 case, for instance, is absent when clouds are set transparent to radiation. The resulting increase of incoming short-wave radiation at the surface, in the order of 200 W m^{-2} in DA_transp compared to DA, is able to offset the opposing increase of surface outgoing long-wave radiative flux of about 30 W m^{-2}. This surplus of radiative energy in DA_transp causes a slight increase of surface latent heat flux over wet soils because the simulation lies in an energy-limited regime due to the abundance of soil moisture, and a slight increase of surface sensible heat fluxes over dry soils, as the
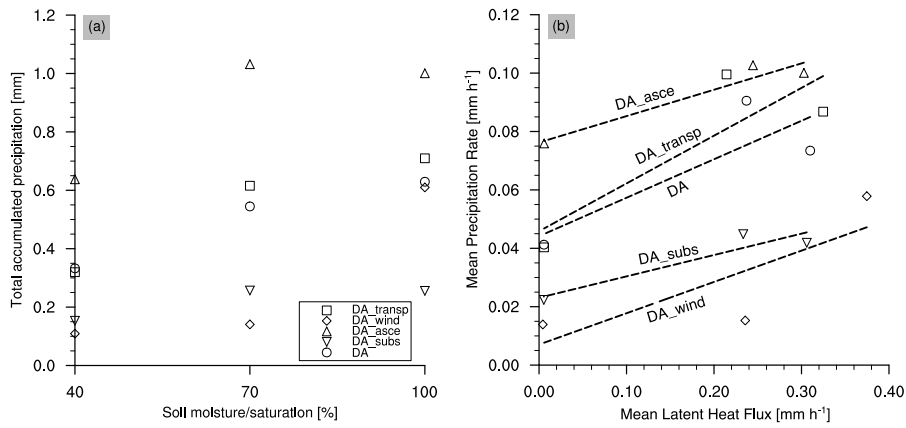
Figure 3.10: As in Fig. 3.9 but for the experiments DA_subs, DA_asce, DA_wind, DA_transp. The DA case is also included for the sake of comparison.

simulation belongs here to the soil moisture-limited regime. The magnitude of the soil moisture-precipitation coupling is enhanced. Hence clouds act to dampen the soil moisture-precipitation coupling but cannot reverse its sign. These findings contrast with the results of Schär et al. (1999) where the presence of clouds further amplified the feedback due to the long-wave CRE being stronger than the short-wave one. One reason for this discrepancy could be related to the fact that convective cloud features, including their interaction with radiation, are parametrized in the Regional Climate Model (RCM) employed by Schär et al. (1999). Another reason could be a distinct distribution of low and high clouds between the two studies.

3.4.3 *Large-scale forcing*

Figure 3.10 (a) highlights a decrease of total accumulated precipitation over dry soils in DA_subs and DA_asce, thus confirming the presence of a wet soil advantage in both cases. However, with subsidence, the convection is so heavily suppressed that the difference between the wettest soil and the driest soil in terms of precipitation is small. This is the result of two main factors. First, a smaller slope in the relationship between $\widetilde{RR}$ and $\widetilde{LH}$ (Fig. 3.10, b), which is reasonable as convection is more strongly forced and less dependent upon the surface state. Second, the convection remains triggered earlier over dry soils as sensible heating is more efficient to break the inversion. Regarding DA_asce, even though the $\widetilde{RR}$-$\widetilde{LH}$ relationship exhibits a similar slope as in DA_subs, the duration term shows a different behavior, with a triggering time almost constant regardless of the soil moisture value (not shown). Introducing ascent forces the air to rise and to reach its LFC without having to rely too heavily on moistening or heating of the PBL through surface fluxes. The offset of the $\widetilde{RR}$-$\widetilde{LH}$ relationship is also modified in both the DA_subs and DA_asce cases

compared to DA and reflects the additional source of buoyancy (more precipitation, larger offset when compared to DA) and the suppression of convection (less precipitation, smaller offset when compared to DA). These various differences are nevertheless not sufficient to alter the coupling sign. In both cases the points in Fig. 3.10 (b) show no considerable spread, which is reflected in values of χ^2 higher than 0.9.

3.4.4 *Winds*

The inclusion of winds leads to a different evolution of the atmospheric state over time. Figure 3.11 shows a comparison of the vertically integrated cloud water and rain mixing ratios, and of the virtual potential temperature perturbation in the lowermost atmospheric level, for the DA and DA_wind simulations. The DA case does not show
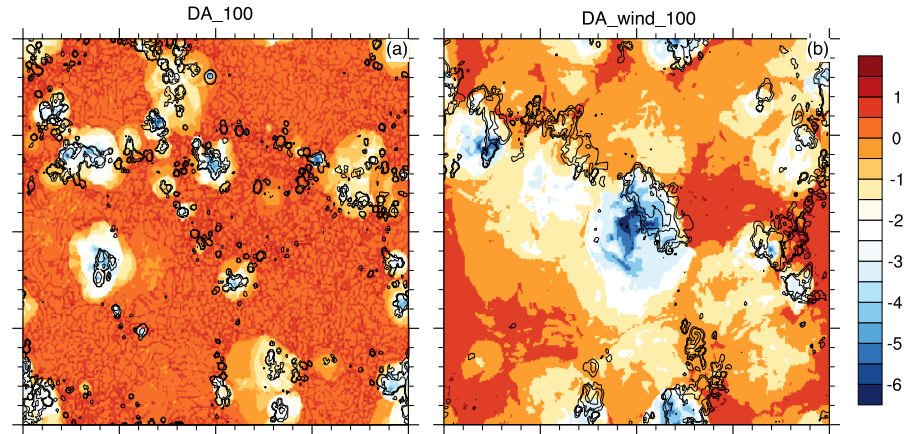
Figure 3.11: Spatial distribution of clouds and cold pools in (a) DA_100 and (b) DA_wind_100. Color shading shows the near-surface (20 meters) virtual potential temperature θ_v spatial anomaly [K], computed as deviation from the domain horizontal mean. Black contours show the vertically integrated sum of cloud water mixing ratio (q_c) and rain mixing ratio (q_r): lines from 0.0001 to 0.01 every 0.005 [kg kg^{-1}]. Both snapshots refer to 1730 LST.

an appreciable degree of organization since only scattered convection is simulated, probably because of the absence of wind shear and of the homogeneous surface state (Chen and Avissar, 1994). In contrast, the DA_wind simulation shows stronger and larger cold pools, as well as bigger clouds which tend to be organized along lines. Given that the strength of the cold pools is larger in DA_wind than in DA one can argue that this case is indeed more organized, also considering the importance of cold pools on convective organization (Tompkins, 2001). Although only qualitative, the differences between DA and DA_wind observed in Fig. 3.11 are reminiscent of the differences obtained in Schlemmer and Hohenegger (2014) between simulations with and without wind shear (see their Fig. 5).

Despite these differences in the spatial organization of convection, the coupling sign is not altered in this set of simulations . The `DA_wind` case still shows a decrease of total accumulated precipitation with soil moisture (see Fig. 3.10). The presence of stronger winds increases the surface latent heat flux for a given value of soil moisture, as expected because of the drag-law formulation, but decreases the precipitation rate for a given latent heat flux. This decrease in precipitation rate may be related to the CAPE, which is always smaller when compared to the `DA` simulation. The presence of winds already at the beginning of the simulation induces more mixing and prevents an efficient build-up of instability, which would lead to an abrupt release of energy and ensuing higher precipitation rates (as already observed in section 3.3). This results in a weaker dependency of $\widetilde{RR}$ on $\widetilde{LH}$ and, given similar changes in duration with soil moisture as in `DA`, leads to a weaker variation of total accumulated precipitation across the experiments. The weakening of the soil moisture-precipitation coupling in presence of winds is consistent with Findell and Eltahir (2003a) and with the idea that stronger cold pools in `DA_wind` more strongly determine the precipitation rate evolution, making `DA_wind` less dependent on the surface state.

Weakening of the coupling with winds

3.4.5 Plants

Whereas the water reservoir used by the evaporation from bare soil is limited to the uppermost soil layer, plants are able to extract moisture from deeper soil layers, thus contributing to larger values of surface latent heat flux over dry soils when compared to the bare soil case. An inspection of the surface fluxes time series (not shown) confirms that, even in the `DA_plants_40` case, latent heat flux reaches a maximum of 0.7 mm h^{-1}. Moreover, the presence of a deeper soil reservoir reduces the sensitivity of the latent heat flux to soil moisture, as can be recognized by comparing the variations in latent heat flux in Fig. 3.12 (c) with the ones in Fig. 3.7 (b).

Given the larger value of latent heat flux, larger precipitation rates are recorded for a given soil moisture in the `_plants` simulations as compared to the control simulations (compare Fig. 3.12, a and 3.9, a). More importantly, also in these experiments, total accumulated precipitation decreases over dry soils for all of the four considered atmospheric profiles. Splitting up the response in the contribution from duration and $\widetilde{RR}$ nevertheless shows a more subtle behavior. First, in `WA_plants`, `WA2_plants` and `DA_plants` there is almost no sensitivity of $\widetilde{RR}$ to $\widetilde{LH}$, i.e. the slopes of the regression lines are one-tenth of the ones observed in the bare soil cases. Second, the `DA2_plants` exhibits a negative slope. These differences to the bare soil case are partly an artifact in the sense that, due to their high latent heat flux, the cases with plants fall into the rightmost part ($\widetilde{LH} > 0.3$ mm h^{-1}) of Fig.
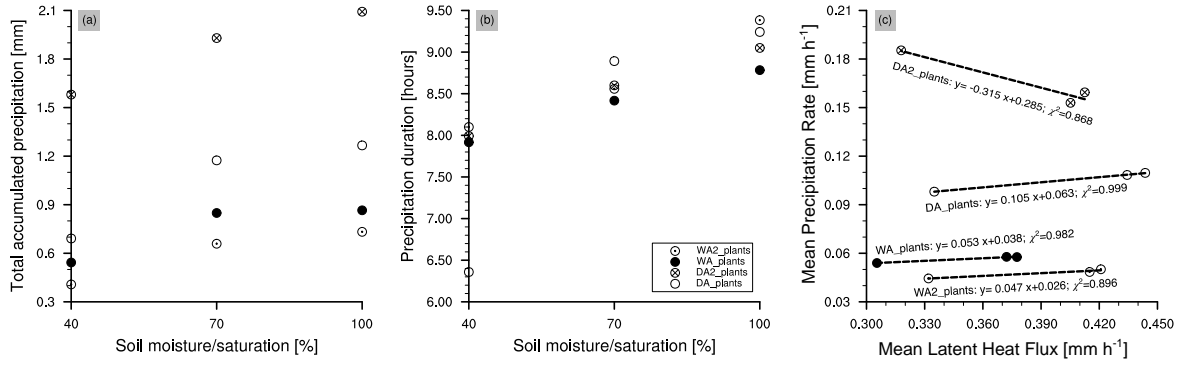
Figure 3.12: (a) Total domain-averaged accumulated precipitation (b) Precipitation duration and (c) Scatter plot of $\widetilde{RR}$ vs. $\widetilde{LH}$ for simulations `WA_plants`, `DA_plants`, `WA2_plants`, `DA2_plants`. The equations represent the regression lines (slope and offset) together with the square of the Pearson correlation coefficient χ^2.

3.7 (a), where a strong scaling of $\widetilde{RR}$ with $\widetilde{LH}$ is also not observed in the bare soil case. This is also equivalent to the right part of Fig. 3.8 where the isolines become flat. The smaller spread of the points in Fig. 3.12 (c), which results in values of χ^2 close to 1, is probably due to this weaker dependency of $\widetilde{RR}$ to $\widetilde{LH}$.

3.5 SUMMARY

The goal of this chapter was to determine under which conditions drier soils may produce more precipitation than wetter ones. To that aim several idealized experiments mimicking the full diurnal cycle of convection were performed with ICON-LEM and TERRA-ML starting from different spatially homogeneous soil moisture conditions.

It has been shown that the modeling framework is able to reproduce the expected sensitivity of the surface fluxes to soil moisture and to simulate the typical convective evolution over one diurnal cycle. The triggering of convection happens earlier over dry soils than over wet soils for the dry soil advantage case and vice versa for the wet soil advantage case. This stands in agreement with the results of Findell and Eltahir (2003b) and confirms that certain atmospheric conditions may be preconditioned to different mechanisms of convection triggering. The cloud water content also shows a similar behavior with larger values over dry soil in the dry soil advantage case but larger values over wet soils in the wet soil advantage case. However, the precipitation is found to always decrease with decreasing soil moisture, irrespective of the initial sounding. This indicates the presence of a wet soil advantage. These different sensitivities of cloud water and precipitation to soil moisture can be explained by the way convective instability is exploited depending on the atmospheric state.

To understand these results and to infer under which conditions drier

soils may receive more precipitation than wetter ones I propose a sim-ple conceptual model based on a linear fit to disentangle the effects of the surface on the precipitation amounts. The total domain-averaged accumulated precipitation is split into two main contributions: the value of precipitation rate averaged over the time when precipitation is occurring, and the duration of precipitation. While the latter de-pends upon the time of triggering and can exhibit a dry soil advan-tage, the precipitation rate is found to closely follow the values of the surface latent heat flux and thus always exhibits a wet soil advan-tage.

The relationship between precipitation rate and surface latent heat flux (Eq. 3.4) is linear and, surprisingly enough, the slope of this linear relationship doesn't change appreciably with different atmo-spheric states. Using this simple linear relationship and combining it with a range of duration indicates that in this idealized set-up a larger amount of precipitation is unlikely to be observed over drier soils. The relationship predicts that a halve of latent heat flux, as ob-tained over soils with a 40% soil moisture saturation, must be offset by a doubling of precipitation duration. This is unlikely to occur over one diurnal cycle.

The effects of other factors on the coupling of soil moisture and pre-cipitation, namely CREs, large-scale forcing, winds and plants are in-vestigated by conducting further sensitivity experiments. All the ex-periments support a wet soil advantage. The strength of the coupling is reduced when large-scale effects or winds are included as the evo-lution of convection becomes more dictated by the large-scale forcing or the organization of convection by cold pools than by the surface state. The occurrence of clouds also leads to a weakening of the cou-pling due to their short-wave effects that overcompensate long-wave changes and reduce the surface energy input. These results differ from other studies that employed models with parametrized convec-tion, e.g. Schär et al. (1999). Finally, plants also reduce the sensitivity of convection to the tested soil moisture through a much weaker de-pendency of latent heat flux on soil moisture.

A SIMPLIFIED CONCEPTUAL MODEL OF PRECIPITATION ENHANCEMENT OVER A HETEROGENEOUS SURFACE

4.1 INTRODUCTION

In Chapter 3 it has been shown that, over a homogeneous surface, precipitation is expected to increase with surface evaporation, and thus with soil moisture in a soil moisture-limited regime (Manabe, 1969; Budyko, 1974), regardless of the atmospheric state, as long as convection can be triggered on both dry or wet surfaces. However the real world is far from being homogeneous. The presence of heterogeneities in soil moisture induces thermally-driven mesoscale circulations (Segal and Arritt, 1992) which transport moist air from spatially wetter patches to spatially drier patches, acting against the initial perturbation of soil moisture, and which can then affect the distribution of precipitation. These circulations are comparable, in terms of dynamical features, to land-sea breezes (Crosman and Horel, 2010).

Many idealized studies have investigated the effect of such circulations on convection and ensuing precipitation. Avissar and Liu (1996) found that the land-surface wetness heterogeneity (i.e. spatial gradients of soil moisture) controls the transition from a randomly scattered state of convection to a more organized one where clouds form ahead of the front associated with the mesoscale circulation. The presence of such circulations also tend to enhance the precipitation amount. Further analyses have shown that this basic response can be modified by many environmental factors.

Features affecting the distribution of precipitation over a heterogeneous surface

Yan and Anthes (1988) found that accumulated precipitation is maximized over spatially dry patches when the patch length is comparable to the local Rossby radius of deformation ($\sim$ 100 km in mid-latitudes), a result that was later confirmed by Chen and Avissar (1994) and Lynn et al. (1998). Robinson, Sherwood, et al. (2008) proposed an alternative explanation by which the effect of surface hot spots is maximized for wavelength of roughly 50 km, that is when the aspect ratio of the applied heating matches the ratio of vertical and horizontal wavenumbers demanded by the dispersion relation for buoyancy (gravity) waves.

Froidevaux et al. (2014) explored the interaction between horizontal soil moisture heterogeneities, wind and precipitation. They found that, only when winds are too weak to control the propagation of thunderstorms, more precipitation is observed over drier surfaces. Finally, the response of precipitation also depends upon the back-

ground atmospheric profile. Chen and Avissar ([1994](#)) found that the presence of a moist atmospheric profile over a spatially drier surface reduces the precipitation advantage as the surface heat fluxes, which drive the surface heating and thus the circulation, are reduced. Hence, from such studies, an increase of precipitation over spatially drier patches is maximized when the gradient of surface soil moisture is high, the soil moisture heterogeneity length-scale is around 50-100 km and no background wind is present.

Hot-spots of land-atmosphere interactions

These same mechanisms can be observed in some areas of the world, the so-called hot spots of land-atmosphere interactions (Koster et al., [2004](#)). Several observational studies (e.g. Taylor et al., [2012](#)) showed that in the Sahel region thunderstorms occur preferably over regions drier than their surroundings. In other areas of the world the synoptic forcing is usually so strong that a robust relationship of causality between soil moisture and precipitation cannot be found (Tuttle and Salvucci, [2017](#)). Instead of speaking of heterogeneous or homogeneous conditions, Guillod et al. ([2015](#)) have indicated that over most areas of the world, except the Sahel, a negative spatial coupling coexists together with a positive temporal coupling. That is, areas drier than their surrounding (spatial component) but wetter than the climatological value (temporal component) may receive more precipitation than other ones.

Main goals

Although the aforementioned studies have qualitatively shown how precipitation is influenced by soil moisture, soil moisture gradients and by the atmospheric environment, in this chapter I aim at developing a simplified conceptual model to formally isolate the control of soil moisture on precipitation. In particular, I aim at developing a mathematical expression for the derivative of precipitation with respect to soil moisture in the case of a heterogeneous surface to understand the response of precipitation to soil moisture changes. In this case, precipitation is not only affected by the advection of moisture due to the mesoscale circulation but also by local evaporation (Wei et al., [2016](#)). These two factors depend differently on soil moisture.

The mesoscale circulation triggered by the surface wetness heterogeneity strengthens with decreasing soil moisture of the dry patch, as this gives a larger spatial gradient of surface heat fluxes and thus of surface pressure. Instead, local evaporation is limited with reduced local soil moisture. The superposition of local evaporation and remote moisture advection eventually contributes to the observed precipitation, with the atmosphere being the medium that weights these two different contributions.

Lintner et al. ([2013](#)) already derived an equation for the derivative of precipitation with respect to soil moisture based on a model of intermediate-level complexity of the tropical atmosphere (Neelin and Zeng, [2000](#)). Inspired by their work, I develop a conceptual model which is based on similar assumptions but simplifies the formula-

tion of moisture advection and evaporation. In particular, the fact
that I consider the specific case of advection by a thermally-induced
mesoscale circulation, and not by the large-scale flow, will allow me
to greatly simplify the idealized framework.

Section 4.2 describes the model and experimental set-up that allows
me to simulate the evolution of convective clouds and precipitation
over a heterogeneous land-surface during a diurnal period. After a
brief analysis of the features of the convective diurnal cycle done in
section 4.3.1, I estimate the various terms of the moisture balance and
in particular the efficiencies of the conversion of evaporation and ad-
vection into precipitation in section 4.3.2. These results are used in
section 4.4 to derive a simple conceptual model of how precipitation
responds to soil moisture changes over a heterogeneous surface. I
will show that, at least to a first order, the change of precipitation
with soil moisture does not depend on the soil moisture content itself
but only on the atmospheric state. The results are summarized in
section 4.5.

Outline of the chapter

4.2 METHODS

The modeling framework used in this work is, in terms of physical
parametrizations and dynamical core, identical to the one described
in Chapter 2 and in Chapter 3. The ICON-LEM model is used as at-
mospheric model coupled to the land-surface model, TERRA-ML, to
simulate the diurnal cycle of convection over idealized land surfaces
from 6 LST to 24 LST. As in Chapter 3 the only difference to the basic
setup of Chapter 2 pertains the microphysical processes which are
treated using a single-moment 3-cat ice scheme (Doms et al., 2011).

The horizontal periodic domain spans 1600×400 points with a resolu-
tion of 250 m, which results in a size of approximately 400×100 km^2.
In the vertical dimension 150 levels are distributed from the surface
up to the model top located at 21 km: the spacing reaches 20 m in the
lower levels and 400 m close to the model top. In contrast to chap-
ter 3, heterogeneous surface conditions are used as bottom boundary
condition. The heterogeneity is prescribed by dividing the domain's
x-direction into two patches having the same surface area of 200×100
km^2. Figure 4.1 displays a sketch of the domain setup, together with
a visual representation of convective features that will be discussed
later.

The domain is rectangular in order to limit computational expenses
and is elongated in the x-axis given that the front associated with
the simulated mesoscale circulation is expected to propagate with a
direction parallel to the x-axis. The chosen patch size of 200 km is
larger than the optimal value of the heterogeneity wavelength ($\sim$ 100
km) identified by Yan and Anthes (1988), Chen and Avissar (1994),
and Lynn et al. (1998). Therefore I do not expect to maximize, in

terms of the strength of the mesoscale circulation, the response of the atmosphere to the surface heterogeneity. This could eventually reduce the dynamic contribution of advection on precipitation. The larger domain has nevertheless the advantage that the opposite fronts, formed due to the doubly-periodic Torus domain, collide later in the day so that the daily precipitation amounts are less affected by what happens after the fronts have collided. The sensitivity of the diurnal evolution of precipitation to different y-axis size was tested and found to not affect the results.

The surface heterogeneity is introduced by setting two different
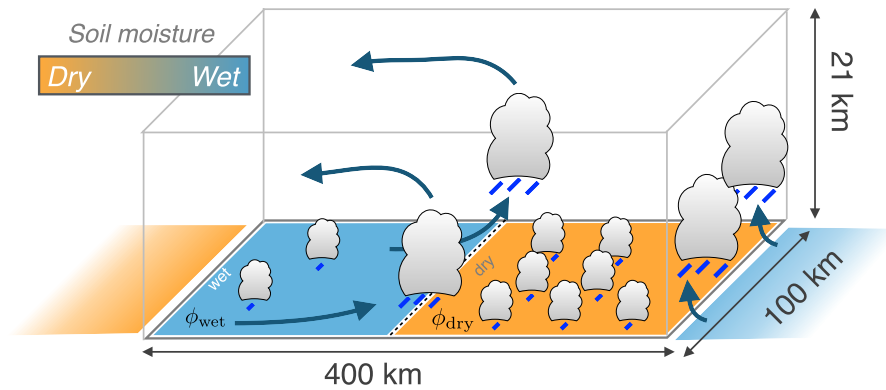
Figure 4.1: Idealized sketch of the employed experimental framework. The initial condition for soil moisture and the expected initial development of convection are also sketched in order to ease the interpretation of the results.

Prescribing heterogeneity in the model

initial values of volumetric soil moisture[1] ϕ [m^3 m^{-3}] for the two patches, ϕ_{wet} and ϕ_{dry}, respectively. The value is set to the entire soil column to ease the interpretation of the results. The other parameters that characterize the land surface, including e.g. soil temperature, are horizontally homogeneous over the entire domain. The soil temperature is initially prescribed using a linear profile which includes a climatological layer with a temperature of 281 K at 14.58 m below the surface and a surface layer which has the same temperature as the overlying lowermost level of the atmosphere as done in chapter 3.

The atmospheric initial state is spatially homogeneous except for random perturbations added to the vertical velocity and the virtual potential temperature in the lowermost three levels to break the perfectly symmetric initial state (see again Chapter 2). The atmosphere is initialized using the dry-soil advantage profile of Findell and Eltahir (2003b), albeit with winds set to zero to simplify the analysis (see Fig. 4.2). This sounding, indicated here as DA, was observed on 23 July 1999 in Lincoln (Illinois, USA) and was chosen as a typical example by Findell and Eltahir (2003b) for cases when a strong heating of a homogeneous surface favors the triggering of convection. This is

---

1 Note that throughout this chapter I will use ϕ in place of w (used in Chapter 2 and Tab. A.1) to indicate the fractional content of water in the soil.
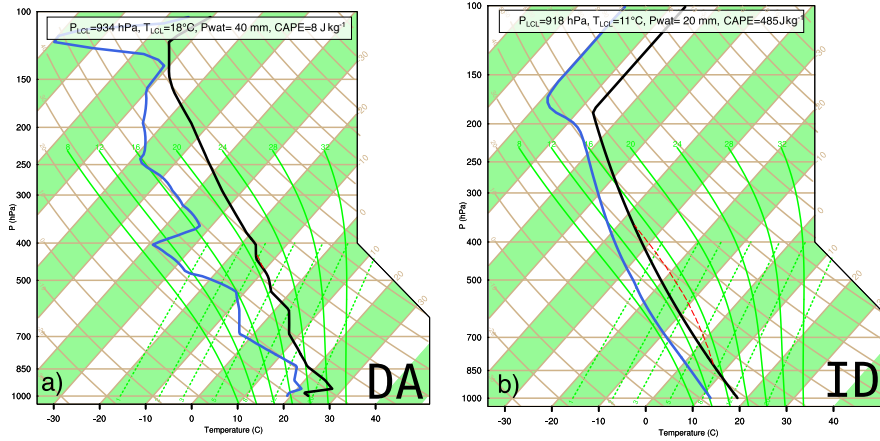
Figure 4.2: Skew-T diagrams of the two soundings used to initialize the atmosphere in the simulations. Panel (a) shows the dry soil advantage sounding of Findell and Eltahir (2003b), DA, while panel (b) shows the idealized sounding of Schlemmer, Hohenegger, et al. (2012), ID. The upper inset in both panels shows the value of pressure at the LCL, temperature at the LCL, precipitable water and CAPE.

identical to the DA sounding already used in chapter 3.

To study the response of precipitation to variations in soil moisture, I perform a set of experiments by setting at the initial time ϕ_{wet} to the saturation value and varying ϕ_{dry}, with values ranging from the saturation to 20% of the saturation value. The latter value is below the wilting point for the chosen soil type (loam). More details about the soil type can be found in appendix A. The upper part of Tab. 4.1 summarizes the simulations performed with this basic configuration.

Basic experiments

In order to test the validity of the theory proposed in section 4.4 based on this set of basic experiments I perform further sensitivity experiments. First, I decrease the initial value of ϕ_{wet} to 70 % of the saturation value. Second, I change the initial atmospheric profile. Preliminary experiments also included the wet soil advantage sounding of Findell and Eltahir (2003b) where, in contrast to the dry soil advantage sounding, convection triggering requires a strong moistening of the boundary layer. I also tested the sounding of Schlemmer, Hohenegger, et al. (2012), indicated as ID, which represents an idealization of the typical atmospheric state prone to convection in Europe (see Fig. 4.2, b). This sounding thus greatly differs from the conditions as observed in Lincoln. It has a lower surface temperature, a lower integrated water vapor content but a larger initial instability. As the use of the wet soil advantage sounding of Findell and Eltahir (2003b) yields very similar results as in DA, which is not the case when using ID, I only report here on the ID simulations.

Additional experiments

Experiment	Sounding	ϕ_{dry}	ϕ_{wet}
Basic configuration			
DA_20_100	DA	20	100
DA_30_100		30	100
DA_40_100		40	100
DA_50_100		50	100
DA_60_100		60	100
DA_65_100		65	100
DA_70_100		70	100
DA_80_100		80	100
DA_100_100		100	100
Partially saturated wet patch			
DA_20_70	DA	20	70
DA_30_70		30	70
DA_40_70		40	70
DA_50_70		50	70
DA_60_70		60	70
DA_70_70		70	70
ID sounding			
ID_20_100	ID	20	100
|	|	|	|
ID_100_100	ID	100	100

Table 4.1: Overview of the performed simulations. The first column indicates the experiment name, whereas the second column indicates the sounding used for initialization: DA for dry soil advantage, after Findell and Eltahir (2003b), and ID for idealized, after Schlemmer, Hohenegger, et al. (2012). Third and fourth columns indicate the value of soil moisture over the dry and wet patches, respectively, in percentage of the saturation value. The naming convention for the experiments follows SOUNDING_ϕ_{dry}_ϕ_{wet}. The vertical lines that characterize the ID cases are used to omit the repetition of the same experiments description, i.e. ID_30_100, ID_40_100, etc. .

4.3 RESULTS

4.3.1 *General features of convection*

Here, I describe the general features of the extreme case, DA_20_100, which reproduces the features expected from this kind of simulations. The differential heating of the two patches, caused by the heterogeneity in soil moisture, manifests itself in a gradient of both sensible and latent heat fluxes. At 12 LST the difference in sensible heat flux between the two patches reaches almost 280 W m^{-2}. This results in a difference in near-surface virtual potential temperature of about 4 K at the same time (see the colored contours in Fig. 4.3). As a consequence, a pressure gradient of about 1 hPa develops close to the surface, which supports a thermally-driven circulation (Segal and Arritt,

1992). The circulation is constituted by a front of moist air moving inland over the dry patch at lower levels (from the surface up to 1 km) and a return flow between 1 and 3 km, as shown by the wind vectors in Fig. 4.3. As a result of the circulation, and as found in past studies, convection preferentially develops over the dry patch and in particular at the edge of the front associated with the mesoscale circulation.

In order to track this front I use an algorithm designed to follow one
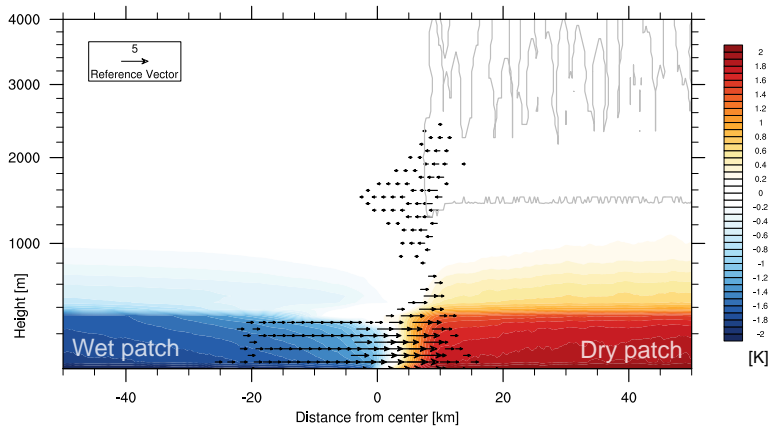
Figure 4.3: *x-z* diagram at 1200 LST of *y*-averaged quantities for the DA_20_100 case. Zonal temperature anomaly (color contours), zonal wind (vectors, values between -0.5 and 1 m s^{-1} are masked) and cloud water mixing ratio (grey contour, only 10^{-5} g kg^{-1} isoline). On the *x*-axis numbers indicate the distance from the center of the domain in km.

Tracking of the front

of the front moving over the dry patch. The algorithm is based on the *y*-averaged zonal wind speed at 150 m of height. It is triggered when the wind speed in the middle of the domain reaches 1 m s^{-1} and automatically stops when the opposite fronts collide in the center of the dry patch. At every output time step (15 minutes) a search of the maximum value of zonal wind speed is performed in a box which is suitably chosen in order to maintain the focus of the tracking algorithm on the front.

More specifically, at the first two time instants the maximum is searched over the entire dry patch while from the third time step onward the maximum search is performed in a box centered on a first guess obtained from a simple linear extrapolation of the previous time instants. The size of the box is the only parameter that needs to be tuned when tracking the front in different simulations. Otherwise, the algorithm is robust. As an example, in the DA_20_100 case shown in Fig. 4.4, the box comprises 5 grid points, thus approximately 1.25 km.

Figure 4.4 (a) shows the Hovmöller diagram of the zonal wind and the tracked position of the front every 15 minutes with shaded circles for the case DA_20_100. In Fig. 4.4 (b) the position and speed of the

front obtained with the aforementioned algorithm are displayed. The
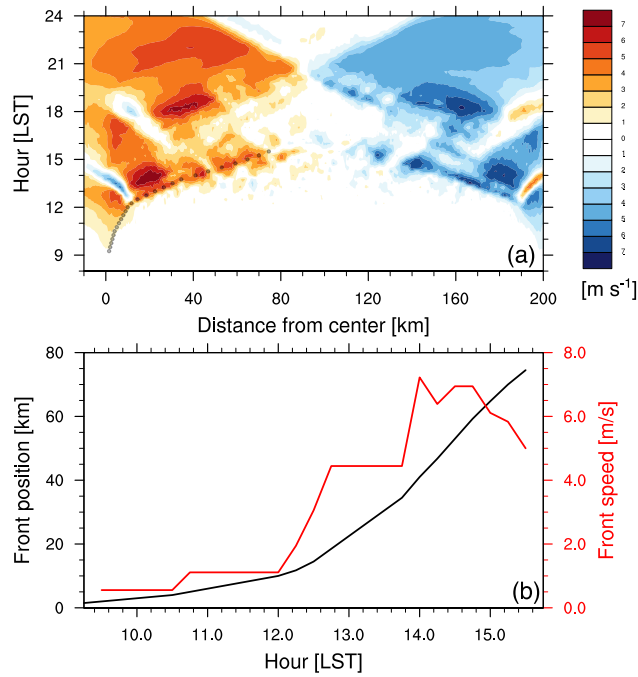
Figure 4.4: Tracking of the front associated with the mesoscale circulation for the case `DA_20_100`. (a) Hovmöller diagram (distance from domain center vs. time) of the y-averaged zonal wind at a height of 150 m above the surface. Dots indicate the position of the front tracked every 15 minutes (see text for details). (b) Front inland propagation (black line) with respect to the center of the domain [km] and front speed (red line) derived using finite differences [m s^{-1}].

front starts to slowly propagate in the late morning with a velocity smaller than 2 m s^{-1} but is later accelerated by cold pools, in agreement with Rieck et al. (2015). The cold pools are formed after the first strong precipitation event between 12 and 13 LST. The speed of the front reaches values of up to 7 m s^{-1} before the front collides with the opposing front coming from the outer boundary due to the periodic domain. When the soil moisture of the dry patch exceeds 70% of the saturation value no circulation forms because the gradient in surface temperature is too weak to cause a pressure difference between the patches. In this case the convection transitions to a randomly scattered state (Avissar and Liu, 1996) and I define the speed of the front to be 0 m s^{-1}.

4.3.2   *Local and remote sources of precipitation*

The diurnal cycle of precipitation can be inspected and compared to the one of evaporation and advection, using the methodology introduced in appendix C.3. This is needed to later formally express precipitation as a function of soil moisture (see section 4.4). Figure 4.5 shows the various components of the moisture balance computed

every 5 minutes from the model output and averaged over the dry patch as well as over the entire domain. It can be verified that the
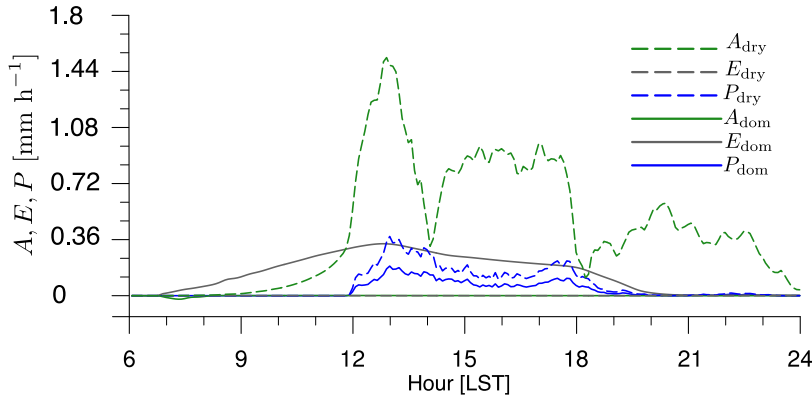
Figure 4.5: Different terms of the moisture balance (Eq. C.3) computed for the entire domain (subscript $_{\text{dom}}$, solid lines) and for the dry patch (subscript dry, dashed lines) in the `DA_20_100` case. A indicates advection, E evaporation and P precipitation. Units are mm h^{-1}. Note that all variables in this figure are instantaneous. See Appendix C.3 for details on how these terms are computed.

advection term averaged over the entire domain is zero, as expected. Instead, when considering the residual averaged over the dry patch, A_{dry}, it is always positive, indicating a net transport of moisture from the wet to the dry patch.

Evolution of advection

The advection of moisture over the dry patch increases in the late morning as a result of the propagation of the front (see Fig. 4.4) and reaches a maximum at around 13 LST. This behavior is similar to the one observed by Yan and Anthes (1988, their Fig. 9). The first heavy precipitation event in `DA_20_100` between 12 and 13 LST produces a strong cold pool which causes a strong surface divergence, explaining the minimum at about 14 LST in Fig. 4.5. Given that the maximum of precipitation associated with this event is located in the vicinity of the boundary between the wet and the dry patch, this induces a net negative effect on A_{dry}.

In order to study the variation of the moisture budget terms as a function of ϕ_{dry} I conduct the same moisture balance analysis for every simulation and integrate the values over the entire diurnal cycle (18 hours). Results are reported in Tab. 4.2. As expected the advection term decreases with increasing local soil moisture whereas local evaporation increases. Overall the accumulated precipitation averaged over the dry patch decreases when the soil moisture increases, as shown also in Fig. 4.6. The sharp decrease of precipitation with increasing values of soil moisture seems to suggest that advection and evaporation are characterized by different weights when producing precipitation. In fact, if the contribution of these processes would be the same, we would expect to observe a flattening of the precipitation values (blue asterisks in Fig. 4.6) instead than a decrease. In

Case	ϕ_{dry}	A_{dry}	E_{dry}	P_{dry}	η
DA_20_100	0.0908	7.796	0.0008	1.255	0.161
DA_30_100	0.1362	7.467	0.0113	1.077	0.144
DA_40_100	0.1816	7.223	0.1140	1.005	0.137
DA_50_100	0.2270	6.673	0.6373	0.912	0.125
DA_60_100	0.2724	4.665	2.0271	0.888	0.133
DA_65_100	0.2951	3.222	3.0393	0.805	0.129
DA_70_100	0.3178	1.734	4.0920	0.708	0.122
DA_80_100	0.3632	-0.412	5.2770	0.533	0.094
DA_100_100	0.4540	0.031	5.0800	0.560	0.110

Table 4.2: Values of soil moisture [m^3 m^{-3}], advection [mm], evaporation [mm] and precipitation [mm] over the dry patch accumulated over the diurnal cycle. The rightmost column shows the precipitation efficiency (dimensionless) computed as $\frac{P_{\text{dry}}}{A_{\text{dry}}+E_{\text{dry}}}$.

other words, advection appears to be more efficient than evaporation in producing precipitation, as the increase of E_{dry} with soil moisture is followed by a sharp decrease of P_{dry}.

These qualitative observations can be formalized by defining the
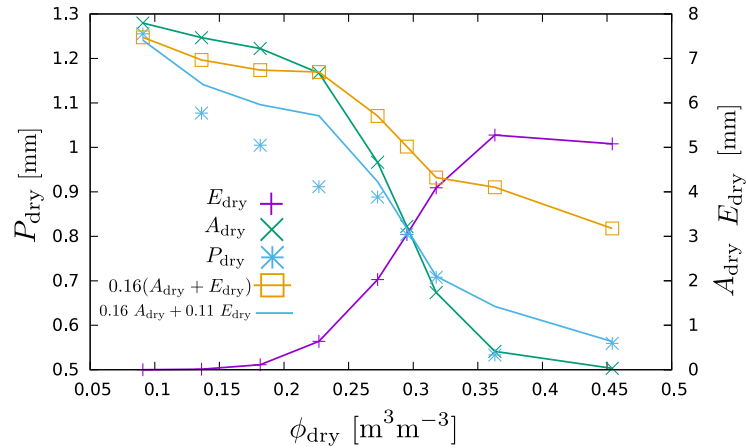
Figure 4.6: Values of advection (green line and crosses), evaporation (purple line and plus symbols) and precipitation (blue asterisks) from Tab. 4.2 as function of soil moisture. The orange line represents an estimate of precipitation obtained as a sum of advection and evaporation weighted by the same efficiency, i.e. $0.16(A_{\text{dry}} + E_{\text{dry}})$ while the blue line represents a similar estimate obtained by using two different efficiencies, i.e. $0.16\,A_{\text{dry}} + 0.11\,E_{\text{dry}}$.

Precipitation efficiency

precipitation efficiency. This approach was first proposed by Budyko (1974) and later adopted by many studies including the one of Schär et al. (1999). The overall assumption underlying the pioneering work of Budyko (1974) is that moisture coming from inside (local evaporation) or outside (remote advection) of some closed domain is well

mixed. Under this assumption one can express the precipitation over a certain area as:

$$P_{\text{area}} = \eta(A_{\text{area}} + E_{\text{area}}) \tag{4.1}$$

where η is the precipitation efficiency. All the terms are considered as areal averages and integrated over a certain time period. The rightmost column of Tab. 4.2 shows the efficiency η computed according to Eq. 4.1. It can be seen that, in this case, convection is not so efficient in converting local and remote sources of moisture into precipitation as the values range from 16% to 9%. More importantly, the efficiency values vary by up to 7% depending on the initial ϕ_{dry}. In fact, in the case DA_20_100, evaporation over the dry patch is negligible, i.e. $E_{\text{dry}} \simeq 0$, so that Eq. 4.1 applied to the dry patch reads $P_{\text{dry}} \simeq \eta A_{\text{dry}}$. Thus, the efficiency obtained in this case is representative of the advection process and can be interpreted as an *advection efficiency* η_A. On the other hand, in DA_100_100 the advection is negligible so that in this case I obtain an *evaporation efficiency* η_E. Taking all these findings together Eq. 4.1 can be rewritten as:

$$P_{\text{area}} = \eta_A \cdot A_{\text{area}} + \eta_E \cdot E_{\text{area}} \tag{4.2}$$

where now $\eta_A \neq \eta_E$. The values estimated from Tab. 4.2 are $\eta_A = 0.16$ and $\eta_E = 0.11$.

Advection and evaporation efficiencies

Fig. 4.6 confirms that, regardless of the particular choice of a single efficiency η, the decrease of precipitation over wetter soils cannot be captured (orange line in Fig. 4.6). In contrast, using the two efficiencies η_A and η_E gives a much better match with the simulated value of P_{dry} (see blue line in Fig. 4.6). Also, by using two efficiencies, the latter become independent of soil moisture. The efficiencies can be alternatively estimated through a fit of Eq. 4.2 using all the values of A_{dry} and E_{dry} in Tab. 4.2. In this case I obtain the values $\eta_A = 0.15$ and $\eta_E = 0.10$ which, as expected, do not differ much from the ones computed using the two extreme cases.

The fact that one efficiency is not enough to describe the variations of precipitation, in contrast to previous studies, may be linked to the fact that I consider a small domain and a short timescale. The assumption of a well-mixed atmosphere likely holds better on a continental (e.g. Europe) and seasonal scale, as in Schär et al. (1999). Using two efficiencies nevertheless requires data from at least two simulations with different values of advection, evaporation and precipitation.

Initializing the atmosphere with a different sounding will likely lead to different efficiencies. This is illustrated with the ID_ cases (see Tab. 4.3), where the idealized sounding of Schlemmer, Hohenegger, et al. (2012) is used to initialize the atmosphere (see section 4.2). For a given soil moisture, advection reaches smaller values that in the DA case. This is mainly an effect of larger precipitation amounts that fall on the wet patch which in turn prevents an efficient advection of

Results with the additional sounding

moisture from the wet to the dry patch.

The efficiencies computed for this case range from 47% to 31%, indi-

Case	$A_{\mathbf{dry}}$	$E_{\mathbf{dry}}$	$P_{\mathbf{dry}}$	η
ID_20_100	3.814	0.008	1.789	0.468
ID_30_100	3.861	0.028	1.912	0.492
ID_40_100	3.920	0.143	1.671	0.411
ID_50_100	3.557	0.659	1.740	0.413
ID_60_100	2.631	2.054	1.759	0.376
ID_70_100	0.865	4.080	1.542	0.312
ID_80_100	-0.068	4.884	1.652	0.334
ID_100_100	0.022	4.776	1.662	0.346

Table 4.3: As in Tab. 4.2 but for the ID sounding.

cating that the atmosphere is more efficient at converting advection and evaporation into precipitation than in DA. The higher efficiencies obtained with the ID sounding are due to a combination of different effects. One of those is the different convection triggering. With the ID sounding convection is triggered almost 1 hour before than with the DA sounding (not shown). This allows the atmosphere to fully exploit the instability caused by the morning heating which manifests itself in a stronger enhancement of precipitation at the front, as shown in Fig. 4.7. This is also corroborated by the fact that CAPE at 15 LST is larger than the one at the initial time over both patches in DA_20_100 whereas it is depleted over the dry patch in the ID_20_100 case (not shown). Moreover, as indicated by Fig. 4.2, the dew-point depression in the ID sounding is smaller than in the DA sounding throughout most of the atmospheric column. This suggests that, in the ID case, convective updrafts are less affected by the entrainment of environmental dry air. I verify this by computing the average difference in MSE between updrafts, defined as grid points with vertical velocity greater than 1 m s^{-1} and cloud water content greater than 10^{-4} kg kg^{-1}, and the environment. Results show that this difference in the ID case is less than 50 % the values observed in the DA case. The figure containing the vertical profiles of MSE is available in Appendix C.2. Despite the differences, the ID case confirms that advection and evaporation exhibit distinct efficiencies and that precipitation decreases with increased local soil moisture. Here the decrease of precipitation is smaller than the one obtained in the DA_ cases. Although this could be related to a weaker sensitivity of the ID atmospheric state to modifications in the land-surface heterogeneity, we note that the amount of precipitation strongly depends on the collision of the fronts. As shown in Fig. 4.7 the collision of the fronts in the center of the dry patch has different effects on precipitation depending on the atmospheric state. In the ID_20_100 case strong precipitation events with local maxima of 10 mm h^{-1} are produced in the center of the patch

after the fronts' collision and several secondary events develop due to the fronts propagating away from the collision. Instead, in the
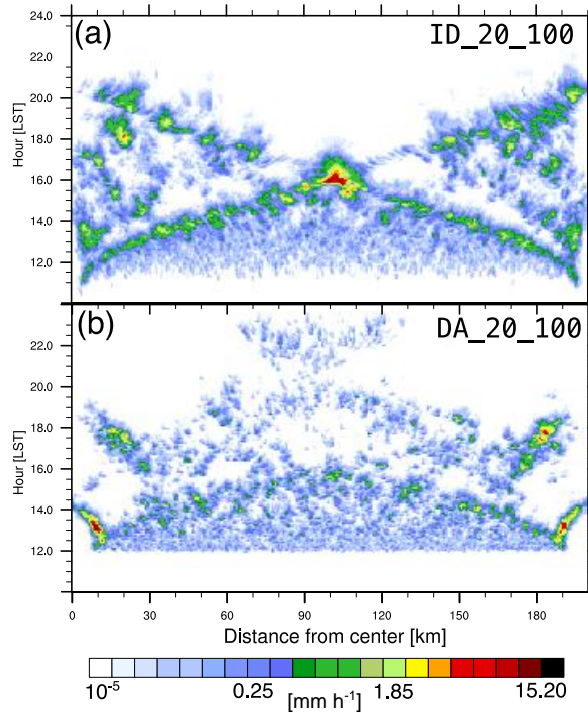
Figure 4.7: Hovmöller diagrams of precipitation rate [mm h^{-1}] in case ID_20_100 and DA_20_100.

DA_20_100 case, no strong precipitation event is produced when the fronts collide.

4.4 CONCEPTUAL MODEL

In section 4.3.2 we showed that precipitation can be expressed as a linear combination of advection and evaporation weighted by different efficiencies which are assumed independent of soil moisture (Eq. 4.2). Knowing this we can now try to answer one of the first questions that was posed in the introduction:

What are the minimum parameters that control the variation of precipitation with soil moisture?

In order to do so we first have to derive some functional forms of evaporation and advection in terms of soil moisture.

4.4.1 *Surface evaporation*

The simplest parametrization of evaporation (we will neglect the transpiration part given that the present study does not include plants) is the so-called *bucket model* introduced by Budyko (1961) and extended

by Manabe ([1969]). Evaporation is defined as a potential term controlled by a limiting factor (also called stress factor). Here we use such a formulation to approximate first the surface latent heat flux LH [mm h^{-1}] at a certain point in space and time as a function of soil moisture ϕ [m^3 m^{-3}]:

$$\text{LH}(\phi) = \mathcal{A} Q_{\text{net}} \times \begin{cases} 0 & \text{for } \phi < \phi_{\text{wp}} \\ \frac{\phi - \phi_{\text{wp}}}{\phi_{\text{crit}} - \phi_{\text{wp}}} & \text{for } \phi_{\text{wp}} \leq \phi \leq \phi_{\text{crit}} \\ 1 & \text{for } \phi > \phi_{\text{crit}} \end{cases} \qquad (4.3)$$

where Q_{net} [mm h^{-1}] is the net incoming radiation at the surface (long-wave+short-wave), ϕ_{wp} [m^3 m^{-3}] the soil moisture at the permanent wilting point and ϕ_{crit} [m^3 m^{-3}] is the critical soil moisture at which evaporation does not increase any more with increasing soil moisture. As explained by Seneviratne, Corti, et al. ([2010]) this does not usually correspond to the field capacity.

$\mathcal{A}$ is a proportionality constant which needs to be introduced and specified given that, even in the extreme case of a saturated soil, non-zero sensible heat fluxes and ground heat flux prevent the entire conversion of Q_{net} into LH. The constant $\mathcal{A}$ clearly depends on the particular soil model employed as well as on the different parameters that characterize the soil type considered (e.g. albedo, heat capacity) and partially also on the atmosphere.

In order to link Eq. 4.3 to the accumulated evaporation E_{dry} needed in Eq 4.2 I average Eq. 4.3 over the dry patch and integrate it over the accumulation period τ. By doing so I assume a constant value for soil moisture and replace it with the value at the initialization time. Such assumption is motivated by the fact that changes in soil moisture over one diurnal cycle are not expected to be able to significantly feed back on evaporation and precipitation on such a short timescale. The assumption is also well justify as the daily average value of soil moisture remains similar to its initial value (see also section 3.3.2).

Parametrization of surface evaporation   This gives:

$$E_{\text{dry}}(\phi_{\text{dry}}) = \tau \mathcal{A} \langle Q_{\text{net}} \rangle \times \begin{cases} 0 & \text{for } \phi_{\text{dry}} < \phi_{\text{wp}} \\ \frac{\phi_{\text{dry}} - \phi_{\text{wp}}}{\phi_{\text{crit}} - \phi_{\text{wp}}} & \text{for } \phi_{\text{wp}} \leq \phi_{\text{dry}} \leq \phi_{\text{crit}} \\ 1 & \text{for } \phi_{\text{dry}} > \phi_{\text{crit}} \end{cases} \quad (4.4)$$

where now E_{dry} does not depend on time nor space. $\langle Q_{\text{net}} \rangle$ denotes the net surface incoming radiation averaged over the period τ, whereas ϕ_{dry} corresponds to the initial value of soil moisture.

Equation 4.4 can now be used to fit the values of E_{dry} computed from the simulations (Tab. 4.2) to obtain an unambiguous value for the parameters $\mathcal{A}$, ϕ_{wp} and ϕ_{crit} (see Fig. 4.8). These are estimated to be $\mathcal{A} = 0.663$, $\phi_{\text{wp}} = 0.213$ m^{3}m^{-3} and $\phi_{\text{crit}} = 0.350$ m^{3}m^{-3}. Note that

the latter estimate is not far from the field capacity of this soil type, i.e. 0.340 m^3m^{-3}, while the estimated wilting point is almost double the expected one, i.e. 0.110 m^3m^{-3} (see Appendix A). This is related to the fact that the employed bare soil evaporation scheme tends to shut down evaporation too early as noted by Schulz et al. (2016) and in Chapter 3. Thus, both $\phi_{wp,crit}$ depend not only on the employed soil type but also on the soil model.

Figure 4.8 shows the fit of Eq. 4.4, together with the values obtained in the simulations. It reveals an excellent agreement between theory
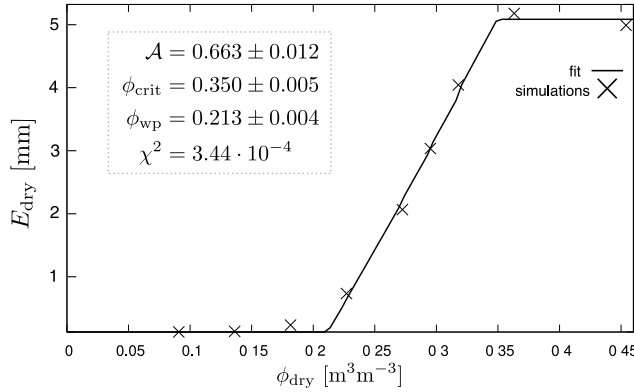
Figure 4.8: Fit of E_{dry} with values obtained from the simulations of the default configuration (`DA_20_100` to `DA_100_100`). Crosses indicate values obtained from simulations while the line indicates the fit performed using Eq. 4.4. The upper left inset shows the values obtained by the fit together with absolute errors and the residual sum of squares χ^2, i.e. the sum of the squared difference between the values predicted by the fit and the ones obtained in the simulations.

and simulations. The small discrepancies mainly come from the fact that I assume a constant value of $\langle Q_{net} \rangle = 300$ W $m^{-2} = 0.43$ mm h^{-1} across the simulations, although the simulated value depends on soil moisture and varies by about 7%. This is due to different cloud regimes which alter the surface radiation balance (see section 3.4.2). Furthermore, I use the average of Q_{net} over the entire domain, while it should only be considered over the dry patch.

It should be noted that the adopted formulation of evaporation differs from the one used in the model of Lintner et al. (2013) where potential evaporation was used in place of Q_{net}, which is the main difference between the original framework of Budyko (1961) and the one of Manabe (1969).

4.4.2 *Advection*

The goal of this section is to find a formulation of A_{dry} as a function of soil moisture. This can be achieved starting from the definition of Eq. C.2 and assuming that the advection of every tracer is mainly

due to the propagation of the front associated with the mesoscale circulation, hence $H = H_{\text{front}}$. In this case

$$
\begin{aligned}
A_{\text{dry}} &= -\frac{1}{\rho_w} \int_0^\tau \int_0^{H_{\text{front}}} \mathbf{v}_{\text{front}} \cdot \nabla q_{\text{tot}}\Big|_{\text{dry}} \rho_a \, dz \, dt \\
&\simeq -\frac{1}{\rho_w} \int_0^\tau \int_0^{H_{\text{front}}} u_{\text{front}} \frac{\partial q_{\text{tot}}}{\partial x}\Big|_{\text{dry}} \rho_a \, dz \, dt
\end{aligned}
\tag{4.5}
$$

where H_{front} is the height of the front associated with the mesoscale circulation or, equally, the PBL height, $\mathbf{v}_{\text{front}}$ its speed, ρ_a is the air density and ρ_w the water density. Eq. 4.5 has been already approximated given that the front propagates mainly in the x direction (see Sec. 4.3.1), so that there is no y component of ∇q_{tot}.

Propagation speed of the front The propagation speed of the front u_{front} and ρ_a can be seen as constants in the vertical within the height H_{front}, while q_{tot} remains a function of x, z and time t. The time integration can be replaced by considering the average over time multiplied by the timescale τ to obtain

$$
\begin{aligned}
A_{\text{dry}} &= -\tau \frac{\rho_a}{\rho_w} \langle u_{\text{front}} \rangle_{\text{dry}} \langle \int_0^{H_{\text{front}}} \frac{\partial q_{\text{tot}}}{\partial x}\Big|_{\text{dry}} \, dz \rangle \\
&= -\tau \frac{\rho_a}{\rho_w} \langle u_{\text{front}} \rangle_{\text{dry}} \langle \int_0^{H_{\text{front}}} \frac{\Delta q_{\text{tot}}}{L_{\text{front}}} \, dz \rangle \\
&= -\tau \frac{\rho_a}{\rho_w} \langle u_{\text{front}} \rangle_{\text{dry}} \frac{H_{\text{front}}}{L_{\text{front}}} \langle \Delta q_{\text{tot}} \rangle
\end{aligned}
\tag{4.6}
$$

In Eq. 4.6 I approximated the derivative of q_{tot} as the difference between the two patches Δq_{tot} divided by the penetration length of the front, L_{front} (Crosman and Horel, 2010).

Approximation for the gradient in specific humidity To simplify the problem I assume $\Delta q_{\text{tot}} \simeq \Delta q_v$, which is viewed as the difference in specific humidity ahead of the front and behind it. As in studies which have viewed sea breezes as gravity current (Robinson, Patterson, et al., 2013), I assume that this difference is not directly affected by the circulation, which gives an upper bound estimate. The changes in q_v due to surface evaporation accumulated up to a certain time τ can then be written as

$$
q_v(\tau) = q_v(0) + \frac{\rho_w E}{\rho_a H_{\text{moist}}} \Rightarrow \Delta q_v = -\frac{\rho_w}{\rho_a H_{\text{moist}}} \underbrace{(E_{\text{wet}} - E_{\text{dry}})}_{\Delta E} \tag{4.7}
$$

where H_{moist} is the vertical extent of the moistening process due to the accumulated surface evaporation E and $q_v(0)$ is the specific humidity at the initial time. By assuming that the moistening is confined to the PBL, so that $H_{\text{moist}} = H_{\text{front}}$ I can substitute Eq. 4.7 into Eq. 4.6 to obtain

$$
A_{\text{dry}} = \frac{\tau \langle u_{\text{front}} \rangle}{L_{\text{front}}} \Delta E \tag{4.8}
$$

My analysis thus indicates that the advection only depends on four terms: τ, which is a constant, the difference in E between the two

patches, which can be estimated from Eq. 4.4 and which depends on the soil moisture, as well as L_{front} and u_{front}. In all simulations the front has a constant inland propagation of $L_{\text{front}} \simeq 100$ km, which corresponds to half of the patch size. More importantly, the front speed does not vary much with different surface heterogeneity gradients, against my initial expectations that motivated this study (see Introduction). For example, between the `DA_20_100` and the `DA_60_100` cases only a 3% relative decrease in the front speed is observed. This can be seen in the additional figure provided in Appendix C.1.

This counter-intuitive behavior is related to the fact that cold pools lead to a noticeable acceleration of the front, as seen in section 4.3.1. Although the front is initially triggered by the surface heterogeneity, and different surface heterogeneities may lead to different initial propagation velocities, the much faster cold pools end up determining the front velocity, thus masking the effect of the surface heterogeneity. This stands in agreement with what found by Rieck et al. (2015), and in particular with the thermodynamic contribution of cold pools to the propagation speed of the front (their Eq. 1). Moreover, cold pools are distributed along the front and continuously fed by precipitation events, similarly to what happens in squall-lines. Given this spatial organization, their strength and propagation do not depend on the surface state, as in the case for isolated convection (Gentine, Garelli, et al., 2016). Instead, they solely depend on the state of the mid- to upper-troposphere (Peters and Hohenegger, 2017) which is also not significantly modified by surface fluxes over the course of one diurnal cycle.

Homogenization of the front speed due to cold pools

Advection can thus be finally expressed as:

Parametrization of advection

$$A_{\text{dry}}(\phi_{\text{dry}}) = \mathcal{B} \Delta E(\phi_{\text{dry}}) \tag{4.9}$$

where $\mathcal{B} = \tau \langle u_{\text{front}} \rangle / L_{\text{front}}$ is a proportionality constant that does not depend on soil moisture. Using the parameters $\mathcal{A}, \phi_{\text{wp}}, \phi_{\text{crit}}$ obtained from the fit of Eq. 4.4 (see Fig. 4.8) the difference $\Delta E(\phi_{\text{dry}})$ can be computed. Together with the values of A_{dry} obtained in the simulations the values of $\Delta E(\phi_{\text{dry}})$ can be used to fit Eq. 4.9 and compute a value for the parameter $\mathcal{B}$: in the `DA` cases $\mathcal{B} = 1.47$. This is smaller than the value that would be obtained by estimating instead $\langle u_{\text{front}} \rangle$ and L_{front} directly, as this latter approximation does not take into account moisture losses due to advection.

Figure 4.9 shows the values of A_{dry} and the fit performed using Eq. 4.9 for the basic set of experiments and for further cases, the latter used to test the finding that $\mathcal{B}$ does not depend on ϕ but solely on the atmospheric state. Overall the fit matches the variation of A_{dry} with ϕ_{dry} remarkably well given the various assumptions. Both the simulated decrease of A_{dry} with higher values of soil moisture and the flattening of advection by soil moisture lower than the wilting point are reproduced, although both effects seem to be overestimated

Figure 4.9: Fit of the advection in cases `DA_*_100`, `DA_*_70` and `ID_*_100`. Symbols indicate the values obtained from the simulations while lines represent the fit performed using Eq. 4.9. The obtained values of $\mathcal{B}$ are reported in the insets, together with the absolute error and the χ^2 value (see Fig. 4.8 for the definition). Note that for the `DA_*_100` and `DA_*_70` cases the fits yielded similar results: for this reason the obtained value for $\mathcal{B}$ is reported only once.

by Eq. 4.9.

In the simulations where the initial value of ϕ_{wet} is reduced to just 70% of saturation, the estimated value of $\mathcal{B}$ is almost the same as the one of the default configuration, confirming that $\mathcal{B}$ does not depend on soil moisture. Instead, in the `ID_` cases (Tab. 4.3), which use a different atmospheric profile and hence support distinct cold pool strength, the value of $\mathcal{B}$ is reduced by about half.

4.4.3 *Computing the derivative of precipitation*

Equations 4.2, 4.4 and 4.9 can be combined in order to compute P_{dry}. I am, however, interested in its variation with soil moisture, $\frac{\partial P_{dry}}{\partial \phi_{dry}}$, which can be computed as:

$$
\begin{aligned}
\frac{\partial P_{dry}}{\partial \phi_{dry}} &= \eta_A \frac{\partial A_{dry}}{\partial \phi_{dry}} + \eta_E \frac{\partial E_{dry}}{\partial \phi_{dry}} \\
&= \eta_A \frac{\partial}{\partial \phi_{dry}} \left(\mathcal{B} \left(E_{wet} - E_{dry} \right) \right) + \eta_E \frac{\partial E_{dry}}{\partial \phi_{dry}} \\
&= -\eta_A \mathcal{B} \frac{\partial E_{dry}}{\partial \phi_{dry}} + \eta_E \frac{\partial E_{dry}}{\partial \phi_{dry}}
\end{aligned}
\tag{4.10}
$$

Note that the derivation of Eq. 4.10 retains only one term of the difference given that E_{wet} does not depend on ϕ_{dry}. Using Eq. 4.4 it is straightforward to compute the derivative of E_{dry} as

$$\frac{\partial E_{\text{dry}}}{\partial \phi_{\text{dry}}} = \tau \mathcal{A} \langle Q_{\text{net}} \rangle \times \begin{cases} 0 & \text{for } \phi_{\text{dry}} < \phi_{\text{wp}} \\ (\phi_{\text{crit}} - \phi_{\text{wp}})^{-1} & \text{for } \phi_{\text{wp}} \leq \phi_{\text{dry}} \leq \phi_{\text{crit}} \\ 0 & \text{for } \phi_{\text{dry}} > \phi_{\text{crit}} \end{cases}$$

(4.11)

which is a step-wise function constituted by constant values. Equations 4.10 and 4.11 indicate that for $\phi_{\text{dry}} < \phi_{\text{wp}}$ and $\phi_{\text{dry}} > \phi_{\text{crit}}$ there is no change in precipitation with soil moisture independently of the value of the efficiencies. In contrast, for $\phi_{\text{wp}} \leq \phi_{\text{dry}} \leq \phi_{\text{crit}}$ then $\frac{\partial E_{\text{dry}}}{\partial \phi_{\text{dry}}} \neq 0$ but still the derivative of precipitation with respect to soil moisture does not depend upon the soil moisture content itself. These findings contrast with the ones of Lintner et al. (2013), who found a minimum of the derivative for intermediate values of soil moisture. This is a consequence of the formulation of E_{dry} as a linear function of ϕ_{dry} and the fact that A_{dry} also turned out to be a linear function of ϕ_{dry} as u_{front} is constant. This remains true as long as the convection is strongly organized by the front associated with the mesoscale circulation and produces strong cold pools that end up determining the propagation velocity. It should be noted that, although the derivative $\frac{\partial P_{\text{dry}}}{\partial \phi_{\text{dry}}}$ does not depend on soil moisture, the absolute value of precipitation P_{dry} does indeed depend on soil moisture, as I will show later. Coming back to Eqs. 4.10 and 4.11, I can now determine under which conditions P_{dry} will increase or decrease.

Derivative does not depend on soil moisture

Sign of the derivative

$$\frac{\partial P_{\text{dry}}}{\partial \phi_{\text{dry}}} \lessgtr 0 \Leftrightarrow -\eta_A \mathcal{B} + \eta_E \lessgtr 0 \Leftrightarrow \eta_E \lessgtr \eta_A \mathcal{B}$$

(4.12)

The atmospheric conditions, through the terms η_A, η_E and $\mathcal{B}$, determine whether increasing or decreasing the soil moisture of the dry patch is needed to increase the precipitation amount. Inserting the values of the efficiencies and of $\mathcal{B}$ obtained from the DA_ simulations in Eq. 4.12 confirms that $\frac{\partial P_{\text{dry}}}{\partial \phi_{\text{dry}}} < 0$, which agrees with the simulated increase of precipitation with decreasing values of soil moisture. These results are generalized with the help of Fig. 4.10 for three different values of $\mathcal{B}$.

In Fig. 4.10 positive values indicate an increase of precipitation over the dry patch with soil moisture, and vice-versa. Not surprisingly (see Eq. 4.12) using a value of $\mathcal{B} = 1$ gives a symmetric picture where an increase of precipitation with soil moisture is obtained for those cases when $\eta_E > \eta_A$. This relationship is modified by the value of $\mathcal{B}$. Figure 4.10 overall shows that, as long as $\eta_A > \eta_E$, it is very unlikely
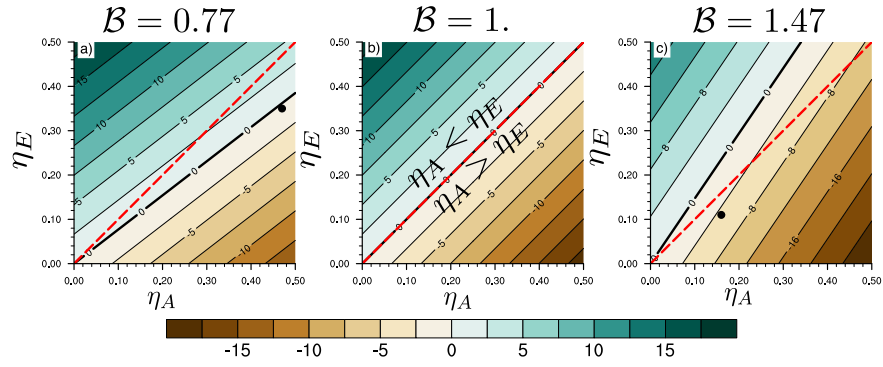
Figure 4.10: Contour plot of $\frac{\partial P_{\text{dry}}}{\partial \phi_{\text{dry}}}$ [mm m^3 m^{-3}] as a function of η_A, η_E for different values of the parameter $\mathcal{B}$. The black points in (a) and (c) are placed using the efficiencies obtained in the ID_ and DA_ cases, respectively. The dashed red line distinguishes the areas where $\eta_A > \eta_E$ and vice versa. Note the symmetric color scale and the thicker zero contour line.

to get a positive derivative. Only with values of $\mathcal{B}$ small enough, which would mean weaker and slower cold pools, the derivative may change sign even with $\eta_A > \eta_E$. This situation almost happens in the ID simulation, where the theory predicts a derivative close to zero. This agrees with the weaker sensitivity of precipitation to soil moisture observed in that case. Alternatively, to get a positive derivative, evaporation should become much more efficient than advection, i.e. $\eta_E \gg \eta_A$. This, however, did not happen in the performed simulations.

These findings already answer the main question posed in the introduction and can be further generalized to the case when both ϕ_{wet}

Precipitation as function of soil moisture of both patches

and ϕ_{dry} are changed at the same time. This allows one to investigate the dependency of precipitation on the soil moisture values of the two patches when the η_A, η_E and $\mathcal{B}$ parameters are fixed. First of all, $\frac{\partial P_{\text{dry}}}{\partial \phi_{\text{wet}}}$ can be computed with the same method as before:

$$\frac{\partial P_{\text{dry}}}{\partial \phi_{\text{wet}}} = \eta_A \mathcal{B} \frac{\partial E_{\text{wet}}}{\partial \phi_{\text{wet}}} \tag{4.13}$$

given that the evaporation over the dry patch does not depend on the soil moisture of the wet patch. Second, the two derivatives $\frac{\partial P_{\text{dry}}}{\partial \phi_{\text{wet}}}, \frac{\partial P_{\text{dry}}}{\partial \phi_{\text{dry}}}$ can be combined to obtain the total precipitation change over the dry patch.

$$\Delta P_{\text{dry}} = \frac{\partial P_{\text{dry}}}{\partial \phi_{\text{dry}}} \Delta \phi_{\text{dry}} + \frac{\partial P_{\text{dry}}}{\partial \phi_{\text{wet}}} \Delta \phi_{\text{wet}}$$

$$= (\eta_E - \eta_A \mathcal{B}) \frac{\partial E_{\text{dry}}}{\partial \phi_{\text{dry}}} \Delta \phi_{\text{dry}} + \eta_A \mathcal{B} \frac{\partial E_{\text{wet}}}{\partial \phi_{\text{wet}}} \Delta \phi_{\text{wet}} \tag{4.14}$$

Assuming that the soil type of both patches is the same, only the case $\phi_{\text{wp}} < \phi_{\text{dry,wet}} < \phi_{\text{crit}}$ is of interest. The other cases either revert to the

previously discussed case (Eq. 4.12) or reduce to the trivial solution where only $\Delta\phi_{\text{wet}}$ is affecting ΔP_{dry}. For $\phi_{\text{wp}} < \phi_{\text{dry,wet}} < \phi_{\text{crit}}$ I obtain $\frac{\partial E_{\text{dry}}}{\partial \phi_{\text{dry}}} = \frac{\partial E_{\text{wet}}}{\partial \phi_{\text{wet}}}$. Thus, changes in precipitation in the idealized model can be formulated as

$$\Delta P_{\text{dry}} = \tau \frac{\mathcal{A} \langle Q_{\text{net}} \rangle}{\phi_{\text{crit}} - \phi_{\text{wp}}} \left((\eta_E - \eta_A \mathcal{B}) \Delta\phi_{\text{dry}} + \eta_A \mathcal{B} \Delta\phi_{\text{wet}} \right) \qquad (4.15)$$

The behavior of Eq. 4.15 as function of $\Delta\phi_{\text{dry}}$, $\Delta\phi_{\text{wet}}$ and $\mathcal{B}$ is investigated with the help of Fig. 4.11.

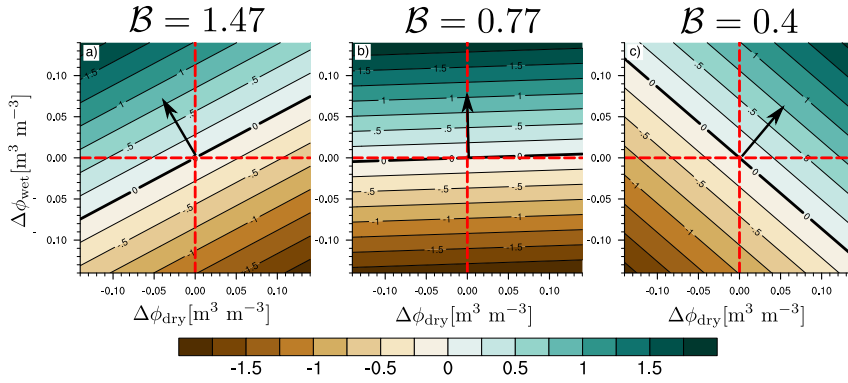In the default configuration described in section 4.3.1 the soil mois-

Figure 4.11: ΔP_{dry} as function of $\Delta\phi_{\text{dry}}$ and $\Delta\phi_{\text{wet}}$ for different values of the parameter $\mathcal{B}$. The x- and y-axes represent the variation of ϕ_{dry} and ϕ_{wet}, respectively. Note that the maximum variation is $\phi_{\text{crit}} - \phi_{\text{wp}}$, as ΔP_{dry} is computed for the regime $\phi_{\text{wp}} < \phi_{\text{dry,wet}} < \phi_{\text{crit}}$. The red dashed lines indicate no variation of the soil moisture of either one of the patches. The efficiencies are set to $(\eta_A, \eta_E) = (0.16, 0.11)$ in (a) and to $(\eta_A, \eta_E) = (0.47, 0.35)$ in (b) and (c) to match the simulation results. The black arrow indicates the direction of maximum growth, i.e. when an increase of precipitation is expected.

ture of the wet patch was kept constant, i.e. $\Delta\phi_{\text{wet}} = 0$, while the soil moisture of the dry patch was increased, i.e. $\Delta\phi_{\text{dry}} > 0$. Figure 4.11 (a) shows that, in the aforementioned case, ΔP_{dry} is negative, as in my simulations. In this case decreasing ϕ_{dry} and increasing ϕ_{wet} is the most efficient way to increase precipitation.

Figure 4.11 (b) presents the case characteristic of the simulations performed with the ID sounding. The flattening of the contour lines shows that there is little sensitivity on ϕ_{dry}, as previously discussed. Mainly increasing ϕ_{wet} would allow precipitation to increase. In the extreme case where $\mathcal{B}$ is further reduced (Fig. 4.11, c) the picture partly reverses. Both soil moisture of the wet and of the dry patch should be increased to sustain an increase of precipitation, as evaporation becomes now relevant and advection has a negligible contribution.

Figure 4.11 thus indicates that, in any case, the soil moisture of the wet patch should be increased to get more precipitation on the dry

patch. The response to changes in soil moisture of the dry patch is more subtle, and the combination of the two responses can lead to positive or negative coupling depending on the atmosphere state. This may explain why in reality both signs of the coupling are observed with different atmospheric states.

4.5 SUMMARY

Motivated by the ambiguous relationship between soil moisture, soil moisture heterogeneity and precipitation, in this Chapter I designed idealized simulations of a convective diurnal cycle using ICON-LEM. The heterogeneity in the land surface was prescribed by dividing the domain into two patches with different initial values of soil moisture. Inspired by the results of the simulations, I specifically wanted to derive a simple conceptual model that retains the minimum parameters that control precipitation over a spatially drier patch. Moreover, I wanted to use this model to understand which is the most efficient way to increase precipitation by acting on soil moisture given the opposite control of soil moisture on advection and evaporation.

Results from the simulations show, as expected, that the moisture advection over the dry patch decreases with increasing local soil moisture, while evaporation increases. The interplay between these two effects produces a decrease of precipitation with increasing values of local soil moisture for the considered case. More importantly, the simulation results indicated that such a decrease can only be correctly reproduced by assuming that advection and evaporation processes contribute differently to precipitation. Hence I model precipitation as the sum of advection and evaporation each weighted by its own efficiency (see Eq. 4.2). By using two efficiencies they become independent of soil moisture and only dependent on the initial atmospheric state.

As a second step, I conceptualize the variations of evaporation and advection with soil moisture. Evaporation can be approximated using the *bucket* model owing to Budyko (1961) (see Eq. 4.3). The advection is estimated as the product of the breeze front velocity and the gradient in near-surface specific humidity (see Eq. 4.5). A priori one would have expected a squared dependency of advection on soil moisture since both the velocity of the front and the gradient in specific humidity should be related to soil moisture. However, it turns out that the velocity of the front is independent of soil moisture as the development of convection at the breeze front and the generation of strong cold pools lead to a strong acceleration of the front that fully masks the effect of the initial surface heterogeneity.

Putting all the results together indicates that the derivative of precipitation with respect to the soil moisture of the dry patch does not depend on the actual soil moisture value. This is due to the fact that

the functional forms of advection and evaporation end up to be linear functions in soil moisture. The idealized model is valid as long as the evaporation keeps its linearity as function of soil moisture and the propagation speed of the front does not depend on the surface heterogeneity gradient, meaning strong enough cold pools.

The parameters that control the variations of precipitation with local soil moisture are the aforementioned efficiencies and a scale parameter that defines the magnitude of the advection. All these parameters depend solely on the atmospheric state. According to the values of these parameters, as estimated from the simulations, the most efficient way to increase precipitation over the dry patch is to decrease the soil moisture of the dry patch. However, if either the efficiency of evaporation becomes much larger than the one of advection or the scale parameter that defines the importance of advection decreases under a certain threshold then the response of precipitation can be reversed.

Part II

THE COUPLING OF CONVECTION WITH THE
LAND SURFACE AND THE LARGE-SCALE
FLOW IN REALISTIC SIMULATIONS

THE EFFECTS OF ADVECTION AND EVAPORATION ON PRECIPITATION OVER GERMANY

5.1 INTRODUCTION

In Chapter 3 and 4 two conceptual models have been developed to explain the variations of precipitation with respect to soil moisture over either homogeneous or heterogeneous surfaces. Although these conceptual models improved our understanding of the physical process linking soil moisture to precipitation, it is not clear whether they can help explain what is observed in reality and in particular over mid-latitude regions. Over this area of the globe the coupling of soil moisture and precipitation, and in general the strength of land-atmosphere interaction, is weakened (Koster et al., 2004).

Taylor (2015), for example, showed that over Europe the specific impact of soil moisture on convective initiation is weakened with respect to the Sahel region because of three main reasons. First, due to the abundance of vegetated areas the sensitivity of evapotranspiration to soil moisture is strongly limited. As shown in Chapter 3 plants extract soil moisture from deeper layers through their roots, thus enhancing evapotranspiration even in dry conditions. For this reason, evapotranspiration is not expected to change much with soil moisture (Budyko, 1974). Second, the synoptic forcing, that is the presence of almost constant winds in the middle troposphere, will suppress the development of mesoscale circulations mainly through a decrease of the surface temperature gradient and a modification of the thunderstorms' propagation (Froidevaux et al., 2014). Finally, over Europe thunderstorms only develop during particular periods characterized by convective instability (usually summer), while in the Sahel they are observed for most of the rainy season (Zipser et al., 2006).

This, however, does not mean that the conceptual models developed in Chapters 3 and 4 cannot be applied to more realistic data obtained from model simulations over Europe. In particular, in Chapter 4 it has been shown that precipitation variations over a spatially drier patch can be expressed as a function of soil moisture and three parameters, namely the efficiency of advection η_A, the efficiency of evaporation η_E and a scale parameter for advection $\mathcal{B}$. Computing $\mathcal{B}$ would require a knowledge of the advection dependency on soil moisture, which is difficult to derive from more realistic simulations over Europe given the aforementioned weak coupling of the land-surface with the at-

Land-atmosphere interactions weakened over Europe

mosphere. Instead, the parametrization of precipitation as weighted sum of advection and evaporation (Eq. 4.2)

$$P = \eta_A A + \eta_E E \tag{5.1}$$

Main goals

can be used to estimate the two efficiencies η_A, η_E to understand whether A and E have really different weights in a less idealized framework. This is one of the goals underlying the analysis presented in this chapter.

To that aim, I will first need to evaluate whether the conceptual model of Eq. 5.1 is still valid to explain precipitation spatial variability and its dependence on advection and evaporation in a realistic setup. More specifically, I need to assess whether two efficiencies are, as stated in Chapter 4, really necessary to express variations in precipitation, or if the simpler conceptual model of Schär et al. (1999)

$$P = \eta(A + E) \tag{5.2}$$

is enough to represent precipitation variability.

Using this model, several authors have tried to estimate the efficiency using model simulations or re-analyses. For example, Asharaf et al. (2012) quantified the importance of soil moisture-precipitation feedback processes in the Indian Monsoon by splitting the contributions of precipitation efficiency η, local evapotranspiration and remote advection to precipitation. They found that local evapotranspiration attains a minor role while remote advection and precipitation efficiency are the main drivers of precipitation variability. Wei et al. (2016) found, instead, that remote advection affects precipitation directly through the modification of the moisture balance in wet areas and indirectly by changing the precipitation efficiency in transitional zones.

Other authors have focused on estimating the precipitation recycling ratio, i.e. the fraction of precipitation that comes from evaporation in the same region (Eltahir and Bras, 1996; Trenberth, 1999; Burde and Zangvil, 2001; Van der Ent et al., 2010). This fraction of precipitation is formally equivalent to $\eta_E E$ in my conceptual model of Eq. 5.1. Van der Ent et al. (2010) found that, on average 40 % of the terrestrial precipitation originates from land evaporation. This value is heavily reduced when considering a limited area: for example, over Europe the regional precipitation recycling ratio is about 20 %. All these studies focused on continental to global scales and on seasonal to yearly time scales, often using models where convection is parametrized and only considering the model of Schär et al. (1999) to estimate precipitation efficiency.

Instead, in this chapter I want to focus on the effect of the local (evaporation) and remote (advection) processes on a diurnal time scale in models where convection is explicitly resolved. A diurnal cycle over

Germany will be simulated using realistic forcing and a modeling framework similar to the one employed in Chapters 3 and 4. The realistic forcing is derived from an exceptional period of severe thunderstorms that affected Germany between May and June 2016, which was also characterized by a weak synoptic forcing. First, the basic observational features of this period will be described in section 5.2. In section 5.3.1 and 5.3.2 the modeling framework and the method used to estimate the efficiencies will be briefly described. Results will be presented in section 5.4.1, 5.4.2 and 5.4.3 for 6 June 2016 and in section 5.5 for the additional day simulated, 5 June 2016. Finally, a brief discussion of the results will be presented in section 5.6.

Outline of the chapter

5.2 THE EXCEPTIONAL SEQUENCE OF THUNDERSTORMS OVER GERMANY IN MAY-JUNE 2016

During a 15-day period, spanning from 26 May to 10 June 2016, Germany and the neighboring regions were affected by a period of severe thunderstorms producing heavy precipitation, 10 Tornadoes and hail which caused damages running into billions of Euros (Piper et al., 2016). The accumulated precipitation amounts widely exceeded 100 mm in most of the country and 250 mm in several parts of Baden-Württemberg and Bavaria. Only the north-eastern part of Germany was affected by drier conditions which brought total accumulated precipitation to almost zero (Piper et al., 2016, their Figures 1, 4).

The strongest events were concentrated between 26 and 29 May 2016, due to the vicinity of an upper-level trough which induced the formation of multiple Mesoscale Convective Systems (MCSs) over southwestern Germany (Piper et al., 2016). Instead, during the remaining days of May and June, an Ω-blocking pattern (Rex, 1950; Tibaldi and Molteni, 1990) established over Europe, as shown by Fig. 5.1. Such configuration prevented the typical westerly flow to reach central Europe and enhanced instability caused by diurnal surface heating and nocturnal cooling. During these days the synoptic forcing reached an absolute minimum: the wind speed at 500 hPa at four German sounding stations decreased below 3 m s^{-1} between 6 and 8 June 2016 (Piper et al., 2016). This resulted in convection being strongly forced by the surface and quasi-randomly distributed over most of Germany. As a consequence, during the same period, the precipitation evolution over time followed a distinct diurnal cycle.

Synoptic configuration

This can be seen in Fig. 5.2 where the hourly precipitation averaged over Germany was extracted from radar data. The aforementioned strong events strike out in the period between 29 and 31 May 2016 with a peak of 0.58 mm h^{-1} on 30 May 2016. Instead, between 3 and 8 June 2016, the maxima of precipitation rarely exceed 0.2 mm h^{-1} and closely follow a sin^2 shape, i.e. the diurnal cycle induced by diurnal radiation. As shown in the upper right inset of Fig. 5.2, dur-

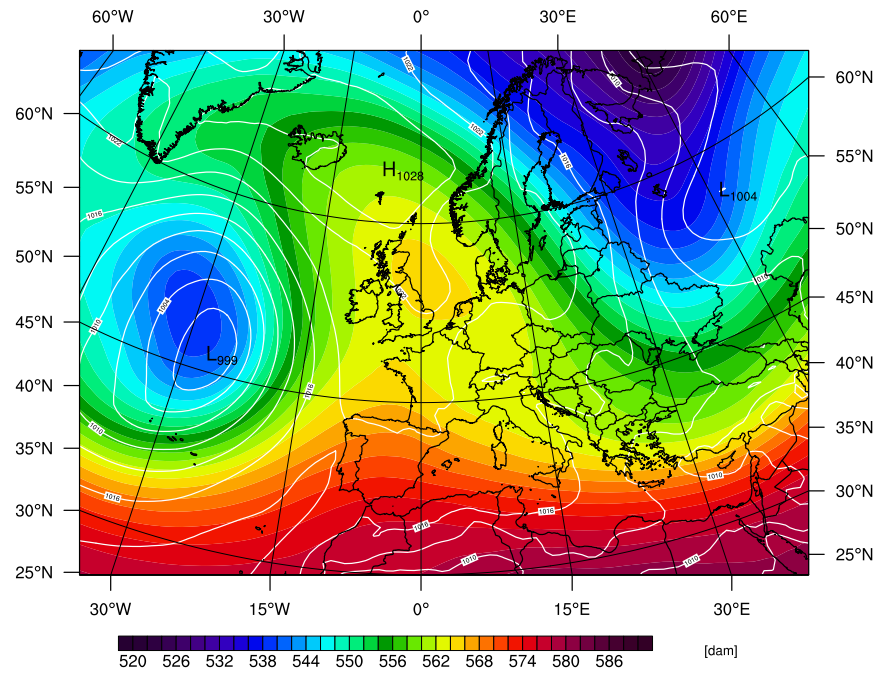*Observed diurnal cycle of precipitation*

Figure 5.1: 500 hPa Geopotential Height (color shading, dam) and MSLP (hPa) averaged between 4 June 2016 and 8 June 2016. Data from ERA-INTERIM.
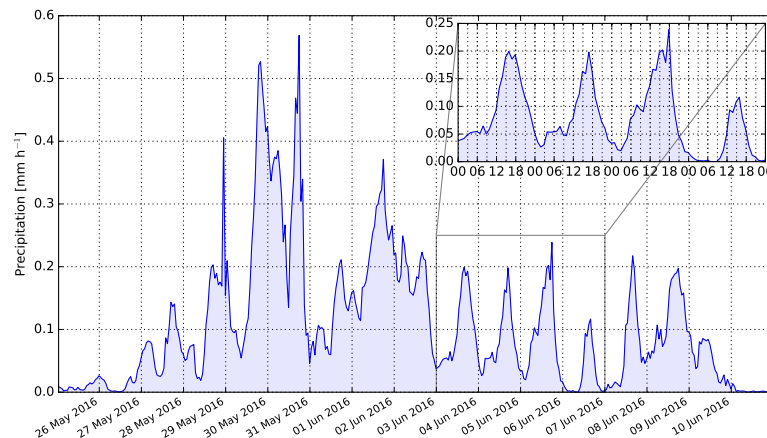
Figure 5.2: Hourly precipitation rate derived from RADOLAN data, that is radar data calibrated with surface observations. The upper-right inset shows a detail of the time series between 3 June 2016 00 UTC and 7 June 2016 00 UTC.

ing this period the diurnal cycle of precipitation peaked in the late afternoon and showed a nocturnal minimum which extended up to 06 UTC in the morning and reached zero on 6 June.

This day was specifically interesting for several reasons. First, as stated before, the synoptic forcing was negligible. Second, as shown by satellite imagery (e.g. Fig. 5.3) clouds appeared to be strongly forced by the surface. The spatial structure of clouds observed in this image partially resembles the one described in Fig. 1.3. Clouds over

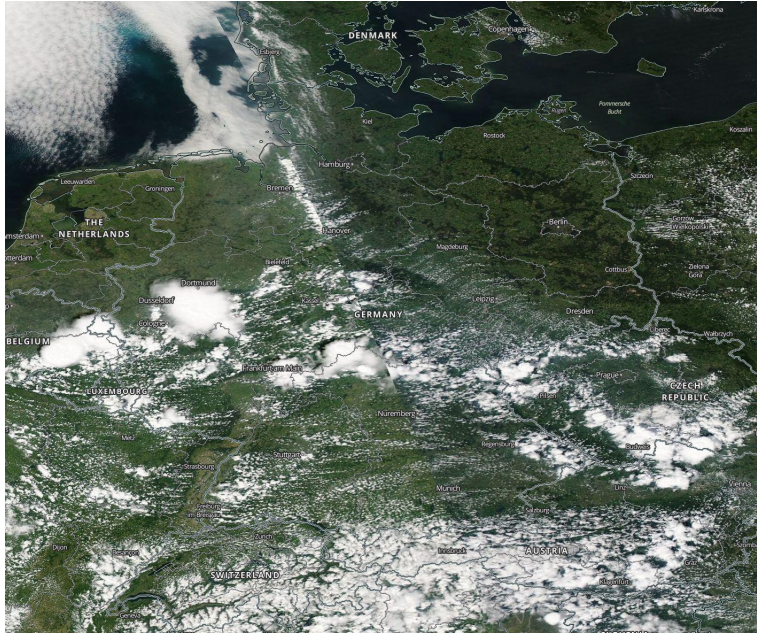**Figure 5.3:** MODIS satellite imagery acquired on 6 June 2016 at 13 UTC.

south-western Germany appear to have formed mostly over forest or vegetated areas while the Rhine valley and the few lakes appearing in the bottom of the picture are cloud-free. The thunderstorms appearing at this time in south-western Germany remained active during the afternoon but did not grow into organized structures, albeit having cloud top brightness temperature of about -60°C (not shown). For this reason, the diurnal peak of precipitation intensity during this day was the smallest among the entire period (see Fig. 5.2). Given the low synoptic forcing and the distinct diurnal cycle that characterized this day, it was chosen as an ideal candidate for the analysis.

5.3 METHODS

5.3.1 *Modeling framework and simulations*

In order to study the interplay between advection, evaporation and precipitation over Germany, model simulations of a diurnal cycle are performed with ICON-LEM in hind-cast mode. The configuration is identical to the one used in Heinze et al. (2016) in terms of the dynamical core, model physics, domain and of the way initial and boundary conditions are prescribed. The only difference concerns the representation of microphysical processes which employs the single-moment 3-cat ice microphysics. This is the same microphysical scheme used in the model configuration of Chapters 3, 4 and allows to have better consistency when comparing results. In fact, the employment of a different microphysics scheme would greatly affect the partition of the terms in the moisture balance (see Appendix C.3) thus making a

comparison difficult.

From the set of domains available in Heinze et al. (2016) the outermost domain, DOM01, with a grid spacing of approximately 625 m, was chosen. Although this corresponds to more than a doubling of the grid spacing previously used in Chapters 3 and 4, performing the runs with a much higher resolution would have been too much expensive. Furthermore, a grid spacing of approximately 600 m already allows for an explicit representation of deep convection (Bryan et al., 2003). The domain covers entirely Germany and parts of the surrounding regions, including the Alps and the North Sea.

Convection parametrization is turned off and the turbulence is parametrized as in Dipankar et al. (2015) and in Chapters 3, 4. Initial and boundary conditions are taken from the COSMO-DE model (Doms et al., 2011): the latter are prescribed every hour in a nudging area 8 cells wide. The model output is saved every 15 minutes to allow for a comprehensive description of the convective and diurnal cycle and to obtain data comparable to Chapter 4. The simulations are run for 24 hours starting at midnight. I simulate a total of 2 days, namely 5 and 6 June 2016, in order to have a larger data sample to test the conceptual model against.

In order to obtain the terms of the moisture balance E, A, P the same methodology delineated in Chapter 4 and Appendix C.3 is used. That is, from the 2-D model output vertically integrated values of microphysical tracers (cloud water, rain, ice, graupel, snow and hail) are used to estimate the variation in time of the total moisture content, which is combined with surface evaporation and precipitation to estimate advection as residual.

5.3.2   *Estimation of the efficiencies*

As shown in Chapter 4, in order to estimate the efficiencies one needs to have at least 2 individual values for each one of the terms in Eq. 5.1, namely precipitation P, advection A and evaporation E. This is easy to achieve in an idealized framework, as several sensitivity experiments can be performed by modifying the surface state, thus obtaining different values for A, E and P. This way, the same initial atmospheric state is used for every sensitivity experiment, thus strengthening the hypothesis that the efficiencies are strictly related to the atmospheric state (see again Chapter 4). However, when analyzing data from a single realistic simulation the same approach can not be used. Furthermore, in the idealized model of Chapter 4, I only considered the superposition of a single dry and wet patch, while in reality patches of different area and with different soil and vegetation types are distributed over the land surface.

Although it is evident that several issues should be considered when applying the conceptual model of Chapter 4 to more realistic simu-

lations, an extensive treatment of these issues is beyond the scope of this chapter. For this reason, my approach aims at providing a first simple method needed to obtain the values of the efficiencies η_A and η_E by using different values of A, E, P. Suggestions on how to refine this method will be given in the summary, section 5.6.

First of all, in order to reduce the spurious effect of orography and large-scale heterogeneities, the analysis is focused on limited regions of the simulation domain where the terrain is approximately flat and the land-surface shows similar features. Second, in order to obtain different values of A, E and P the aforementioned regions of the simulation domain are divided into several non-overlapping squared latitude-longitude boxes having the same width, which can then be varied when performing the analysis (see Fig. 5.6 for a graphical explanation of this subsetting algorithm). For every box, averaged values of A_{box}, E_{box} and P_{box} are computed similarly to what was done in Chapter 4. By collecting all these values one can then fit Eq. 5.1 and obtain the values of the two efficiencies.

Estimating A, E and P over the domain

Only the positive values of A_{box} and E_{box} are retained when performing the fit to ease the interpretation of results. The fit employs a non-linear least squares algorithm and provides as output the optimal values of the parameters η_A and η_E as well as the estimated covariance matrix ($\mathcal{S}_{i,j}$ with $i \in [1,2]$, $j \in [1,2]$) of the parameters. The diagonals of this matrix ($\mathcal{S}_{0,1}$ or $\mathcal{S}_{1,0}$) provide the variance of the parameters estimate which can be used to compute one standard deviation errors of the parameters $\sigma = \sqrt{\mathcal{S}_{0,1}}$. For every box also a single efficiency $\eta_{\text{box}} = \frac{P_{\text{box}}}{A_{\text{box}} + E_{\text{box}}}$ is computed following Schär et al. (1999) in order to compare it to the estimated η_A, η_E.

Since one of the goals is to understand which one of the two conceptual models (Eq. 5.2 or 5.1) can better explain precipitation variability over the chosen regions, the coefficient of determination χ^2 (Steel and Torrie, 1960) is computed in both cases using the methodology explained hereinafter. If P_{box} is the average of precipitation over a box and $P_{\text{box}}^{\text{fit}}$ the respective value predicted with the fit, χ^2 is computed as:

Estimating the goodness of the fit

$$\chi^2 = 1 - \frac{\sum_{\text{boxes}} (P_{\text{box}} - P_{\text{box}}^{\text{fit}})^2}{\sum_{\text{boxes}} (P_{\text{box}} - \sum_{\text{boxes}} P_{\text{box}} / N_{\text{boxes}})^2} \tag{5.3}$$

where $\sum_{\text{boxes}} P_{\text{box}} / N_{\text{boxes}}$ is, effectively, the average precipitation over all the boxes. $P_{\text{box}}^{\text{fit}}$ may be computed using one of the two conceptual models of Eq.s 5.1, 5.2. In the first case, the two efficiencies obtained with the fit are used in Eq. 5.1 to obtain $P_{\text{box}}^{\text{fit}}$. In the second case, a single efficiency representative of all the boxes is estimated by computing the average of all the single efficiencies in every box, i.e.

$$\eta = \frac{1}{N_{\text{boxes}}} \sum_{\text{boxes}} \eta_{\text{box}} \tag{5.4}$$

In the latter case, the χ^2 may be negative given that η hasn't been obtained through a fit but rather estimated using Eq. 5.4. When observed, negative values of χ^2 essentially mean that the model is a poor fit to the data. For the conceptual model characterized by two efficiencies, instead, χ^2 varies between 1, when the model completely explains the variability of the observed precipitation, and 0, when the model doesn't explain at all the variability.

I would like to stress that, by using this method, in both cases I'm attempting to predict precipitation in every box by using a mean state over the whole region. More precisely, by using values estimated from contiguous areas of the domain I assume that the atmospheric state in every box does not differ appreciably. This is also supported by the fact that the large-scale state consists of a high-pressure ridge within which the atmospheric state does not vary much (see Fig. 5.1). Regarding the latter remark, it should be noted that the choice of this particular day is fundamental, as days with strong synoptic forcing will likely change the horizontal structure of the atmosphere.

5.4   ANALYSIS FOR 6 JUNE 2016

5.4.1   *General features of the diurnal cycle*

Precipitation

The simulated diurnal cycle of convection and precipitation resembles the observed one and follows the typical behavior that one expect to see for mid-latitude regions with weak synoptic forcing (Schlemmer, Hohenegger, et al., 2012). As shown in Fig. 5.4 (a) precipitation peaks between 12 and 15 UTC with a maximum of about 0.15 mm h^{-1}, not far away from the observed one (Fig. 5.2). The difference is likely due to various reasons, including the fact that the area used for the average is different and precipitation rate derived from radar data use approximated equations. Furthermore, in Fig. 5.4 the average is computed only for grid point located at an altitude less than 400 m. It should be also noted that the first precipitating events observed between 00 and 06 UTC are likely spurious and due to the initial spin-up

Evaporation

of the model. Evaporation also shows a distinct diurnal cycle with a peak around 12 UTC, as expected because of the weak synoptic forcing and distribution of the surface radiative heating. Note that this average includes different soil types as well as vegetated, bare soil or urban areas.

CAPE and CIN

Figure 5.4 (b) delineates a decrease of convective inhibition and the subsequent increase in convective instability during the early morning. Not surprisingly, when CIN reaches a minimum and CAPE starts to increase, convection is triggered and the first precipitation events are recorded. The fact that the absolute maximum of CAPE and CIN are comparable in magnitude indicates that conditions are not prone to very deep convection during this day. The diurnal cycle of relative
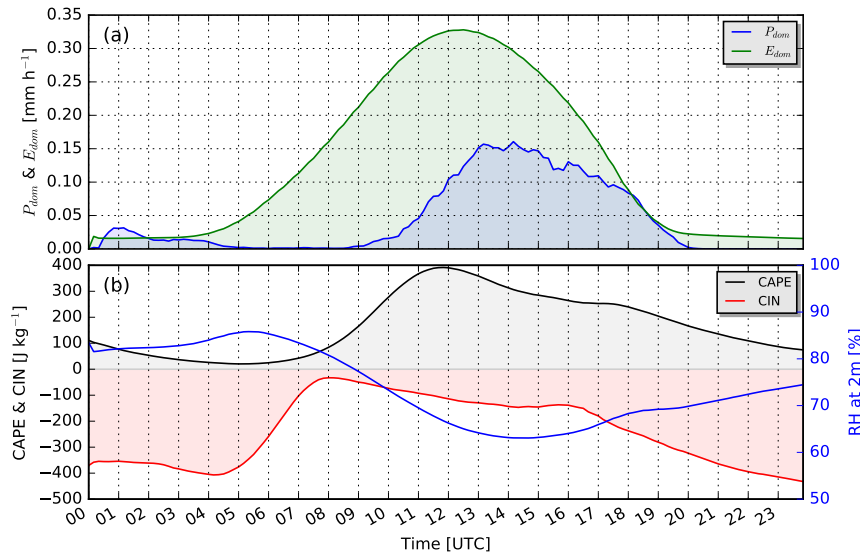
Figure 5.4: Time series of domain-averaged variables for grid points located below
400 m. Upper panel shows precipitation (blue line) and evaporation
(green line) while the lower panel shows CAPE (black line), CIN (red line)
and relative humidity at 2 m (blue line).

humidity close to the surface includes a moistening during nightly
hours and a drying during daytime likely because of the surface heat-
ing.

By integrating the values of Fig. 5.4 (a) over the entire diurnal cy-
cle, and computing the advection as residual, Fig. 5.5 is obtained.
Although I am not interested in validating the skill of the modeling
framework against observations, it can be noted that the horizontal
distribution of precipitation resembles the one measured by the radar
(not shown). Events are randomly distributed, especially over the   *P, A and E*
south-western part of Germany, and do not show any appreciable de-
gree of organization. Local maxima exceeding 40 mm are surrounded
by dry patches with a length scale comparable to the employed grid
spacing. By inspecting the horizontal distribution of the precipitation
diurnal cycle (not shown) it appears that the events over the south-
western part of Germany peak in the afternoon (between 12 and 18
UTC), while the ones developing in the eastern part of the domain are
developing mostly in the morning (between 09 and 12 UTC).

Evaporation shows different horizontal features which are related
both to the terrain characteristics (e.g. soil type, orography) and to
the synoptic evolution. For example, the minimum observed in the
north-western part of Germany (both over land and sea) is mainly
due to the persistence of fog and low-level clouds which prevented ra-
diation from reaching the surface. The persistence of this cloud layer
can be observed also in satellite imagery (not shown). Conversely,
the stripe-like distribution of minima observed in the southern part
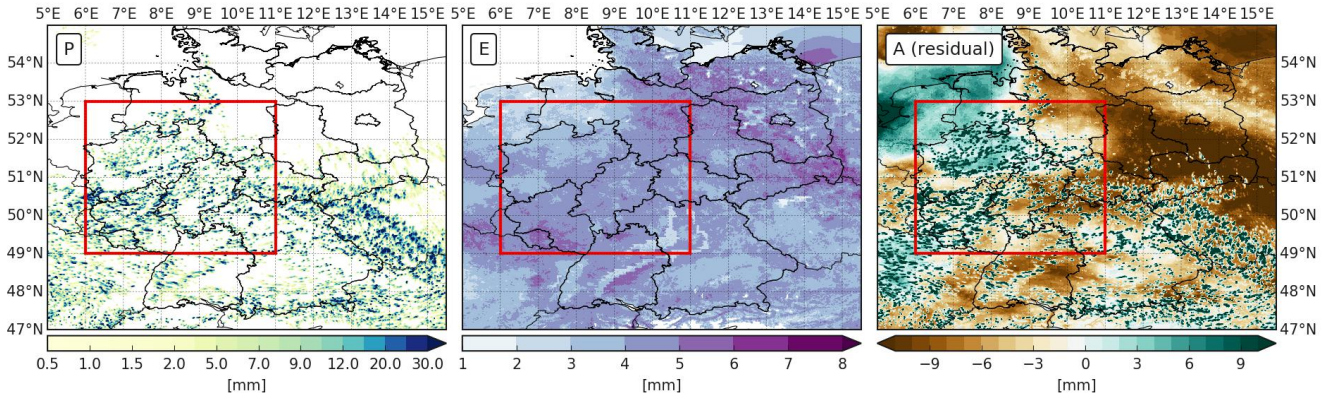of Germany is due to the presence of orography. Thus, during this

Figure 5.5: Precipitation *P*, Evaporation *E* and Advection *A* terms of the moisture balance integrated over the entire diurnal cycle. The red box highlights the region used for the analysis afterward.

day high values of evaporation are mainly observed over cloud-free and flat regions.

Advection inherits many small-scale structures observed in the precipitation distribution, as it is computed as residual from *P* and *E*. In precipitating areas it exhibits intense localized maxima, given that here precipitation removes most of the moisture in the atmospheric column which cannot be replenished by evaporation alone. Large patches of positive (convergence) and negative (divergence) advection appear to be superimposed over this small-scale structures.

What does $\eta > 1$ mean?

Note that the overall balance of advection over Germany is negative as the average over the entire domain is approximately -2.8 mm. Since the domain averages of *P* and *E* are 1.6 mm and 3.2 mm, respectively, according to the definition used in Schär et al. (1999) this would yield a precipitation efficiency $\eta = 4.3 \gg 1$ which contrasts with the results of Schär et al. (1999) and Asharaf et al. (2012).

This is probably due to the different time scale considered, as noted by Zhou et al. (2016). When considering long time scales (monthly to seasonal) the atmospheric storage term ($\frac{1}{\rho_w} \int_0^\tau \int_0^H \frac{\partial q_{tot}}{\partial t} \rho_a \, dz \, dt$ in Eq. C.3) is negligible (Burde and Zangvil, 2001; Fitzmaurice, 2007). In other words, over seasonal time scales, *P*, *E* and *A* are balanced together and yield a null sum. Instead, over a diurnal cycle and a limited region, like the one considered in my study, the atmospheric storage term can not be neglected. This causes an underestimation of the denominator in Eq. 5.2, which results in a larger efficiency.

5.4.2 *Analysis of the moisture balance terms*

Figure 5.6 shows a detail from Fig. 5.5 where the 4×5 degrees region used for the analysis is highlighted. For this region, box-averaged values of *A*, *E* and *P* are computed as explained in section 5.3.1. However, before fitting Eq. 5.1 to these values, it is useful to in-
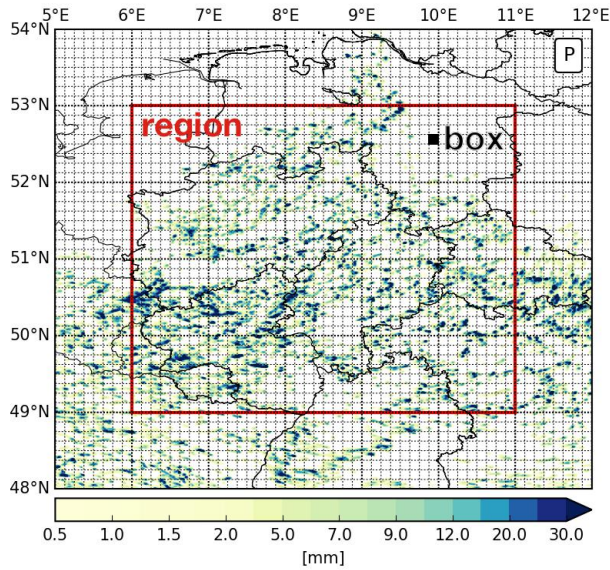
Figure 5.6: As in Fig. 5.5 but for a portion of the domain. Latitude/Longitude minor ticks are placed every 0.125 degrees to highlight the size of the boxes used in the analysis afterward.

spect the data and its dependency on the selected region. For this reason, Fig. 5.7 shows the histograms and Gaussian Kernel Density Estimate (GKDE) of P_{box}, A_{box} and E_{box} computed within two different regions. In particular, the two nested regions with boundaries lat$\in$ [49, 53], lon$\in$ [6, 11] and lat$\in$ [50, 53], lon$\in$ [6, 9] have been chosen. This choice is mainly driven by the necessity of including most of the precipitating events that are peaking in the afternoon and of considering a relatively flat terrain. By analyzing Fig. 5.7 it can be seen that the choice of a different region does not greatly affect the distribution of *A*, *E* and *P*. In both the chosen regions precipitation shows a maximum number of events for small values, which is expected given the presence of small-scale events. Local maxima appear in the right side of the distribution but are fairly rare, as one can see from Fig. 5.6. Evaporation shows a distribution with two distinct maxima, probably because of the presence of two different soil types in this area. It is also interesting to note how the distribution of evaporation is narrower than the one associated with precipitation or advection. The latter term is distributed similarly to precipitation but shows instead a peak for intermediate values, around 3 mm.

Regions chosen for the analysis

5.4.3 *Efficiencies*

A constant value of the spacing (0.125 degrees) and a fixed region (lat$\in$ [49, 53], lon$\in$ [6, 11]) are used at first to aggregate all the box-averaged values of *A*, *E* and *P*. Figures 5.8 (a) and (b) show that evaporation and advection are positively correlated to precipitation.
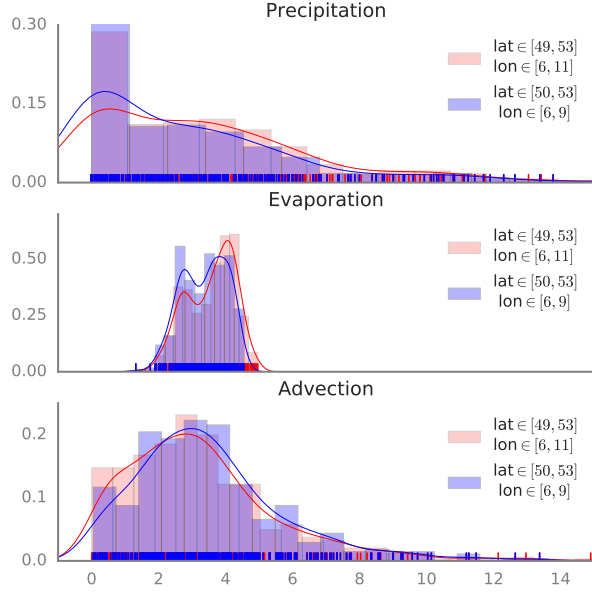
Figure 5.7: Normalized histograms and GKDEs of box-averaged diurnal-accumulated precipitation P_{box}, evaporation E_{box} and advection A_{box} [mm] computed in regions with different extents. Note that the y-axis doesn't have units since it represents the value of both the density function and of the normalized histogram. It can be interpreted as a normalized frequency of occurrence.

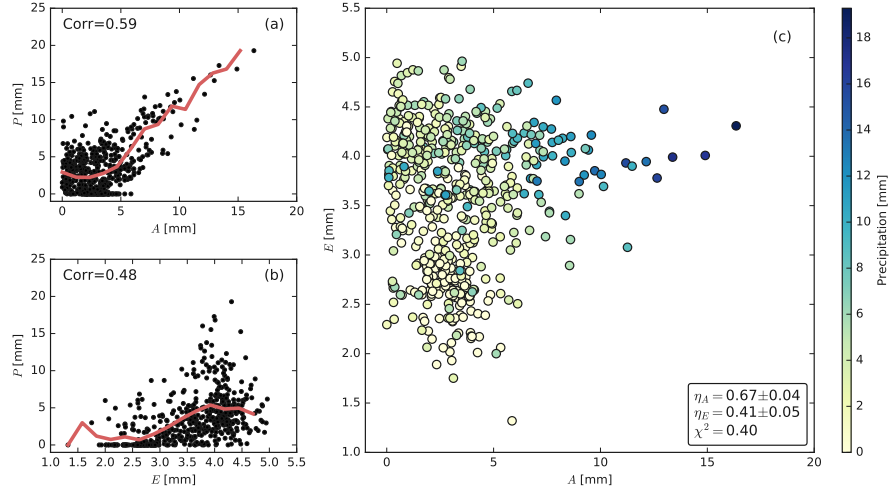This suggests that evaporation, advection and precipitation are cor-

Figure 5.8: Scatter plot of (a) P vs. A and (b) P vs. E. The red line represents a binning of the data using a total of 15 bins while Corr indicates the Pearson correlation coefficient bounded between -1, completely anti-correlated, and 1, completely correlated. In (c) a scatter plot of A vs. E is represented by means of circular marker colored according to the value of P. In the lower-right inset the values of the parameters obtained from the fit are reported, namely the advective efficiency η_A, evaporative efficiency η_E and the coefficient of determination χ^2. The model used to fit the data follows Eq. 5.1. See section 5.3.2 for details.

related not only in the conceptual model but also in more realistic simulations. However, in order to find statistically significant and plausible values for the efficiencies, the weighted sum of A and E needs to be correlated with precipitation as well.

Fit of the conceptual model

This can be seen by analyzing Fig. 5.8 (c), where the scatter plot of A and E is combined with precipitation amounts shown through a color scale. If the conceptual model, i.e. Eq. 5.1, would perfectly explain the values of precipitation then one would expect to see larger values of P in the upper-right corner of Fig. 5.8 (c) linearly decreasing towards the bottom-left corner with a gradient proportional to the efficiencies. However, Fig. 5.8 (c) already suggests that the correlation is not perfect.

The efficiencies computed from the fit are shown in the lower-right inset of Fig. 5.8 (c). They show a larger value of η_A with respect to η_E, which agrees with the finding of Chapter 4. However, as already anticipated, the fit is not able to entirely explain the variance of precipitation, as shown by the coefficient of determination χ^2. The latter is slightly larger than 0.4, indicating that the model is only partially able to explain the variance of P_{box} among the boxes in the chosen region using the two estimated efficiencies.

Efficiencies with different box widths

These estimates strongly depend on the width of the box chosen to compute the averages, as it can be seen in Fig. 5.9. There the values obtained from the fit using different box widths are reported, together with the value of χ^2. In Fig. 5.9 (a) it can be seen that the efficiency of advection η_A quickly approaches 0 for box widths bigger than 30 km. Instead, the efficiency of evaporation η_E (Fig. 5.9, b) increases with a similar but positive trend and reaches a stable value of approximately 0.7. These observations, taken together with the fact that χ^2 steadily increases with the grid spacing (blue markers in Fig. 5.9, d), suggests that the conceptual model of Eq. 5.1 is able to better explain the variability of precipitation when the dependency on A is removed.

Effective contributions of advection and precipitation

These results need to be carefully interpreted. Although one would expect A to decrease as the size of a chosen region over Earth is increased, the condition $\eta_A \to 0$ more precisely means that, for example, an increase in advection does not lead to an increase in precipitation. That is, although $A \neq 0$, the amount of precipitation correlates more with E, thus yielding $\eta_A \simeq 0$ and $\eta_E > 0$. This agrees with the fact that, during this day, convection was strongly forced by surface evaporation, as almost no synoptic forcing was present. Mesoscale circulations induced by surface heterogeneity do contribute to precipitation through the advection term for small box widths but average out to 0 when increasing the size of the box. Furthermore, given that precipitation is randomly distributed over the domain (Fig. 5.6), and given that the presence of mesoscale circulations would cause convection to organize (Avissar and Liu, 1996), it is very likely that the contribution of advection through mesoscale circulations is not so
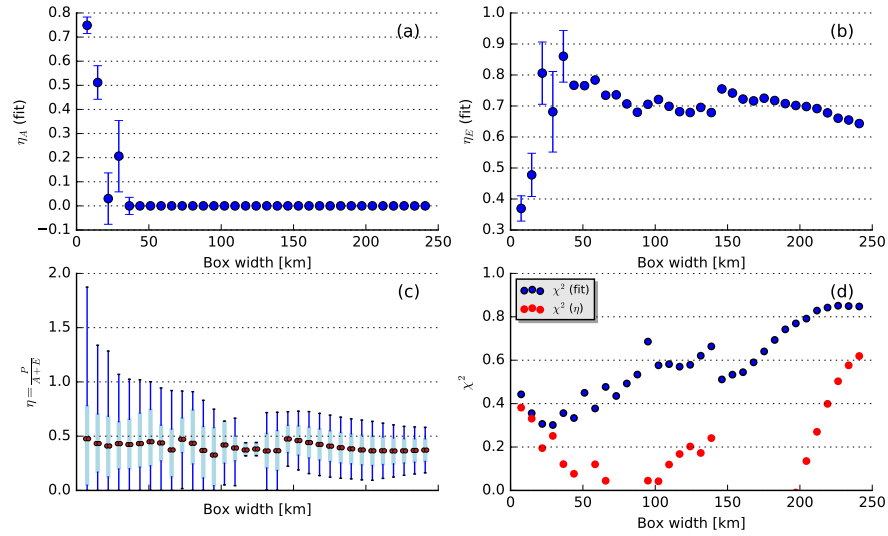
Figure 5.9: Values of (a) η_A and (b) η_E obtained with the fit as in Fig. 5.8 but for different box widths. The vertical bar on every point is showing the range of the estimated parameter using 1 standard deviation. When no bar appears the fit was not able to determine the covariance matrix. In (c) a box plot of the efficiency, computed simply as $\eta_{\text{box}} = \frac{P_{\text{box}}}{A_{\text{box}} + E_{\text{box}}}$, is shown. The box extends from the lower to upper quartile values of the data, while a closed circle indicates the mean value. The whiskers extend from the box to show the range of the data while fliers points are not shown. In (d) the χ^2 of the fit is shown with the blue markers while the χ^2 obtained by using a single efficiency is shown with the red markers. The value of the box width has been converted into km from degree taking into account the Earth's curvature to ease the interpretation of results.

pronounced during this day and over this region.

Single efficiency   When computing a single efficiency $\eta_{\text{box}} = P_{\text{box}}/(A_{\text{box}} + E_{\text{box}})$ for every single box (Fig. 5.9, c) it shows a considerable spread for box widths smaller than 50 km, probably because of local maxima in precipitation which are not smoothed out over such a limited area. It is interesting to note that the range of η_{box} reaches a minimum for box widths around 120 km. The efficiency estimated with such box width is approximately 0.45, which is different from the residual efficiency of evaporation estimated from the fit with the same box width, i.e. around 0.7 (Fig. 5.9, b). This is a consequence of the chosen model, that is Eq. 5.1. In fact, when removing the dependency on advection with a zero η_A the only source of moisture available in the model is evaporation, while in the computation of η both sources are always available.

Something interesting appears when considering the χ^2 relative to the single efficiency η (red markers in Fig. 5.9, d). First of all, one can note that the χ^2 of this simpler model (Eq. 5.2) is always smaller than the one obtained with the more complex model using two efficiencies. Thus, the conceptual model of Eq. 5.1 is more able to explain precip-

itation variations inside this region by removing the dependency on advection while still effectively using a single efficiency (the reader should be reminded that, already for box widths larger than 50 km, η_A is estimated to be 0). Second, the increase of χ^2 with larger box widths agrees with the fact that, when converging to the whole region, the simple model is able to explain precipitation's variability, as can be seen by computing the average of P, A and E over the entire region highlighted in Fig. 5.5 and 5.6. In this case, I obtain an estimated efficiency of $\eta = 0.402$ which is not far from the one estimated from the average of all the boxes with different widths in Fig. 5.9 (c).

5.5 ANALYSIS FOR 5 JUNE 2016

In this section I present results obtained with the additional day simulated, i.e. 5 June 2016. The observed evolution of convection and precipitation during this day showed a less pronounced diurnal cycle, with many organized thunderstorms developing in the south-western part of Germany already during the morning (not shown). Furthermore, as noted already in Fig. 5.2, precipitation events remained active during the night and precipitation intensity never reached 0. This is also observed in the simulation where the precipitation intensity reaches a minimum of about 0.05 mm h^{-1} around 05 UTC and a diurnal peak of about 0.25 mm h^{-1} around 14 UTC (not shown), which is similar to the one observed in radar data (Fig. 5.2). The evolution of CAPE and CIN (not shown) is very similar to the one simulated on the day after although convection seems to be capped by a stronger inversion due to larger values of CIN which never vanishes.

Figure 5.10 presents the same analysis of the moisture balance terms done in Fig. 5.5 but for 5 June 2016. The horizontal distribution of precipitation in this case greatly differs from the one observed on the day after. Although the north-western regions are still affected by dry conditions, in the southern part of the domain precipitation appears to be organized in bands which have larger size than the individual cells. Evaporation is enhanced over the northern part of the domain and reduced in the south probably because of the presence of several thunderstorms which developed during the morning and reduced the surface incoming radiation. The domain-averaged value of evaporation shows nevertheless a similar diurnal evolution in both days (not shown). Advection shows again a superposition of large-scale features and small-scale features due to the presence of local precipitation maxima. Also for this day the advection averaged over the entire domain is negative (-1.2 mm). Combining this with the values of domain-average precipitation and evaporation an efficiency of 2.3 is obtained.

The analysis for this day focuses on two different regions (red boxes in Fig. 5.10) which present different features. In the first region,
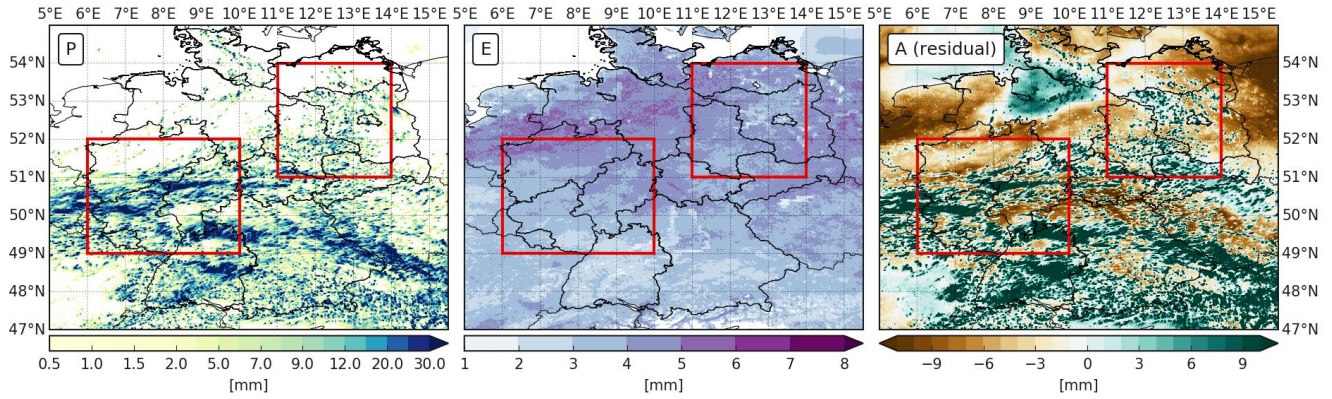
Moisture balance terms

Figure 5.10: Precipitation *P*, Evaporation *E* and Advection *A* terms of the moisture balance integrated over the entire diurnal cycle for 5 June 2016. The two red boxes represent the ones used for the analysis.

over north-eastern Germany, mostly scattered convection is observed, while in the second region, over south-western Germany, several organized thunderstorms develop in the afternoon. The resulting values of precipitation for these two regions, averaged in boxes of 0.125 degrees width, show indeed different distributions, as displayed in Fig. 5.11. In the south-western region individual maxima reach up
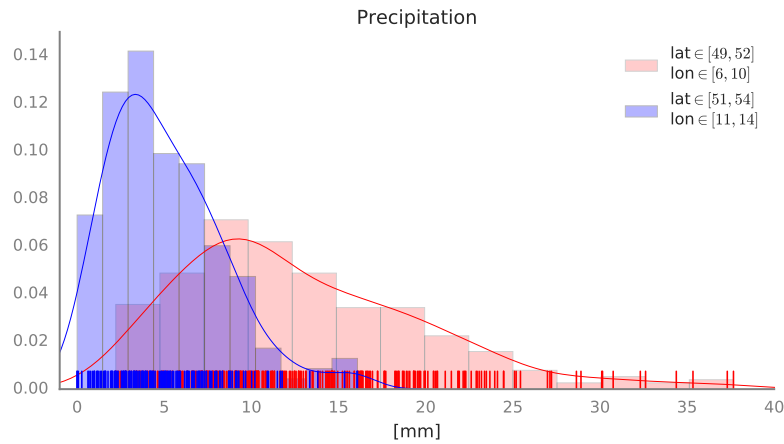

Figure 5.11: Normalized histograms and GKDEs of diurnal accumulated precipitation, evaporation and advection [mm] computed in regions with different extents.

to 40 mm, while overall precipitation values are spread over a wide interval. Instead, in the north-eastern region, precipitation values are smaller and narrowly distributed.

Analysis of A, E, P for the western region

Analyzing the data collected in the western region (Fig. 5.12) a strong positive correlation between precipitation and advection stands out. Instead, evaporation does not appear to be correlated with precipitation. However, when both advection and evaporation are combined together in the conceptual model, precipitation can be explained with
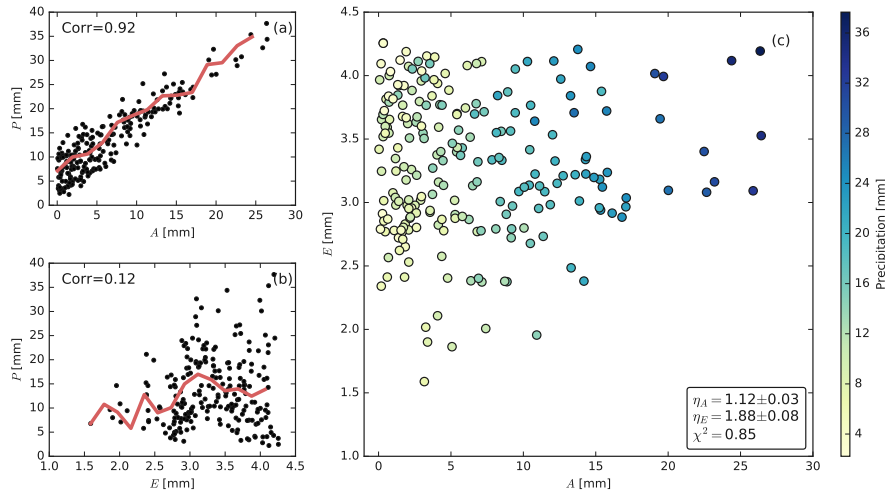
Figure 5.12: Same as in Fig. 5.8 but for the area in western Germany highlighted in Fig. 5.10.

surprisingly good accuracy. The distribution of the color shades in Fig. 5.12 already suggests that the model represents pretty well the values of precipitation as the transition between blue and yellow colors approximately follows tilted lines in the (A, E) space. The χ^2 obtained from the fit is above 0.8 and the efficiencies computed in this case are $\eta_A = 1.12$ and $\eta_E = 1.88$.

By computing the efficiencies for different box widths it can be again noted that the efficiency of advection becomes 0 when the grid spacing exceeds 100 km (Fig. 5.13, a). As a result of this, since the values of evaporation are not large enough to be the only source for precipitation, η_E steadily increases and reaches values larger than 2.5. However, the values of χ^2 (Fig. 5.13, d) do not clearly indicate that
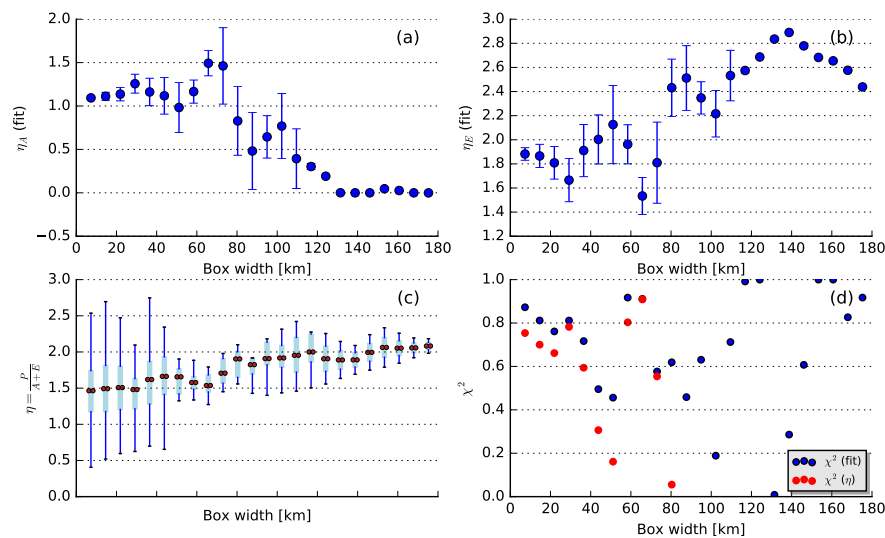

Figure 5.13: As in Fig. 5.9 but for the western region of Fig. 5.10.

the model is able to better capture the variations of precipitation with increasing width of the boxes. Instead, the values of χ^2 oscillate between 1 and 0, making it hard to draw any conclusions about the performance of the conceptual model. Nevertheless, it appears that, during this day, both advection and evaporation have a role in determining precipitation variability. The best agreement with the simulated values of precipitation is obtained for box widths of 60 and 120 km, respectively. For these values the estimated efficiencies are $\eta_A = 1.2$, $\eta_E = 1.8$ and $\eta_A = 0.5$, $\eta_E = 2.5$.

Some words are needed on the interpretation of these specific results. In fact, the contribution of advection and evaporation on precipitation can not be only measured by the efficiencies, as these values are then multiplied by the relative source. Evaporation, in absolute terms, shows values smaller than the one of advection (see e.g. Fig. 5.7 and 5.8). Thus, when estimating the contribution of A (namely $\eta_A A$) and E ($\eta_E E$), in some of the boxes $\eta_A A$ may be larger than $\eta_E E$, even though $\eta_A < \eta_E$.

Single efficiency   It is interesting to note that, also in this case, the single efficiency η does not converge to the value of η_E when the dependency on the advection is removed, i.e. for larger box widths. Furthermore, even when considering the single efficiency, the values appear to be larger than 1 for almost every box width larger than 50 km. This is a strong indication of the fact that, even when considering larger areas, efficiency is not bounded to 1, as explained in the introduction.

In this case the conceptual model with a single efficiency is not able to explain precipitation variations at all, as proved by the decrease of χ^2 (red points in Fig. 5.13) for widths larger than 80 km. It should be noted that this decrease of χ^2 does not necessarily contradict the reduction seen in the range of the computed efficiency (Fig. 5.13, c). This means that, although the ratio $P_{box}/(A_{box} + E_{box})$ is similar in the boxes, the spatial variability of precipitation can not be explained using a single efficiency, thus the null or even negative χ^2 (see again section 5.3.2).

For the northern region the correlation P vs. A is much smaller and the precipitation values are more scattered in the E-A space (see Fig. 5.14 c). As a result, the difference between the value predicted by the model and the simulated values of precipitation is large and the χ^2 small. Thus, the values of the efficiencies computed are not representative of the atmospheric state given that the model is not able to capture the variations of precipitation. This shows how different regimes of precipitation can affect the estimate of the efficiencies and that a correlation between P and one of the two variables A, E is not sufficient to say that those are correlated together using Eq. 5.1. Finally, it should be noted that, in this area, the estimate of the efficiencies is made difficult by the fact that many grid points are characterized by small amounts of precipitation, which cause numerical instability
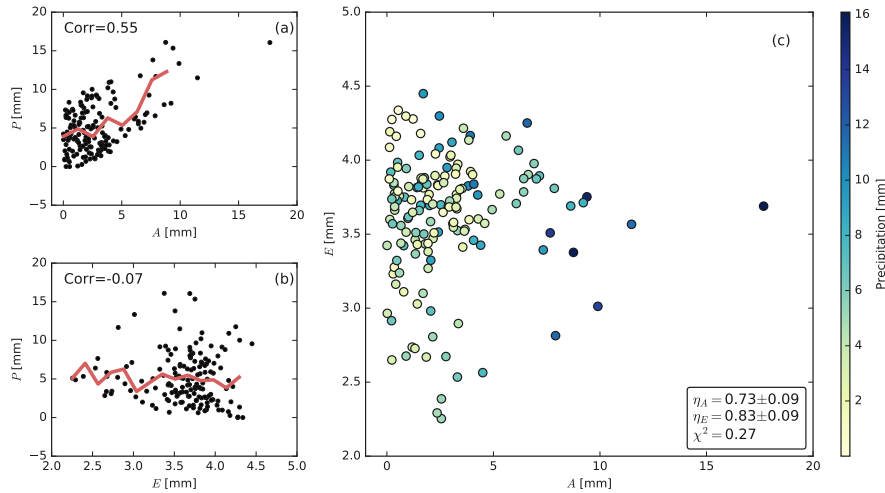
Figure 5.14: Same as in Fig. 5.8 but for the area in north-eastern Germany high-lighted in Fig. 5.10.

when determining the optimal values of the parameters through the least-squared fit. For this reason a similar plot to Fig. 5.13 is not shown for this area.

5.6 SUMMARY

The conceptual model developed in Chapter 4 was here applied to a realistic simulation of a diurnal cycle over Germany to understand whether it has some value in explaining the simulated variability of precipitation. A total of two days (5 and 6 June 2016) were simulated. The main goal was to derive the values of the efficiencies η_A, η_E, as well as the single efficiency η, to verify whether advection and evaporation processes are characterized by different weights and whether two efficiencies are really necessary to express precipitation variations over a chosen region

Depending on the region, the width of the boxes and on the simulated day, the obtained values of the efficiencies fluctuate between 0 and 3. For the case of scattered convection observed during 6 June 2016 the conceptual model was able to explain the observed variability of precipitation when the width of the box was increased above 100 km. Interestingly enough, this coincided with an estimated null efficiency of advection, showing that during this day precipitation and convection were mainly correlated with surface evaporation.

The results obtained from the additional simulated day, 5 June 2016, showed many differences also because the evolution of convection and precipitation during this day had a less pronounced diurnal cycle. The estimated efficiency of advection reached 0 only for box widths larger than 130 km, while the efficiency of evaporation steadily increased and reached a maximum of almost 3. In this case the model

was able to explain the variability of precipitation with good accuracy even with small box widths. However, when selecting a different region with more scattered convection the model failed in explaining precipitation variability, given the weaker correlation of precipitation to advection and evaporation. In both cases the conceptual model characterized by two different efficiencies appeared to be more skilled with respect to the simpler model using only one efficiency in explaining variations of precipitation with respect to advection and evaporation.

Although some of the presented results are encouraging, the method proposed here need to be extensively revised to allow for a more accurate estimate of the efficiencies. Suggestions on how to improve the method used to derive the efficiencies are given in the following. First of all, a different period to be simulated could be selected, as well as a different region over central Europe, to increase the number of days to sample. Second, there is an explicit need for an objective selection of precipitating events. In the present work only squared lat-lon boxes were used to compute the values of A, E and P. Instead, a segmentation algorithm (Hauser et al., 2007) could be applied to the precipitation horizontal distribution to derive the position and extent of either single convective cells or organized thunderstorms. For every one of these individual objects the analysis of the moisture balance terms could then be applied. Finally, additional filtering using land-surface features like soil type, orography or vegetation is needed to objectively choose different regions of the simulation domain.

6

PREDICTION OF A MEDITERRANEAN
TROPICAL-LIKE CYCLONE USING ICON-LEM

6.1 INTRODUCTION

Chapters 3 and 4 have demonstrated that ICON-LEM can be used to develop conceptual models of the interaction between soil moisture and convective precipitation. The conceptual model developed in Chapter 4 was also applied to more realistic simulations of a diurnal cycle over Germany in Chapter 5. Although the main goal of Chapter 5 was not to evaluate the model forecast skill, it was highlighted that ICON-LEM captured fairly well the diurnal cycle in terms of precipitation intensity and distribution.

However, the atmospheric configuration adopted as forcing in Chapter 5 was characterized by a weak synoptic forcing. On the other hand, atmospheric predictability and model errors are highly flow-dependent (Ferranti et al., 2002; Grazzini, 2007). This means that, for example, atmospheric states characterized by an anticyclonic flow with embedded large-scale subsidence (like the one employed in Chapter 5) may be more predictable than those characterized by an upper-level cold-core low which induces surface cyclogenesis. Thus, it is interesting to ask to what extent ICON-LEM can still be used to develop conceptual models of the interaction between convection and the environmental atmospheric condition when convection itself is embedded into a structure characterized by a strong synoptic forcing.

A clear example of such structures are certainly synoptic cyclones, i.e. atmospheric vortices with scales of $\mathcal{O}(100\text{-}1000$ km) (Holton and Hakim, 2012). These are one of the main mechanisms of large-scale energy transport in mid-latitude regions, where they are also the main cause of weather variability. The Mediterranean Sea, in particular, has one of the highest concentration of cyclogenesis events in the world (Campins et al., 2011). In this area cyclones with hybrid tropical features, mainly driven by deep convection close to the center of the structure, have been also observed with a characteristic frequency of about 1.5 events per year (Cavicchia et al., 2014). These cyclones, called MTLCs, cause several damages due to heavy precipitation and strong winds in coastal areas, and are difficult to predict due to their small-scale structure. In this chapter one of these cyclones, which interested the central Mediterranean between 7 and 9 November 2014, will be used as case study to investigate the interaction of deep convection with the large-scale flow, taking advantage of

ICON-LEM, where this interaction can be explicitly resolved.

This event was particularly interesting given both the observed features of the cyclone, which developed over a portion of the Mediterranean covered by many active weather stations, and the poor performances of the global NWP models National Centers for Environmental Prediction (NCEP)-Global Forecasting System (GFS) and ECMWF-IFS, which failed to identify the correct trajectory already after a few hours of forecast lead time. Pytharoulis et al. (2017) was the first study to show that even higher resolution LAMs forced by ECMWF-IFS data were showing similar biases. In a follow-up study Pytharoulis (2017) obtained a slightly better trajectory by decreasing the grid spacing from 10 km to 7.5 km. Carrió et al. (2017) obtained a similar trajectory to Pytharoulis et al. (2017) using a comparable model setup with an even finer resolution. To my knowledge, no other study presented a simulated trajectory that resembles the observed one for this particular MTLC case.

Motivated by the low predictability of this case, in this chapter I conduct a retrospective analysis by performing several simulations with ICON using a setup similar to the one employed in Chapter 5. The
Chapter goals
main goal of the analysis is to verify whether the employed model is able to reproduce the observed trajectory of the MTLC which occurred in November 2014. In particular, I aim at identifying the minimum resolution needed to correctly forecast the MTLC's evolution. In order to do so I will develop a simple conceptual model which explains how the latent heat release due to deep convection embedded in the MTLC changes with model resolution. This will be eventually used to assess whether increasing the resolution is really necessary to increase the forecast skill of such structure. Although being generally recognized that convection-permitting NWP models show better performance in capturing the updrafts produced by strong convection taking place in MTLCs (Davolio et al., 2009), no particular study has focused on this aspect.

*Outline of the
chapter*
In section 6.2 I first present all the available observational data collected by the authors and attempt to retrace the observed trajectory of the cyclone. Subsequently, in section 6.3, I introduce the modeling setup. The results of simulations performed with the aforementioned configuration are extensively described in section 6.4. Here several hypotheses regarding the sensitivity of the cyclone trajectory to the model setup are explored. Furthermore, the internal structure and the physical features of the cyclone are described using data from simulations with a sub-km grid spacing that allows me to explicitly resolve convective eddies. Conclusions are presented in section 6.5.

6.2 OBSERVATIONAL ANALYSIS

Figure 6.1 shows the observational-based best-track (see Appendix D for details) of the 7-8 November 2014 MTLC together with the operational NWP forecasts of the ECMWF-IFS model and of the NCEP-GFS model. It can be seen that the ECMWF-IFS model forecast initialized
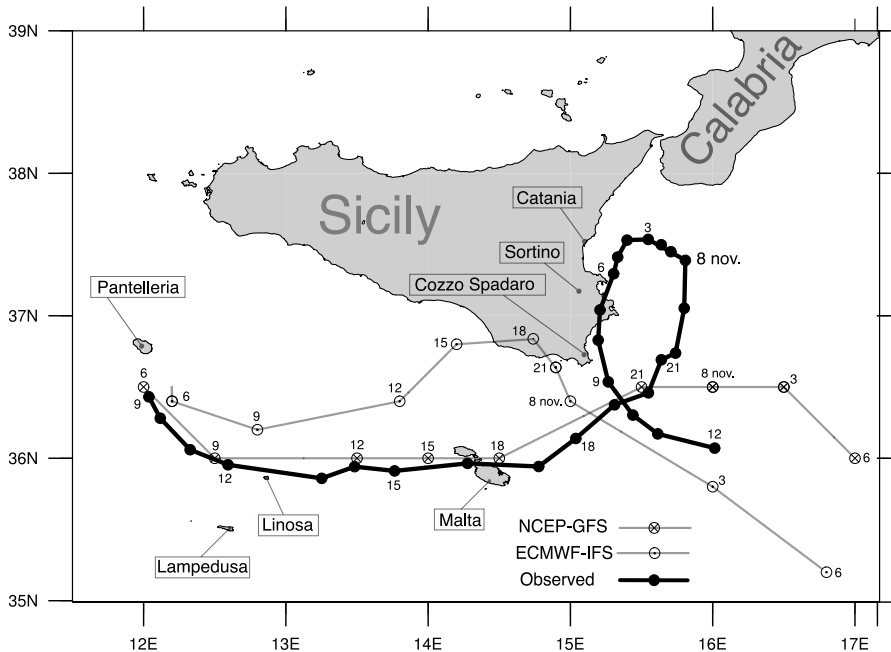

Figure 6.1: Trajectory of the cyclone in NWP forecasts and observations. The closed circles and the thick black line indicate the observational-based best-track of the 7-8 November 2014 MTLC (see text for details). The position is reported every hour while time labels, relative to 7-8 November 2014 and in UTC, are placed every 3 hours for clarity. MTLC trajectories predicted by the NCEP-GFS and ECMWF-IFS operational forecasts initialized on 7 November 2014 at 00 UTC are represented by the two gray lines with different markers. For these trajectories points are placed every 3 hours starting on 7 November 2014 at 06 UTC and ending on 8 November 2014 at 06 UTC.

Biases of operational models

on 7 November 2014 at 00 UTC placed the cyclone too northward too early, thus predicting a landfall on the southern coast of Sicily. On the other hand, the NCEP-GFS model forecast initialized at the same time missed the approach with Sicily and resulted in an eastward drift of the system in the evening of 7 November 2014. In both models this resulted in a missed approach over the eastern coast of Sicily. The trajectory and characteristic features of the MTLC are now briefly described. Given that Pytharoulis (2017) already presented an exhaustive observational analysis of this event, I will only recall some of the main aspects of the cyclone life cycle which are both necessary for this study and that were not presented before. The reader is referred to Pytharoulis (2017) for further details on the observational analysis of the MTLC.

The synoptic configuration prior to the cyclone formation is presented in in Fig.s D.1 and D.2. The main feature was constituted by an elongated upper-level trough which, at 00 UTC on 7 November 2014, extended from the North Sea to the Lybian region. The combination of this upper-level trough with a pre-existent MSLP minimum that moved towards Sicily the previous day led to the initial intensification of the cyclone, which took place during the night between 6 and 7 November 2014.

Formation and intensification

The weather station located on the island of Pantelleria (see Fig. 6.1 for an exhaustive representation of all the toponyms mentioned in the text) reported a minimum MSLP of 992 hPa at 08 UTC (Carrió et al., 2017, their Fig. 5). Between 09 and 12 UTC the low-pressure system rapidly deepened, as perceived from satellite imagery and predicted by almost all operational models at that time. Figure 6.2 shows the cyclone shortly after, at 1215 UTC, in its mature stage. The cloud structure depicted in Fig. 6.2 highlights the presence of a cloud-free region in the center of the system, together with spiraling distributed cloud bands. At this time Infra-Red (IR) satellite imagery did not

Figure 6.2: MODIS RGB composite imagery of the MTLC acquired on 7 November 2014 at 1215 UTC by the satellite Aqua.

indicate the presence of deep convection near the cloud-free region (not shown), a circumstance observed also by Claud et al. (2010) and Miglietta, Laviola, et al. (2013) during the mature phase of MTLCs.

At around 1230 UTC the central cloud-free region of the cyclone passed over *Linosa* island, where an active weather station was measuring data every 5 minutes, providing insights into the cyclone structure: these data are shown in Fig. 6.3. Figure 6.3 (a) underlines the sudden drop of pressure, which occurred between 1000 and 1230 UTC from approximately 1000 hPa to a minimum of 981.9 hPa. This value is

not far from the one measured shortly after on the island of Malta (978.6 hPa, see Tab. D.1 for an overview of all the observational values mentioned hereinafter), and represents a good approximation of the pressure reached in the center of the MTLC, since satellite imagery shows that the system crossed Linosa around 1200 UTC (see Figure 6.2). Figure 6.3 (a) also shows an abrupt decrease of wind speed be-
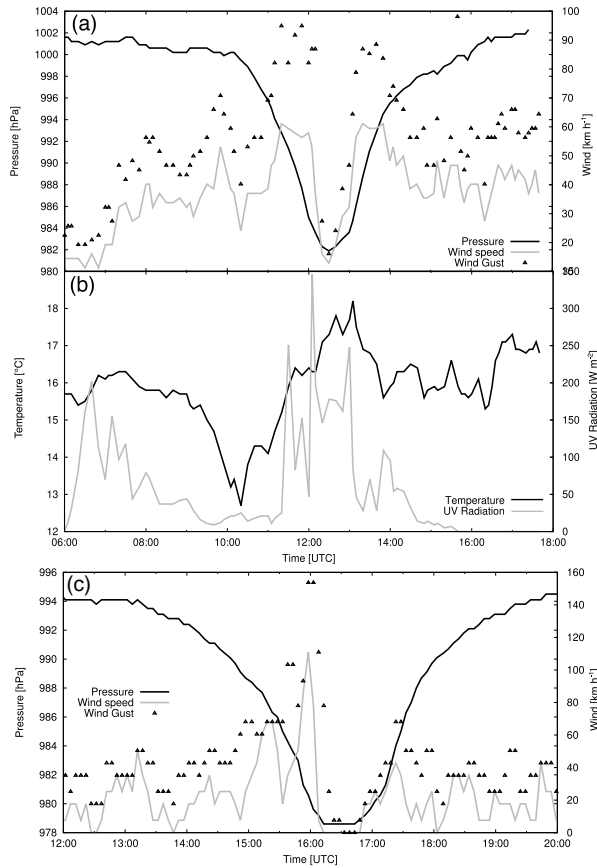

Figure 6.3: Weather observations at (a)-(b) the station situated on Linosa island from 06 UTC to 18 UTC on 7 November 2014 and at (c) the station located in Bugibba (North-eastern Malta) from 12 UTC to 20 UTC on 7 November 2014. In (a) and (c) the black line indicates MSLP [hPa], the gray line wind speed [km h^{-1}] while gusts are reported by filled black triangles. In (b) the black line is the 2-m air temperature [$^\circ$ C] while UV radiation [W m^{-2}] is indicated by the grey line. Details on these stations can be found in Appendix D while the position of both sites is indicated in Fig. 6.1.

tween 12 and 13 UTC, which appears similar to the calm that is often found in the eye of a TC and has been observed for other MTLC cases (see e.g. Moscatello et al., 2008). During this period, the air temperature (Fig. 6.3, b) first increased from 13°C to 18°C and then decreased to 16 °C at 14 UTC, when the cyclone had already crossed the island. This sudden rise in temperature suggests the presence of a low-level warm core in the center of the cyclone. The cooling preceding the cyclone arrival (between 09 and 10 UTC) was likely caused by the cold front associated with the earlier baroclinic phase of the cyclone.

The passage of the cyclone center is also outlined by the change in UV radiation (Fig. 6.3, b). The first arrival of thick cumulonimbi marks a sudden drop from approximately 350 W m^{-2} to nearly 0 W m^{-2}, while the lowest pressure values are observed together with high values of UV radiation, thus indicating a cloud-free region. The subsequent decrease of UV radiation measured by the weather station is due to sunset (1559 UTC).

Malta's approach   At 1630 UTC the cyclone approached Malta, where a weather radar was operating at the Malta International Airport. The precipitation-free region in the center of the cyclone, which crossed the northern part of the island, is visible in the radar rain intensity estimate reported in Figure 6.4 (a). The weather station of Bugibba, on the
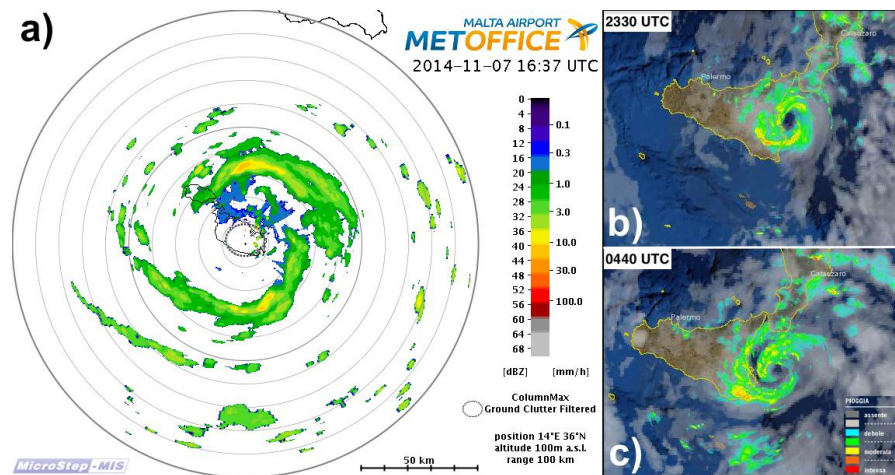

Figure 6.4: Radar precipitation intensity estimate [mm h^{-1}] from (a) Malta international airport at 1637 UTC on 7 November 2014 and from the Italian national radar mosaic at (b) 2330 UTC on 7 November 2014 and (c) at 0440 UTC on 8 November 2014. Details on the radar data may be found in Appendix D.

Northern side of the Malta island (see Fig. 6.1), recorded a minimum pressure of 978.6 hPa and a maximum wind gust of 153.7 km h^{-1} around 16 UTC: the time variation of both MSLP and wind speed seen in Fig. 6.3 (c) is similar to the one observed few hours before in Linosa.

Off the coast of Sicily   After having crossed the Malta island the cyclone turned northward towards the Gulf of Catania (Sicily) where it slowed down. As shown in Figure 6.4 (c), at 05 UTC the system was still producing moderate intensity rainfall on the eastern coast of Sicily. During this entire period a precipitating-free, as well as cloud-free, region was always visible. At about 0930 UTC on 8 November 2014 the cyclone was eventually leaving the Gulf of Catania and Sicily. Table D.1 contains all the relevant values measured by weather stations in chronological order: in this discussion I only mentioned some of them.

6.3 METHODS

In order to study the evolution and the internal structure of the MTLC the ICON model is used in NWP configuration. Although the dynamical core and most of the model features are the same described in Chapters 2 and 5, the parametrizations used in this chapter are slightly different given that a wide variety of simulations with different grid spacing are performed. Table 6.1 presents an overview of the different parametrization schemes available and used in the present configuration. The reader is referred to the relevant publications (Table D.2) for further details.

Several simulations are performed using ICON in hind-cast mode,

Parametrized process	Name
Radiation	RRTM
Microphysics	Single-Moment
	3-cat ice Microphysics
Convection	Mass-Flux shallow/deep
Cloud cover	All-or-nothing scheme
	Diagnostic PDF
Turbulence	2-D Prognostic TKE
	3-D Smagorinsky
Sub-Grid Scale Orographic drag	Lott & Miller
Non-orographic Gravity wave drag	Wave dissipation at critical level
Land-Surface	Tiled TERRA+FLAKE

Table 6.1: List of the sub-grid parametrizations available in ICON and employed in this work. A list of all the relevant references can be found in Table D.2.

Modeling strategy

that is using a forecast forced by continuously updated analyses, similar to what was done in Chapter 5. In this chapter, however, the combination of 6-hourly operational analyses taken from ECMWF-IFS given that the area to be simulated is not located over the COSMO-DE domain. Note that this configuration does not necessarily reproduce an operational setup, given that the analyses are always updated with a new assimilation cycle. However, since the boundary conditions affect only the large-scale flow, which is supposed not to differ much between forecasts and analyses over daily time scales considered in my study given the high skill of the host model, I don't expect the results to be greatly affected by this choice. Although I didn't test the sensitivity of the results to different prescribed boundary conditions it should be highlighted that a similar approach has been already successfully employed in Klocke et al. (2017).

In order to isolate the effects of the model resolution on the MTLC predictability, several simulations where only the grid spacing is grad-

ually decreased from 10 km to 1 km are designed. These cases are highlighted in Table 6.2 and share most elements of the basic configuration in terms of model physics, including the microphysical processes, radiation and surface parametrizations. Regarding the latter, it should be noted that SSTs are constant in time and initially prescribed by the initial conditions as done in the operational version of ICON, hence they can not change because of surface fluxes. The reader is referred to Pytharoulis (2017) for a sensitivity study of this MTLC to SSTs.

The control simulation adopts a grid spacing of about 1.2 km and

Name	Grid Spacing	Convection	Turbulence	Gravity Waves
10km	9806 m	Parametrized	2-D Prognostic TKE	Parametrized
5km	4903 m	Parametrized	2-D Prognostic TKE	Parametrized
2km	2451 m	Explicit	2-D Prognostic TKE	Parametrized
control	1226 m	Explicit	2-D Prognostic TKE	Parametrized
nested	1226 m			
	613 m	Explicit	3-D Smagorinsky	Explicit
	306 m			
nolatheat	1226 m	Explicit	2-D Prognostic TKE	Parametrized
		No lat. heat release		

Table 6.2: Overview of simulation configurations.

a domain that encloses Sicily and part of the Central Mediterranean (see black line in Fig. 6.5). A total of 91 vertical levels extend from the surface up to a top of 75 km. The spacing between vertical levels ranges from 20 m in the lower levels to 400 m in the middle troposphere and 2-3 km in the stratosphere. This is the same configuration used operationally for global weather forecasts.

Using this setup I progressively increase the grid spacing (degrade the resolution) to about 2.5, 5 and 10 km in the cases 2km, 5km and 10km, respectively. In the 10km and 5km cases the convection is parametrized (see Tab. 6.1). For all the aforementioned cases the sub-grid cloud cover parametrization employs a simple diagnostic Probability Density Function (PDF) scheme. An additional simulation using the same setup of the control case where the release of latent heat by condensation processes is turned off is also performed (nolatheat). This will be fundamental to validate the main idea underlying the conceptual model.

The nested *simulation.* Finally, I design another simulation (nested) where the grid spacing is decreased up to 306 m. In this case 3 domains with grid spacing of 1.2 km, 613 m and 306 m, respectively, are one-way nested. While the initial and boundary conditions for the outermost domain (1.2 km grid spacing) are taken from ECMWF-IFS, like in the control simulation, the forcing for the two inner domains is derived from the

1.2 km domain simulation, similar to what was done in Heinze et al. (2016). The area covered by the two inner nested domains is smaller (see grey rectangle in Fig. 6.5) to reduce computational costs. Note that the two innermost domains cover almost the same area except for a 8-cells wide nudging area at the boundaries: this difference is small enough to be not recognizable in Fig. 6.5. The area of the two
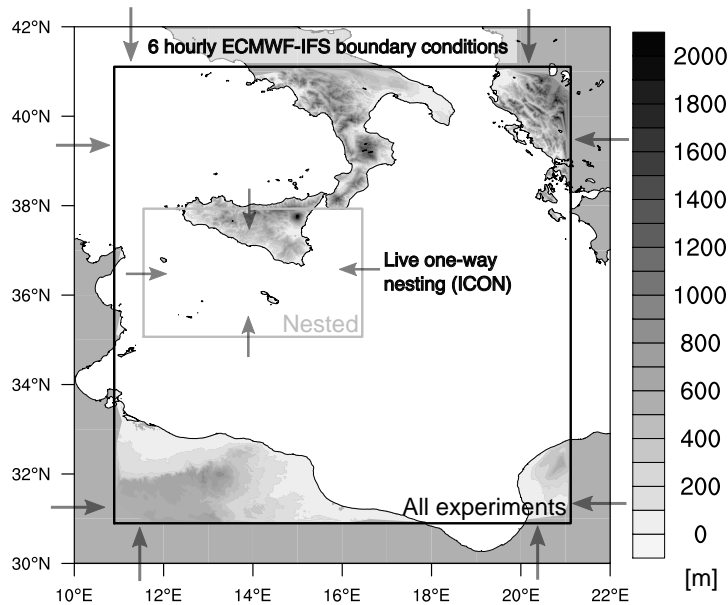

Figure 6.5: Topography data (shading) and different domains (solid lines) employed in the simulations. The black solid line indicates the domain used in the `control` case as well as `2km`, `5km` and `10km` cases. The grey rectangle represents the inner nested domain, obtained as a refinement from the parent one (black line), used in the `nested` simulations.

innermost domains is chosen in such a way that the first 36 hours of the cyclone's life cycle are contained inside. Within this set of simulations the 3-D Smagorinsky scheme for the parametrization of sub-grid scale turbulence (Dipankar et al., 2015) is used. The cloud cover parametrization employs a simple all-or-nothing scheme (see Tab. 6.1).

External data are aggregated and interpolated to the target resolution of the specific model configuration from observations. The data-sets of soil type and orography have an original resolution of about 30 and 100 m, respectively, so that the characteristic features of the land-surface are retained up to the resolution of the `nested` case.

All simulations cover a 48-hours forecast period beginning on 7 November 2014 at 00 UTC in order to capture the whole observed life cycle of the cyclone (see Fig. 6.1). This study, however, focuses only on the first 36 hours given that this period includes the initial intensification and tropical transition of the cyclone. The model output is analyzed every hour in order to extract the MTLC trajectory and its internal structure. In order to track the cyclone an algorithm similar to the

Analyzed model output

one developed in Cioni et al. (2016) is employed. The minimum of MSLP is used as a proxy for the cyclone position and a linear extrapolation of the previous time steps is adopted to obtain a first guess of the cyclone position at every time.

The study of the upper- and low-level PV structure is performed through the analysis of the quantities introduced in Miglietta, Cerrai, et al. (2017): the Dry Potential Vorticity (DPV) and Wet Potential Vorticity (WPV). These allow distinguishing between the different sources of PV generation, namely local and remote sources. The DPV is helpful in distinguishing areas of tropopause folding, characterized by very low relative humidity and high PV, thus leading to local maxima of DPV. The generation of PV by means of diabatic heating is instead represented by the so-called WPV. The WPV attains large values where high values of potential vorticity and relative humidity coincide (e.g. deep moist convection).

6.4 RESULTS

6.4.1 *Simulated trajectories and general features*

Low-resolution simulations

The trajectories of the simulated cyclone obtained for the cases presented in Table 6.2 can be found in Fig. 6.6. The overall performance of the model in simulating the MTLC's trajectory increases with the resolution. In the 10km and 5km cases the system moves northward earlier than in the other cases, probably because the model is not able to resolve the internal dynamics of the MTLC and thus closely follows the large-scale evolution provided by boundary conditions (recall Fig. 6.1). The deepening of the system is completely missed in these cases as the MSLP minimum does not reach the values observed in the simulations with higher resolution (compare the color of the lines in Fig. 6.6). The cyclone further weakens after the early landfall over Sicily in the 10km and 5km cases. In order to evaluate the effect of the convection parametrization on these results, I performed an additional simulation identical to the 5km case where the convection scheme was turned off. I found no significant differences in terms of the simulated cyclone's trajectory and evolution (not shown).

High-resolution simulations

By decreasing the grid spacing to approximately 2.5 km in the 2km case the simulated track of the cyclone resembles more the observed one. Not only the trajectory now includes a small loop off the eastern coast of Sicily, but also the initial deepening of the cyclone is captured fairly well. The control case shows a similar trajectory although with a loop off the coast of Sicily characterized by a smaller radius. The absence of latent heat release in the nolatheat causes the simulated cyclone to miss the first intensification phase: the MSLP increases already in the first 8 hours and reaches almost 1000 hPa at 13 UTC on 7 November 2014. The system moves then eastward with an overall
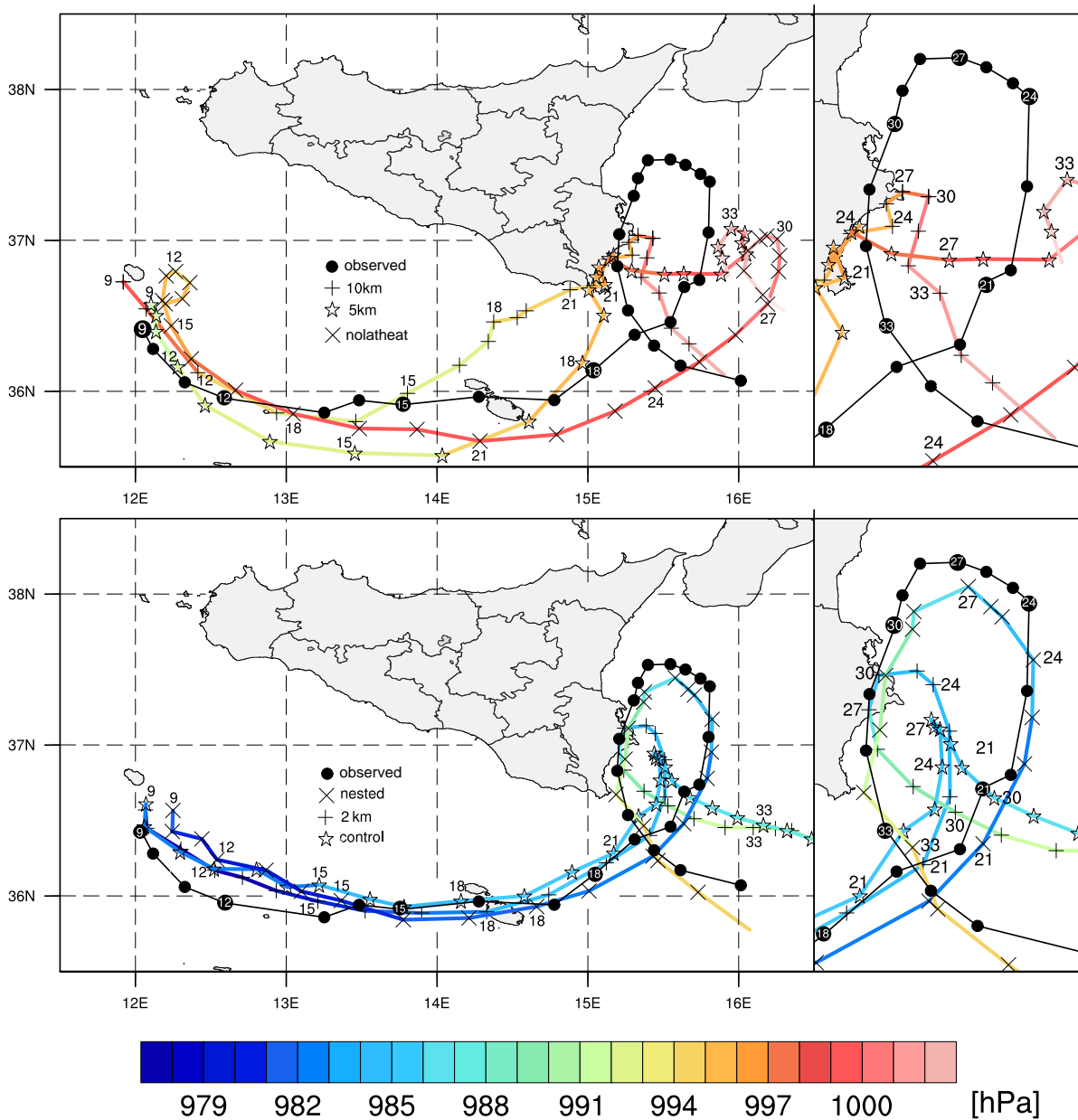
Figure 6.6: MTLC trajectories obtained in the simulations described in Tab. 6.2. The points are placed every hour (starting on 7 November 2014 at 09 UTC and ending on 8 November 2014 at 12 UTC) while the lines are colored according to the attained MSLP minimum found by the tracking algorithm. The observed trajectory is superimposed and delineated by the solid line in order to allow for a direct comparison between all the cases. The right inset shows a magnification of the same plot in a small area close to the eastern coast of Sicily. Time labels are placed manually according to the density of the points on the plot.

delay of about 5 hours and passes southward of Malta at 00 UTC on 8 November 2014. Interestingly enough, a northward deviation and a loop of the trajectory are predicted also in this case but about 100 km eastward of the location found in the `control` case (see Fig. 6.6).

With a further increase of resolution, and the consequent employ-ment of a 3-D Smagorinsky parametrization for sub-grid scale turbu-lence, the simulated trajectory approaches even more the observed one, with a wider loop that extends far northward. While in the first 18 hours the cyclone track is similar to the one simulated in the `control` and `2km` cases, after having passed Malta the MTLC moves eastward and makes a larger loop off the eastern coast of Sicily in `nested`.

As already anticipated before, those experiments that simulate a wrong trajectory (`10km` and `5km`) also miss the first period of intensification. This can be clearly seen in Fig. 6.7, where the minimum of MSLP and the average wind speed in a 50 km radius around the cyclone center are displayed. The 20-hPa initial deepening of the cyclone is only
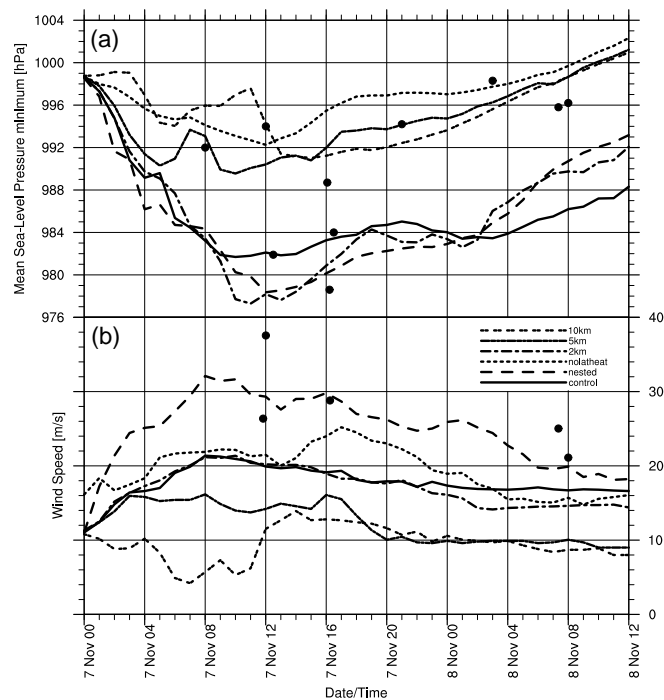
Figure 6.7: Cyclone MSLP minimum (a) and average 10-meters wind speed (b) in a 50 km radius around the cyclone in different simulations. Markers represent the observed values presented in Tab. D.1.

found in cases with grid spacing smaller or equal than 2.5 km, while the `5km` and `10km` cases show only a slight decrease in MSLP which is quickly followed by a MSLP increase. Winds are clearly related to the deepening of the cyclone with larger values being observed in the `control` and `2km` cases. In the `nested` case wind speeds of up to 32 m s^{-1} are simulated. Note that the difference in winds between the `control` and `nested` simulation may be partially related to a bug in the surface momentum flux formulation which has been found at the time of writing (Dipankar, personal communication) and causes an overestimation of surface winds.

The MTLC approach over Malta predicted in the `nested` case shows

some similarities with the observed one. To show that in Fig. 6.8 I extracted temperature, winds and relative humidity data together with surface winds and pressure from the grid point located at (lat, lon)=(35.992, 14.372) every 5 minutes. This was necessary to have data comparable to the observation of Bugibba shown in Fig. 6.3 (c). The pressure drops from 999 hPa to about 983 hPa when the cy-
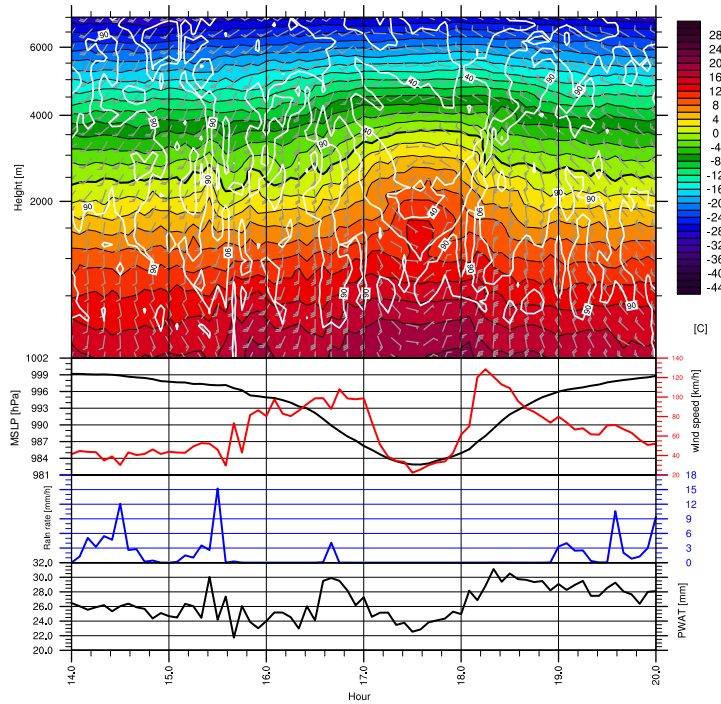

Figure 6.8: Time-height plot and time series (meteogram) obtained from the nested case for the grid point located at (lat, lon)=(35.992, 14.372) in the vicinity of Bugibba, Malta. Data are every 5 minutes and times (lowermost x-axis) are in UTC. Upper panel shows temperature (color shading, contour every 2 degrees, 0-degree line with enhanced thickness), wind speed and direction (grey barbs) and relative humidity (white contours, 40-60-90 % isolines are shown) at model levels (left axis, meters). Lower panels indicate, respectively, MSLP (black line, hPa), 10-m wind speed (red line, km h^{-1}), rain rate (blue line, mm h^{-1}) and PWAT (black line, mm).

clone crosses the island: note that there is a 1-hour delay between the simulated landfall and the observed one. The relative humidity field highlights the presence of a dry region between 1500 m and 5000 m while the temperature shows a warm core extending from the surface up to approximately 4000 meters. The 10-m wind speed decreases in the center of the cyclone and increases immediately before and after with winds up to 140 km h^{-1}, which is close to the 150 km/h registered at Bugibba (Fig. 6.3, c). The decrease of precipitable water in the cyclone center remarks the presence of dry air in the core of the system.

Figure 6.9 shows a 3-D representation of the cyclone in the nested simulation using a volume rendering of clouds, obtained as the sum of cloud water and cloud ice mixing ratios, together with stream-

lines colored according to wind speed. The spirally distributed cloud
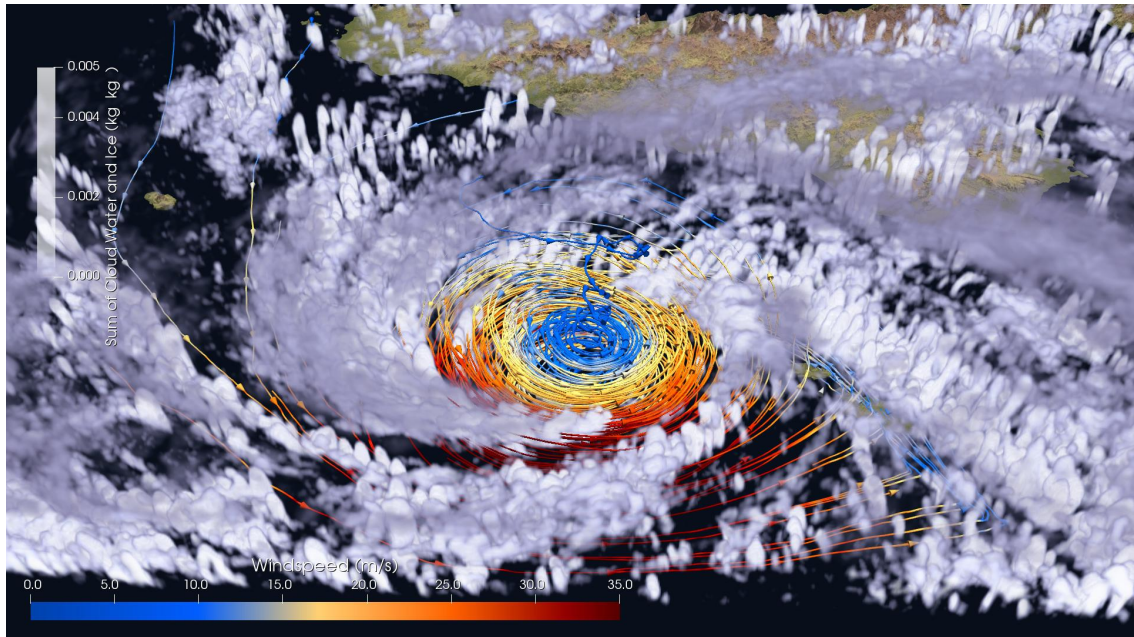

Figure 6.9: Results of the `nested` simulation at 14 UTC. 3-D volume rendering of the sum of cloud water and cloud ice mixing ratios [kg kg^{-1}] is shown by means of gray-white shadings. Forward-backward time-integrated trajectories of air parcels randomly selected around the cyclone and colored according to the magnitude of surface winds are also shown.

bands stand out, including the cloud-free region at the center which appears larger than in reality (see Fig. 6.2). This could be simply an artifact of the particular visualization method employed to create the figure. The trajectories of air parcels randomly selected around the cyclone at different heights show that there is a strong convergence towards the center of the cyclone, with winds being substantially more intense in the southern flank of the system and calm in its center. The cold front preceding the cyclone formation is also visible as a sharp contrast of surface winds in the lower-right corner of Fig. 6.9. Finally, it is interesting to note the presence of a subsiding trajectory in the center of the cyclone, as expected in tropical structures.

6.4.2 *Internal thermal structure and predictability*

Motivated by the good performances of the `nested`, `control` and `2km` simulations I aim at understanding why other simulations fail to reproduce the observed trajectory of the cyclone and in particular its initial intensification phase. It has already been shown that, by using a grid spacing larger than 2.5 km, the initial deepening of the cyclone is missed. This may arise from the fact that, without a sufficiently small grid spacing, the internal convective structure of the cyclone that drives its intensification is not correctly represented as

the model is not convection-explicit but rather convection-permitting. In order to understand the impact of the simulated internal structure on the MTLC evolution over time the model data is examined in circles centered on the cyclone position having a 100 km radius.

Figures 6.10 (a, b, d) show the cyclone-centered plots for the control, 5km and the nested cases on 7 November 2014 at 12 UTC. In order to highlight the inner structure of the cyclone the temperature anomaly w.r.t. the average value over the 100 km circle around the cyclone was computed: it is shown through the color-filled contour. This anomaly is averaged in a vertical layer between 500 and 1000 m to smooth out small-scale horizontal variations. This method allows identifying the warm core that is usually associated with the mature phase of MTLCs (Picornell et al., 2014) and that was already individuated by Pytharoulis (2017) for this particular case.

Analysis of the cyclone-centered plots

By comparing Fig. 6.10 (a) and (b) it is evident that a warm core is almost non-existent in the 5km simulation, given the lower value of the anomaly in the center of the cyclone. In the control case, instead, a wider anomaly with local maxima of about 3°C is found in the center of the cyclone. The warm anomaly widens and strengthens in the nested simulation (Fig. 6.10 d), where additional features are visible. The lack of a strong warm core in the 5km case suggests that the convection predicted in this particular case is not deep enough to produce significant latent heat release and subsiding motions in the center of the cyclone. Given that the deep convection found close to the central region is the main mechanism driving the intensification of tropical structures (Houze Jr, 2014), the poor performance of these simulations is most likely related to the lack of an inner warm core.

Lack of warm core in low-resolution simulations

To further test the hypothesis that the lack of latent heat release due to non-resolved convection influences the cyclone's forecast evolution I performed the same analysis also for the nolatheat case where the release of latent heat due to condensation process is turned off. The cyclone structure predicted in the nolatheat case (Fig.6.10, c) includes a shallower warm core with respect to the control case although still deeper than the one obtained in the 5km case. This can be explained considering that, first of all, in the nolatheat case only latent heat release due to condensation processes is turned off. Other microphysical processes, especially those related to ice formation, may contribute to the latent heat release. Second, the temperature anomaly in the nolatheat case is not concentrated in the center of the cyclone but rather widely spread over the chosen radius of exploration. Thus, it is likely related to frontal structures which suggest the presence of an extra-tropical structure. This strengthens my hypothesis that the lack of an intense warm core is playing a role in determining the cyclone evolution forecast by the model.
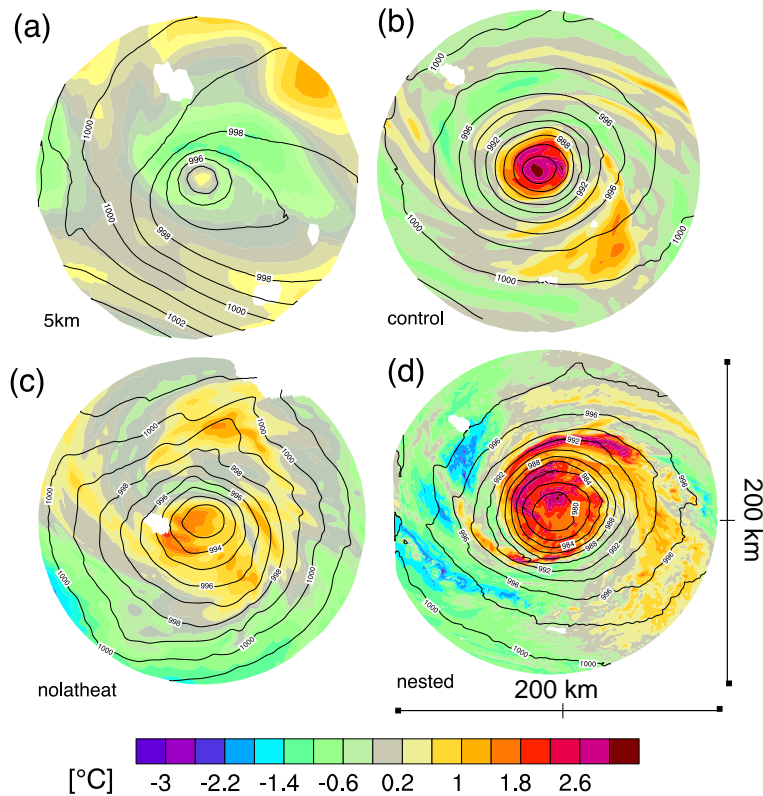
Figure 6.10: Cyclone-centered plots for the (a) `5km`, (b) `control`, (c) `nolatheat` and (d) `nested` cases on 7 November 2014 at 12 UTC. These are obtained as horizontal cross-sections of the cyclone centered on the position of the MSLP minimum and spanning a 100 km radius. Color shadings show the temperature anomaly w.r.t. to the average computed over the 100 km radius: the vertical average of temperature between 500 m and 1000 m is used instead of the value from a single level to smooth out the field. Note that temperature and MSLP are masked over land to avoid contamination when computing anomalies.

6.4.3 *The role of Potential Vorticity*

The lack of a diabatically-generated warm core in simulations with poorly-resolved convection affects the forecast of the cyclone trajectory since the atmospheric state is heavily modified in most of the troposphere. This can be verified by analyzing the PV balance in different simulations.

I here consider the evolution of PV and of the derived quantities DPV and WPV (see introduction and Miglietta, Cerrai, et al. (2017)) to better distinguish the origin of different air masses. In Fig. 6.11 these quantities are shown for the `control` case at different time instants of the simulation. Prior to the MTLC formation, a stratospheric air intrusion characterized by high DPV values (often referred to as PV *streamer*, see e.g. in Massacand et al., 1998) is located south of the cyclone center. This PV streamer is part of a synoptic-scale stratospheric intrusion which moved from the North Atlantic towards the Western
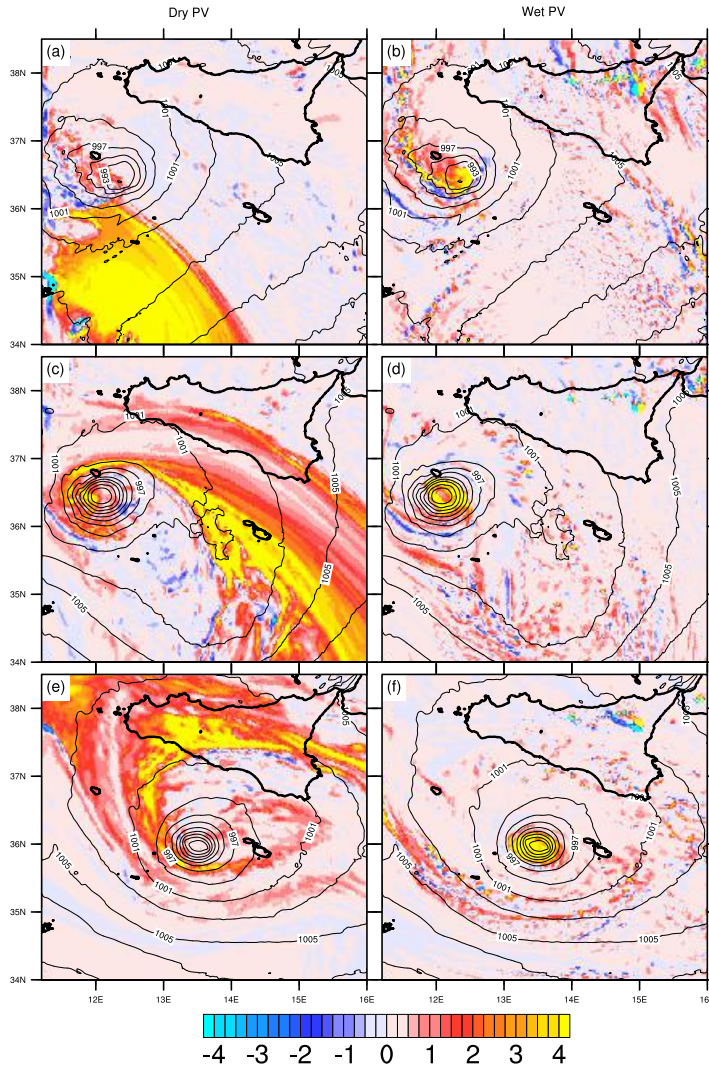
Figure 6.11: Dry (left) and wet (right) PV, respectively at 350 hPa and 850 hPa, at 03 UTC (upper panel - a,b), 10 UTC (central panel - c,d) and 16 UTC (lower panel - e,f) on 7 November 2014. The data from the `control` case is used.

Mediterranean basin during the previous days, turning northward around the pre-existing MSLP minimum (Carrió et al., 2017, their Fig. 3). During this early stage preceding the MTLC formation the center and the northern sector of the pre-existing MSLP minimum are characterized by high values of WPV in the lower troposphere (Figure 6.11, b), sign of extensive convection developing in the area.

Between 03 UTC and 10 UTC (Fig. 6.11 a,c) the PV streamer wraps around the cyclone center, transforming into a narrow and elongated structure characterized by high DPV values surrounded by much lower but still positive values of DPV to the north of the streamer. The increase of WPV seen in Fig. 6.11 (b,d) is driven, instead, mainly by diabatic PV generation and low-level convergence. In particular, convergence driven by the cyclonic circulation leads the PV generated

during the formation and maintenance of the cyclone outer convective bands to accumulate at the cyclone center (Figure 6.11 d, f).

The vertical structure of PV can be better delineated by considering the evolution of the PV profile over time, as done in Fig. 6.12 for a 100-km radial average around the cyclone. Many studies in literature (e.g. Delden, 2003) have shown that a vertically symmetric heat source in the troposphere, caused by the occurrence of deep convection, induces a PV dipole characterized by a positive PV maximum located immediately below the level of maximum heating and a slightly negative PV minimum located aloft. A low-level maximum of PV is indeed evident between 950 and 600 hPa in Fig. 6.12 (a) for the `control` simulation. Above this low-level maximum, a minimum of PV values
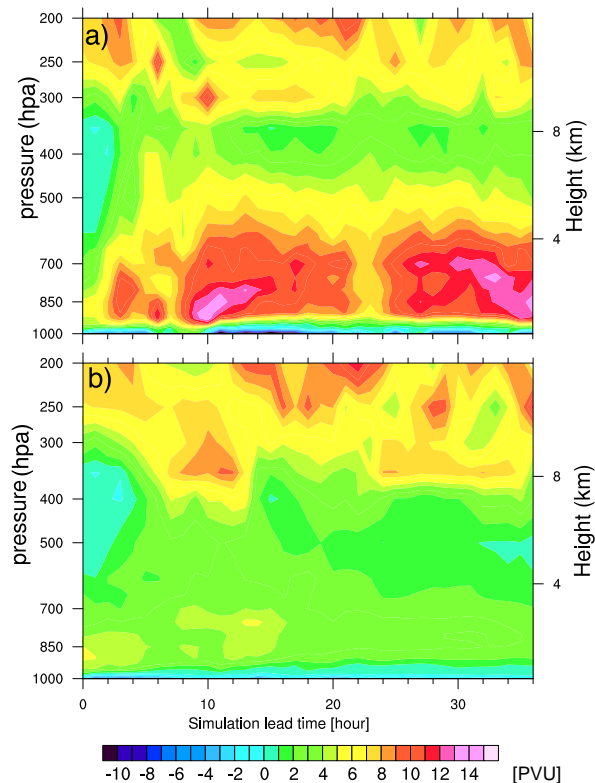
Figure 6.12: Time-pressure diagrams of the PV on isobaric levels averaged over a 100 km radius around the cyclone position. (a) shows the diagram obtained in the `control` simulation while (b) shows the diagram obtained in the `nolatheat` simulation, i.e. the `control` simulation where the release of latent heat due to condensation is suppressed.

is located between 350 and 450 hPa. This minimum results from the superposition of the aforementioned PV dipole and of the large-scale PV structure. The upper-levels layer, between 200 and 350 hPa, shows part of the PV streamer highlighted before.

The vertical distribution of PV changes appreciably when considering the experiment `nolatheat`, where the release of latent heat by condensation is turned off. There we observe the disappearance of the

low-level PV maximum and a vertical expansion of the upper-level maximum (Fig. 6.12 b) which now extends more into the upper troposphere. A similar vertical redistribution of PV is observed also in the 10km case (not shown).

The effect of the redistribution of PV on the MTLC structure can also be seen by analyzing the horizontal structure of the upper-level (350 hPa) PV anomaly and of the geopotential height depression at 500 hPa in different simulations, as shown in Fig. 6.13. Although the

Change in the horizontal distribution of PV
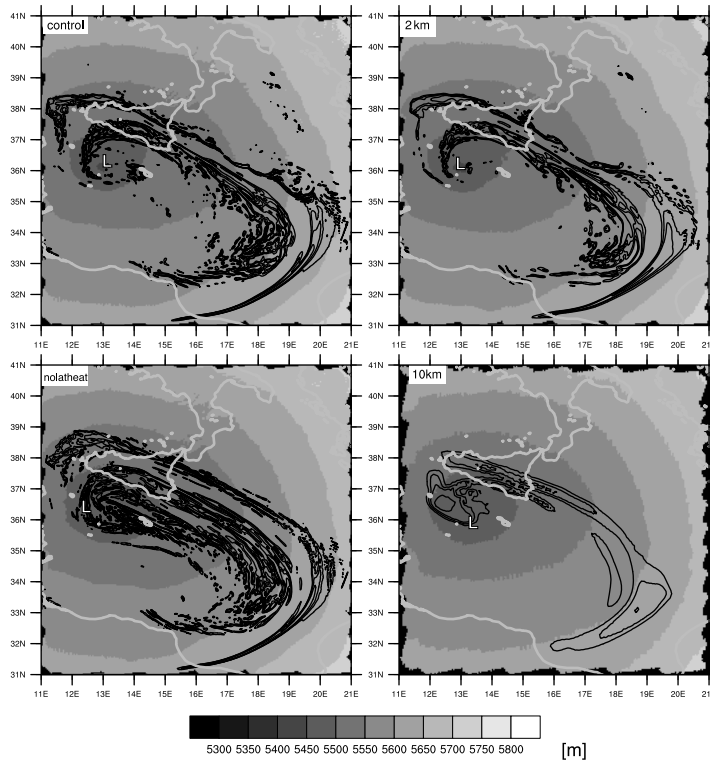
Figure 6.13: Comparison of Geopotential Height at 500 hPa [m, gray scale] and PV at 350 hPa [PVU, countour at 4,5,6,8] predicted on 7 November 2014 at 14 UTC in the cases control, 2km, nolatheat and 10km. The position of the cyclone in every case is indicated by the L symbol.

geopotential height does not show appreciable differences between the simulations, a local closed minimum of about 540 dam is present only in control and 2km, in agreement with the fact that in these cases a deeper cyclone is predicted. The PV distribution predicted close to the cyclone center, instead, greatly differs between the cases. In particular, the PV maxima observed in control and 2km are mainly related to the PV streamer structure and do not appear to be concentrated above the cyclone center. In the nolatheat and the 10km cases, instead, intense localized maxima of PV appear over the cyclone central region.

This is so because the smaller grid spacing adopted in the control and 2km cases allows the model to explicitly resolve the latent heat release by convection, which in turn induces a vertical dipole of PV,

as explained before. Therefore, in these simulations, the PV at 350 hPa is partially depleted above the area with deep convection, that is close to the cyclone center. In the 10km simulation, the lack of properly resolved convection close to the cyclone center does not allow a decrease of the upper-levels PV values. Such occurrence of PV maxima close to the cyclone center is observed also in the nolatheat experiment.

It appears, therefore, that poorly resolved convection results in a modification of the low-level PV distribution which, in turn, modifies the upper-level PV structure. Given that the PV distribution is uniquely determined by the wind and temperature field, its modification will affect to some extent the forecast of the atmospheric state. Homar et al. (2003) have already shown, using a PV inversion technique, that the upper-level PV structures indirectly acts on the cyclone deepening through a modification of the surface circulation. Thus, it is very likely that the modification of PV in the simulations with poorly resolved convection affects the forecast of the MTLC trajectory in ICON and more generally in similar NWP models.

Effect of the low-resolution on PV distribution.

6.5 SUMMARY

In this chapter the MTLC event of 7-8 November 2014 was used as case study to determine the NWP model requirements needed to correctly forecast its evolution over a 48 hours period. The trajectory of this particular MTLC was poorly predicted by operational global NWP models at that time and resulted in a missed landfall over Sicily.

I firstly focused on the dependency of the MTLC forecast on the model resolution by setting up different simulations with a similar model setup but different horizontal grid spacing ranging from 10 to 1 km. The simulations characterized by a grid spacing equal or greater than 5 km missed the first intensification phase of the cyclone and did not predict the correct landfall time over Sicily. Instead, simulations performed with a grid spacing equal or smaller than 2.5 km correctly reproduced the initial deepening of the cyclone and the northward turn towards Sicily during the evening of 7 November.

By studying the internal structure of the simulated MTLC in the different cases, the lack of a central warm core was observed in simulations with grid spacing equal or larger than 5 km. This was due to the fact that, in theses cases, the model was not able to correctly resolve the deep convection, and thus the associated latent heat release, developing into the central region of the MTLC. Given that deep moist convection is the main mechanism leading to the sustainment and deepening of the system, its weakening or even absence compromises the forecast of the MTLC evolution over time. Decreasing the grid spacing to 300 m produced a more intense cyclone characterized by a trajectory with a wider loop, similar to the one seen in observa-

tions.

Finally, given the importance attained by lower- and upper-levels PV anomalies in the formation and intensification of the MTLC, I studied the temporal and spatial distribution of DPV, which highlighted areas of low relative humidity and high PV, and WPV, which instead attains large values where high values of PV coincide with moist air. Positive anomalies of DPV in the upper- and of WPV in the lower-troposphere evolved and intensified in the hours before the MTLC formation. The intensification of the low-level WPV anomaly, due to combined convergence and latent heat release, and its interaction with the upper-level DPV are candidates as main dynamical factors responsible for the cyclone evolution. Simulations where convection is poorly reproduced were characterized by a negligible release of latent heat by convection in the lower-levels, which prevented both the formation of a low-level PV positive anomaly and the reduction of PV aloft. This eventually affected the forecast of the cyclone evolution due to a modification of the large-scale atmospheric state.

CONCLUSIONS

In this dissertation I developed conceptual models of the interaction between convection and different atmospheric processes including land-atmosphere interactions and mid-latitude storms by taking advantage of simulations performed with Icosahedral Non-hydrostatic Large-Eddy Model (ICON-LEM). In this final chapter I will summarize the results of my work, and return to the research questions posed in the introduction.

7.1 CONCLUSIONS BY CHAPTER

Part I: Conceptual models of the interaction between soil moisture, convection and precipitation

Although highly idealized, the conceptual models developed in this part of the dissertation proved to be valuable tools for providing a physical understanding of the interaction between soil moisture and convective precipitation. Even though the main goal was not to evaluate the skill of the conceptual models, in both Chapters 3 and 4 the simulated precipitation was predicted *a priori* using the conceptual models developed here, with a relative error ranging from 1% to 20%. This is a remarkable result considering the degree of simplification adopted.

Implementation of the coupling between TERRA-ML and ICON-LEM in an idealized configuration

In Chapter 2 a new test-case was included in the ICON-LEM code in order to couple its atmospheric component to the Land-Surface Model (LSM) TERRA-ML over a doubly-periodic idealized domain. After having described the main features of the model components, the setup was validated against similar frameworks constituted by the University of California Los Angeles Large-Eddy Simulation (UCLA-LES) and Dutch Atmospheric Large-Eddy Simulation (DALES) models, which were used in the past for similar idealized studies. The comparison of the results obtained with these three models for a case of Dry Convective Boundary Layer (DCBL) showed that ICON-LEM was able to reproduce the evolution of surface fluxes and of the corresponding atmospheric state over time. Differences observed between the models were marginal in the case with fixed incoming radiation. In the case adopting interactive radiation, ICON-LEM showed a different evolution of near-surface atmospheric temperature and humidity

close to the surface in the first hour. This was related to the different formulation of surface latent heat flux in TERRA-ML and caused an initial overestimation of surface moisture, and equivalently and underestimation of surface temperature, both of which quickly adjusted in the following hours.

May drier soils receive more precipitation than wetter ones in homogeneous conditions?

In Chapter 3 the previously developed modeling framework was used to investigate the coupling between soil moisture and precipitation over a homogeneous surface. It was found that, depending on the initial atmospheric state, convection can be triggered earlier or later in the day. However, total accumulated precipitation always decreases over dry soils regardless of the employed atmospheric profile, implying a wet soil advantage. The development of a simple conceptual model showed that precipitation strongly scales with surface evaporation, thus preventing the appearance of a dry-soil advantage in this idealized setup. Perturbed experiments investigating the effects of cloud-radiation interactions, large-scale forcing, winds and plants all supported a wet soil advantage.

Overall, the results of this chapter suggest that changes in convection efficiency are unable to compensate for the reduction of evaporation over dry soils. This only partially dismisses the ideas of Findell and Eltahir (2003b) since a dry soil advantage (or equivalently wet soil advantage) is indeed found in terms of convection-triggering but not in terms of total accumulated precipitation. These findings are only valid for those situations where changes in soil moisture do not affect or generate circulations, an effect that will be investigated in Chapter 4. Moreover, a true feedback loop would imply that the increase in soil moisture due to precipitation affects the subsequent precipitation development. This is unlikely to occur over one diurnal cycle.

Can a simple conceptual model explain how precipitation responds to soil moisture changes over a heterogeneous surface?

The transition to a heterogeneous land surface in Chapter 4 caused convection to organize along a front created by a mesoscale circulation similar to a land-sea breeze. While such a circulation contributes to the moisture balance as an advection term, local evaporation also plays a role in moistening the atmosphere, thus eventually modifying the potential amount of precipitation. To understand the role of these processes, simulations on a surface with various degrees of heterogeneity were performed using ICON-LEM to develop a simple conceptual model of precipitation enhancement over spatially drier surfaces.

Results obtained in different cases showed that advection sources are

more efficient than evaporation sources in producing precipitation. This was explained through the development of a simple conceptual model, which expresses precipitation as a sum of advection and evaporation weighted by two different efficiencies. In contrast with previous studies, where a single efficiency was used to express the contribution of advection and evaporation (e.g. Schär et al., 1999), the importance of using two different efficiencies on diurnal timescales was highlighted.

The conceptual model was then used to derive a mathematical expression for the derivative of precipitation with respect to soil moisture. It was found that changes in precipitation with respect to soil moisture over a spatially drier patch surprisingly do not depend on soil moisture itself. Instead, they depend on three parameters, namely the two aforementioned efficiencies and a magnitude scale of advection, which are representative of the initial atmospheric state only. This is caused by the fact that strong cold pools accelerate the front and effectively remove its dependency on the surface state, in agreement with Rieck et al. (2015). Older studies that scaled the velocity of the front with the difference in surface sensible heat fluxes between dry and wet patches did not consider the production of precipitation and thus missed this effect.

The absolute value of precipitation over the dry patch thus depends both on the parameters of the conceptual model and on the value of soil moisture. While the most efficient way to increase precipitation over the dry patch is to decrease its soil moisture, if the aforementioned parameters are modified, this behavior can be reversed. Since this was not observed in the simulations, even when changing the initial atmospheric state, it can be inferred that in order to increase precipitation over drier areas, more precipitation should first fall on wetter ones. In other words, the most efficient way to obtain more precipitation over dry areas is to let them dry out over an extended period so that a stronger gradient can build up, inducing stronger mesoscale circulations and therefore more explosive convective events.

Part II: The coupling of convection with the land surface and the large-scale flow in realistic simulations

In this part of the dissertation, ICON-LEM was used in two more realistic setups: a convective diurnal cycle over Germany and a Tropical-Like Cyclone (TLC) over the Mediterranean Sea. Both the former process–strongly modulated by the land surface–and the latter–strongly forced by large-scale dynamics–were captured with good accuracy. Thus, the obtained results were used to validate different conceptual models of the interaction between convection and the environment in which it is embedded.

Can the effects of advection and evaporation on precipitation be recognized in a diurnal cycle over Germany?

In Chapter 5 I quantified the relative weights of advection and evaporation on precipitation using the conceptual model developed in Chapter 4 and simulations of a single diurnal cycle over Germany. Two days (5, 6 June 2016) were chosen among an exceptional period of severe weather that interested Germany in the summer of 2016. By analyzing the data obtained with the simulation relative to 6 June 2016, it was shown that the efficiency of advection is larger than that of evaporation when the width of the box chosen for the analysis is smaller than 50 km. When averaging over larger scales, evaporation turned out to be the only process contributing to precipitation. This behavior is corroborated by the fact that, on this day, clouds were randomly distributed over the region and not clustered or organized along fronts reminiscent of mesoscale circulations.

However, it was also found that the results are highly dependent upon the initial atmospheric state and the method used to select the sampling region. Efficiencies computed for the previous day, 5 June 2016, demonstrated a different behavior, with the efficiency of evaporation being always larger than the one related to advection, which approaches 0 for scales above 130 km. In both cases the complex model introduced in Chapter 4 was able to explain precipitation variations better than the simple one, which uses only one single efficiency. Although the proposed method needs to be extensively revised, it demonstrates that over diurnal time scales the atmospheric moisture storage term is not negligible and may bias the estimation of the atmospheric efficiency in converting advection and evaporation sources into precipitation.

Does poorly resolved convection influence the forecast of a Mediterranean tropical-like cyclone?

While the diurnal cycle simulated in Chapter 5 was characterized by a weak synoptic forcing, in Chapter 6 I performed simulations of a synoptic configuration characterized by a strong cyclonic circulation. The goal was to develop a simple conceptual model of how convection interacts with the large-scale flow in a configuration where convection itself is embedded in a cyclonic circulation. A Mediterranean Tropical-Like Cyclone (MTLC), which was poorly predicted by operational General Circulation Models (GCMs) at the time, was chosen as case study.

The simulations employing a grid spacing of $\mathcal{O}(1\ \text{km})$ showed a substantial increase of the forecast skill, in terms of the cyclone's trajectory, over the National Centers for Environmental Prediction (NCEP)-Global Forecasting System (GFS) and European Center for Medium range Weather Forecast (ECMWF)-Integrated Forecast System (IFS) mod-

els forecasts. Simulations characterized by a grid spacing larger than 2.5 km instead failed to represent the main observed features of the cyclone. By analyzing the simulated internal structure of the cyclone in different cases, it was shown that simulations characterized by a grid spacing larger than 2.5 km contained a cyclone characterized by a shallow, if not absent, central warm core. This was due to the fact that poorly-resolved convective processes were not causing a significant release of latent heat. The identified threshold of approximately 2 km is similar to the one found by Miyamoto, Kajikawa, et al. (2013) in a global sub-km resolution.

Using a Potential Vorticity (PV)-thinking method, it was shown that the biases in the representation of the latent heat release by convection propagate to the large-scale flow, eventually modifying the cyclone evolution over time. Additional nested simulations with sub-km grid spacing (300 m) revealed the ability of the model to fully capture the internal structure and in particular the central warm core, although the model did produce a cyclone more intense than the observed.

The results of this chapter, despite being related to a specific case, can provide guidance regarding the modeling setup of new studies that will need to use Numerical Weather Prediction (NWP) models to investigate the evolution of MTLCs. Adopting a grid spacing of $\mathcal{O}(1$ km) in future state-of-the-art NWP models will improve our ability to forecast intense storms like the one described here. A correct prediction of these hybrid cyclones would help the affected territories to be prepared and promptly respond to emergencies with an informed damage mitigation strategy.

7.2 OVERALL CONCLUSIONS

The first attempt to predict the weather evolution is usually attributed to Lewis Fry Richardson who, back in 1922, imagined the first *forecast factory* made up of human calculators (Richardson, 1922). The year 1950 saw one of the first true weather forecasts provided by a model which integrated the quasi-geostrophic PV equation (Charney et al., 1950) on the only available computer at that time, the Electronic Numerical Integrator and Computer (ENIAC) located in Aberdeen, Maryland (Lynch, 2008). In the following years, more conventional approaches to represent the atmospheric evolution over time used simplified models, in which the horizontal transport of energy was parametrized (e.g. Earth System Models of Intermediate Complexity (EMIC), Claussen et al., 2002). The first big leap in the science of NWP was ushered in by the new generation of NWP models, which treated the horizontal transport explicitly, while parametrizing vertical motions with the hydrostatic approximation (e.g. the family of Coupled Model Intercomparison Project (CMIP) models, Meehl et al., 2000, and many GCMs widely used at the time of writing). Technolog-

A hierarchy of NWP models

ical and scientific progress has allowed more recent models to fully resolve the energy transport in 3 dimensions (e.g. the already cited ICOsahedral Non-hydrostatic (ICON) used to produce global forecasts at the Deutscher WetterDienst (DWD)).

The "quiet" evolution of NWPs

Such advances in the science of NWPs represent a "quiet" evolution, since they have not usually been perceived as fundamental breakthroughs in physics (Bauer et al., 2015). Nevertheless, these advances in NWP can be counted among the greatest in the modern physical sciences, since accurate forecasts save lives, support emergency management and mitigation of economic losses from high impact weather, as already highlighted for the case of Hurricane *Ophelia*.

To appreciate such advances more quantitatively, consider that at the time of writing a 10-day forecast obtained from the ECMWF-IFS model has the same accuracy as a 7-day forecast from 1995, while a 5-days forecast has the same skill as a 3-days forecast from 1999. This advance is illustrated by the famous figure depicting the anomaly correlation of predicted geopotential height at 500 hPa[1].

Although an increase in forecast skill is unequivocal up to 2010, more recent years have not witnessed the same rapid progress. This is especially evident when one considers the evolution of the lead time of the anomaly correlation reaching 80%, essentially a measure of high accuracy forecasts[2]. This value steadily increased from 5 to 6.5 days between 1998 and 2010 but has since then been oscillating between 6.5 and 7 days without any further sign of improvement.

Therefore, one may ask:

Why has our ability to forecast the weather evolution not improved in the last 10 years?

One reason is certainly related to the intrinsic low predictability of the atmosphere, which is a chaotic system characterized by large *Lyapunov* exponents (Cecconi et al., 2012). Another reason is the introduction of unwanted biases due to the need of parametrizing sub-grid scale processes in coarse resolution NWP models. Our skill in predicting the weather is still bounded by the employment of such parametrizations, which unfortunately can not be yet completely abandoned (Maher et al., 2018). Alternative approaches to increase the model resolution, and thus reduce the number of required parametrizations while limiting computational costs, exist and have been explored in this dissertation. The main goal was to show that such convection-explicit models provide us with a deeper level of understanding of different physical processes describing the interaction of convection with the mesoscale and with large-scale atmospheric processes.

Parametrizations

---

1 Always available and up-to-date at https://www.ecmwf.int/en/forecasts/charts/catalogue/plwww_m_hr_ccaf_adrian_ts

2 Available also on the ECMWF website at https://www.ecmwf.int/en/forecasts/charts/catalogue/plwww_m_hr_ccafreach_ts.

One of these processes, which has been shown to exert a strong influence on NWPs, is the interaction between the land surface and the atmosphere. Surface fluxes of momentum, heat and moisture are strongly modulated by the land surface and can affect the atmospheric evolution over daily to seasonal time scales (MacLeod et al., 2016). Soil moisture in particular is an important parameter that can change the response of the earth system to perturbations through its control on surface fluxes of moisture and heat (Seneviratne, Corti, et al., 2010). A modification of surface fluxes alter the moisture and thermal balance of the atmosphere, thus potentially affecting the formation of convective clouds and ensuing precipitation on monthly to seasonal time scales.

Thus, it is evident that land-atmosphere interactions are strongly affected by global warming and represent a key element for climate change. This is due to the fact that the northwards shift of climatic zones predicted on the European continent, due to enhanced greenhouse gas concentrations, will make central and eastern Europe more susceptible to the effect of land-atmosphere coupling (Seneviratne, Lüthi, et al., 2006). Therefore, questions like the following will become more relevant for the European continent in the future:

Land-atmosphere interactions and the climate

Will changes in irrigation affect the distribution of precipitation over the same area?
Will planting crops or increasing the fraction of grazing land increase the likelihood of heat waves?

Such projections of future climate scenarios, however, heavily rely on the accuracy of climate models, which still struggle to reproduce convective precipitation (Kendon et al., 2012) and can bias the resulting identification of feedback between soil moisture and precipitation (Hohenegger, Brockhaus, et al., 2009).

According to the results of Chapters 3, 4 and 5, using models where convection is explicitly resolved may help to reduce the aforementioned biases. Furthermore, my results show that, in areas of the world where the surface is approximately homogeneous, precipitation will increase if the soil moisture is increased, regardless of the atmospheric state. This relationship will therefore most likely persist under future global warming scenarios. Instead, in regions where the land surface is heterogeneous the presence of mesoscale circulations effectively removes the dependency on soil moisture: in this case, variations of precipitation are more dependent on the atmosphere, which controls the redistribution of advection and evaporation sources. More investigations are needed to assess the response of mesoscale circulations created by surface heterogeneities to climate change.

The second aspect which is intimately related to NWPs and to the results of this dissertation concerns the prediction of high-impact weather events. Local thunderstorms, such as the ones simulated

High-impact weather events prediction in the future

in Chapter 5, or more organized thunderstorms embedded in a cyclonic circulation, such as those reproduced in Chapter 6, are likely to become either more frequent or stronger in the future. Púčik et al. (2017), for example, found a robust increase in the frequency of occurrence of unstable environments favorable for severe convective storms across central and south-central Europe in the late 21st century. Such an increase is primarily caused by an enhanced latent instability due to increases in the lower tropospheric moisture. Equivalently, several authors (Romero and Emanuel, 2013; Tous, Zappa, et al., 2016; Romera et al., 2017) have found a decrease in the number of MTLCs in the future, albeit with an increase in the intensity of stronger events. Although the vertical static stability of the atmosphere is projected to increase in the future, the warming of Sea Surface Temperatures (SSTs) and consequent enhancement of surface fluxes will likely give birth to fewer but stronger cyclones.

Projections such as these rely on simulations performed with Regional Climate Models (RCMs) which can only reproduce the *average* environmental conditions prone to convection development. The latter may not be necessarily representative of the actual convective activity (Tippett et al., 2015). Furthermore, models characterized by coarse resolutions may produce less intense storms as a result of missing thermodynamic processes related to convection development, as shown in Chapter 6. However, since environmental conditions may explain up to 80% of the variance associated with modeled severe weather reports (Gensini and Mote, 2015), RCMs still provide us consistent statistics of the increase in severe storms over Europe. In the future these will be eventually replaced by more precise estimates obtained through convection-permitting or even convection-explicit models (Púčik et al., 2017).

Therefore, NWP models that can explicitly resolve convection on large scales are important not only for weather forecast but also for climate prediction. In the beginning of this section we left the timeline of NWPs advances at the arrival of global models that can explicitly reproduce horizontal and vertical transport or energy (e.g. ICON) while still needing to parametrize sub-grid scale processes like moist convection. The results of this dissertation show that the time has come to take the next great leap by trying to implement $\mathcal{O}(1$ km) or even sub-km grid spacing in operational NWP models. Although this may sound like an impossible task, already 5 years ago Miyamoto, Kajikawa, et al. (2013) showed that sub-km global simulations are feasible by performing a 3-day integration using the Nonhydrostatic ICosahedral Atmospheric Model (NICAM) characterized by a grid spacing of 870 m. In a follow-up study, Miyamoto, Yamaura, et al. (2016) showed how results from such simulations can be used to identify the precursors of deep moist convection over many areas of the world. In fact, sub-km global resolutions have many ad-

Towards global sub-km NWPs

vantages. On top of explicitly resolving deep moist convection, they can explicitly reproduce orographic drag, gravity waves, realistic land surface features and shallow mesoscale circulations created by cloud-radiation interactions. But, most importantly, they can provide us with results directly comparable to observations, especially those regarding local point measurements. Such comparisons have until now been difficult, given the coarse resolution employed in earlier generation models.

Models like NICAM and ICON-LEM finally allow us to consider the full set of Navier-Stokes equations, without having to make compromises on account of computational expense. It should be stressed that this is maybe one of the greatest leaps yet in the science of NWPs, as such models are entirely based on physical principles and not on empirical laws. This does not only mean that convective processes are explicitly represented, which was already the case in former idealized Large Eddy Simulation (LES) models, but that their interactions with all the scales of motions, from the mesoscale to the planetary scale, are captured. Therefore, such models may be used in the future to understand how individual convective clouds develop, grow and decay or even evolve into more organized structures which can eventually become Hurricanes or Extra-Tropical Cyclones. In this dissertation I have been able to glimpse such interactions and appreciate the power of unraveling their secrets. It is, indeed, a golden age for atmospheric sciences.

Part III

APPENDIX

APPENDIX TO CHAPTER 2

A.1 PARAMETERS OF THE SOIL MODEL

Table A.1 shows some of the parameters used in TERRA-ML for different soil types. For an exhaustive list of all the parameters the reader is referred to Doms et al. (2011).

soil type	sandy loam	loam
volume of voids w_{pv}	0.445	0.455
field capacity w_{fc}	0.260	0.340
permanent wilting point w_{pwp}	0.100	0.110
air dryness point w_{adp}	0.030	0.035
hydraulic diffusivity parameter D_0 [$10^{-9}\mathrm{m^2/s}$]	3460	3570
hydraulic diffusivity parameter D_1	-9.47	-7.44
hydraulic conductivity parameter K_0 [$10^{-9}\mathrm{m/s}$]	9430	5310
hydraulic conductivity parameter K_1	-20.86	-19.66
heat capacity $\rho_0 c_0$ [$10^6\ \mathrm{Jm^{-3}K^{-1}}$]	1.35	1.42
heat conductivity λ_0 [$\mathrm{WK^{-1}m^{-1}}$]	0.28	0.25
heat conductivity $\Delta\lambda$ [$\mathrm{WK^{-1}m^{-1}}$]	2.40	1.58

Table A.1: Hydraulic and thermal parameters of the different soil types.

A.2 PARAMETERS USED IN THE EXTPAR FILE

Table A.2 shows the values used to create the `extpar` file that is employed to initialize TERRA-ML.

Fraction of sand	100
Fraction of silt	0
Fraction of clay	0
Fraction of oc for soil index	0
Bulk density for soil index	1
Soil type	5 (loam)
Fraction of land	100
Fraction of ice	0
Plant cover maximum	0
Leaf Area Index Maximum	0
Minimum stomatal resistance	150 s m^{-1}
Fraction of urban areas	0
Fraction of deciduous forests	0
Fraction of evergreen forests	0

Longwave surface emissivity	1
Root depth	0 m
Surface roughness length	0.1 m
NDVI (maximum, minimum, average)	0
Topography	0 m
Climatological layer temperature	281 K
Fraction of Lake	0
Depth of Lake	0 m
Land use class fraction	0
Surface albedo	15.3

Table A.2: Hydraulic and thermal parameters of the different soil types.

APPENDIX TO CHAPTER 3

Figure B.1 presents additional results of the conceptual model developed in Chapter 3 with different values of the slope m and offset q used for the linear regression. It can be noted how increasing the slope causes a higher sensitivity of precipitation to latent heat fluxes, while increasing the offset flattens the contour lines, thus indicating a weaker sensitivity of the atmosphere to the surface state.
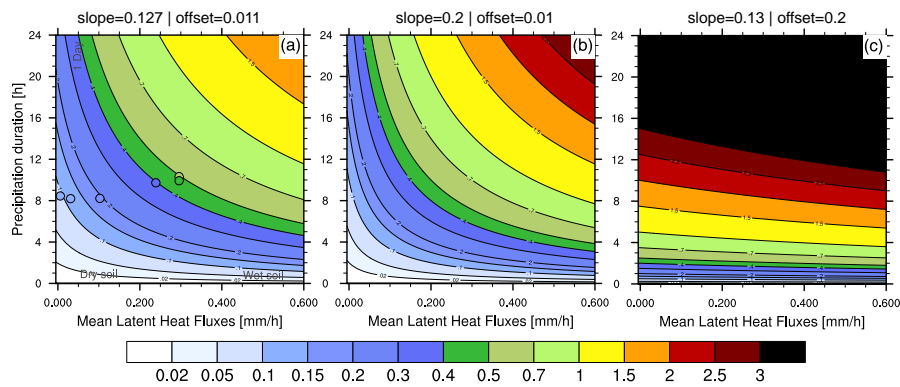
Figure B.1: Contour plot showing the estimated accumulated precipitation R [shading, mm] as function of $\widetilde{LH}$ [mm h^{-1}] and $t_1 - t_0$ [h] for different values of slope m and offset q. Panel a is equivalent to Fig. 3.8.

C

APPENDIX TO CHAPTER 4

C.1 FRONT VELOCITY

Figure C.1 shows the diurnal-averaged speed of the front tracked with the algorithm presented in chapter 4 for different cases. It shows how the speed is approximately constant when changing the gradient in soil moisture, which affects the gradient in surface sensible heat fluxes.
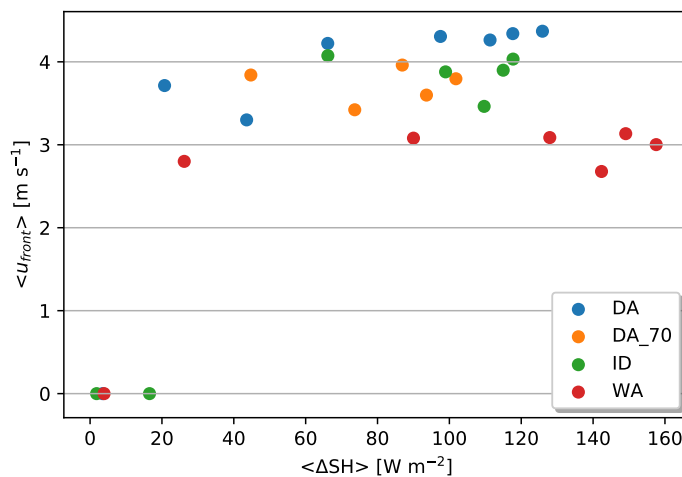
Figure C.1: Diurnal-averaged speed of the front [m s^{-1}] as function of diurnal-averaged difference in sensible heat fluxes between the wet and dry patch [W m^{-2}] in different simulations. For details see Chapter 4.

C.2 MOIST STATIC ENERGY PROFILES

Figure C.2 shows the profiles of updraft-averaged Moist Static Energy (MSE) and of the difference between the updraft and the environment computed for the DA and ID simulations. Updraft points are selected using a threshold for vertical velocity v_3 and cloud water content mixing ratio q_c of 1 m s^{-1} and 10^{-4} kg kg^{-1}, respectively.
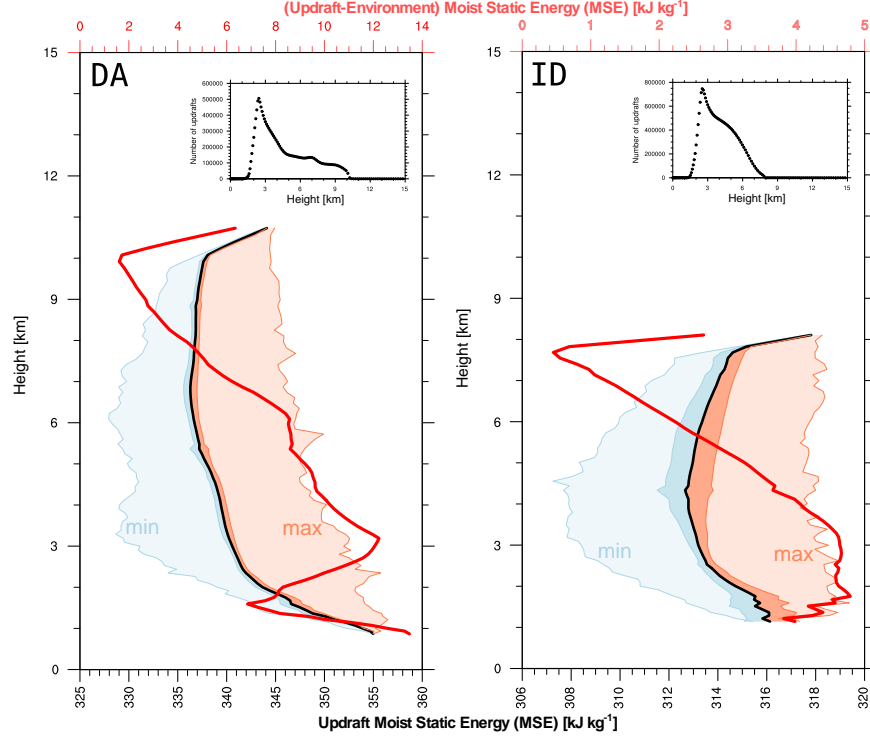
Figure C.2: Vertical profiles of updraft and environmental MSE for the DA (left) and ID (right) cases. Data are averaged in time during the entire length of the simulation. Black line, dark and light red (blue) shadings represent, respectively, the average, 1-standard deviation range and maximum (minimum) values averaged over all the updraft points. All these values are referred to the bottom *x*-axis. Red solid line shows instead the difference in MSE between the updraft and the environment and is represented by the upper *x*-axis. The upper right inset contains the number of updrafts sampled at every height level [m] and used to compute the average.

C.3 COMPUTATION OF THE ADVECTION AS RESIDUAL TERM

The advection of every tracer is computed directly from the moisture balance equation as a residual. I use the following formulation, which applies for a certain point (x, y) over a 2-dimensional domain:

$$\frac{1}{\rho_w} \int_0^\tau \int_0^H \frac{Dq_{tot}}{Dt} \rho_a \, dz \, dt =$$

$$\frac{1}{\rho_w} \int_0^\tau \int_0^H \left[\frac{\partial q_{tot}}{\partial t} + \mathbf{v} \cdot \nabla q_{tot} \right] \rho_a \, dz \, dt = E - P \qquad \text{(C.1)}$$

where D indicates the total derivative, P [m] is the accumulated precipitation, E [m] the accumulated evaporation, q_{tot} [kg kg^{-1}] represents the sum of all tracers (water vapour q_v, clouds q_c, rain q_r, snow q_s, ice q_i, graupel q_g and hail q_h) mixing ratios, ρ_w [kg m^{-3}] the density of water, ρ_a [kg m^{-3}] the air density and $\mathbf{v}$ the velocity of air as a vector. H indicates the top of the simulation domain and τ the lenght

of the accumulation period (18 hours in our experiments). The total derivative can be divided into its advective term:

$$A \equiv -\frac{1}{\rho_w} \int_0^\tau \int_0^H \mathbf{v} \cdot \nabla q_{\text{tot}} \rho_a \, dz \, dt \qquad (C.2)$$

and the local derivative:

$$\frac{1}{\rho_w} \int_0^\tau \int_0^H \frac{\partial q_{\text{tot}}}{\partial t} \rho_a \, dz \, dt = A + E - P \qquad (C.3)$$

In both equations C.2 and C.3 the variables A, E, P are solely functions of (x, y) whereas q_{tot} depends also on time t and on the vertical coordinate z. The dependency on (x, y) can be removed by applying an average operator over a certain area, indicated with the subscript area:

$$\frac{1}{\rho_w} \int_0^\tau \int_0^H \frac{\partial q_{\text{tot}}}{\partial t} \bigg|_{\text{area}} \rho_a \, dz \, dt = A_{\text{area}} + E_{\text{area}} - P_{\text{area}} \qquad (C.4)$$

Throughout Chapters 4 and 5 I use as area either the full domain, denoted with the suffix $_{\text{dom}}$, or the dry patch only, denoted by the suffix $_{\text{dry}}$. By indicating the weighted vertical integral of q_{tot} as $\bar{q}_{\text{tot}} \equiv \int_0^H q_{\text{tot}} \rho_a \, dz$ I can further simplify the previous equation to:

$$\frac{1}{\rho_w} \int_0^\tau \frac{\partial \bar{q}_{\text{tot}}}{\partial t} \bigg|_{\text{area}} dt = A_{\text{area}} + E_{\text{area}} - P_{\text{area}} \qquad (C.5)$$

Although other studies only considered the advection of water vapour, i.e. of $\bar{q}_v$, in order to close the balance it is necessary to consider all species. In fact, although $\bar{q}_i, \bar{q}_g, \bar{q}_h, \bar{q}_s$ are order of magnitudes smaller than $\bar{q}_v, \bar{q}_c, \bar{q}_r$, their variations over time are not, so that neglecting these terms in Eq. C.5 would lead to an unbalance.

From the 5-min simulation output I use Eq. C.5 and estimate the advection as the residual $R_{\text{area}} = \frac{1}{\rho_w} \int_0^\tau \frac{\partial \bar{q}_{\text{tot}}}{\partial t} \big|_{\text{area}} dt + P_{\text{area}} - E_{\text{area}} \equiv A_{\text{area}}$. When averaged over the entire domain, $R_{\text{dom}} = 0$, which shows that the balance is closed.

D

APPENDIX TO CHAPTER 6

D.1 ADDITIONAL FIGURES

Figures D.1 and D.2 show the synoptic configuration preceding the cyclone formation.
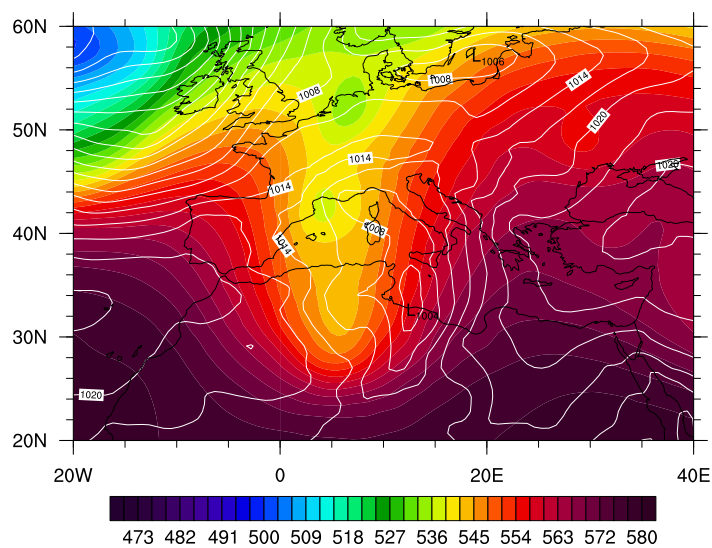
Figure D.1: Geopotential height [dam] at 500 hPa (color scale) and MSLP [hPa] on 6 November 2014 at 1200 UTC. Data from ERA-INTERIM.
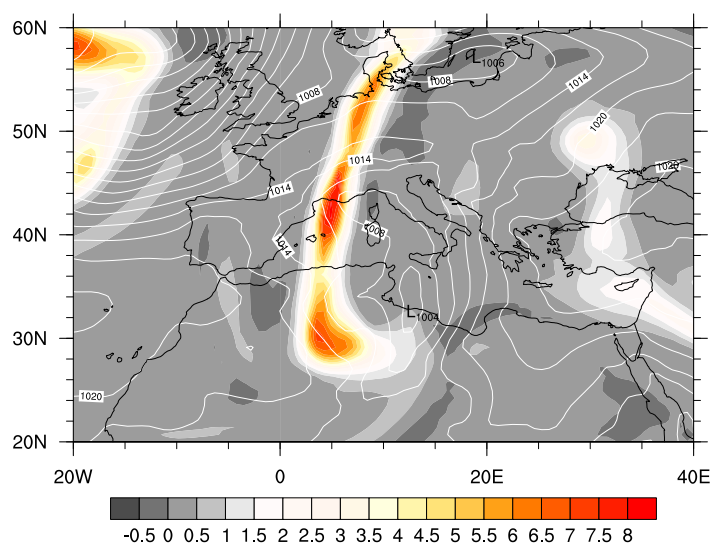
Figure D.2: Potential Vorticity [PVU] at 350 hPa (color scale) and MSLP [hPa] on 6 November 2014 at 1200 UTC. Data from ERA-INTERIM.

D.2 CYCLONE TRACKING USING SATELLITE DATA

In order to obtain the reference track presented in Fig. 6.1 I first computed the brightness temperature using the radiance measured in the Infra-Red (IR) 10.8 μm channel by the SEVIRI instrument aboard the MSG satellite using Rapid-scan data (every 5 minutes). Then, given that the cyclone showed a cloud-free region coincident with the cyclone center for most of its life-cycle (until the late morning of 8 November 2014), I obtained a first-guess trajectory by tracking the maximum of brightness temperature located in the center of the cyclone (see Fig. D.3). The obtained trajectory, which contained a new position of the cloud-free region every 5 minutes, was then smoothed to hourly data.
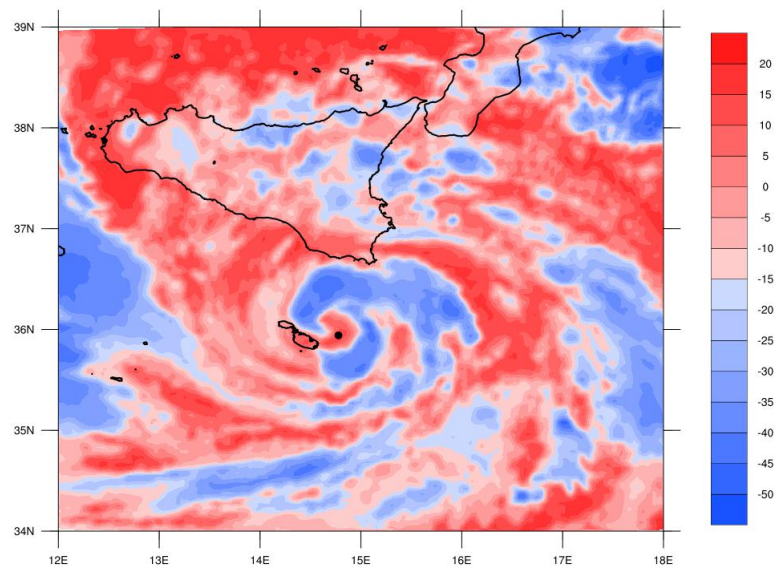
Figure D.3: High-Rate SEVIRI Infra-red imagery (10.8 μm channel brightness temperature, $^\circ C$) acquired at 1700 UTC. Black point shows the position of the cyclone center as found by the tracking algorithm using the local maximum of brightness temperature.

D.3 DATA SOURCES

- Fig. 6.2 was generated using the imagery from the NASA Worldview application (https://worldview.earthdata.nasa.gov/) operated by the NASA/Goddard Space Flight Center Earth Science Data and Information System (ESDIS) project.

- MSG-SEVIRI data used for the tracking of the cyclone were obtained using the EUMETSAT Data Centre.

- The *Linosa* weather station (Fig. 6.3 a and b) is part of *Meteonetwork*, an Italian network of amateur weather stations following WMO-standards (http://www.meteonetwork.it/) while the

Bugibba weather station (Fig. 6.3 c) is part of the Weather Underground network (http://www.wunderground.com).

- The radar data of Fig. 6.4 (a) were obtained from the Malta International Airport MetOffice (https://www.maltairport.com/weather/radar-images/) while the data used in Fig. 6.4 (b,c) were obtained from Italian National Radar Mosaic (Protezione Civile, http://www.protezionecivile.gov.it/jcms/it/mappa_radar.wp).

- Figure 6.9 was contributed by Felicia Brisc, Climate Visualization Laboratory, Center for Earth System Research and Sustainability, University of Hamburg.

D.4 OBSERVED VALUES

Table 4.2 summarizes all the relevant values measured by weather stations in chronological order.

Location	Date	Time (UTC)	Type	Value
Pantelleria	7/11/2014	0800	MSLP minimum	992 hPa
Linosa	7/11/2014	1150	Wind gust maximum	94.9 km h^{-1}
Lampedusa	7/11/2014	1206	Wind gust maximum	135.2 km h^{-1}
Lampedusa	7/11/2014	1206	MSLP minimum	994 hPa
Linosa	7/11/2014	1230	MSLP minimum	981.9 hPa
Bugibba (Malta)	7/11/2014	1558	Wind gust maximum	153.7 km h^{-1}
Gharb (Malta)	7/11/2014	1604	MSLP minimum	988.7 hPa
Bugibba (Malta)	7/11/2014	1613	MSLP minimum	978.6 hPa
Malta airport	7/11/2014	1615	Wind gust maximum	103.7 km h^{-1}
Malta airport	7/11/2014	1634	MSLP minimum	984 hPa
Cozzo Spadaro	7/11/2014	2100	MSLP minimum	994.2 hPa
Catania (Sigonella airport)	8/11/2014	0300	MSLP minimum	998.3 hPa
Sortino	8/11/2014	0721	MSLP minimum	995.8 hPa
Sortino	8/11/2014	0721	Wind gust maximum	90.1 km h^{-1}
Cozzo Spadaro	8/11/2014	0800	MSLP minimum	996.2 hPa

Table D.1: Values measured by weather stations displayed in chronological order.

D.5 REFERENCES FOR THE EMPLOYED PARAMETRIZATION SCHEMES

Table D.2 contains all the relevant references for the parametrization schemes used in the model. See Tab. 6.1 for further details.

Name	References
RRTM	Clough et al. (2005)
Single-Moment 3-cat ice Microphysics	Doms et al. (2011)
Mass-Flux shallow/deep	Bechtold et al. (2008)
All-or-nothing scheme	Sommeria and Deardorff (1977)
Diagnostic PDF	
2-D Prognostic Turbulent Kinetic Energy (TKE)	Raschendorfer (2001)
3-D Smagorinsky	Dipankar et al. (2015)
Lott & Miller	Lott and Miller (1997)
Wave dissipation at critical level	Orr et al. (2010)
Tiled TERRA+FLAKE	Schrodin and Heise (2002)

Table D.2: List of the references for the parametrizations listed in Table 6.1.

Asharaf, S., A. Dobler, and B. Ahrens (2012). "Soil moisture–precipitation feedback processes in the Indian summer monsoon season." *Journal of Hydrometeorology* 13.5, pp. 1461–1474. DOI: `10.1175/JHM-D-12-06.1`.

Avissar, R. (1995). "Scaling of land-atmosphere interactions: An atmospheric modelling perspective." *Hydrological Processes* 9.5-6, pp. 679–695. DOI: `10.1002/hyp.3360090514`.

Avissar, R. and Y. Liu (1996). "Three-dimensional numerical study of shallow convective clouds and precipitation induced by land surface forcing." *Journal of Geophysical Research: Atmospheres* 101.D3, pp. 7499–7518. DOI: `10.1029/95JD03031`.

Barthlott, C. and N. Kalthoff (2011). "A numerical sensitivity study on the impact of soil moisture on convection-related parameters and convective precipitation over complex terrain." *Journal of the Atmospheric Sciences* 68.12, pp. 2971–2987. DOI: `10.1175/JAS-D-11-027.1`.

Bauer, P., A. Thorpe, and G. Brunet (2015). "The quiet revolution of numerical weather prediction." *Nature* 525.7567, p. 47. DOI: `10.1038/nature14956`.

Bechtold, P., M. Köhler, T. Jung, F. Doblas-Reyes, M. Leutbecher, M. J. Rodwell, F. Vitart, and G. Balsamo (2008). "Advances in simulating atmospheric variability with the ECMWF model: From synoptic to decadal time-scales." *Quarterly Journal of the Royal Meteorological Society* 134.634, pp. 1337–1351. DOI: `10.1002/qj.289`.

Billing, H., I. Haupt, and W. Tonn (1983). "Evolution of a hurricane-like cyclone in the Mediterranean Sea." *Beiträge zur Physik der Atmosphäre* 56.4, pp. 508–510.

Boschovich, P. R. G. (1749). *Dissertazione sopra il turbine atmosferico che la notte fra gli XI e i XII di Giugno 1749 devastò una gran parte di Roma*.

Bryan, G. H., J. C. Wyngaard, and J. M. Fritsch (2003). "Resolution requirements for the simulation of deep moist convection." *Monthly Weather Review* 131.10, pp. 2394–2416. DOI: `10.1175/1520-0493(2003)131%3C2394:RRFTSO%3E2.0.CO;2`.

Budyko, M. I. (1961). "The heat balance of the Earth's surface." *Soviet Geography* 2.4, pp. 3–13. DOI: `10.1080/00385417.1962.10769936`.

— (1974). *Climate and Life*. Academic Press, New York.

Burde, G. and A. Zangvil (2001). "The estimation of regional precipitation recycling. part i: Review of recycling models." *Journal of climate* 14.12, pp. 2497–2508. DOI: `10.1175/1520-0442(2001)014%3C2497:TEORPR%3E2.0.CO;2`.

Campins, J., A. Genovés, M. Picornell, and A. Jansà (2011). "Climatology of Mediterranean cyclones using the ERA-40 dataset." *International Journal of Climatology* 31.11, pp. 1596–1614. DOI: `10.1002/joc.2183`.

Carrió, D., V. Homar, A. Jansà, R. Romero, and M. Picornell (2017). "Tropicalization process of the 7 November 2014 Mediterranean cyclone: Numerical sensitivity study." *Atmospheric Research* 197, pp. 300–312. DOI: `10.1016/j.atmosres.2017.07.018`.

Cavicchia, L., H. von Storch, and S. Gualdi (2014). "A long-term climatology of medicanes." *Climate dynamics* 43.5-6, pp. 1183–1195. DOI: `10.1007/s00382-013-1893-7`.

Cecconi, F., M. Cencini, M. Falcioni, and A. Vulpiani (2012). "The prediction of future from the past: an old problem from a modern perspective." *arXiv preprint arXiv:1210.6758*.

Charney, J. G., R. Fjörtoft, and J. v. Neumann (1950). "Numerical integration of the barotropic vorticity equation." *Tellus* 2.4, pp. 237–254. DOI: `10.3402/tellusa.v2i4.8607`.

Chen, F. and R. Avissar (1994). "Impact of land-surface moisture variability on local shallow convective cumulus and precipitation in large-scale models." *Journal of Applied Meteorology* 33.12, pp. 1382–1401. DOI: `10.1175/1520-0450(1994)033%3C1382:IOLSMV%3E2.0.CO;2`.

CIESIN, I. (2004). "CIAT Global rural-urban mapping project (GRUMP)." *Alpha Version: Population grids*.

Cioni, G., P. Malguzzi, and A. Buzzi (2016). "Thermal structure and dynamical precursor of a Mediterranean tropical-like cyclone." *Quarterly Journal of the Royal Meteorological Society* 142.697, pp. 1757–1766. DOI: `10.1002/qj.2773`.

Claud, C., B. Alhammoud, B. Funatsu, and J.-P. Chaboureau (2010). "Mediterranean hurricanes: large-scale environment and convective and precipitating areas from satellite microwave observations." *Natural Hazards and Earth System Sciences* 10.10, p. 2199. DOI: `10.5194/nhess-10-2199-2010`.

Claussen, M., L. Mysak, A. Weaver, M. Crucifix, T. Fichefet, M.-F. Loutre, S. Weber, J. Alcamo, V. Alexeev, A. Berger, et al. (2002). "Earth system models of intermediate complexity: closing the gap in the spectrum of climate system models." *Climate dynamics* 18.7, pp. 579–586.

Clough, S., M. Shephard, E. Mlawer, J. Delamere, M. Iacono, K. Cady-Pereira, S. Boukabara, and P. Brown (2005). "Atmospheric radiative transfer modeling: a summary of the AER codes." *Journal of Quantitative Spectroscopy and Radiative Transfer* 91.2, pp. 233–244. DOI: `10.1016/j.jqsrt.2004.05.058`.

Couvreux, F., C. Rio, F. Guichard, M. Lothon, G. Canut, D. Bouniol, and A. Gounou (2012). "Initiation of daytime local convection in a semi-arid region analysed with high-resolution simulations and

AMMA observations." *Quarterly Journal of the Royal Meteorological Society* 138.662, pp. 56–71. DOI: `10.1002/qj.903`.

Crosman, E. T. and J. D. Horel (2010). "Sea and lake breezes: a review of numerical studies." *Boundary-layer meteorology* 137.1, pp. 1–29. DOI: `10.1007/s10546-010-9517-9`.

Davolio, S., M. Miglietta, A. Moscatello, F. Pacifico, A. Buzzi, and R. Rotunno (2009). "Numerical forecast and analysis of a tropical-like cyclone in the Ionian Sea." *Natural Hazards and Earth System Sciences* 9.2, pp. 551–562. DOI: `10.5194/nhess-9-551-2009`.

Delden, A. V. (2003). "Adjustment to heating, potential vorticity and cyclogenesis." *Quarterly Journal of the Royal Meteorological Society* 129.595, pp. 3305–3322. DOI: `10.1256/qj.01.65`.

Dickinson, R. E. (1984). "Modeling evapotranspiration for three-dimensional global climate models." *Climate processes and climate sensitivity*, pp. 58–72. DOI: `10.1029/GM029p0058`.

Dipankar, A., B. Stevens, R. Heinze, C. Moseley, G. Zängl, M. Giorgetta, and S. Brdar (2015). "Large eddy simulation using the general circulation model ICON." *Journal of Advances in Modeling Earth Systems*. DOI: `10.1002/2015MS000431`.

Doms, G. et al. (2011). *A Description of the Nonhydrostatic Regional COSMO Model. Part II: Physical Parametrization*. Consortium for Small-Scale Modeling.

Eltahir, E. A. and R. L. Bras (1996). "Precipitation recycling." *Reviews of geophysics* 34.3, pp. 367–378. DOI: `10.1029/96RG01927`.

Emanuel, K. (2005). "Genesis and maintenance of" Mediterranean hurricanes"." *Advances in Geosciences* 2.2, pp. 217–220. DOI: `10.5194/adgeo-2-217-2005`.

EMCWF (2001). "Key issues in the parametrization of subgrid physical processes." In: *ECMWF Seminar proceedings*, p. 349.

Ernst, J. and M. Matson (1983). "A Mediterranean tropical storm?" *Weather* 38.11, pp. 332–337. DOI: `10.1002/j.1477-8696.1983.tb04818.x`.

Fermepin, S. and S. Bony (2014). "Influence of low-cloud radiative effects on tropical circulation and precipitation." *Journal of Advances in Modeling Earth Systems* 6.3, pp. 513–526. DOI: `10.1002/2013MS000288`.

Ferranti, L., E. Klinker, A. Hollingsworth, and B. Hoskins (2002). "Diagnosis of systematic forecast errors dependent on flow pattern." *Quarterly Journal of the Royal Meteorological Society* 128.583, pp. 1623–1640. DOI: `10.1002/qj.200212858312`.

Findell, K. L. and E. A. Eltahir (2003a). "Atmospheric controls on soil moisture-boundary layer interactions: Three-dimensional wind effects." *Journal of Geophysical Research: Atmospheres* 108.D8. DOI: `10.1029/2001JD001515`.

— (2003b). "Atmospheric controls on soil moisture-boundary layer interactions. Part I: Framework development." *Journal of Hydrom-*

eteorology 4.3, pp. 552–569. DOI: 10.1175/1525-7541(2003)004%3C0552:ACOSML%3E2.0.CO;2.

Fischer, E. M., S. Seneviratne, P. Vidale, D. Lüthi, and C. Schär (2007). "Soil moisture-atmosphere interactions during the 2003 European summer heat wave." *Journal of Climate* 20.20, pp. 5081–5099. DOI: 10.1175/JCLI4288.1.

Fita, L., R. Romero, A. Luque, K. Emanuel, and C. Ramis (2007). "Analysis of the environments of seven Mediterranean tropical-like storms using an axisymmetric, nonhydrostatic, cloud resolving model." *Natural Hazards and Earth System Sciences* 7.1, pp. 41–56. DOI: 10.5194/nhess-7-41-2007.

Fitzmaurice, J. A. (2007). "A critical analysis of bulk precipitation recycling models." PhD thesis. Massachusetts Institute of Technology.

Ford, T. W., A. D. Rapp, S. M. Quiring, and J. Blake (2015). "Soil moisture-precipitation coupling: observations from the Oklahoma Mesonet and underlying physical mechanisms." *Hydrology and Earth System Sciences* 19.8, pp. 3617–3631. DOI: 10.5194/hess-19-3617-2015.

Froidevaux, P., L. Schlemmer, J. Schmidli, W. Langhans, and C. Schär (2014). "Influence of the background wind on the local soil moisture–precipitation feedback." *Journal of the Atmospheric Sciences* 71.2, pp. 782–799. DOI: 10.1175/JAS-D-13-0180.1.

Fukutome, S., C. Prim, and C. Schär (2001). "The role of soil states in medium-range weather predictability." *Nonlinear Processes in Geophysics* 8.6, pp. 373–386. DOI: 10.5194/npg-8-373-2001.

Gensini, V. A. and T. L. Mote (2015). "Downscaled estimates of late 21st century severe weather from CCSM3." *Climatic Change* 129.1-2, pp. 307–321. DOI: 10.1007/s10584-014-1320-z.

Gentine, P., A. Garelli, S.-B. Park, J. Nie, G. Torri, and Z. Kuang (2016). "Role of surface heat fluxes underneath cold pools." *Geophysical research letters* 43.2, pp. 874–883. DOI: 10.1002/2015GL067262.

Gentine, P., A. A. Holtslag, F. D'Andrea, and M. Ek (2013). "Surface and atmospheric controls on the onset of moist convection over land." *Journal of Hydrometeorology* 14.5, pp. 1443–1462. DOI: 10.1175/JHM-D-12-0137.1.

Grazzini, F. (2007). "Predictability of a large-scale flow conducive to extreme precipitation over the western Alps." *Meteorology and Atmospheric Physics* 95.3-4, pp. 123–138. DOI: 10.1007/s00703-006-0205-8.

Guillod, B. P., B. Orlowsky, D. G. Miralles, A. J. Teuling, and S. I. Seneviratne (2015). "Reconciling spatial and temporal soil moisture effects on afternoon rainfall." *Nature communications* 6. DOI: 10.1038/ncomms7443.

Hauser, H., H. Hagen, and H. Theisel (2007). *Topology-based methods in visualization*. Springer Science. DOI: 10.1007/978-3-540-70823-0.

Heinze, R., A. Dipankar, C. C. Henken, C. Moseley, O. Sourdeval, S. Trömel, X. Xie, P. Adamidis, F. Ament, H. Baars, et al. (2016). "Large-eddy simulations over Germany using ICON: A comprehensive evaluation." *Quarterly Journal of the Royal Meteorological Society* In Review. DOI: `10.1002/qj.2947`.

Heus, T., C. Van Heerwaarden, H. Jonker, A. Pier Siebesma, S. Axelsen, K. Dries, O. Geoffroy, A. Moene, D. Pino, S. De Roode, et al. (2010). "Formulation of the Dutch Atmospheric Large-Eddy Simulation (DALES) and overview of its applications." *Geoscientific Model Development* 3.2, pp. 415–444. DOI: `10.5194/gmd-3-415-2010`.

Hillel, D. (2012). *Applications of soil physics*. Elsevier.

Hinze, J. O. (1975). *Turbulence*. N.Y.: McGraw-Hill. DOI: `10.1115/1.3644063`.

Hohenegger, C., P. Brockhaus, C. S. Bretherton, and C. Schär (2009). "The soil moisture-precipitation feedback in simulations with explicit and parameterized convection." *Journal of Climate* 22.19, pp. 5003–5020. DOI: `10.1175/2009JCLI2604.1`.

Hohenegger, C., A. Walser, W. Langhans, and C. Schär (2008). "Cloud-resolving ensemble simulations of the August 2005 Alpine flood." *Quarterly Journal of the Royal Meteorological Society* 134.633, pp. 889–904. DOI: `10.1002/qj.252`.

Holton, J. R. and G. J. Hakim (2012). *An introduction to dynamic meteorology*. Vol. 88. Academic press. DOI: `10.1119/1.1987371`.

Homar, V., R. Romero, D. Stensrud, C. Ramis, and S. Alonso (2003). "Numerical diagnosis of a small, quasi-tropical cyclone over the western Mediterranean: Dynamical vs. boundary factors." *Quarterly Journal of the Royal Meteorological Society* 129.590, pp. 1469–1490. DOI: `10.1256/qj.01.91`.

Hoskins, B. J., M. McIntyre, and A. W. Robertson (1985). "On the use and significance of isentropic potential vorticity maps." *Quarterly Journal of the Royal Meteorological Society* 111.470, pp. 877–946. DOI: `10.1002/qj.49711147002`.

Houze Jr, R. A. (2014). *Cloud dynamics*. Vol. 104. Academic press.

Hurk, B. van den, F. Doblas-Reyes, G. Balsamo, R. D. Koster, S. I. Seneviratne, and H. Camargo (2012). "Soil moisture effects on seasonal temperature and precipitation forecast scores in Europe." *Climate dynamics* 38.1-2, pp. 349–362. DOI: `10.1007/s00382-010-0956-2`.

Kendon, E. J., N. M. Roberts, C. A. Senior, and M. J. Roberts (2012). "Realism of rainfall in a very high-resolution regional climate model." *Journal of Climate* 25.17, pp. 5791–5806. DOI: `10.1175/JCLI-D-11-00562.1`.

Klemp, J., J. Dudhia, and A. Hassiotis (2008). "An upper gravity-wave absorbing layer for NWP applications." *Monthly Weather Review* 136.10, pp. 3987–4004. DOI: `10.1175/2008MWR2596.1`.

Klocke, D., M. Brueck, C. Hohenegger, and B. Stevens (2017). "Rediscovery of the doldrums in storm-resolving simulations over the tropical Atlantic." *Nature Geoscience* 10.12, p. 891. DOI: 10.1038/s41561-017-0005-4.

Koster, R. D., P. A. Dirmeyer, Z. Guo, G. Bonan, E. Chan, P. Cox, C. Gordon, S. Kanae, E. Kowalczyk, D. Lawrence, et al. (2004). "Regions of strong coupling between soil moisture and precipitation." *Science* 305.5687, pp. 1138–1140. DOI: 10.1126/science.1100217.

Lilly, D. K. (1962). "On the numerical simulation of buoyant convection." *Tellus* 14.2, pp. 148–172. DOI: 10.3402/tellusa.v14i2.9537.

Lintner, B. R., P. Gentine, K. L. Findell, F. D'Andrea, A. H. Sobel, and G. D. Salvucci (2013). "An idealized prototype for large-scale land–atmosphere coupling." *Journal of Climate* 26.7, pp. 2379–2389. DOI: 10.1175/JCLI-D-11-00561.1.

Lott, F. and M. J. Miller (1997). "A new subgrid-scale orographic drag parametrization: Its formulation and testing." *Quarterly Journal of the Royal Meteorological Society* 123.537, pp. 101–127. DOI: 10.1002/qj.49712353704.

Lynch, P. (2006). *The emergence of numerical weather prediction: Richardson's dream*. Cambridge University Press.

— (2008). "The origins of computer weather prediction and climate modeling." *Journal of Computational Physics* 227.7, pp. 3431–3444. DOI: 10.1016/j.jcp.2007.02.034.

Lynn, B. H., W.-K. Tao, and P. J. Wetzel (1998). "A study of landscape-generated deep moist convection." *Monthly weather review* 126.4, pp. 928–942. DOI: 10.1175/1520-0493(1998)126%3C0928:ASOLGD%3E2.0.CO;2.

MacLeod, D. A., H. L. Cloke, F. Pappenberger, and A. Weisheimer (2016). "Improved seasonal prediction of the hot summer of 2003 over Europe through better representation of uncertainty in the land surface." *Quarterly Journal of the Royal Meteorological Society* 142.694, pp. 79–90. DOI: 10.1002/qj.2631.

Maher, P., G. K. Vallis, S. C. Sherwood, M. J. Webb, and P. G. Sansom (2018). "The Impact of Parameterized Convection on Climatological Precipitation in Atmospheric Global Climate Models." *Geophysical Research Letters*. DOI: 10.1002/2017GL076826.

Manabe, S. (1969). "Climate and the ocean circulation 1: i. The atmospheric circulation and the hydrology of the earth's surface." *Monthly Weather Review* 97.11, pp. 739–774.

Maronga, B., M. Gryschka, R. Heinze, F. Hoffmann, F. Kanani-Sühring, M. Keck, K. Ketelsen, M. Letzel, M. Sühring, and S. Raasch (2015). "The Parallelized Large-Eddy Simulation Model (PALM) version 4.0 for atmospheric and oceanic flows: model formulation, recent developments, and future perspectives." *Geoscientific Model Devel-*

opment Discussions 8.2, pp. 1539–1637. DOI: `10.5194/gmd-8-2515-2015`.

Massacand, A. C., H. Wernli, and H. C. Davies (1998). "Heavy precipitation on the alpine southside: An upper-level precursor." *Geophysical Research Letters* 25.9, pp. 1435–1438.

Meehl, G. A., G. J. Boer, C. Covey, M. Latif, and R. J. Stouffer (2000). "The coupled model intercomparison project (CMIP)." *Bulletin of the American Meteorological Society* 81.2, pp. 313–318. DOI: `10.1175/1520-0477(2000)081%3C0313:TCMIPC%3E2.3.CO;2`.

Miglietta, M. M., D. Cerrai, S. Laviola, E. Cattani, and V. Levizzani (2017). "Potential vorticity patterns in Mediterranean "hurricanes"." *Geophysical Research Letters* 44.5, pp. 2537–2545. DOI: `10.1002/2017GL072670`.

Miglietta, M. M., S. Laviola, A. Malvaldi, D. Conte, V. Levizzani, and C. Price (2013). "Analysis of tropical-like cyclones over the Mediterranean Sea through a combined modeling and satellite approach." *Geophysical Research Letters* 40.10, pp. 2400–2405. DOI: `10.1002/grl.50432`.

Miglietta, M. M., D. Mastrangelo, and D. Conte (2015). "Influence of physics parameterization schemes on the simulation of a tropical-like cyclone in the Mediterranean Sea." *Atmospheric Research* 153, pp. 360–375. DOI: `10.1016/j.atmosres.2014.09.008`.

Miglietta, M. M., A. Moscatello, D. Conte, G. Mannarini, G. Lacorata, and R. Rotunno (2011). "Numerical analysis of a Mediterranean 'hurricane' over south-eastern Italy: sensitivity experiments to sea surface temperature." *Atmospheric research* 101.1, pp. 412–426.

Miralles, D. G., M. v. den Berg, A. Teuling, and R. d. Jeu (2012). "Soil moisture-temperature coupling: A multiscale observational analysis." *Geophysical Research Letters* 39.21. DOI: `10.1029/2012GL053703`.

Miralles, D. G., A. J. Teuling, C. C. van Heerwaarden, and J. V.-G. de Arellano (2014). "Mega-heatwave temperatures due to combined soil desiccation and atmospheric heat accumulation." *Nature Geoscience* 7.5, pp. 345–349. DOI: `10.1038/ngeo2141`.

Miyamoto, Y., Y. Kajikawa, R. Yoshida, T. Yamaura, H. Yashiro, and H. Tomita (2013). "Deep moist atmospheric convection in a sub-kilometer global simulation." *Geophysical Research Letters* 40.18, pp. 4922–4926. DOI: `10.1002/grl.50944`.

Miyamoto, Y., T. Yamaura, R. Yoshida, H. Yashiro, H. Tomita, and Y. Kajikawa (2016). "Precursors of deep moist convection in a subkilometer global simulation." *Journal of Geophysical Research: Atmospheres* 121.20. DOI: `10.1002/2016JD024965`.

Moscatello, A., M. Marcello Miglietta, and R. Rotunno (2008). "Observational analysis of a Mediterranean 'hurricane' over south-eastern Italy." *Weather* 63.10, p. 306. DOI: `10.1002/wea.231`.

Narcowich, F. J. and J. D. Ward (1994). "Generalized Hermite interpolation via matrix-valued conditionally positive definite func-

tions." *Mathematics of Computation* 63.208, pp. 661–687. DOI: `10.1090/S0025-5718-1994-1254147-6`.

Neelin, J. D. and N. Zeng (2000). "A quasi-equilibrium tropical circulation model – Formulation." *Journal of the atmospheric sciences* 57.11, pp. 1741–1766. DOI: `10.1175/1520-0469(2000)057%3C1741:AQETCM%3E2.0.CO;2`.

Orr, A., P. Bechtold, J. Scinocca, M. Ern, and M. Janiskova (2010). "Improved middle atmosphere climate and forecasts in the ECMWF model through a nonorographic gravity wave drag parameterization." *Journal of Climate* 23.22, pp. 5905–5926. DOI: `10.1175/2010JCLI3490.1`.

Petch, J., A. Brown, and M. Gray (2002). "The impact of horizontal resolution on the simulations of convective development over land." *Quarterly Journal of the Royal Meteorological Society* 128.584, pp. 2031–2044. DOI: `10.1256/003590002320603511`.

Peters, K. and C. Hohenegger (2017). "On the Dependence of Squall-Line Characteristics on Surface Conditions." *Journal of the Atmospheric Sciences* 74.7, pp. 2211–2228. DOI: `10.1175/JAS-D-16-0290.1`.

Picornell, M., J. Campins, and A. Jansà (2014). "Detection and thermal description of medicanes from numerical simulation." *Natural Hazards and Earth System Sciences* 14.5, p. 1059. DOI: `10.5194/nhess-14-1059-2014`.

Pincus, R. and B. Stevens (2009). "Monte Carlo spectral integration: A consistent approximation for radiative transfer in large eddy simulations." *Journal of Advances in Modelling Earth Systems* 2. DOI: `10.3894/JAMES.2009.1.1`.

Piper, D., M. Kunz, F. Ehmele, S. Mohr, B. Mühr, A. Kron, and J. Daniell (2016). "Exceptional sequence of severe thunderstorms and related flash floods in May and June 2016 in Germany-Part 1: Meteorological background." *Natural Hazards and Earth System Sciences* 16.12, p. 2835. DOI: `10.5194/nhess-16-2835-2016`.

Púčik, T., P. Groenemeijer, A. T. Rädler, L. Tijssen, G. Nikulin, A. F. Prein, E. van Meijgaard, R. Fealy, D. Jacob, and C. Teichmann (2017). "Future Changes in European Severe Convection Environments in a Regional Climate Model Ensemble." *Journal of Climate* 30.17, pp. 6771–6794.

Pytharoulis, I. (2017). "Analysis of a Mediterranean tropical-like cyclone and its sensitivity to the sea surface temperatures." *Atmospheric Research*. DOI: `10.1016/j.atmosres.2017.08.009`.

Pytharoulis, I., I. T. Matsangouras, I. Tegoulias, S. Kotsopoulos, T. S. Karacostas, and P. Nastos (2017). "Numerical Study of the Medicane of November 2014." In: *Perspectives on Atmospheric Sciences*. Springer, pp. 115–121. DOI: `10.1007/978-3-319-35095-0_17`.

Randall, D. A. and D. G. Cripe (1999). "Alternative methods for specification of observed forcing in single-column models and cloud

system models." *Journal of Geophysical Research: Atmospheres* 104.D20, pp. 24527–24545.

Raschendorfer, M. (2001). "The new turbulence parameterization of LM." *COSMO newsletter* 1, pp. 89–97.

Reale, O. and R. Atlas (2001). "Tropical cyclone–like vortices in the extratropics: Observational evidence and synoptic analysis." *Weather and forecasting* 16.1, pp. 7–34. DOI: 10.1175/1520-0434(2001)016%3C0007:TCLVIT%3E2.0.CO;2.

Rex, D. F. (1950). "Blocking action in the middle troposphere and its effect upon regional climate." *Tellus* 2.4, pp. 275–301. DOI: 10.3402/tellusa.v2i3.8546.

Ricchi, A., M. M. Miglietta, F. Barbariol, A. Benetazzo, A. Bergamasco, D. Bonaldo, C. Cassardo, F. M. Falcieri, G. Modugno, A. Russo, et al. (2017). "Sensitivity of a Mediterranean Tropical-Like Cyclone to Different Model Configurations and Coupling Strategies." *Atmosphere* 8.5, p. 92. DOI: 10.3390/atmos8050092.

Richardson, L. F. (1922). *Weather Prediction by Numerical Process*. Cambridge University Press. DOI: 10.1017/CBO9780511618291.

Rieck, M. (2015). "The role of heterogeneities and land-atmosphere interactions in the development of moist convection." PhD thesis. Universität Hamburg Hamburg.

Rieck, M., C. Hohenegger, and P. Gentine (2015). "The effect of moist convection on thermally induced mesoscale circulations." *Quarterly Journal of the Royal Meteorological Society* 141.691, pp. 2418–2428. DOI: 10.1002/qj.2532.

Rijtema, P. (1969). "Soil Moisture Forecasting. Publication No 513." *Institute for Land and Water Management Resources, Waginengen, The Netherlands*.

Robinson, F. J., M. D. Patterson, and S. Sherwood (2013). "A numerical modeling study of the propagation of idealized sea-breeze density currents." *Journal of the Atmospheric Sciences* 70.2, pp. 653–668. DOI: 10.1175/JAS-D-12-0113.1.

Robinson, F. J., S. Sherwood, and Y. Li (2008). "Resonant response of deep convection to surface hot spots." *Journal of the Atmospheric Sciences* 65.1, pp. 276–286. DOI: 10.1175/2007JAS2398.1.

Romera, R., M. Á. Gaertner, E. Sánchez, M. Domínguez, J. J. González-Alemán, and M. M. Miglietta (2017). "Climate change projections of medicanes with a large multi-model ensemble of regional climate models." *Global and Planetary Change* 151, pp. 134–143. DOI: 10.1016/j.gloplacha.2016.10.008.

Romero, R. and K. Emanuel (2013). "Medicane risk in a changing climate." *Journal of Geophysical Research: Atmospheres* 118.12, pp. 5992–6001. DOI: 10.1002/jgrd.50475.

Rotunno, R., J. B. Klemp, and M. L. Weisman (1988). "A theory for strong, long-lived squall lines." *Journal of the Atmospheric Sciences*

45.3, pp. 463–485. DOI: 10.1175/1520-0469(1988)045%3C0463:ATFSLL%3E2.0.CO;2.

Sagaut, P. (2006). *Large eddy simulation for incompressible flows: an introduction*. Springer Science & Business Media. DOI: 10.1088/0957-0233/12/10/707.

Savic-Jovcic, V. and B. Stevens (2008). "The structure and mesoscale organization of precipitating stratocumulus." *Journal of the Atmospheric Sciences* 65.5, pp. 1587–1605. DOI: 10.1175/2007JAS2456.1.

Schär, C., D. Lüthi, U. Beyerle, and E. Heise (1999). "The soil-precipitation feedback: A process study with a regional climate model." *Journal of Climate* 12.3, pp. 722–741. DOI: 10.1175/1520-0442(1999)012%3C0722:TSPFAP%3E2.0.CO;2.

Schlemmer, L. and C. Hohenegger (2014). "The formation of wider and deeper clouds as a result of cold-pool dynamics." *Journal of the Atmospheric Sciences* 71.8, pp. 2842–2858. DOI: 10.1175/JAS-D-13-0170.1.

Schlemmer, L., C. Hohenegger, J. Schmidli, and C. Schär (2012). "Diurnal equilibrium convection and land surface-atmosphere interactions in an idealized cloud-resolving model." *Quarterly Journal of the Royal Meteorological Society* 138.667, pp. 1526–1539. DOI: 10.1002/qj.1892.

Schrodin, R. and E. Heise (2002). "A new multi-layer soil model." *COSMO newsletter* 2, pp. 149–151.

Schulz, J.-P., G. Vogel, C. Becker, S. Kothe, U. Rummel, and B. Ahrens (July 2016). "Evaluation of the ground heat flux simulated by a multi-layer land surface scheme using high-quality observations at grass land and bare soil." *Meteorologische Zeitschrift*. DOI: 10.1127/metz/2016/0537.

Segal, M. and R. Arritt (1992). "Nonclassical mesoscale circulations caused by surface sensible heat-flux gradients." *Bulletin of the American Meteorological Society* 73.10, pp. 1593–1604. DOI: 10.1175/1520-0477(1992)073%3C1593:NMCCBS%3E2.0.CO;2.

Seibert, P., F. Beyrich, S.-E. Gryning, S. Joffre, A. Rasmussen, and P. Tercier (2000). "Review and intercomparison of operational methods for the determination of the mixing height." *Atmospheric environment* 34.7, pp. 1001–1027. DOI: 10.1016/S1352-2310(99)00349-0.

Seifert, A. and K. Beheng (2006). "A two-moment cloud microphysics parameterization for mixed-phase clouds. Part 2: Maritime vs. continental deep convective storms." *Meteorology and Atmospheric Physics* 92.1-2, pp. 67–82. DOI: 10.1007/s00703-005-0113-3.

Seneviratne, S. I., T. Corti, E. L. Davin, M. Hirschi, E. B. Jaeger, I. Lehner, B. Orlowsky, and A. J. Teuling (2010). "Investigating soil moisture–climate interactions in a changing climate: A review." *Earth-Science Reviews* 99.3, pp. 125–161. DOI: 10.1016/j.earscirev.2010.02.004.

Seneviratne, S. I., D. Lüthi, M. Litschi, and C. Schär (2006). "Land–atmosphere coupling and climate change in Europe." *Nature* 443.7108, p. 205. DOI: 10.1038/nature05095.

Siebesma, A. P., C. S. Bretherton, A. Brown, A. Chlond, J. Cuxart, P. G. Duynkerke, H. Jiang, M. Khairoutdinov, D. Lewellen, C.-H. Moeng, et al. (2003). "A large eddy simulation intercomparison study of shallow cumulus convection." *Journal of the Atmospheric Sciences* 60.10, pp. 1201–1219. DOI: 10.1175/1520-0469(2003)60%3C1201:ALESIS%3E2.0.CO;2.

Skamarock, W. C. (2004). "Evaluating mesoscale NWP models using kinetic energy spectra." *Monthly weather review* 132.12, pp. 3019–3032. DOI: 10.1175/MWR2830.1.

Sommeria, G. and J. Deardorff (1977). "Subgrid-scale condensation in models of nonprecipitating clouds." *Journal of the Atmospheric Sciences* 34.2, pp. 344–355. DOI: 10.1175/1520-0469(1977)034%3C0344:SSCIMO%3E2.0.CO;2.

Steel, R. and J. Torrie (1960). *Principles and procedures of statistics, with special reference to the biological sciences.*

Stevens, B., S. Bony, and M. Webb (2012). "Clouds on-off klimate intercomparison experiment (COOKIE)."

Stevens, B., C.-H. Moeng, A. S. Ackerman, C. S. Bretherton, A. Chlond, S. de Roode, J. Edwards, J.-C. Golaz, H. Jiang, M. Khairoutdinov, et al. (2005). "Evaluation of large-eddy simulations via observations of nocturnal marine stratocumulus." *Monthly weather review* 133.6, pp. 1443–1462. DOI: 10.1175/MWR2930.1.

Stewart, S. R. (2018). *Tropical Cyclone Report: Hurricane Ophelia*. Tech. rep. National Hurricane Center.

Stull, R. B. (2000). *Meteorology for scientists and engineers: a technical companion book with Ahrens' Meteorology Today*. Brooks/Cole.

Tawfik, A. B., P. A. Dirmeyer, and J. A. Santanello Jr (2015). "The heated condensation framework. Part I: Description and southern Great Plains case study." *Journal of Hydrometeorology* 16.5, pp. 1929–1945. DOI: 10.1175/JHM-D-14-0117.1.

Taylor, C. M. (2015). "Detecting soil moisture impacts on convective initiation in Europe." *Geophysical Research Letters* 42.11, pp. 4631–4638. DOI: 10.1002/2015GL064030.

Taylor, C. M., R. A. de Jeu, F. Guichard, P. P. Harris, and W. A. Dorigo (2012). "Afternoon rain more likely over drier soils." *Nature* 489.7416, pp. 423–426. DOI: 10.1038/nature11377.

Tibaldi, S. and F. Molteni (1990). "On the operational predictability of blocking." *Tellus A: Dynamic Meteorology and Oceanography* 42.3, pp. 343–365. DOI: 10.3402/tellusa.v42i3.11882.

Tippett, M. K., J. T. Allen, V. A. Gensini, and H. E. Brooks (2015). "Climate and hazardous convective weather." *Current Climate Change Reports* 1.2, pp. 60–73. DOI: 10.1007/s40641-015-0006-6.

Tompkins, A. M. (2001). "Organization of tropical convection in low vertical wind shears: The role of cold pools." *Journal of the Atmospheric Sciences* 58.13, pp. 1650–1672. DOI: `10.1175/1520-0469(2001) 058%3C1650:OOTCIL%3E2.0.CO;2`.

Tous, M. and R. Romero (2013). "Meteorological environments associated with medicane development." *International Journal of Climatology* 33.1, pp. 1–14. DOI: `10.1002/joc.3428`.

Tous, M., R. Romero, and C. Ramis (2013). "Surface heat fluxes influence on medicane trajectories and intensification." *Atmospheric research* 123, pp. 400–411. DOI: `10.1016/j.atmosres.2012.05.022`.

Tous, M., G. Zappa, R. Romero, L. Shaffrey, and P. L. Vidale (2016). "Projected changes in medicanes in the HadGEM3 N512 high-resolution global climate model." *Climate Dynamics* 47.5-6, pp. 1913–1924. DOI: `10.1007/s00382-015-2941-2`.

Trenberth, K. E. (1999). "Atmospheric moisture recycling: Role of advection and local evaporation." *Journal of Climate* 12.5, pp. 1368–1381. DOI: `10.1175/1520-0442(1999)012%3C1368:AMRROA%3E2.0. CO;2`.

Tuttle, S. and G. Salvucci (2017). "Confounding factors in determining causal soil moisture-precipitation feedback." *Water Resources Research*. DOI: `10.1002/2016WR019869`.

Van der Ent, R. J., H. H. Savenije, B. Schaefli, and S. C. Steele-Dunne (2010). "Origin and fate of atmospheric moisture over continents." *Water Resources Research* 46.9. DOI: `10.1029/2010WR009127`.

Van Heerwaarden, C. C., J. Vilà-Guerau de Arellano, A. Gounou, F. Guichard, and F. Couvreux (2010). "Understanding the daily cycle of evapotranspiration: A method to quantify the influence of forcings and feedbacks." *Journal of Hydrometeorology* 11.6, pp. 1405–1422. DOI: `10.1175/2010JHM1272.1`.

VanZanten, M. C., B. Stevens, L. Nuijens, A. P. Siebesma, A. Ackerman, F. Burnet, A. Cheng, F. Couvreux, H. Jiang, M. Khairoutdinov, et al. (2011). "Controls on precipitation and cloudiness in simulations of trade-wind cumulus as observed during RICO." *Journal of Advances in Modeling Earth Systems* 3.2. DOI: `10.1029/ 2011MS000056`.

Wan, H., M. A. Giorgetta, G. Zängl, M. Restelli, D. Majewski, L. Bonaventura, K. Fröhlich, D. Reinert, P. Rıpodas, L. Kornblueh, et al. (2013). "The ICON-1.2 hydrostatic atmospheric dynamical core on triangular grids, Part I: formulation and performance of the baseline version." *Geoscientific Model Development* 6, pp. 735–763. DOI: `10.5194/gmd-6-735-2013`.

Wang, G., Y. Kim, and D. Wang (2007). "Quantifying the strength of soil moisture-precipitation coupling and its sensitivity to changes in surface water budget." *Journal of Hydrometeorology* 8.3, pp. 551–570. DOI: `10.1175/JHM573.1`.

Wedi, N. P. (2014). "Increasing horizontal resolution in numerical weather prediction and climate simulations: illusion or panacea?" *Phil. Trans. R. Soc. A* 372.2018, p. 20130289. DOI: 10.1098/rsta.2013.0289.

Wei, J., H. Su, and Z.-L. Yang (2016). "Impact of moisture flux convergence and soil moisture on precipitation: a case study for the southern United States with implications for the globe." *Climate Dynamics* 46.1-2, pp. 467–481. DOI: 10.1007/s00382-015-2593-2.

Weisman, M. L., W. C. Skamarock, and J. B. Klemp (1997). "The resolution dependence of explicitly modeled convective systems." *Monthly Weather Review* 125.4, pp. 527–548. DOI: 10.1175/1520-0493(1997)125%3C0527:TRDOEM%3E2.0.CO;2.

Yan, H. and R. A. Anthes (1988). "The effect of variations in surface moisture on mesoscale circulation." *Monthly Weather Review* 116.1, pp. 192–208. DOI: 10.1175/1520-0493(1988)116%3C0192:TEOVIS%3E2.0.CO;2.

Zängl, G., D. Reinert, P. Rípodas, and M. Baldauf (2015). "The ICON (ICOsahedral Non-hydrostatic) modelling framework of DWD and MPI-M: Description of the non-hydrostatic dynamical core." *Quarterly Journal of the Royal Meteorological Society* 141.687, pp. 563–579. DOI: 10.1002/qj.2378.

Zhou, Y., D. Wu, W. K.-M. Lau, and W.-K. Tao (2016). "Scale Dependence of Land–Atmosphere Interactions in Wet and Dry Regions as Simulated with NU-WRF over the Southwestern and South-Central United States." *Journal of Hydrometeorology* 17.8, pp. 2121–2136. DOI: 10.1175/JHM-D-16-0024.1.

Zipser, E. J., D. J. Cecil, C. Liu, S. W. Nesbitt, and D. P. Yorty (2006). "Where are the most intense thunderstorms on Earth?" *Bulletin of the American Meteorological Society* 87.8, pp. 1057–1072. DOI: 10.1175/BAMS-87-8-1057.

Hiermit erkläre ich an Eides statt, dass ich die vorliegende Dissertationschrift selbst verfasst und keine andereen als die angegebenen Quellen und Hiflsmittel benutzt habe.

I hereby declare, on oath, that I have written the present dissertation by myself and have not used other than the acknowledged resources and aids.

Hamburg, den 30 April 2018

Guido Cioni